

Washington University in St. Louis

## Washington University Open Scholarship

---

McKelvey School of Engineering Theses & Dissertations

McKelvey School of Engineering

---

Summer 8-15-2022

### Plasmonic Nanomaterials-Based Point-of-Care Biosensors

Rohit Gupta

*Washington University in St. Louis*

Follow this and additional works at: [https://openscholarship.wustl.edu/eng\\_etds](https://openscholarship.wustl.edu/eng_etds)



Part of the [Biomedical Engineering and Bioengineering Commons](#), [Elementary Particles and Fields and String Theory Commons](#), [Materials Science and Engineering Commons](#), and the [Mechanics of Materials Commons](#)

---

#### Recommended Citation

Gupta, Rohit, "Plasmonic Nanomaterials-Based Point-of-Care Biosensors" (2022). *McKelvey School of Engineering Theses & Dissertations*. 786.

[https://openscholarship.wustl.edu/eng\\_etds/786](https://openscholarship.wustl.edu/eng_etds/786)

This Dissertation is brought to you for free and open access by the McKelvey School of Engineering at Washington University Open Scholarship. It has been accepted for inclusion in McKelvey School of Engineering Theses & Dissertations by an authorized administrator of Washington University Open Scholarship. For more information, please contact [digital@wumail.wustl.edu](mailto:digital@wumail.wustl.edu).

WASHINGTON UNIVERSITY IN ST. LOUIS

McKelvey School of Engineering  
The Institute of Materials Science and Engineering

Dissertation Examination Committee:

Srikanth Singamaneni, Chair

Shantanu Chakrabartty

Jianjun Guan

Jeremiah J. Morrissey

Erica L. Scheller

Plasmonic Nanomaterials-Based Point-of-Care Biosensors  
by  
Rohit Gupta

A dissertation presented to  
the McKelvey School of Engineering  
of Washington University in  
partial fulfillment of the  
requirements for the degree  
of Doctor of Philosophy

August 2022  
St. Louis, Missouri

© 2022, Rohit Gupta

# Table of Contents

List of Figures .....	vi
List of Tables .....	xix
Acknowledgments.....	xx
Abstract.....	xxiii
Chapter 1: Introduction.....	1
1.1 Research Objectives .....	4
1.1.1 Objective 1: Design and realize paper-based SERS and LSPR label-free biosensors for point-of-care diagnostics.....	4
1.1.2 Objective 2: Enhance the stability of antibodies immobilized on plasmonic transducers through organosilica encapsulation for POC applications. ....	5
1.1.3 Objective 3: Realize plasmonically-active tissue analogs for rapid, ultrasensitive, and quantitative detection of inflammatory disease burden. ....	6
1.1.4 Objective 4: Design and realize plasmonically-enhanced ultrasensitive immunoassays that can be implemented in clinical labs and at the point-of-care. ....	6
1.2 Background and Motivation.....	8
1.2.1 Plasmonic paper microneedle patch for point-of-care diagnosis of biomolecules in interstitial fluid (ISF).....	8
1.2.2 Plasmonic paper for non-invasive and point-of-care diagnosis of renal cancer.....	11
1.2.3 Organosilica encapsulated biorecognition elements for stable and refreshable plasmonic biosensor. ....	15
1.2.4 Collagen foam-based biosensors for detection of collagenase and periodontal disease monitoring. ....	17
1.2.5 Digital fluoroimmunoassay for sub-femtomolar detection of protein biomarkers.....	20
1.2.6 Plasmon-enhanced, quantitative lateral flow Assay for femtomolar detection of protein biomarkers in point-of-care settings. ....	24
1.3 Dissertation outline .....	26
Chapter 2: Plasmonic Paper Microneedle Patch for On-Patch Detection of Molecules in Dermal Interstitial Fluid.....	29
2.1 Abstract .....	29
2.2 Materials and Methods .....	30
2.3 Plasmonic paper .....	34

2.4 ISF Collection Using Plasmonic Paper Microneedle Patch .....	35
2.5 SERS Performance of Plasmonic Paper .....	36
2.6 R6G Pharmacokinetics in ISF Determined by On Patch SERS Measurement Using Plasmonic Paper Microneedle Patches.....	38
2.7 Binding of R6G to Plasma Proteins .....	39
2.8 Conclusions and Outlook .....	40
Chapter 3: Bioplasmonic Paper-based Assay for Non-invasive Detection of Perilipin-2 for Renal Cancer .....	42
3.1 Abstract .....	42
3.2 Materials and Methods .....	43
3.3 Bioplasmonic paper characterization and PLIN-2 dose-response.....	47
3.4 PLIN-2 dose-response curve and repeatability .....	48
3.5 Clinical study.....	50
3.6 Conclusions and Outlook .....	50
Chapter 4: Refreshable Nanobiosensor-based on Organosilica Encapsulation of Biorecognition Elements.....	53
4.1 Abstract .....	53
4.2 Materials and Methods .....	54
4.3 LSPR-based biosensor for detection of IgG.....	57
4.4 Refreshability of AuNR-IgG biosensor.....	58
4.5 Polymer encapsulation strategy to achieve refreshability .....	62
4.6 Characterization and optimization of organosilica silica layer thickness .....	63
4.7 Specificity of polymer encapsulated AuNR-IgG biosensor .....	65
4.8 Refreshability of polymer encapsulated AuNR-IgG biosensor.....	66
4.9 Long-term usability of polymer encapsulated AuNR-IgG biosensor .....	68
4.10 Biological stability of AuNR-IgG biosensor.....	69
4.11 Other chemical regeneration agents to Refresh polymer encapsulated biosensors.....	70
4.12 Universality of polymer encapsulation strategy .....	71
4.13 Conclusions and Outlook .....	74
Chapter 5: Plasmonically-active Tissue Analogs for Rapid and Ultrasensitive Quantification of Inflammatory Disease Burden .....	75
5.1 Abstract .....	75

5.2 Materials and Methods .....	76
5.3 Plasmonic-fluor as reporter element .....	80
5.4 Collagen plasmonic foam characterization .....	81
5.5 Specificity and kinetics of collagen plasmonic foam.....	83
5.6 Comparison with commercial kit and real-world applicability.....	86
5.7 Conclusions and Outlook .....	88
Chapter 6: Digital fluoroimmunoassay for Sub-Femtomolar Detection of Protein Biomarkers ..	89
6.1 Abstract .....	89
6.2 Materials and Methods .....	90
6.3 Digital plasmonic fluor-linked immunosorbent assay .....	96
6.4 Ultrasensitive detection of SARS-CoV-2 antigens using plasmon-enhanced digital assay .....	103
6.5 ACE-2 and E06 bind to non-overlapping epitopes of the spike protein .....	104
6.6 Testing clinical samples .....	105
6.7 Comparison with commercial antigen kit and the ability to detect variants: .....	108
6.8 Conclusions and Outlook .....	111
6.9 Supplementary information.....	111
Chapter 7: Plasmon-enhanced, Quantitative Lateral Flow Assay for Femtomolar Detection of Protein Biomarkers in Point-of-care Settings .....	112
7.1 Abstract .....	112
7.2 Materials and Methods .....	113
7.3 Plasmonic-fluors increases sensitivity over AuNPs by 10000-fold in LFAs.....	123
7.4 Bioanalytical parameters of p-LFA compared to LFA .....	125
7.5 p-LFA for quantitative detection of human IL-6 .....	129
7.6 Ultrasensitive p-LFA for SARS-CoV-2 serology .....	131
7.7 p-LFA for SARS-CoV-2 antigen detection.....	134
7.8 Point-of-care p-LFA using an inexpensive, portable fluorescence scanner.....	138
7.9 Conclusions and Outlook .....	142
7.10 Supplementary information.....	143
Chapter 8: Conclusions and Outlook .....	144
8.1 Conclusion.....	144

8.2 Outlook.....	146
References.....	149
Appendix A: Supporting Information for Chapter 6.....	173
Appendix B: Supporting Information for Chapter 7.....	179
Human IL-6 enzyme-linked immunosorbent immunoassay .....	179
Biotinylation of anti-human IgG.....	179
Biotinylation of N protein detection antibody .....	180
Antibody conjugation on plasmonic-fluor .....	180
RMC calculations.....	180
Data processing on the data acquired by portable scanner: .....	182

# List of Figures

<b>Figure 1. 1:</b> Schematic illustration of (left) label-free and (right) labelled immunoassay. In case of label-free biosensors we employ transduction platform based on plasmonic nanoparticles, while in case of labeled immunoassay we augment the sensitivity of the nanolabel by utilizing plasmonically enhanced ultrabright fluorescent nanoparticles to augment bioanalytical parameters of the biosensors. ....	2
<b>Figure 1. 2:</b> Detection of biomarkers from ISF using plasmonic paper MN patch for on-patch detection by SERS versus conventional paper MN patch requiring multiple sample processing steps. (A) After ISF is collected using a plasmonic paper MN patch, biomarker analysis can be performed in situ on the plasmonic paper using SERS. (B) After ISF is collected using a conventional paper MN patch, biomarkers must be eluted and undergo additional steps for sample processing and biomarker analysis. ....	11
<b>Figure 1. 3:</b> Schematic illustration of plasmonic paper manufacture. Gold nanorattles (AuNRTs) coated with cetyltrimethylammonium chloride (CTAC) were functionalized with monoclonal antibody by means of a bifunctional polyethylene glycol (PEG). The functionalized AuNRTs were then coated on filter paper and non-specific binding sites neutralized by further PEGylation. The paper-bound functionalized AuNRTs then bind specific analyte; in this case, perilipin-2 (PLIN-2) and cause a red shift in the localized surface plasmon resonance (LSPR) for the AuNRTs. ....	14
<b>Figure 1. 4:</b> (Left) Schematic illustration of the steps involved in the organosilica-based biopreservation of bioconjugates to realize refreshable biosensors. (Right) Typical LSPR wavelength shift response after alternate exposure of polymer encapsulated biosensors to analyte and SDS. ....	17
<b>Figure 1. 5:</b> Schematic illustration of steps involved in measurement of collagenase concentration in saliva using collagen plasmonic foam. ....	20
<b>Figure 1. 6:</b> Schematic illustration analog and digital p-FLISA.....	21
<b>Figure 1. 7:</b> (A) Schematic illustration of plasmonic-fluor, employed as a bimodal nanolabel (colorimetric+fluorescent) in LFAs, comprising of gold nanorod as plasmonic core, polymer layer as spacer, molecular fluorophores (800CW), and biotin as recognition element. (B) Transmission electron microscopy image of plasmonic-fluors.....	25
<b>Figure 2. 1:</b> Characterization of AuNRs and plasmonic paper. (A) Representative transmission electron microscopy image of AuNRs dispersed in nanopure water. (B) Representative ultraviolet-visible light extinction spectrum of PSS-AuNRs in nanopure water. (C) Representative scanning	



electron microscopy image of PSS-AuNRs adsorbed on filter paper after “drawing” by plasmonic calligraphy..... 35

**Figure 2. 2:** Collection of ISF using a plasmonic paper microneedle patch. (A) Representative photographic image of a MN patch showing a row of nine MNs measuring 650  $\mu\text{m}$  in length extending from a patch backing with a thin rectangular strip of plasmonic paper adhered to one side. (B) Representative photographic image of the onset of ISF collection after two insertions of a MN patch into the skin of a hairless rat in vivo. The MNs, which are on the lower edge of the patch, are not visible because they are inserted into the skin. ISF is collected in the paper reservoir as observed by wetness of the paper (arrow). (C) Representative photographic image of rat skin 1 min after ISF collection by MN patch. The site of MN insertion has been marked with a rectangular box..... 36

**Figure 2. 3:** Measurement of R6G in plasmonic paper by SERS. Representative SERS spectra obtained from plasmonic paper soaked in different concentrations of R6G in (A) ISF and (C) serum. The Raman spectra show an increase in characteristic Raman peaks for R6G at 610, 1364 and 1512  $\text{cm}^{-1}$  with increase in concentration. The Raman band at 1364  $\text{cm}^{-1}$  (indicated with a black rectangular box) was used to generate calibration curves for R6G concentration in (B) ISF and (D) serum. Data points show mean  $\pm$  standard deviation from 6 spectra collected from each plasmonic paper substrate. .... 37

**Figure 2. 4:** Representative spectra from on-patch SERS measurement of samples collected in rats in vivo. (A) ISF was collected on plasmonic paper MN patches. (B) Blood was collected by intravenous catheter, from which serum was isolated and placed on plasmonic paper MN patches. .... 40

**Figure 2. 5:** Pharmacokinetics of R6G in ISF and serum. (A) On-patch SERS measurement using plasmonic paper MN patches or (B) fluorescence spectroscopy of R6G eluted from conventional paper MN patches. Data points show mean  $\pm$  standard deviation ( $n = 6$  rats). .... 40

**Figure 3. 1:** (A) TEM image of gold nanorattles (AuNRTs). (B) vis-NIR extinction spectra demonstrating successful conjugation of SH-PEG-anti PLIN2 on AuNRTs. After incubating with SH-PEG-IgG, the  $\lambda_{\text{max}}$  shifts by 6 nm (AuNRTs-anti PLIN2, red). (C) SEM images of paper adsorbed with AuNRTs-anti PLIN2 conjugates. (D) Surface enhanced Raman scattering spectra with on AuNRTs reveals the Raman bands corresponding to anti human PLIN2 IgG<sub>2B</sub>. .... 48

**Figure 3. 2:** (A) Comparison of PLIN-2 standard curves from November 2016 (solid line and diamonds) and March 2019 (dashed line and triangles). The mean and standard deviation of five standard curves from November 2016 and three replicates at each concentration in March 2019 are depicted. (B) Dilution of PLIN-2 standard in synthetic urine (solid line) or pooled human urine of normal individuals (dashed line). Mean and standard deviation of three replicates at each concentration is depicted..... 49

**Figure 3. 3:** (A) Representative localized surface plasmon resonance spectra of anti-perilipin-2 (anti-PLIN-2) functionalized gold nanorattles (AuNRTs) (black), functionalized AuNRTs incubated with urine from a healthy volunteer (red), and functionalized AuNRTs incubated with urine from a patient with renal clear cell carcinoma (blue). (B) Box and whisker plot of the urine PLIN-2 concentrations of 20 control patients, 20 patients with renal cell cancer, 8 patients with bladder cancer, and 10 patients with diabetic nephropathy. The median with whiskers and boxes depicting the interquartile range is shown. The concentration of each patient is depicted as a solid dot or a plus sign. The plus signs are outliers more than 1.5 times but less than 3.0 times the interquartile range. Patients with renal cell cancer have significantly higher urine PLIN-2 concentrations than that of other cohorts ( $P < 0.001$  by Kruskal-Wallis). (C) Urine PLIN-2 concentration of patients with renal cell cancer as a function of tumor size. The Spearman correlation coefficient is 0.59 ( $P = 0.009$ ). Regression line, solid line; 95% prediction interval, dashed lines. (D) Urine PLIN-2 concentration determined by plasmonic paper versus relative absorbance by Western blot. Dashed line of identity. Spearman correlation = 0.94 ( $P < 0.001$ ). PEG, polyethylene glycol. .... 51

**Figure 4. 1:** (A) Representative TEM image of AuNRs used as plasmonic nanotransducers. (B) Normalized vis-NIR extinction spectra of AuNR and AuNR conjugated with IgG, depicting ~8 nm redshift in LSPR wavelength. (C) Representative AFM image showing uniform distribution of AuNR-IgG bioconjugates on glass substrate. (D) Schematic illustration of steps involved in the fabrication of refreshable sensor. (E) Extinction spectra of AuNR-IgG bioconjugates obtained after each fabrication step shown in (D). Inset shows zoomed in spectra highlighting the shifts in the LSPR wavelength. (F) LSPR shifts corresponding to biodetection and sensor refreshing. (G) LSPR shift upon exposure of plasmonic biochips to different concentrations of anti-IgG before (black) and after SDS (red) treatment. Error bars represent standard deviations from three different samples..... 60

**Figure 4. 2:** (A) Schematic illustration of the steps involved in the organosilica-based biopreservation of bioconjugates to realize refreshable biosensors. (B) Representative AFM image of AuNR-IgG bioconjugates on glass substrate before (top) and after (bottom) polymer encapsulation with optimum monomer concentration (0.8 mg/ml). (C) Surface enhanced Raman scattering spectra of AuNR-IgG bioconjugates before and after polymerization. (D) Biorecognition capability corresponding to different monomer concentrations, which determines the polymer thickness. (E) Retained biorecognition capability of AuNR-IgG bioconjugates corresponding to different monomer concentrations, after SDS treatment. (F) LSPR shift of the polymer encapsulated biosensor after treatment with HSA and anti-IgG. Error bars represent standard deviations from three different samples. .... 61

**Figure 4. 3:** (A) AuNR extinction spectra corresponding to each step involved in the polymer encapsulation strategy. Inset shows zoomed in spectra highlighting the shifts in the LSPR wavelength. (B) LSPR shift corresponding to each step involved in the polymer encapsulation

strategy. **(C)** LSPR shift upon exposure of polymer-encapsulated biosensors to different concentrations of anti-IgG before (black) and after SDS (red) treatment. **(D)** LSPR wavelength shift after alternate exposure to anti-IgG and SDS. **(E)** Retained biorecognition capability of biosensors with and without polymer encapsulation over multiple capture/release cycles of the analyte. **(F)** Retained biorecognition capability of AuNR-IgG bioconjugates with and without polymer encapsulation stored at room temperature, 40 and 60°C for different durations. Error bars represent standard deviations from three different samples. .... 66

**Figure 4. 4:** **(A)** (%) Retained biorecognition capability of pristine and polymer encapsulated AuNR-IgG based biosensors after it had been subjected to different conditions of proteolytic degradation at room temperature. LSPR wavelength shift after alternate exposure of polymer encapsulated biosensors to anti-IgG and NaOH **(B)**, PA **(C)** and glycine buffer **(D)**. Error bar represents standard deviation from three independent samples..... 70

**Figure 4. 5:** **(A)** Representative TEM image of Au nanorattles (AuNRT) used as nanotransducers. **(B)** LSPR shift upon exposure of AuNRT-NGAL antibody bioconjugates to different concentrations of NGAL before (black) and after SDS (red) treatment. **(C)** Extinction spectra corresponding to each step involved in the polymer encapsulation strategy of AuNRT-NGAL antibody bioconjugates. Inset shows zoomed in spectra highlighting the shifts in the LSPR wavelength. **(D)** LSPR shift upon exposure of polymer encapsulated AuNRT-NGAL antibody bioconjugates to different concentrations of NGAL before (black) and after SDS (red) treatment. **(E)** Retained biorecognition capability of biosensors with and without polymer encapsulation over multiple capture/release cycles of NGAL. **(F)** Retained biorecognition capability of AuNR-IgG bioconjugates with and without polymer encapsulation stored at room temperature, 40 and 60°C for different durations. Error bar represents standard deviations from three different samples... 73

**Figure 5. 1:** **(A)** Schematic illustration of plasmonic-fluor, employed as the reporter element, comprising of gold nanorod as plasmonic core, polymer layer as spacer, molecular fluorophores (800CW), and biotin as recognition element. **(B)** Transmission electron microscopy image of plasmonic-fluors. **(C)** UV-vis absorbance spectra of plasmonic-fluor in solution. Inset depicts the UV-vis absorbance of the collagen foam loaded with plasmonic-fluors. **(D)** Schematic illustration of collagen foam based approach for quantitative detection of collagenase. SEM images of **(E)** freeze dried collagen foam, **(F)** collagen foam after pre-treatment, **(G)** collagen plasmonic foam and **(H)** individual collagen fibers decorated with PFs (inset shows photograph of collagen foam with (right) and without (left) plasmonic-fluors)..... 82

**Figure 5. 2:** **(A)** Dose-dependence of plasmonic-fluor with respect to its fluorescence intensity (black) and extinction (blue). **(B)** Fluorescence intensities of collagen foams (n=20) with conventional fluorophore (CF\_strep-800CW) and PF (CF\_strep-800CW\_PF). **(C)** The fluorescence intensity from both plasmonic-fluors and conventional fluorophore over period of time when exposed to high concentration of collagenase (1mg/ml). Confocal fluorescence image of collagen foam loaded with **(D)** conventional fluorophores and **(E and F)** plasmonic-fluors.. 83

**Figure 5. 3:** (A) Kinetics study of action of collagenase on different collagen foams. Change in fluorescence intensities with respect to time at different concentration of collagenase. (B) TEM image of the solution obtained after degradation of collagen plasmonic foam in collagenase solution. (C) Change in fluorescence intensity with respect to time at different concentration of trypsin and collagenase, corroborating specificity of collagenase action on collagen foam. (D) Fluorescence intensity obtained from the solution containing collagen plasmonic foam and same concentration of collagenase over a period of time. n=3. .... 84

**Figure 5. 4:** (A) Change in fluorescence intensities with respect to time at different concentration of collagenase when measured using collagen plasmonic foam. (B) Change in absorbance with respect to time at different concentration of collagenase when measured using commercially available collagenase colorimetric kit. (C) Dose response curve to determine collagenase concentration, depicting increase fluorescence intensity in 10 minutes with respect to different concentration of collagenase. (D) Dose response curve to determine collagenase concentration, depicting change in absorbance in 10 minutes with respect to different concentration of collagenase. (E) Change in fluorescence intensities with respect to time and different human saliva samples when measured using collagen plasmonic foam. (F) Change in absorbance with respect to time and different human saliva samples when measured using commercially available collagenase colorimetric kit. .... 85

**Figure 6. 1:** (A) Schematic illustration comparing ELISA, Analog p-FLISA and Digital p-FLISA. (B) Confirmation of single particle fluorescence by correlating scanning electron microscopic images (left) and epifluorescence microscopy images (right) of the same plasmonic-fluor nanolabel. Scale bar: 5  $\mu$ m. (C) Theoretical model for comparing analog and digital p-FLISA and its effect on the slope of the standard curve for low concentration of analyte. (D) Schematic illustration representing the effect of background on the signal for analog and digital imaging. Confirmation of single particle fluorescence by correlating scanning electron microscopic images (left) and epifluorescence microscopy images (right) of the same plasmonic-fluor nanolabel. Scale bar: 5  $\mu$ m. .... 100

**Figure 6. 2:** Sensitivity of Human IL-6 digital p-FLISA is better than analog p-FLISA and ELISA (A) Fluorescence image of analog p-FLISA, (B) Epifluorescence microscopic images of digital p-FLISA, (C) zoomed-in epifluorescence images of digital p-FLISA for 0.512 fg/ml and 1.6 fg/ml of human IL-6. (D) Particle count vs. concentration plot of digital p-FLISA of human IL-6. n=2 (5 images per well). (E) Fluorescence intensity vs. concentration plot for analog p-FLISA. n=3. (F) Comparison of analog vs. digital. (G) ELISA (n=3). Digital R<sup>2</sup>= 0.9939, Analog R<sup>2</sup>= 0.9995, ELISA R<sup>2</sup>=0.9992. .... 101

**Figure 6. 3:** Left panel (A), (B), (C) shows the schematic illustration representing different combinations of biorecognition elements used for detecting SARS-CoV-2 virus and protein. Middle panel: Fluorescence intensity vs. concentration plot (analog p-FLISA) for detection of (A) spike protein on the intact virus, (B) recombinant spike protein, (C) recombinant nucleocapsid

protein. n=2. Right panel: Particle count vs. concentration plot (digital p-FLISA) of A spike protein on the intact virus, (B) recombinant spike protein, (C) recombinant nucleocapsid protein. n=2 (5 images per well). Spike protein on virus: analog  $R^2= 0.9901$ , digital  $R^2= 0.9932$ , recombinant spike protein: analog  $R^2= 0.9989$ , digital  $R^2 = 0.9875$ , recombinant nucleocapsid protein: analog  $R^2 = 0.9967$ , digital  $R^2 = 0.9953$ ..... 102

**Figure 6. 4:** (A) Schematic illustration representing the collection of human nasopharyngeal (NP) swabs and saliva samples followed by digital pFLISA. (B) Concentration of nucleocapsid protein in PCR-positive and PCR-negative human swabs and saliva, \*\*p=0.0041, unpaired t test (two-tailed) with Welch’s correction, (C) Concentration of nucleocapsid protein and spike protein in PCR-positive and PCR-negative human NP swabs and saliva. and (D) Correlation between the concentration of nucleocapsid protein and spike protein in PCR-positive patient samples (Pearson’s correlation  $r= 0.4254$ ). Lack of cross-reactivity of (E) nucleocapsid protein and (F) spike protein assay against recombinant protein from HCoV-HKU1 and MERS-CoV. Particle count corresponding to concentration of G) nucleocapsid protein and H) spike protein in patient samples tested positive for seasonal coronaviruses and other respiratory viruses..... 106

**Figure 6. 5:** (A) Digital assay for nucleocapsid protein derived from SARS-CoV-2 variants B.1.1.7 (alpha) and B.1.351 (beta). (B) Concentration of nucleocapsid protein in samples positive for SARS-CoV-2 variant B.1.617.2 (delta). (C) Comparison of the performance of commercial antigen kit (BD Veritor™) with that of nucleocapsid protein digital assay (n=2). (D) Detected nucleocapsid protein by digital assay (black bars) and BD Veritor kit™ (marked with #) in PCR positive patient samples (n=19). ..... 108

**Figure 7. 1:** Gold nanoparticles and plasmonic-fluors as nanolabels for LFA. (A) Schematic illustration of plasmonic-fluor, employed as a bimodal nanolabel (colorimetric+fluorescent) in LFAs, comprising of gold nanorod as plasmonic core, polymer layer as spacer, molecular fluorophores (800CW), and biotin as recognition element. Transmission electron microscopy image of (B) AuNPs and (C) plasmonic-fluors. (D) Mean gray values obtained from nitrocellulose membrane drop-casted with different concentrations of AuNPs. Inset shows the 8-bit ImageJ-processed image of the nitrocellulose membrane. Fluorescence intensities obtained from nitrocellulose membrane drop-casted with different concentrations of (E) plasmonic-fluors and (F) molecular fluorophores. Inset shows the corresponding fluorescence image of the nitrocellulose membrane. (G) Mean gray values obtained from nitrocellulose membranes, with biotinylated-BSA used as capture-ligand at test sites, after exposure to different concentrations of streptavidin-conjugated AuNPs. Inset shows the schematic illustration of streptavidin-conjugated AuNPs. (H) Fluorescence intensities obtained from nitrocellulose membranes, with biotinylated-BSA as recognition elements at test sites, after exposure to different concentrations of streptavidin-conjugated plasmonic-fluors. Inset shows the schematic illustration of streptavidin-conjugated plasmonic-fluors. Purple arrows indicate the direction of flow of the nanoconjugates. Error bars represent standard deviations from four different samples (n=4). ..... 127

**Figure 7. 2:** Quantitative p-LFA of human IL-6. (A) Schematic illustration of IL-6 LFA strips comprising an IL-6 capture antibody test spot and a sheep IgG control spot. (B) Schematic illustration of AuNP-based IL-6 LFA, and (C) dose-dependent mean gray values, corresponding to different IL-6 concentrations, acquired from these AuNP-based LFAs. (D) Schematic illustration of IL-6 p-LFA and (E) dose-dependent fluorescence intensities of IL-6 p-LFA. 8-bit, ImageJ processed images of (F) AuNP-based IL-6 LFAs and (G) IL-6 p-LFAs, depicting the visual readout mode. (H) Fluorescence images of the IL-6 p-LFA strips depicting the fluorescence readout mode. (I) Resolution of molecular concentration (RMC) curves for ELISA, p-FLISA and p-LFA. The dashed lines indicate RMC cutoffs at  $\mu=2$  and  $\mu=5$ ; intersections of dashed lines and RMC curves indicate the range of concentrations over which a specific quantitative performance of the assay is achieved. For IL-6 p-LFA,  $\mu < 2$  over a concentration range over of 0.13–86.0 pg/mL, suggesting that IL-6 p-LFA can distinguish signals corresponding to any two concentrations within that range that differ by at least 100% with at least 99% confidence. The relevant RMC parameters are listed in Table S1. (J) Stability of IL-6 p-LFA over 7 months, as evidenced by the error in concentration estimates of IL-6 concentration deduced using four different standard curves obtained over a span of seven months..... 128

**Figure 7. 3:** SARS-CoV-2 serological p-LFA. (A) Schematic illustration of the SARS-CoV-2 S1 antibody LFA strips comprising recombinant SARS-CoV-2 S1 protein as capture element at the test spot and sheep IgG at the control spot. Schematic illustrations of (B) AuNP-based SARS-CoV-2 S1 antibody LFA and (D) p-LFA. (C) Dose-dependent mean gray values, corresponding to different concentrations of SARS-CoV-2 S1 antibody, acquired from AuNP-based LFA. (E) Dose-dependent signal-to-noise ratio of SARS-CoV-2 S1 antibody p-LFA performed in 20 min. 8-bit ImageJ processed images of (F) AuNP-based SARS-CoV-2 S1 antibody LFA and (G) SARS-CoV-2 S1 antibody p-LFA, depicting the visual readout mode. (H) Fluorescence images of SARS-CoV-2 S1 antibody p-LFA strips, depicting the fluorescence readout mode. (I) Dose-dependent optical densities and fluorescence intensities, corresponding to different SARS-CoV-2 S1 antibody concentrations, obtained by standard ELISA (red) and p-FLISA (black) implemented on a microtiter plate, performed in 4 h. (J) Table depicting the clinical sensitivity and specificity of the SARS-CoV-2 S1 antibody p-LFA. .... 133

**Figure 7. 4:** p-LFA for SARS-CoV-2 N protein and variants-of-concern. (A) Schematic illustration of the nucleocapsid (N) protein p-LFA strips comprising of N protein capture antibody as test spot and sheep IgG as control spot. (B) Colorimetric and (C) fluorometric readout modes of p-LFA for N protein detection. (D) Dose-dependent mean gray values, corresponding to different concentrations of N protein, acquired from colorimetric p-LFA (black) and dose-dependent signal-to-noise ratio of N protein fluorometric p-LFA performed in 20 min (red). (E) Dose-dependent optical densities and fluorescence intensities, corresponding to different N protein concentrations, obtained by standard ELISA (black) and p-FLISA (red) implemented on a microtiter plate, performed in 4 h. (F) Comparison of fluorometric p-LFA (red) and commercial point-of-care rapid antigen kit (BD Veritor™) (black). (G) N-protein signal-to-noise ratio in

PCR-positive NP swab samples (wild type SARS-CoV-2) determined by colorimetric p-LFA (gray), fluorometric p-LFA (black) and BD Veritor™ (marked with #). **(H)** Comparison of colorimetric (gray) and fluorometric (black) p-LFA in terms of their ability to quantify N protein concentrations present in NP swab samples of 35 PCR-positive samples (19 wild type SARS-CoV-2 and 16 Delta variant). **(I)** N protein signal-to-noise ratio in NP swab samples tested negative for COVID-19 and positive for different seasonal coronaviruses and other respiratory viruses. .... 135

**Figure 7. 5:** Validation of p-LFA using an inexpensive, portable fluorescence scanner. **(A)** Photograph of the portable fluorescence scanner. **(B)** Fluorescence intensities (black spheres) and area under the curve values (red spheres) obtained from LFA strips, drop-casted with different concentrations of plasmonic-fluors, scanned using benchtop and portable scanners. **(C)** Schematic illustration of the LFA cassette employed in the study and the workflow of p-LFA. S, C and T correspond to the sample pad, test line and control line, respectively. The blue arrow represents the direction of the fluorescence measurements made on the LFA cassette using the portable scanner. **(D)** Representative positive (black) and negative (red) signals obtained using the portable scanner. **(E)** 8-bit ImageJ processed image of the full strip IL-6 colorimetric p-LFA depicting the visual readout mode. **(F)** Fluorescence image of the full strip IL-6 fluorometric p-LFA depicting the fluorescence readout mode. **(G)** Dose-dependent signal of 15 min IL-6 fluorometric p-LFA measured by benchtop (black) and portable scanners (red). **(H)** Linear regression plot of IL-6 concentration in serum samples determined by fluorometric p-LFA, and measured benchtop and portable scanners. **(I)** Linear regression plot of IL-6 concentration in serum samples determined by 4 h lab-based p-FLISA and a benchtop fluorescence scanner, compared to measurements made using 15 min fluorometric p-LFA and the portable scanner. **(J)** Linear regression plot of N protein concentration in NP swab samples determined by fluorometric p-LFA and measured using the benchtop and portable scanners. .... 141

**Figure A- 1:** Image of a single plasmonic-fluor collected using an epifluorescence microscope using a 20x objective along with line-scan to measure the change in the mean intensity of plasmonic-fluor with respect to that of background. .... 173

**Figure A- 2:** FLISA of human IL-6 performed using quantum dots (QDs). Fluorescence intensity vs. concentration plot for FLISA calculated from **(A)** 20x images and **(B)** 60x images, n=2. **(C)** 20x and 60x epifluorescence microscopic images of FLISA using quantum dots. .... 174

**Figure A- 3:** **(A)** Schematic illustration of the digital p-FLISA of spike protein in SARS-CoV-2 virion. **(B)** Epifluorescence microscopic images of digital p-FLISA of SARS-CoV-2 virion. n=2 (5 images per well). .... 174

**Figure A- 4:** Analog vs. digital plasmonic-FLISA (p-FLISA) of SARS-CoV-2 virion. **(A)** Schematic illustration of the experiment. **(B)** Fluorescence image and fluorescence intensity vs. concentration plot for p-FLISA. n=2. **(C)** Particle count vs. concertation plot of digital p-FLISA

and **(D)** epifluorescence microscopic images of digital p-FLISA of SARS-CoV-2 virion. n=2 (5 images per well). Analog p-FLISA  $R^2= 0.9964$ , digital p-FLISA  $R^2= 0.9986$ . ..... 175

**Figure A- 5:** Analog vs. digital plasmonic-FLISA (p-FLISA) of recombinant spike protein (S-protein). **(A)** Schematic illustration of the experiment S protein. **(B)** Fluorescence intensity vs. concentration plot for S protein analog p-FLISA. n=2. **(C)** Particle count vs. concentration plot of S protein digital p-FLISA. n=2 (5 images per well). Analog p-FLISA  $R^2= 0.9991$ , digital p-FLISA  $R^2= 0.9994$ . ..... 175

**Figure A- 6:** Optimization of N protein capture and detection for implementation in p-FLISA. (n=2) Dilution factors tested are mentioned in the table. .... 176

**Figure A- 7:** ELISA of recombinant nucleocapsid protein in SARS-CoV-2 ..... 176

**Figure A- 8:** Analog vs. digital plasmonic-FLISA (p-FLISA) of nucleocapsid protein in SARS-CoV-2 virion. **(A)** Fluorescence intensity vs. concentration plot for p-FLISA. n=2. **(B)** Particle count vs. concentration plot of digital p-FLISA. n=2 (5 images per well). Analog p-FLISA  $R^2= 0.9795$ , digital p-FLISA  $R^2= 0.9976$ . ..... 176

**Figure A- 9:** Analog vs. digital plasmonic-FLISA (p-FLISA) of recombinant nucleocapsid protein in UTM. **(A)** Fluorescence intensity vs. concentration plot for p-FLISA. n=2. **(B)** Particle count vs. concentration plot of digital p-FLISA. n=2 (5 images per well). Analog p-FLISA  $R^2= 0.9950$ , digital p-FLISA  $R^2= 0.9978$ . ..... 177

**Figure A- 10:** S protein in PCR-positive and PCR-negative human swabs and saliva. .... 177

**Figure A- 11:** Receiver operating characteristic curve for N protein digital pFLISA. .... 178

**Figure B- 1:** Visible-NIR extinction spectra of streptavidin functionalized AuNPs (black) and plasmonic-fluors (red). ..... 185

**Figure B- 2:** **(A)** Digital photograph of a strip drop-casted with different concentrations of AuNPs. **(B)** 8-bit ImageJ processed image. .... 185

**Figure B- 3:** **(A)** Digital photograph of the strip drop-casted with different concentrations of plasmonic-fluors. **(B)** 8-bit ImageJ processed image. **(C)** Corresponding fluorescence image of the nitrocellulose membrane. .... 186

**Figure B- 4:** Mean gray values obtained from nitrocellulose membrane drop-casted with different concentrations of AuNPs (black) and plasmonic-fluors (red). ..... 186

**Figure B- 5:** Schematic representation of **(A)** biotin-streptavidin lateral flow assay and **(B)** corresponding work-flow of p-LFA. .... 187



**Figure B- 6:** (A) Image of the LFA strips (after Image J processing), with different concentrations of BSA-Biotin as capture spot, after exposure to the same concentration of streptavidin as target analyte and biotin-functionalized AuNPs. (B) Corresponding mean gray values as a function of BSA-Biotin concentration..... 187

**Figure B- 7:** (A) Fluorescence image of the LFA strips, with different concentrations of BSA-Biotin as capture spot, after exposure to the same concentration of streptavidin as target analyte and biotin-functionalized plasmonic-fluors. (B) Corresponding fluorescence intensity as a function of BSA-Biotin concentration. .... 188

**Figure B- 8:** (A) 8-bit ImageJ-processed image of the nitrocellulose membranes with the same concentration of BSA-Biotin concentration after exposure to different concentrations of biotin functionalized AuNPs, and identical concentrations of streptavidin as target analyte. (B) Corresponding mean gray values as a function of AuNP concentrations..... 188

**Figure B- 9:** (A) Fluorescence image of LFAs with the same concentration of BSA-Biotin concentration after exposure to different concentrations of biotin functionalized plasmonic-fluors, and identical concentrations of streptavidin as target analyte. (B) Corresponding fluorescence intensity as a function of plasmonic-fluors concentration. .... 189

**Figure B- 10:** 8-bit ImageJ processed images of nitrocellulose membranes corresponding to (A) AuNPs-based streptavidin-biotin LFA and (B) streptavidin-biotin p-LFA depicting the visual or colorimetric readout mode. .... 190

**Figure B- 11:** Dose-dependent mean gray values obtained from nitrocellulose membrane corresponding to different concentrations of streptavidin acquired from (A) AuNP-based and (B) plasmonic-fluor-based biotin-streptavidin LFA. .... 190

**Figure B- 12:** (A) Fluorescence image of the nitrocellulose membranes corresponding to streptavidin-biotin p-LFA strips depicting fluorometric readout mode. (B) Dose-dependent mean gray values obtained from nitrocellulose membrane corresponding to different concentrations of streptavidin acquired from streptavidin-biotin p-LFA..... 191

**Figure B- 13:** Schematic representation of IL-6 plasmonic-fluor-based lateral flow assay. .... 191

**Figure B- 14:** Dose-dependent fluorescence intensity values obtained from nitrocellulose membrane corresponding to different concentrations of IL-6 standards acquired from molecular fluorophore-based LFA..... 191

**Figure B- 15:** Dose-dependent mean gray values obtained from nitrocellulose membrane corresponding to different concentrations of IL-6 standards acquired from (A) AuNP-based and (B) plasmonic-fluor-based IL-6 LFA..... 192

**Figure B- 16:** Schematic representation of (A) ELISA and (B) p-FLISA. (Bottom) Dose-dependent fluorescence intensity maps acquired by p-FLISA for different IL-6 concentrations. .... 192

**Figure B- 17:** (A) Dose-dependent fluorescence intensities and optical densities, corresponding to different IL-6 concentrations in plasmonic fluor-linked immunosorbent assay (p-FLISA, black circles) and standard ELISA (red circles), respectively, implemented on a microtiter plate, performed in 4 h. (B) Dose-dependent mean gray values obtained from nitrocellulose membrane corresponding to different concentrations of IL-6 standards acquired from IL-6 p-LFA strips drop-casted with different capture antibody concentrations. (C) Fluorescence intensity obtained for blank and 320 fg/ml human IL-6 standard concentrations from p-LFA strips as a function of capture antibody concentration. .... 193

**Figure B- 18:** (A-D) Dose-dependent signal-to-noise ratio of multiple IL-6 p-LFA standard curves generated on different dates. (E) Overlaid dose-dependent signal-to-noise ratio of different standard curves depicting minimal deviation from one another. (F) Dose-dependent signal-to-noise ratio obtained by taking the average values from all four standard curves and its bioanalytical parameters. Error bars in figure F represent standard deviations from 8 different samples. .... 193

**Figure B- 19:** (A) Overlaid dose-dependent signal-to-noise ratio of different standard curves depicting minimal deviation from one another. (B) Resolution of molecular concentration (RMC) curves for four different standard curves. .... 194

**Figure B- 20:** Multiple IL-6 standard curves were generated and samples with varying IL-6 concentrations (0.5 pg ml<sup>-1</sup> to 62.5 pg ml<sup>-1</sup>) were tested in standard-free manner. Their experimental concentrations were determined using each standard curve, and deviation from actual concentration was calculated. (A) Samples were tested in duplicates in standard-free manner and for each test, experimental values were determined using 4 standard curves, thus, 8 data points corresponding to each concentration are plotted in the box plot. (B) Deviation in the average experimental values of the samples corresponding to each standard curve. Center line is median; center square is mean; box limits are first and third quartile which are 25% and 75% respectively; 1.5 times of interquartile range is defined by cross marks; the upper whisker is the first number that is less than upper quartile + 1.5 times of inter quartile range; Outliers are the data points located outside the 1.5 times of interquartile range. .... 194

**Figure B- 21:** Dose-dependent mean gray values obtained from nitrocellulose membrane corresponding to different concentrations of SARS-CoV-2 S1 antibody solutions acquired from (A) AuNP-based and (B) plasmonic-fluor-based SARS-CoV-2 antibody LFA. .... 195

**Figure B- 22:** Dose-dependent signal-to-noise ratio of (A) colorimetric and (B) fluorometric p-LFA for detection of N protein. (C) Dose-dependent optical density corresponding to different concentrations of N protein in ELISA. (D) Dose-dependent fluorescence intensity corresponding

to different concentrations of N protein in plasmonic-fluor linked immunosorbent assay (p-FLISA). (C and D) Both the assays were implemented on microtiter plate and the sample-to-answer time was 4 h. .... 195

**Figure B- 23:** N-protein signal-to-noise ratio in PCR-positive Delta B.1.617.2 variant NP swab samples determined by colorimetric p-LFA (gray bars) and fluorometric p-LFA (black bars). 196

**Figure B- 24:** N-protein signal-to-noise ratio in PCR-positive Omicron BA.1 variant NP swab samples determined by colorimetric p-LFA (gray bars) and fluorometric p-LFA (black bars). 196

**Figure B- 25:** Photograph of the portable fluorescence scanner for different angle. The size of the scanner is 25 cm x 25 cm x 19 cm (LxBxH). .... 197

**Figure B- 26:** Photographs of LFA cassette employed in the study. S, C and T corresponds to the sample pad, test line and control line, respectively. Representative photographs of LFA cassette displaying (A) positive and (B) negative result from p-LFA strips with colorimetric control line. Representative fluorescence images of the p-LFA strips displaying (C) positive and (D) negative result from p-LFA strips with fluorometric control line. .... 197

**Figure B- 27:** Representative invalid tests obtained using the portable scanner. If a test has no signal at the control line, it is reported as an invalid test. .... 197

**Figure B- 28:** Fluorescence images of the LFA strips drop-casted with 0.5 µl of different numbers of plasmonic-fluors (mentioned in parenthesis). .... 198

**Figure B- 29:** Fluorescence images of the LFA strips drop-casted with 0.5 µl of different concentrations of molecular-fluorophores (mentioned in parenthesis). .... 198

**Figure B- 30:** (A) Fluorescence intensities and (B) area under the curve values obtained from LFA strips, drop-casted with different concentrations of molecular fluorophores, when scanned using benchtop (LI-COR) and portable scanner, respectively. .... 198

**Figure B- 31:** Representative examples of data processing conducted on data acquired by portable scanner from LFA strips drop-casted with (A, B) ~106 and (C, D) ~103 number of plasmonic-fluors, and (E, F) 1XPBS (blank). .... 199

**Figure B- 32:** Dose-dependent mean gray values obtained from test line of the nitrocellulose membrane corresponding to different concentrations of IL-6 solutions acquired from plasmonic-fluor-based IL-6 LFA. .... 200

**Figure B- 33:** (A) Dose-dependent fluorescence images of the nitrocellulose membrane corresponding to different concentrations of N protein solutions acquired from plasmonic-fluor-based N protein LFA and measured by (B) benchtop scanner and (C) portable scanner. .... 200

**Figure B- 34:** Schematic illustration of the full strip IL-6 p-LFA employed for the quantitative detection of IL-6 in the serum of COVID-19 positive (PCR confirmed) individuals. .... 201

**Figure B- 35:** Schematic illustration of the full strip N protein p-LFA employed for the quantitative measurement of N protein concentration present in the nasal swab samples of COVID-19 positive (PCR confirmed) individuals. .... 201

**Figure B- 36:** Schematic illustration of experiment designed to understand the enhancement of fluorescence signal using plasmonic-fluors compared to conventional fluorophores. .... 202

**Figure B- 37:** RMC curves for ELISA, p-FLISA and p-LFA calculated via equations listed in supplementary information. The blue dashed line indicates the RMC cutoffs that can be used to determine the quantitative performance of the assay over a certain range of concentrations. The relevant RMC parameters are listed in **Table B-1**. .... 202

**Figure B- 38:** Schematic illustration of assembly of LFA components. The prepared sample pad, conjugate pad, membrane, and adsorption pad were then assembled with a 2 mm overlap between each pad and cut to strips with a width of 3mm using a strip cutter. .... 203

# List of Tables

<b>Table 5. 1:</b> Comparison of bioanalytical parameters of commercial colorimetric assay and collagen plasmonic foam-based assay.....	86
<b>Table 5. 2:</b> Collagenase activity of healthy volunteer samples determined using commercial colorimetric assay and collagen plasmonic foam-based assay. ....	87
<b>Table B- 1:</b> RMC function and bioanalytical parameters of human IL-6 ELISA, p-FLISA and p-LFA to compare the performance of the assays in terms of their ability to resolve .....	203
<b>Table B- 2:</b> Details of the 19-PCR positive patient samples.....	203
<b>Table B- 3:</b> Results of the 19 PCR-positive patient samples (wild type SARS-CoV-2) tested by fluorometric and colorimetric p-LFA, and commercial antigen test (BD veritor <sup>TM</sup> ). Table also lists the N protein concentration of these samples obtained from fluorometric p-LFA demonstrating its quantitative analysis ability.....	206
<b>Table B- 4:</b> Results of the 16 PCR-positive Delta B.1.617.2 variant samples (confirmed by gene sequencing) tested using fluorometric and colorimetric p-LFA. Table also lists the N protein concentration of these samples obtained from fluorometric p-LFA demonstrating its quantitative analysis ability. ....	207
<b>Table B- 5:</b> Results of the 17 PCR-positive omicron BA.1 samples (confirmed by gene sequencing) tested using fluorometric and colorimetric p-LFA. Table also lists the N protein concentration of these samples obtained from fluorometric p-LFA demonstrating its quantitative analysis ability. ....	208
<b>Table B- 6:</b> Details of 17 PCR-positive omicron BA.1 samples (confirmed by gene sequencing). .....	209
<b>Table B- 7:</b> N protein concentration determined by p-LFA strips and measured by portable and benchtop scanner.....	210
<b>Table B- 8:</b> IL-6 concentration determined by p-LFA strips and measured by portable and benchtop scanner; and determined by p-FLISA and measured by benchtop scanner. ....	211

# Acknowledgments

My fulfilling and long journey toward my Ph.D. has been much more than just an educational experience as it has allowed me to experience different colors of life. I would like to thank everyone I have interacted with during these years for their valuable assistance, encouragement, and guidance. I am grateful to all those who have given me their time, energy, and more importantly their love.

I am short of words while acknowledging my advisor and mentor Prof. Srikanth Singamaneni, without whom I would not have made it this far. After realizing his passion and dedication for science, and clarity of thoughts, joining his lab was a no-brainer. Even after 5 years in his lab, if given a choice to go back in past, I would like to pursue Ph.D. in his lab. His work ethic is contagious and has played an inspirational role in my transformation in multiple aspects of life. For the last 5 years, Prof. Singamaneni has given me his unconditional academic support. I am forever grateful for his presence in my life as he will continue to be an exemplary role model for me.

I would like to thank our collaborators and my committee members Prof. Shantanu Chakrabartty, Prof. Erica L. Scheller, Prof. Jeremiah J. Morrissey, and Prof. Jianjun Guan for their support, guidance, and countless insightful constructive discussions. I would also like to thank Dr. Brian T. Cunningham and his students, Qinglan, Yanyu and Priyash, for involving me in their exciting research projects.

I am grateful for the amazingly positive work environment that Prof. Singamaneni, Prof. Morrissey, my seniors, and labmates have created. I would like to thank my seniors Prof. Keng-

Ku Liu, Dr. Sirimuvva Tadepalli, Dr. Qisheng Jiang, Dr. Jingyi Luan, Dr. Anushree Seth, Dr. Hamed Derami, Dr. Sisi Cao, and Dr. Zheyu Wang for instilling strong work ethics in me. I am also thankful to the current members of the soft nanomaterials lab Dr. Brendan Watson, Ms. Priya Rathi, Ms. Yixuan Wang, Mr. Avishek Debnath, Mr. Yuxiong Liu, Mr. Harsh Baldi, and especially Mr. Prashant Gupta who has been with me since my undergraduate studies, for the congenial and collaborative work environment that they created which allowed me to learn a lot about scientific and collaborative research atmosphere.

I am immensely thankful to the team of Institute of Materials Science (IMSE), especially Ms. Beth Gartin who has always been a resourceful help and support. I am thankful to IMSE and Prof. Srikanth and Prof. Sastri for giving me the opportunities to teach graduate-level classes and mentor new lab students. I am grateful for the wholesome environment of Washington University in St. Louis which allowed me to lead and serve university-wide student organization groups. Such opportunities have given me a lot of confidence and prepared me well for my future after my Ph.D.

Last but not least, I would like to thank my family for their continuous love and support. I am thankful for my amazing friends, Jonathan and Kay to name a few, and the people of St. Louis who have made my stay at St. Louis an everlasting experience of my life.

Rohit Gupta

*Washington University in St. Louis*

*August 2022*

*Dedicated to my family, Sangita Gupta, Dr. Shyam Bihari Gupta and Sumit Gupta, and to all  
who are constantly making our world a better place.*



## ABSTRACT OF THE DISSERTATION

Plasmonic Nanomaterials-Based Point-of-Care Biosensors

by

Rohit Gupta

Doctor of Philosophy in Materials Science and Engineering

Washington University in St. Louis, 2022

Professor Srikanth Singamaneni, Chair

Point-of-care (POC) biosensors, although rapid and easy-to-use, are orders magnitude less sensitive than laboratory-based tests. Further they are plagued by poor stability of recognition element thus limiting its widespread applicability in resource-limited settings. Therefore, there is a critical need for realizing stable POC biosensors with sensitivity comparable to gold-standard laboratory-based tests. This challenge constitutes the fundamental basis of this dissertation work—to expand access to quality and accurate biodiagnostic tools. At the heart of these solutions lies plasmonic nanoparticles which exhibit unique optical properties which are attractive for label-free and labelled biosensors.

Firstly, we improve the stability and applicability of label-free plasmonic biosensors for implementing biodiagnostics in POC and resource-limited settings. We demonstrate a cost-effective plasmonic paper-based biosensor for non-invasive detection of renal cancer. We also demonstrate a facile integration of plasmonic paper and microneedle patch to realize a POC biosensor which enables detection of target biomarkers present in interstitial fluid in an easy-to-use two-step process. We introduce a polymer encapsulation strategy to realize a stable and refreshable biosensor for long-term monitoring of protein biomarkers under harsh conditions.

Next, we demonstrate dramatic improvement in bioanalytical parameters of POC biosensors by designing and realizing an ultrabright fluorescent nanolabel, plasmonic fluor. We discuss a novel approach for detection and quantification of inflammatory disease burden via plasmonically-active tissue analog which can undergo *in vivo* or *ex vivo* degradation in the presence of biological fluid associated with the tissue. We demonstrate a partition-free digital fluoroimmunoassay for ultrasensitive, multiplexed, and quantitative detection of protein biomarkers present in human biospecimens. Significantly, utilizing plasmonic-fluor, we overcome long-standing limitations associated with lateral flow immunoassays (LFA)— limited sensitivity, low accuracy and smaller analytical range compared to laboratory tests, and limited quantitation ability.

Taken together, these advances are expected to overcome fundamental challenges associated with POC biosensors, and to bridge the gap between laboratory-based and at-home or point-of-care (POC) diagnosis. Through this dissertation work we demonstrate a complete workflow of a POC diagnostic platform that outperforms gold-standard laboratory tests in sensitivity, speed, dynamic range, ease of use, and cost.

# Chapter 1: Introduction

Point-of-care (POC) testing – defined as ‘(biochemical) testing at or near the site of patient care whenever the medical care is needed’ - involves immediate acquisition of information on an individual's condition to facilitate future treatment decisions. Although rapid and simple, they are orders magnitude less sensitive than laboratory-based tests and cannot be used for definitive negative diagnosis. This challenge has constituted the fundamental basis of the dissertation work – to expand access to quality and accurate biodiagnostic tools. We aim to solve the fundamental limitations associated with POC biosensors – poor stability, long-term usability, limited sensitivity, and limited quantitation ability compared to laboratory tests, and to bridge the gap between laboratory-based and at-home or point-of-care (POC) diagnosis.

Biosensors can be broadly classified into two types - label-free and labelled biosensors (**Figure 1.1**). To improve the bioanalytical parameters of label-free biosensors, we introduce a novel transduction platform. In case of labeled immunoassay, we introduce ultrabright nanolabels that improve the sensitivity by orders of magnitude. At the heart of these solutions lies plasmonic nanoparticles, which exhibit unique optical properties. In case of label-free biosensor, we employ plasmonic nanoparticle as nanotransducers. We harnessed plasmonically-enhanced ultrabright fluorescent nanoparticles to augment the bioanalytical parameters of the labelled biosensors.

Specifically, we demonstrate cost-effective plasmonic paper-based localized surface plasmon resonance (LSPR) label-free biosensor for non-invasive detection of renal cancer. We also demonstrate a facile integration of plasmonic paper and microneedle patch to realize an easy-to-use and efficient POC biosensor, which enables detection of target biomarkers present in

interstitial fluid in two-step process - apply the plasmonic paper microneedle patch to skin and measure the analyte concentration directly using surface enhanced Raman spectroscopy (SERS).

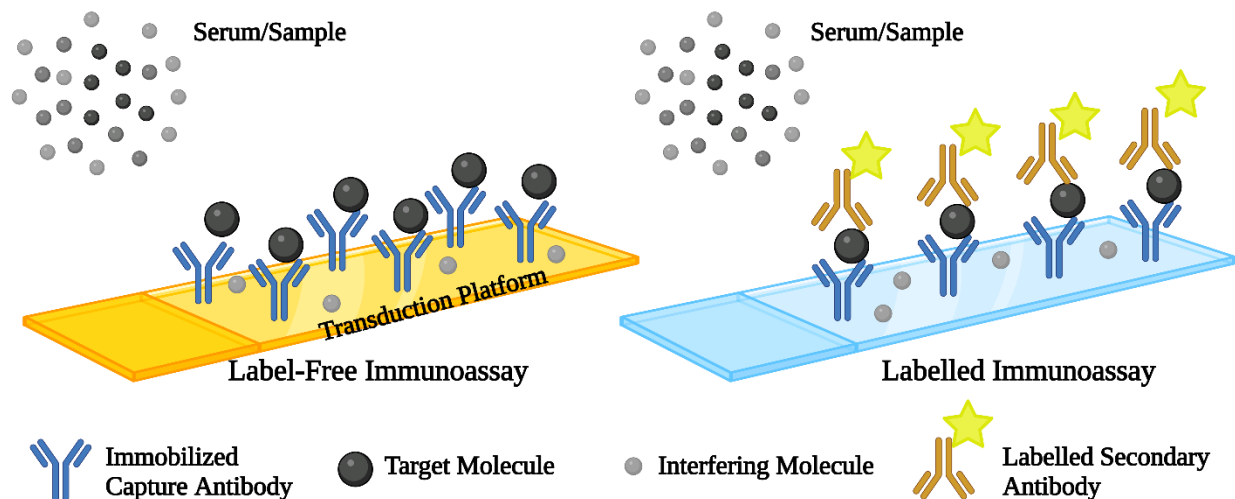


**Figure 1. 1:** Schematic illustration of (left) label-free and (right) labelled immunoassay. In case of label-free biosensors we employ transduction platform based on plasmonic nanoparticles, while in case of labeled immunoassay we augment the sensitivity of the nanolabel by utilizing plasmonically enhanced ultrabright fluorescent nanoparticles to augment bioanalytical parameters of the biosensors.

We also address the long-standing problem associated with the poor stability of antibodies, which limits the reusability and adaptability of biosensors in POC settings, by employing a facile polymer encapsulation strategy. Employing this method, we demonstrate the long-term usability and refreshability of plasmonic biosensors for detection of neutrophil gelatinase-associated lipocalin (NGAL), a biomarker for acute and chronic kidney injury. This novel encapsulation approach can be easily extended to other transduction platforms to realize refreshable biosensors for monitoring of protein biomarkers under harsh conditions and over long durations – features important for POC biosensors.

This dissertation also discusses a novel approach for detection and quantification of inflammatory disease burden via plasmonically-active tissue analog, which can undergo in vivo or

ex vivo degradation in the presence of biological fluid associated with the tissue. Specifically, we employ a collagen foam loaded with ultrabright fluorescent nanolabels for detection of collagenase present in biospecimen. This offers highly sensitive and rapid detection of collagenase present in biospecimen and can help the early detection and progression of pathological conditions.

Harnessing an ultrabright fluorescent nanoconstruct, plasmonic-fluor, as a nanolabel for labelled immunoassay, we demonstrate a partition-free digital fluoroimmunoassay for ultrasensitive, multiplexed, quantitative detection of SARS-CoV-2 antigens present in nasopharyngeal swab and saliva samples of COVID-19 patients. Compared to the “gold standard” enzyme-linked immunosorbent assay (ELISA), the digital fluoroimmunoassay exhibited nearly 7000-fold lower limit-of-detection with virtually no change in the biorecognition elements or assay workflow. This ability to detect and quantify extremely low concentrations of target proteins can have a transformative impact in diagnosing various pathological conditions at an early stage of disease progression.

Lateral flow (immuno)assays (LFAs) are the cornerstone of POC diagnostics and are amongst the simplest, fastest, and cheapest diagnostic methods which offer broad potential for population-level screening for disease. However, this potential has not yet been fully achieved owing to their poor sensitivity and quantitation ability (nearly 1000-fold lower) compared to gold standard laboratory-based diagnostics. We overcome this fundamental limitation by employing plasmonically-enhanced nanoscale fluorescent nanoparticles as nanolabel in LFAs. Plasmon-enhanced LFAs (p-LFAs), completed in 20 min, attained over 30-fold improvement in dynamic range and limits of detection over the 4 hour-long, “gold standard” ELISA. Significantly, concentrations of interleukin-6 (IL-6) in human serum samples and SARS-CoV-2 nucleocapsid (N) protein in nasopharyngeal swab samples determined by p-LFAs using an inexpensive portable

scanner exhibited strong correlation with those determined using a traditional benchtop scanner. Taken together, these advances are expected to overcome fundamental challenges associated with POC biosensors and offers POC diagnostic platform that outperforms standard laboratory tests in sensitivity, speed, dynamic range, ease of use, and cost.

## **1.1 Research Objectives**

The ultimate goal of the dissertation is to overcome several fundamental challenges associated with POC biosensors by employing plasmonic nanomaterials as transduction platform, in case of label-free biosensors, and reporter element, in case of labelled biosensors. Specific objectives include:

### **1.1.1 Objective 1: Design and realize paper-based SERS and LSPR label-free biosensors for point-of-care diagnostics.**

*1A. Realize plasmonically-active microneedle patch for in situ detection of target biomolecules in dermal interstitial fluid.*

We aim to design and demonstrate a microneedle (MN) patch integrated with plasmonic paper to collect interstitial fluid (ISF) and enable on-patch surface-enhanced Raman scattering (SERS) based detection of molecules in dermal ISF. The plasmonic paper MN patch consists of a stainless-steel MN patch that creates micropores in skin to access ISF and a plasmonic paper which acts as ISF reservoir. We established that in contrast to extraction and analysis of ISF using MN, which requires multiple steps, on-patch capture and SERS based detection of molecules in ISF is a simple and efficient two-step process: apply the MN patch to skin and measure concentration of analyte directly on the MN patch by SERS.

### *1B. Plasmonic paper-based assay for non-invasive detection of renal cancer.*

We demonstrate rapid and highly sensitive detection of perilipin-2 (PLIN-2) in clinical urine samples. Common filter paper uniformly absorbed with commercial mono-clonal antibody-conjugated plasmonic nanostructures is employed as a label-free localized surface plasmon resonance (LSPR) based plasmonic biosensor. We demonstrate that this assay is significantly more sensitive than Western blotting and provides the requisite sensitivity for quantifying clinical urine PLIN-2 concentrations for renal cell carcinoma (RCC). More importantly, this technology offers a highly attractive diagnostic platform for rapid detection and quantification of target bioanalyte in preclinical and clinical settings.

#### **1.1.2 Objective 2: Enhance the stability of antibodies immobilized on plasmonic transducers through organosilica encapsulation for POC applications.**

Poor stability of antibodies, which are used as biorecognition elements, and the lack of effective methods to refresh the biosensors upon demand remain significant challenges in realizing protein biosensors for long-term monitoring. We show that the encapsulation of antibodies immobilized on plasmonic nanostructures with an organosilica layer would render refreshability to the biosensors, by preserving the antibody biorecognition capability, when subjected to harsh environment or chemical regeneration agents required to refresh biosensors. The encapsulation-based preservation method proposed here overcome a critical challenge in protein based POC and wearable biosensors and is expected to advance the design and implementation of such biosensors for long-term monitoring of protein biomarkers.

### **1.1.3 Objective 3: Realize plasmonically-active tissue analogs for rapid, ultrasensitive, and quantitative detection of inflammatory disease burden.**

In this research objective, we aim to design and demonstrate a plasmonically-active tissue analog for detection and quantification of inflammatory disease burden through their in vivo or ex vivo degradation in the presence of biological fluid associated with the tissue. As a proof-of-concept, we realize plasmonic collagen foam that undergoes degradation in the presence of collagenase. Specifically, we demonstrate that a three-dimensional collagen foam loaded with plasmonic nanostructures, when incubated in collagenase solution, will exhibit concentration dependent release of plasmonic nanoparticles in the solution due to the degradation of collagen foam. Subsequently, the optical property, such as fluorescence, of the solution was analyzed to determine the rate of release of nanoparticle or rate of increase in fluorescence intensity. Dose response curve i.e. rate of increase in fluorescence intensity vs time, were plotted to determine collagenase concentration. This technique offers quick and sensitive measurement of collagenase concentration present in biospecimens such as saliva.

### **1.1.4 Objective 4: Design and realize plasmonically-enhanced ultrasensitive immunoassays that can be implemented in clinical labs and at the point-of-care.**

#### ***4A. Digital fluoroimmunoassay for sub-femtomolar detection of protein biomarkers.***

Harnessing an ultrabright fluorescent nanoconstruct, plasmonic-fluor, as digital nanolabel, we demonstrate a digital fluoroimmunoassay for ultrasensitive and quantitative detection of SARS-CoV-2 proteins in nasopharyngeal swab and saliva samples from COVID-19 patients. Compared to the “gold standard” enzyme-linked immunosorbent assay (ELISA), the digital p-FLISA exhibited nearly 7000-fold lower limit-of-detection with virtually no change in the biorecognition



elements or assay workflow. This ability to detect and quantify extremely low concentrations of target proteins can have a transformative impact in diagnosing infectious diseases such as COVID-19 and is broadly applicable to various other viral infections and future pandemics.

***4B. Plasmon-enhanced, quantitative lateral flow Assay for femtomolar detection of protein biomarkers in point-of-care settings.***

In this objective, we overcome the fundamental limitation of lateral flow assay, which are considered as the cornerstone of POC diagnosis, by employing plasmonically-enhanced nanoscale fluorescent labels. Plasmon-enhanced LFAs (p-LFAs) enabled standard-free, ultrasensitive quantitative detection of low abundance analytes, without compromising the direct visual detection capability of conventional LFAs. Fluorometric p-LFA, completed in 20 min, attained 30-fold improvement in dynamic range and limits of detection over the 4 hour-long, “gold standard” enzyme-linked immunosorbent assay (ELISA), and achieved 95% clinical sensitivity and 100% specificity for SARS-CoV-2 antibodies and antigens. This improvement over ELISA could be achieved with either a standard benchtop fluorescence scanner or an inexpensive, portable scanner that we developed. Concentrations of interleukin-6 (IL-6) in human serum samples and SARS-CoV-2 nucleocapsid (N) protein in nasopharyngeal swab samples determined using our portable scanner exhibited strong correlation with those determined using a benchtop scanner. p-LFAs offer potential as a broadly adaptable point-of-care diagnostic platform that outperforms standard laboratory tests in sensitivity, speed, dynamic range, ease of use, and cost.

## **1.2 Background and Motivation**

### **1.2.1 Plasmonic paper microneedle patch for point-of-care diagnosis of biomolecules in interstitial fluid (ISF)**

Point-of-care (POC) diagnostics is a rapidly growing field in the era of decentralized healthcare systems <sup>1</sup>. Although blood is considered the gold standard for diagnostic assays, blood sampling involves limitations such as difficulty of continuous monitoring due to blood clotting; need for medical professionals to collect blood by venipuncture; apprehension by patients associated with blood draws<sup>2</sup> and need for additional processing for red blood cell removal before analysis <sup>3</sup>.

Interstitial fluid (ISF) is a novel source of biomarkers that fills the spaces between cells in tissues in the body, and complements conventional sources like blood, urine and saliva. ISF has been shown to contain systemic biomarkers and unique biomarkers compared to other body fluids <sup>4-6</sup>. Also, ISF is a largely colorless fluid devoid of clotting agents and cells, thus simplifying biochemical analysis <sup>7</sup>. ISF is often collected from the skin, due to easier access compared to internal tissues.

ISF has been relatively unexplored largely due to limitations of sampling techniques such as suction blister <sup>8</sup>, which requires specialized equipment, takes ~1 h to perform and causes lasting skin wound; reverse iontophoresis <sup>9</sup>, which is limited to small molecules and requires frequent calibration; and microdialysis <sup>10</sup> and open flow microperfusion <sup>11</sup>, which requires expert personnel to perform minor surgery.

To enable simplified ISF collection, we and others have developed microneedle (MN) patches that can access ISF in a minimally invasive way that is painless, well-tolerated, easy-to-use and effective.<sup>12-13</sup> MNs are solid needles measuring hundreds of microns in length and tapering to a sharp tip that are typically assembled in arrays on a patch that can be applied to the skin<sup>14-16</sup>. MN technology was originally developed for drug delivery into the body. When drug is coated on or encapsulated within MNs, they can be released typically by dissolution in the skin, thereby enabling simple administration of a drug that might otherwise require expert injection.

MN technology has been adapted for ISF collection, including suction-based ISF extraction through micropores<sup>17-18</sup> hydrogel-forming MNs that swell with ISF in skin<sup>19-20</sup>, hollow microneedles that collect ISF by diffusion<sup>21</sup> or pressure-driven flow<sup>22</sup>. In these cases, ISF is collected from the MN device and analyzed in a separate instrument, which requires an added step of ISF transfer. Other approaches involve in-situ biomarker detection such as selectively binding biomarkers to MN surfaces<sup>23-24</sup>, and incorporation of sensors into MNs for in situ analysis of ISF<sup>25-27</sup>. In these cases, the sensor is inserted into the body, which introduces significant design challenges to address safety/toxicity concerns and avoid sensor fouling.

To overcome limitations of other MN technologies, in this study we developed a MN patch that collects ISF from the skin (thereby avoiding complications of in-dwelling sensors) and allows on-patch detection of biomarkers by surface-enhanced Raman spectroscopy (SERS) (thereby avoiding complicating sample transfer from the patch).

We selected surface enhanced Raman scattering (SERS) as a sensing modality for biomarker detection because it is a highly sensitive spectroscopic technique for molecular identification and detection<sup>28-29</sup>. SERS involves large enhancement of Raman scattering from

molecules (analytes) absorbed on or in close proximity to plasmonic nanostructures<sup>30</sup>. These plasmonic nanostructures are inert; photostable; tunable by changing nanostructure size, shape, composition and environment; and surface-stable for facile surface functionalization with various biological and organic molecules through covalent and non-covalent interactions<sup>30-31</sup>. These unique properties enable label-free SERS detection and molecular fingerprinting<sup>32</sup> for medical diagnostic, environmental monitoring and homeland security applications<sup>33</sup>. For example, SERS has been used for in-vivo glucose sensing<sup>34-35</sup> and for West Nile virus<sup>36</sup> and cancer biomarker detection<sup>37</sup>. We and others have developed low-cost, flexible plasmonic substrates called ‘plasmonic paper’ by immobilizing functionalized plasmonic nanostructures (e.g., gold nanorods (AuNRs)) on filter paper for SERS-based detection<sup>38-41</sup>. In this study, we integrated plasmonic paper with MN patches to facilitate SERS-based detection of biomarkers present in ISF, collected by MNs.

Using a plasmonic paper MN patch for on-patch detection of biomarkers in dermal interstitial fluid, we can detect biomarkers via two-step process: apply the MN patch to skin and measure biomarker concentration directly on the MN patch by SERS (**Figure 1.2A**). In contrast, ISF collected using a conventional paper MN patch would require multiple steps for analysis, such as MN patch application to skin, biomarker extraction from the paper MN patch by incubation in extraction media (which dilutes the sample) and centrifugation, loading samples into multi-well plates or other substrates for measurement and finally measuring biomarker concentration by a suitable analytical method (**Figure 1.2B**).

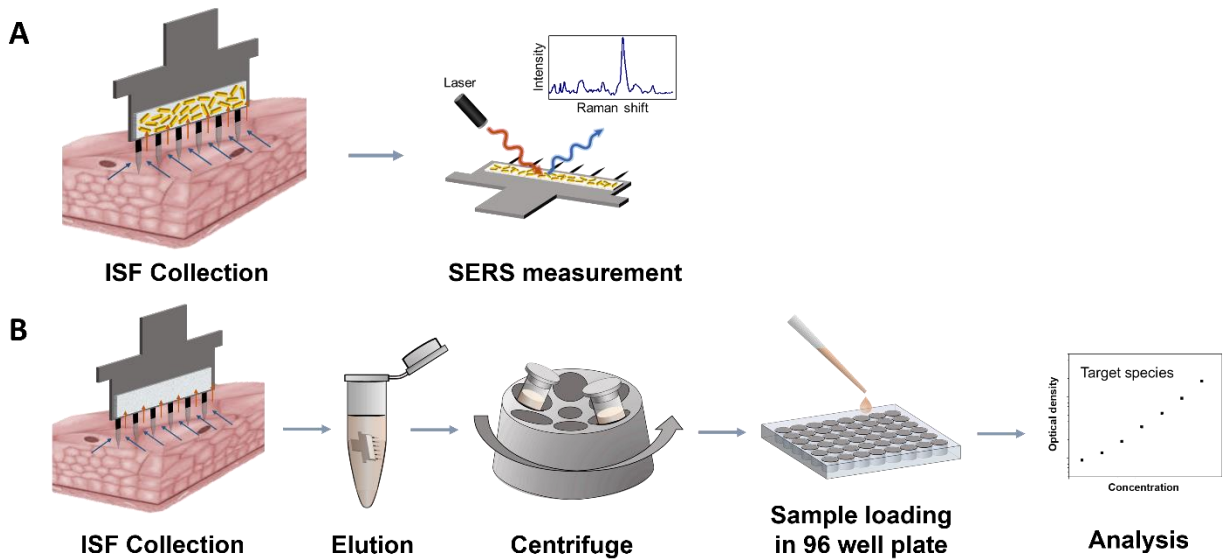


**Figure 1. 2:** Detection of biomarkers from ISF using plasmonic paper MN patch for on-patch detection by SERS versus conventional paper MN patch requiring multiple sample processing steps. **(A)** After ISF is collected using a plasmonic paper MN patch, biomarker analysis can be performed in situ on the plasmonic paper using SERS. **(B)** After ISF is collected using a conventional paper MN patch, biomarkers must be eluted and undergo additional steps for sample processing and biomarker analysis.

### 1.2.2 Plasmonic paper for non-invasive and point-of-care diagnosis of renal cancer

In previous section, the potential advantages, and applications of paper-based on-patch SERS detection of biomarkers was discussed. Here, we discuss the advantages of using plasmonic paper-based localized surface plasmon resonance (LSPR) detection of biomarkers. Paper-based LSPR substrates, compared with conventional rigid substrates such as silicon and glass, paper substrates offer numerous advantages such as high surface area, excellent wicking properties, mechanical flexibility, low cost, easy disposability, small sample volume requirement, facile processing (cutting, bending, and dipping), and compatibility with conventional printing approaches (enabling multiplexed detection and multimarker biochips). Simply involving conventional laboratory filter paper adsorbed with biofunctionalized nanostructures, such bioplasmonic paper devices (BPD) exhibit great potential for the use of label-free, POC bioassays

with the combination of handheld, battery-operated spectrometers. More importantly, with interchangeable recognition elements, BPD can be swiftly adapted for molecular diagnosis of many other diseases.<sup>42-43</sup>

Plasmonic biosensors, based on reflective index sensitivity of LSPR, are highly sensitive, cost-effective, and label-free biodiagnostic platforms. LSPR of noble metal nanostructures involving the coherent oscillation of dielectrically confined conduction electrons is sensitive enough to probe the conformational changes of individual biomacromolecules, detect single biomolecule binding events, monitor the kinetics of catalytic activity of single nanoparticles and even optically detect a single electron.<sup>44-46</sup> Hollow plasmonic nanostructures such as gold (Au) nanoshells, nanocages and nanorattles exhibit significantly higher refractive index sensitivity compared to their solid counterparts, making them excellent candidates for plasmonic biosensors.<sup>47</sup> Recently, our group demonstrated that Au nanorattles (AuNRTs) exhibit much higher refractive index sensitivity compared to Au nanorods with similar LSPR wavelength.<sup>48</sup> Therefore, for this research task we exploit these hollow plasmonic nanostructures.

Kidney cancer accounts for 3% to 4% of the newly found cases of malignant tumors in adults.<sup>49-50</sup> It is estimated that 73,820 new kidney cancer cases and 14,770 kidney cancer related deaths will occur in the United States in 2019.<sup>49</sup> Unfortunately, renal cell carcinoma (RCC) is generally asymptomatic at early stages, and is thereby frequently advanced when a diagnosis is made. Advanced RCC has a poor prognosis. Additionally, most renal masses are incidentally discovered by imaging modalities such as computed tomography (CT) and magnetic resonance imaging (MRI), but imaging cannot reliably distinguish between cancerous and benign tumors.<sup>51-53</sup> The conventional approach to a suspected renal mass is partial or radical nephrectomy. The problem however is that 20% of imaged renal masses are not cancer, and patients incur the loss of

a normal kidney.<sup>51-53</sup> Moreover, surgical reduction of functional renal mass reduces renal function and accelerates progression of underlying chronic kidney diseases.<sup>52, 54-60</sup>

Our research group previously reported that urine perilipin-2 (PLIN-2) and aquaporin-1 (AQP1) are sensitive and specific biomarkers for early noninvasive detection of clear cell or papillary subtypes of RCC (together accounting for 85-90% of malignant RCC).<sup>56-60</sup> AQP1 and PLIN-2 concentrations were significantly correlated with tumor size, stage (but not grade) and were found to decrease more than 83% following tumor excision.<sup>57, 60</sup> These biomarkers were not increased in patients with common non-cancerous kidney diseases (*i.e.* diabetic nephropathy, glomerulonephritis, urinary tract infection<sup>56</sup>), or other urinary tract cancers (bladder or prostate<sup>60</sup>), demonstrating specificity. Results suggested that AQP1 and PLIN-2 have potential utility for population screening through a “screen positive rule” and/or differential diagnosis of imaged renal masses.<sup>58</sup> However, the Western blot procedure for PLIN-2 employed in previous studies is complicated, expensive, is semi-quantitative and time consuming, which is not suitable for analysis of urine samples in clinical lab-settings. It is also challenging to develop an enzyme-linked immunosorbent assay (ELISA) for PLIN-2, particularly for screening of patient urine samples, due to insufficient sensitivity and effects of interindividual variability in urine pH.

Therefore, a convenient and cost-effective assay is needed for fast and quantitative testing of urine PLIN-2. This could significantly facilitate differential diagnosis of imaged renal masses to avoid unnecessary renal excision surgery and its consequences. In this objective, we report a facile approach for rapid and highly sensitive detection of PLIN-2 in clinical urine samples. Common filter paper uniformly absorbed with commercial monoclonal antibody-conjugated AuNRTs is employed as a label-free plasmonic biosensor. A schematic illustration summarizing the building of the bioplasmonic paper to detect PLIN-2 using AuNRTs and a monoclonal antibody

is depicted in **Figure 1.3**. This assay is significantly more sensitive than Western blotting and provides the requisite sensitivity for quantifying clinical urine PLIN-2 concentrations for RCC. More generally, this technology represents a highly attractive diagnostic platform for rapid detection and quantification of target bioanalytes in pre-clinical and clinical settings.

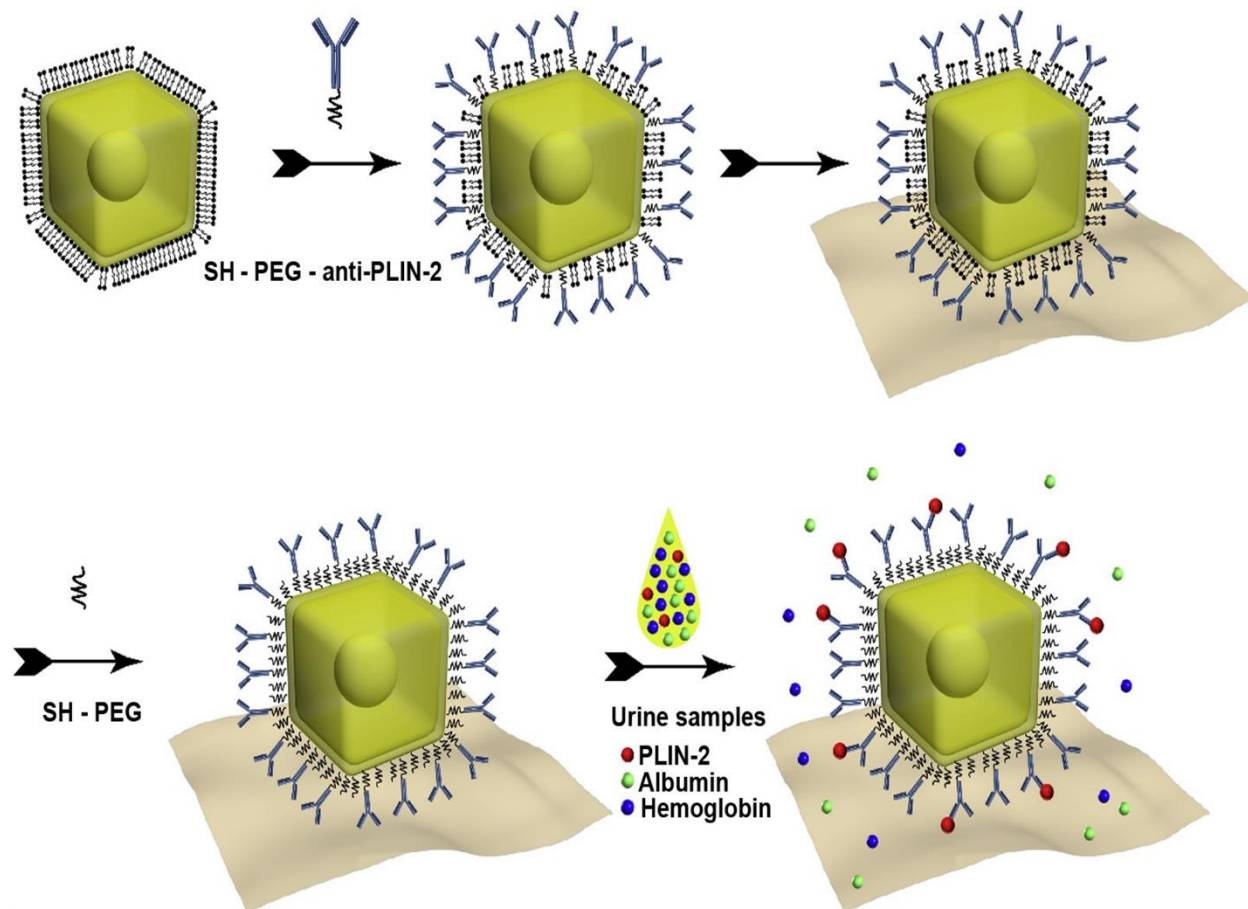


**Figure 1. 3:** Schematic illustration of plasmonic paper manufacture. Gold nanorattles (AuNRTs) coated with cetyltrimethylammonium chloride (CTAC) were functionalized with monoclonal antibody by means of a bifunctional polyethylene glycol (PEG). The functionalized AuNRTs were then coated on filter paper and non-specific binding sites neutralized by further PEGylation. The paper-bound functionalized AuNRTs then bind specific analyte; in this case, perilipin-2 (PLIN-2) and cause a red shift in the localized surface plasmon resonance (LSPR) for the AuNRTs.



### **1.2.3 Organosilica encapsulated biorecognition elements for stable and refreshable plasmonic biosensor.**

Point-of-care, wearable and implantable biosensors have attracted extensive attention owing to their ability to provide continuous monitoring of biophysical and biochemical parameters in biofluids such as sweat, saliva, interstitial fluid and tears.<sup>61-65</sup> In the past few years, the frontiers and the possible applications of such devices are rapidly advancing from tracking physical activity and biophysical parameters to continuous monitoring of target molecular biomarkers at physiological and pathological concentrations. While there have been significant efforts in realizing such biosensors, there are still significant challenges that need to be overcome before such classes of biosensors can be widely used for making timely clinical interventions in pathological conditions that can rapidly manifest into life-threatening events or chronic conditions. In fact, to date, only minimally invasive glucose monitoring devices have some commercial presence.<sup>66</sup>

Biosensors designed for continuous monitoring of biochemical analytes should be able to detect and quantify the target analyte (*e.g.*, biomarker) for an extended duration. However, the number of analyte binding sites in most biosensors are limited and once saturated with target analytes, it becomes insensitive to further changes in the concentration of the analyte as the analyte-recognition element interactions (especially antibody-antigen interactions) are virtually irreversible under normal conditions. Additionally, the long-term usage of biosensor is limited by the poor stability of antibodies. A possible approach to overcome these problems is to design a strategy to preserve the biorecognition elements and refresh the sensor without compromising the sensitivity and specificity of the biorecognition elements. As a proof-of-concept, in this study, we employed plasmonic nanostructures as a transduction platform. Owing to their high refractive

index sensitivity, plasmonic nanostructures are able to transduce biomolecular binding events (capture/release of analyte) into measurable shift in the localized surface plasmon resonance (LSPR) wavelength.<sup>67-70</sup> The refractive index sensitivity of plasmonic nanostructures has been harnessed to realize various chemical and biological sensors.<sup>71-75</sup> Plasmonic biosensors relying on antibodies as recognition elements are highly promising as lab-on-chip devices for label-free protein detection in point-of-care (POC) and resource-limited settings.<sup>76-79</sup>

In most immunosensors, antigens are recognized and captured by antibodies *via* noncovalent interactions such as hydrogen bonds, van der Waals forces, electrostatic and hydrophobic interactions.<sup>80-83</sup> These interactions can be disrupted by extremes of pH, high salt concentrations and surfactants.<sup>83</sup> Under these harsh conditions natural antibodies are unstable and are prone to lose their biorecognition capability owing to their poor chemical and environmental stability.<sup>84-87</sup> We and others have reported various methods to preserve the biorecognition capability of antibodies under harsh conditions, which include encapsulation of immobilized antibodies with metallic-organic frameworks<sup>76-78</sup>, silk<sup>88</sup>, and sucrose<sup>89</sup>, or addition of other preservatives<sup>90-91</sup>. While these strategies successfully preserve the biorecognition capability of biodiagnostic reagents immobilized on plasmonic nanotransducers against harsh environmental conditions during storage and transportation, they do not protect the antibodies during sensor operation or during sensor refreshing.

In this research objective we demonstrate the encapsulation of antibodies immobilized on plasmonic nanostructures with an organosilica layer, which renders refreshability to the biosensors by preserving the antibody biorecognition ability upon subjecting them to harsh chemical treatment for dissociating the antibody-antigen interactions. Schematic illustration of the steps involved in the organosilica-based biopreservation of bioconjugates to realize refreshable

biosensors is depicted in **Figure 1.4**. This novel method overcomes the challenges associated with poor stability of immobilized antibodies under harsh conditions and opens up opportunities for realizing POC, wearable and implantable biosensors for continuous monitoring of protein biomarkers over long durations.

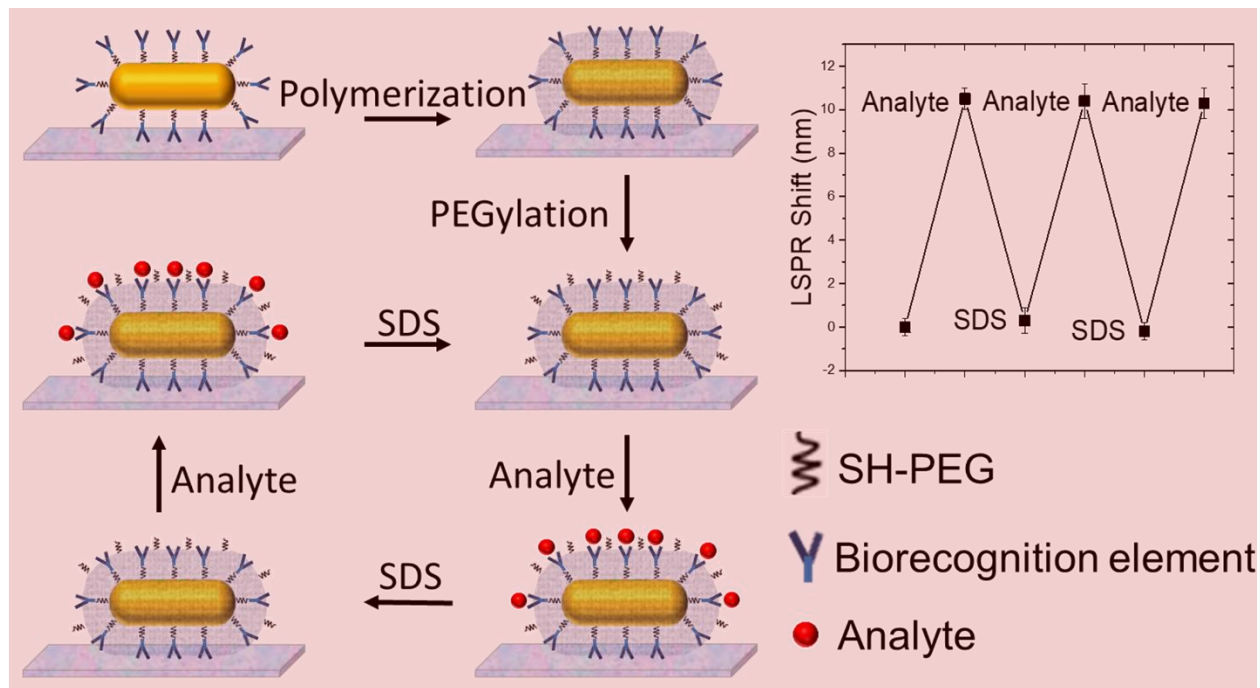


**Figure 1. 4:** (Left) Schematic illustration of the steps involved in the organosilica-based biopreservation of bioconjugates to realize refreshable biosensors. (Right) Typical LSPR wavelength shift response after alternate exposure of polymer encapsulated biosensors to analyte and SDS.

#### 1.2.4 Collagen foam-based biosensors for detection of collagenase and periodontal disease monitoring.

Collagenases such as MMP 1, 8 and 13 are the group enzymes which are responsible for the degradation of most of the extracellular matrix proteins such as collagen. As a family of zinc-dependent neutral metalloproteinases, collagenases are important proteolytic tools for extracellular matrix remodeling during organ development and tissue regeneration. They also play important roles in many pathological situations.<sup>92-93</sup> For example, collagenase can degrade collagen, which

is the major component of gingival fluid. Collagen is also an important component of cell membranes in various tissues, such as skin, heart, blood vessels, cartilage, and synovial fluid. An excess production of collagenases can destroy extracellular matrix and lead to pathological conditions.<sup>94-95</sup> Moreover, several studies have shown that collagenases are biomarkers of various diseases, particularly tumor invasion, metastasis,<sup>96-97</sup> periodontitis, osteoarthritis and rheumatoid arthritis.<sup>98</sup> Therefore, development of new rapid and sensitive and selective detection of collagenase is of great significance in the diagnosis of collagenase relevant diseases.

The activity of collagenases can be determined by the ninhydrin-mediated formation of a purple colored adduct with N-termini that are freshly generated in proteins and peptides by the proteolytic reaction, through an assay based on a method developed by Moore and Stein several decades ago.<sup>99</sup> Activity measurements based on the use of ninhydrin require multiple steps, and the fluctuating formation of purple color makes the assay somewhat unreliable. Over the years, modified versions of this assay have evolved.<sup>95, 100</sup> This method continues to be used. However, the assay remains lengthy, with poor sensitivity (detection being limited to substrate degraded by 10 ng of collagenase in 2 h). Physical changes resulting from the enzymatic reaction of collagen with collagenases, e.g., turbidity and viscosity measurements have also been used in assays.<sup>101</sup> Other methods for measuring collagenase activity include (i) immunological methods, wherein the breakdown of type II collagen is monitored by the use of antibody against the C-terminal neoepitope generated during the reaction,<sup>102-103</sup> or (ii) the formation of specific products, e.g., hydroxyproline,<sup>104</sup> or (iii) use of radio or fluorescence-labelled collagens<sup>105-108</sup> or (iv) use of specially designed synthetic oligopeptides, offering fluorescence, or absorption, as probes of the reaction<sup>109-110</sup>, or v) zymography-based methods.<sup>111-112</sup> All of these methods have their own limitations of being lengthy, or uneconomical, or potentially unsafe to handle (in case of

radiolabels), or they suffer from a lack of sensitivity. Most of them cannot be extended to use with other proteases. Therefore, it is imperative to develop a cost-effective assay for rapid and sensitive detection of collagenase activity.

We hypothesized that instead of using enzyme specific substrates, we can use collagen foam loaded with functional nanoparticles as a substrate. The collagen foam upon exposure to collagenase in solution will degrade, resulting in the release of nanoparticles into the solution. We predicted that there will be collagenase concentration dependent release of nanoparticles. Then instead of relying on extent of ninhydrin-mediated reaction, the concentration of released nanoparticles can be determined to detect collagenase activity. To test this hypothesis we loaded collagen foam with ultrabright plasmonic nanoparticles called plasmonic fluor (PF). PF exhibit detectable fluorescence signal even at concentration as low as 10 nM, thus enabling detection of collagenase activity even at very low concentration of collagenase. This technique will offer quick and sensitive determination of concentration of collagenase present in biospecimens such as saliva.

Next to test the real-life applicability of this technique we aim to analyze the concentration of collagenase in saliva. **Figure 1.5** above illustrates the steps involved in the determination of collagenase concentration in the Saliva. Collagen foam loaded with ultrabright plasmonic nanoparticles is added to the solution containing diluted saliva sample. Small volume of solution will be taken out every 2 mins until 10 mins and added on to 96 well plate. The fluorescence intensity will be measured and from the slope of the thus generated fluorescence vs time graph will be used to determine collagenase concentration or activity. This technique will offer quick and sensitive determination of concentration of collagenase present in biospecimens such as saliva.

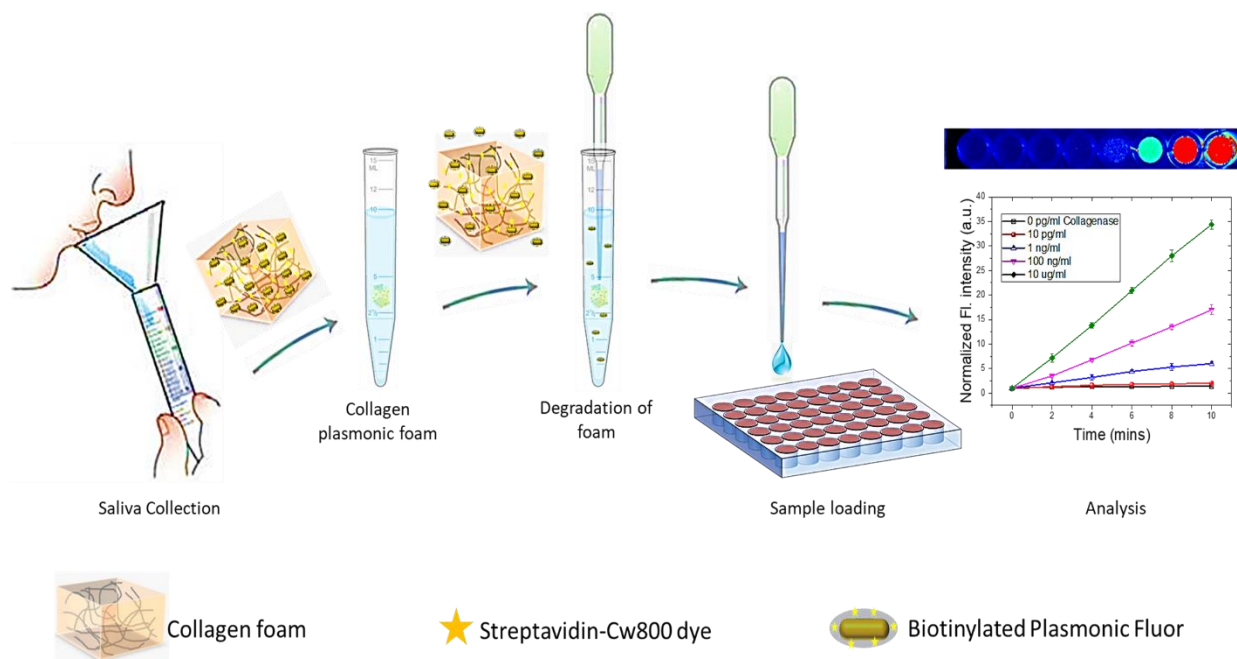


**Figure 1. 5:** Schematic illustration of steps involved in measurement of collagenase concentration in saliva using collagen plasmonic foam.

### 1.2.5 Digital fluoroimmunoassay for sub-femtomolar detection of protein biomarkers.

COVID-19, an infectious disease caused by severe acute respiratory syndrome coronavirus-2 (SARS-CoV-2) has infected more than 239 million people and claimed more than 4.8 million lives as of October 2021 (<https://covid19.who.int/>). The SARS-CoV-2 virus spreads efficiently from one person to another and has led to a worldwide pandemic in a short time. Despite widespread dissemination of vaccination, several countries worldwide are seeing emerging new variants with higher infection rates.<sup>113</sup> According to CDC, 400 million tests have been performed with a positivity rate of 8% in the US to date.<sup>114</sup> Moving forward, access to advanced testing tools that can identify stage of illness and infectivity of individuals, vaccination rates, and efficacy of the vaccines against the emerging variants will determine the trajectory of the pandemic.

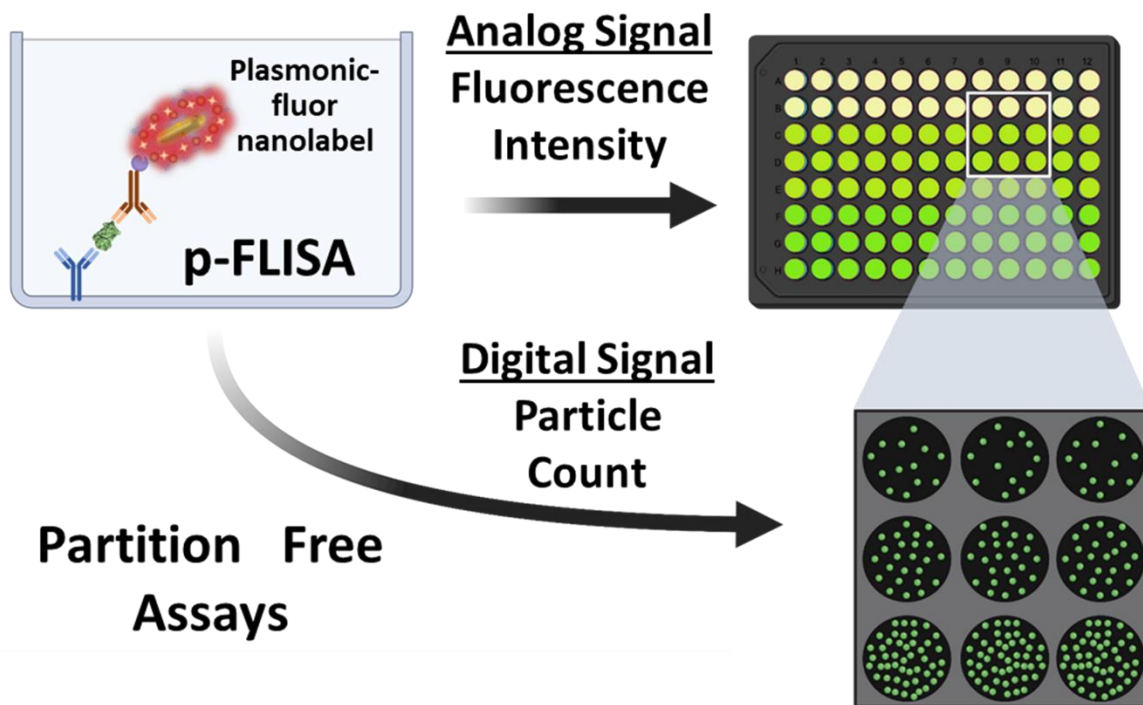


**Figure 1. 6:** Schematic illustration analog and digital p-FLISA.

Reverse-transcription polymerase chain reaction (RT-PCR), used to detect the viral genetic material (RNA) in nasopharyngeal (NP) swabs and saliva, is the current gold standard in diagnosing COVID-19. Although nucleic acid amplification tests have proven highly successful in identifying individuals who have contracted the SARS-CoV-2 virus, they fail to distinguish infectious patients from those who have passed the infectious period, and can yield false positive results for months after a patient has recovered from the disease.<sup>115-118</sup> Severely immunocompromised patients can shed viable SARS-CoV-2 for weeks to months, and identifying these patients using point-of-care non-culture-based tests will be valuable in decision making regarding hospital infection prevention measures.<sup>119-121</sup> Most patients (>95%) with mild to moderate COVID-19 continue to shed SARS-CoV-2 RNA from the nasopharynx  $\geq 10$  days after symptom onset; however, no replication competent virus was found beyond 9 days<sup>122,123</sup>. whereas

replicating virus was cultured through day 20 among critically ill and immunocompromised patients.<sup>124</sup>

There is an urgent need to accelerate COVID-19 testing for identifying active infections, using a simple, high-throughput, non-labor-intensive method that would be more economical and just as accurate as the RT-PCR method. As antigens are expressed only when the virus is actively replicating, the antigen-based tests may have a better correlation with infectiousness than RNA detection by RT-PCR, but are limited by their low and wide ranging accuracy.<sup>116, 118, 123, 125-128</sup> Among four SARS-CoV-2 structural proteins, membrane (M), envelope (E), nucleocapsid (N) and spike (S), the N and S proteins are of great interest as the target antigens due to their abundance and distinct structure compared to previously reported coronaviruses. The N protein aids in transcription, replication, packaging of the viral genome, and the S protein mediates interaction with host angiotensin-converting enzyme 2 (ACE2) receptor, for binding and membrane fusion. Both proteins determine the viral transmission capabilities. Rapid antigen tests have poor agreement with RT-PCR, but are useful in identifying early infections and those with culture positive SARS-CoV-2.<sup>128-130</sup> Antigen tests have the potential to reduce community transmission as they can better differentiate individuals with active infection and past infection.<sup>131-132</sup> However, current antigen tests have lower sensitivity than molecular tests (sensitivity of 37.7-84.1%) and are thus current guidelines recommend the use of molecular test over antigen tests as diagnostic method of choice for diagnosing SARS-COV-2 infection recommended to be performed in conjunction with molecular tests or in situations where a molecular test is not available or not feasible.<sup>133</sup> An ultrasensitive antigen test that can be implemented in standard clinical laboratories and in low-resource settings at low-cost can potentially alter the trajectory of the COVID-19 and future pandemics.



Here, we report an ultrasensitive partition-free digital assay for the detection of SARS-CoV-2 antigens. The assay relies on a novel ultrabright fluorescent nanoconstruct, plasmonic fluor, comprised of a plasmonic nanostructure (gold nanorod, AuNR), a light emitter (molecular fluorophores), and a biological recognition element (*e.g.*, biotin, streptavidin).<sup>134</sup> Plasmonic-fluors have been reported to improve sensitivity by up to three orders of magnitude in various bioassays, including immuno-microarrays, fluorescence linked immunosorbent assay (FLISA), bead-based fluoro-immunoassays, and flow cytometry. In contrast to these analog assays, for the first time, we harness plasmonic-fluor as a digital nanolabel that can be imaged using conventional epifluorescence microscopy and “counted” using a simple image-processing algorithm (**Figure 1.6**). Digital immunoassays involve the detection and counting of single sandwich complex comprised of capture antibody, analyte, and detection antibody, thus significantly improving the limit of detection compared to their analog counterparts. In a standard digital assay, the number of analyte molecules is determined by counting the number of discrete “positive signal” units. The binary signal obtained in conventional digital assay technologies such as single molecule array (SIMOA) relies on partitioning the immunoreaction into femtoliter wells, which results in either 1 or 0 analyte molecules per well, and counting the number of wells with a positive signal.<sup>135-137</sup> The major draw-back of these assays is that only around 5% of the beads used to capture the analyte are loaded into the wells and complex fabrication and read-out procedures are required, limiting their use in standard biomedical research and clinical laboratories.<sup>138-140</sup> Partition-free bead-based assays rely on complicated signal amplification techniques such as rolling-circle amplification which uses an isothermal enzymatic reaction to synthesize long single stranded (ss) DNA on a short circular ss DNA template to improve its sensitivity.<sup>141</sup> The simple and easy-to-implement

digital assay offers nearly 10000-fold lower LOD compared to the “gold standard” ELISA, making it a potentially powerful diagnostic tool in our fight against COVID-19 and future pandemics.

### **1.2.6 Plasmon-enhanced, quantitative lateral flow Assay for femtomolar detection of protein biomarkers in point-of-care settings.**

Lateral flow (immuno)assays (LFAs) are amongst the simplest, fastest, and cheapest point-of-care (POC) diagnostic methods, and offer broad potential for population-level screening for disease.<sup>142-143</sup> However, this potential has not yet been fully achieved. Although numerous LFAs for severe acute respiratory syndrome coronavirus 2 (SARS-CoV-2) antibodies<sup>144-146</sup> and antigens<sup>147-148</sup> have been introduced, none have sensitivity and quantitation comparable to laboratory-based diagnostics such as real-time reverse transcription polymerase chain reaction (RT-PCR) and enzyme-linked immunosorbent assay (ELISA), which constrains their widespread use.<sup>149-151</sup> In general, conventional colorimetric-LFAs are ~1000-fold less sensitive than these standard laboratory tests,<sup>152-153</sup> and diagnosis using LFAs requires an additional confirmatory laboratory-based test to correctly establish negative results. Colorimetric-LFAs offer limited quantification ability owing to the limited color change with respect to variation of the target analyte’s concentration.<sup>154</sup>

The COVID-19 pandemic highlights the need for improved LFAs for precise and rapid clinical diagnoses, mass screenings and epidemiological studies.<sup>155-156</sup> RT-PCR<sup>157-158</sup> and direct antigen tests<sup>159-160</sup> have been the mainstay for diagnosis of COVID-19, and serological assays are important for determination of infection stage and vaccine efficacy, and epidemiological studies.<sup>144, 161-162</sup> These diagnostic assays are available only in qualified microbiology laboratories and remain expert-dependent, labor-intensive, and time-intensive, limitations that have precluded conduction of the millions of tests per day needed during epidemiological surges.<sup>163-164</sup> Therefore,

a critical need exists for diagnostic and screening tools that are not only as accurate as laboratory-based assays, but also rapid, easy-to-use, inexpensive, readily available (*e.g.*, home-based and POC), and scalable for rapid population-level screening.

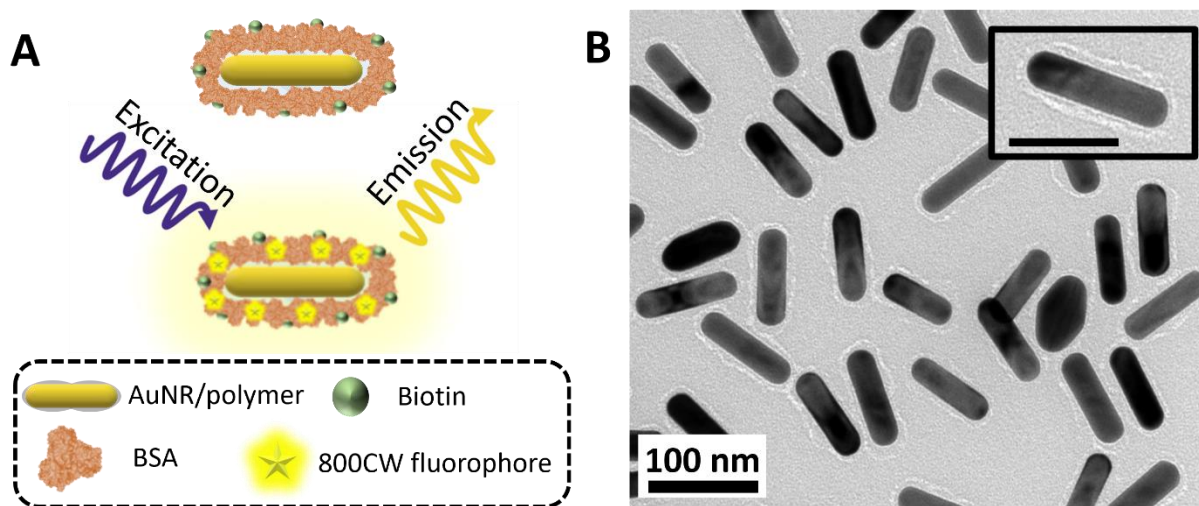


**Figure 1. 7:** (A) Schematic illustration of plasmonic-fluor, employed as a bimodal nanolabel (colorimetric+fluorescent) in LFAs, comprising of gold nanorod as plasmonic core, polymer layer as spacer, molecular fluorophores (800CW), and biotin as recognition element. (B) Transmission electron microscopy image of plasmonic-fluors.

Efforts to improve bioanalytical performance of LFAs have included using fluorescent molecules or quantum dots as reporter elements.<sup>165-166</sup> Although fluorescent reporters improve quantification, their relatively weak signal intensity limits their sensitivity and point-of-care diagnostic utility, and their low light absorption compared to conventional colloidal gold nanoparticles (AuNPs)<sup>30</sup> precludes the direct visual detection available in conventional LFAs, and moreover requires use of LFA readers with highly sensitive detectors or powerful excitation light sources. These limit the utility of fluorescent LFAs in mass screening and resource-limited settings.<sup>151</sup>

We envision a “bimodal” LFA in which an initial screening can be performed with a visual test, and subsequent quantitative testing can be performed when needed on the same LFA strip using a fluorescence reader. To achieve this, we employed an ultrabright fluorescent nanoconstruct

that we have recently introduced,<sup>167</sup> called plasmonic-fluor, as a bimodal colorimetric and fluorescent reporter in LFAs (**Figure 1.7A and B**). These nanoconstructs harness plasmon-enhanced fluorescence<sup>168-172</sup> to achieve nearly 7000-fold brighter fluorescence signal compared to conventional molecular fluorophores. We conjugated plasmonic-fluors with detection antibodies and used them to enable rapid and ultrasensitive colorimetric and fluorescent detection of analytes, using human IL-6 (LOD: 93 fg ml<sup>-1</sup>), SARS-CoV-2 S1 (subunit of the spike protein) antibodies (LOD: 185 pg ml<sup>-1</sup>), and SARS-CoV-2 antigen (nucleocapsid) protein (LOD: 212 pg ml<sup>-1</sup>). We validated the clinical efficacy of the plasmonic-fluor-based LFAs (p-LFAs) by testing plasma, serum and nasopharyngeal (NP) swab samples for detection of SARS-CoV-2 S1 antibodies, IL-6, and SARS-CoV-2 antigen, respectively, and achieved high clinical specificity and sensitivity. We also demonstrate the quantitative ability of p-LFA employing a portable self-designed scanner compatible with plasmonic-fluor to demonstrate its versatile POC application. Significantly, this technology can be immediately deployed as an alternative to laboratory-based test for the diagnosis of clinically-relevant pathogenic infections and possible future pandemics.

### 1.3 Dissertation outline

The dissertation will illustrate ways to augment the bioanalytical parameters of the label-free and labelled biosensors to enable their application in POC and resource-limited settings. The current chapter (**Chapter 1**) provides an overview of the research efforts and provides a brief background on optical properties of plasmonic nanoparticles.

**Chapter 2** describes a label-free biosensor consisting of microneedle (MN) patch and plasmonic paper that collects ISF for on-patch biomarker analysis by SERS. This approach was used to measure pharmacokinetic profiles of R6G in ISF and serum from rats in vivo. In **chapter**

**3**, we discuss the development of a label-free plasmonic biosensor based on the high refractive index sensitivity (LSPR) of gold nanorattles for the rapid detection of PLIN-2 in patient urine. The assay is not compromised by variations in urine pH or high concentrations of interfering proteins such as albumin and hemoglobin, making it an excellent candidate for routine clinical applications.

In **chapter 4**, we introduce a novel method involving organosilica encapsulation of antibodies for preserving their biorecognition capability under harsh conditions, typically encountered during the sensor refreshing process, and elevated temperature. Harnessing this method, we demonstrate the refreshability of plasmonic biosensors for anti-IgG (model bioanalytes) and neutrophil gelatinase-associated lipocalin (NGAL) (a biomarker for acute and chronic kidney injury).

In **chapter 5**, we discuss a novel approach for detection and quantification of inflammatory disease burden via plasmonically-active tissue analog which can undergo in vivo or ex vivo degradation in the presence of biological fluid associated with the tissue. Specifically, we employ a collagen foam loaded with ultrabright fluorescent nanolabels for detection of collagenase present in biospecimen. This offers highly sensitive and rapid detection of collagenase present in biospecimen and can help in determination of early progression of pathological conditions.

In **chapter 6**, we discuss the development of digital fluoroimmunoassay (labelled biosensor) for ultrasensitive and quantitative detection of SARS-CoV-2 proteins in nasopharyngeal swab and saliva samples from COVID-19 patients. Compared to the “gold standard” enzyme-linked immunosorbent assay (ELISA), the digital p-FLISA exhibited nearly 7000-fold lower limit-of-detection with virtually no change in the biorecognition elements or assay workflow.

Finally in **chapter 7** we discuss the development of plasmon-enhanced, quantitative lateral flow assay for femtomolar detection of protein biomarkers in point-of-care settings. Our LFA,

completed in 20 min, attained 30-fold improvement in dynamic range and limits of detection over the 4 hour-long, “gold standard” enzyme-linked immunosorbent assay (ELISA). This improvement over ELISA could be achieved with either a standard benchtop fluorescence scanner or an inexpensive, portable scanner that we developed.

There are two appendices attached at the end of the dissertation. **Appendices A and B** contain the supplementary information of Chapters 6 and 7, respectively. Appendices are followed by my curriculum vitae.

# Chapter 2: Plasmonic Paper Microneedle Patch for On-Patch Detection of Molecules in Dermal Interstitial Fluid

*The results reported in this chapter have been published in – Kolluru, C.\*, Gupta, R.\*, et al, & Singamaneni, S. (2019). “Plasmonic Paper Microneedle Patch for On-Patch Detection of Molecules in Dermal Interstitial Fluid” ACS Sensors, 2019, 4(6), 1569-1576.*

## 2.1 Abstract

Minimally invasive devices to detect biomarkers in dermal interstitial fluid (ISF) are desirable for point-of-care diagnostic and monitoring applications. In this study, we developed a microneedle (MN) patch that collects ISF for on-patch biomarker analysis by surface-enhanced Raman scattering (SERS). The micron-scale MNs create micropores in the skin surface, through which microliter quantities of ISF are collected onto plasmonic paper on the patch backing. The plasmonic paper was prepared by immobilizing poly (styrene sulfonate) (PSS) coated gold nanorods (AuNRs) on a thin strip of filter paper using plasmonic calligraphy. Negatively charged PSS was used to bind positively charged rhodamine 6G (R6G), which served as a model biomarker, and thereby localize R6G on AuNR surface. R6G bound on the AuNR surface was detected and quantified by acquiring SERS spectra from the plasmonic paper detached from the MN patch. This approach was used to measure pharmacokinetic profiles of R6G in ISF and serum from rats in vivo. This proof-of-concept study indicates that a plasmonic paper MN patch has the

potential to enable on-patch measurement of biomarkers in ISF for research and future medical applications.

## 2.2 Materials and Methods

**Materials:** Cetyltrimethylammonium bromide (CTAB), chloroauric acid ( $\text{HAuCl}_4$ ), ascorbic acid, sodium borohydride, poly(styrene sulfonate) (PSS) ( $M_w = 70,000 \text{ g/mol}$ ), rat serum, filter paper (Whatman #1) and rhodamine 6G (R6G) were purchased from Sigma Aldrich (St. Louis, MO). Silver nitrate was purchased from VWR International (Radnor, PA). All chemicals were used as received.

**Microneedle patch fabrication:** MN patch dimensions were drafted using AutoCAD software (Autodesk, Cupertino, CA) and then prepared by lithographically defined chemical etching (Tech Etch, Plymouth, MA). Patches comprised 9 MNs ( $650 \mu\text{m}$  long) each measuring  $50 \mu\text{m} \times 150 \mu\text{m}$  in cross section at the base and tapering to a tip of  $<1 \mu\text{m}$  radius of curvature. Whatman grade 1 filter paper was cut into rectangular strips of desired dimensions ( $2 \text{ mm} \times 7 \text{ mm}$  or  $1 \text{ mm} \times 7 \text{ mm}$ ) using a  $\text{CO}_2$  laser (New Hermes Gravograph Model LS500XL, Gravotech, Duluth, GA). A vector cut at 24 W power and a speed of 8 mm/s was used to make the pattern. To avoid burning due to excessive temperature rise during laser cutting, the heat capacity of the filter paper was increased by attaching it to an adhesive backing (3M, Maplewood, MN), followed by soaking in deionized (DI) water until completely wet. The final MN patch was prepared by adhering the paper strip to the base of each MN patch without covering the needles using adhesive (3M, Maplewood, MN). The MN patches with  $2 \text{ mm} \times 7 \text{ mm}$  filter paper were used as prepared while the MN patches with  $1 \text{ mm} \times 7 \text{ mm}$  filter paper were further modified with AuNRs.



**Plasmonic paper microneedle patch preparation:** AuNRs were synthesized using a seed-mediated approach as previously published<sup>173-174</sup>. The seed solution was prepared by mixing 0.6 ml of 10 mM ice-cold sodium borohydride solution with 10 ml of CTAB (0.1 M) and HAuCl<sub>4</sub> (2.5 × 10<sup>-4</sup> M) solution under vigorous stirring. The growth solution was prepared by gently mixing 95 ml of CTAB (0.1 M), 0.5 ml of silver nitrate (10 mM), 4.5 ml of HAuCl<sub>4</sub> (10 mM), and 0.55 ml of ascorbic acid (0.1 M). AuNR solution was prepared by adding 0.12 ml of freshly prepared seed solution to the growth solution and left in the dark for 14 h. Prior to use, excess CTAB was removed from the AuNR solution by centrifuging twice at 9300 x *g* for 10 min in a centrifuge (Eppendorf 5810 R, Hamburg, Germany) and the AuNRs were redispersed in nanopure water (18.2 MΩ cm). AuNRs were modified with PSS<sup>175</sup> and concentrated to form a plasmonic ink<sup>176</sup>, as described previously. Briefly, 10 ml of PSS (0.2% w/v) in 6 mM NaCl aqueous solution were mixed with 10 ml of twice-centrifuged AuNR solution under vigorous stirring and sonicated for 60 min. Excess PSS solution was removed as supernatant after centrifuging at 9300 x *g* for 10 min. The recovered pellet of PSS-AuNR was then redispersed in nanopure water to obtain 100 μl of plasmonic ink (200-fold concentration). The plasmonic ink was injected into a clean empty ballpoint pen refill (Paper Mate Profile, Oak Brook, IL), and used to “write” PSS-AuNRs onto the 1 mm x 7 mm filter paper, which was then adhered to MN patches to make plasmonic paper MN patches.

**ISF collection procedure:** A MN patch was inserted into rat skin 5–10 times while pinching the skin with a force of 20–40 N until the filter paper on the MN patch was visually determined to be saturated with ISF. This application force was easily administered by hand and has been shown in other studies of MN patch application not to be associated with pain.<sup>177-178</sup> This estimate was performed by determining sodium ion content in the MN patch paper backing using a sodium ion

sensitive electrode (perfectION comb NA, Mettler Toledo, Columbus, OH). The sodium ion content measured in the samples was divided by the physiological sodium ion concentration in rat ISF of 143 mEq/L. The amount of ISF collected was estimated to be  $1.1 \pm 0.3 \mu\text{L}$  or  $2.0 \pm 0.2 \mu\text{L}$  once the  $1 \text{ mm} \times 7 \text{ mm}$  or  $2 \text{ mm} \times 7 \text{ mm}$  filter paper on the MN patch was saturated with ISF, respectively, as described previously.<sup>179</sup>

**Characterization:** Transmission electron microscopy (TEM) micrographs were obtained using a JEM-2100F field emission instrument (JEOL, Peabody, MA) by drying  $2 \mu\text{l}$  of AuNR solution on a glow discharge-treated carbon-coated grid. Scanning electron microscope (SEM) images were recorded on a gold-sputtered plasmonic paper by using a Nova 2300 Field Emission SEM (FEI, Hillsboro, OR) at an accelerating voltage of 10 kV. UV-Vis extinction spectra were measured using a UV-1800 UV-Vis spectrophotometer (Shimadzu Scientific Instruments Inc., Columbia, MD).

**SERS measurements of R6G spiked ISF and serum samples:** Raman spectra were collected using an inVia confocal Raman microscope (Renishaw, Gloucestershire, UK) mounted on Leica microscope and controlled with Wire 3.4 software. The 785 nm wavelength diode laser (0.5mW) coupled to a holographic notch filter with a grating of  $1200 \text{ lines mm}^{-1}$  was focused onto the sample using a 20X objective (NA = 0.4) with 10s exposure time., and 1 accumulation was collected per spot. Six spectra were collected from different spots across each substrate, using a motorized XYZ translational stage integral to the microscope. ISF calibrators were prepared by adding aliquots of R6G stock solution to ISF (extracted from porcine cadaver skin) to create the following concentrations: 0, 0.05, 0.5, 2, 5, 10, 25, 50 and  $100 \mu\text{M}$  R6G in ISF. Serum calibrators were prepared by adding aliquots of R6G stock solution to rat serum (collected from rats in vivo) to create the following concentrations: 0, 0.5, 5, 10, 25, 50 and  $100 \mu\text{M}$  of R6G in Serum. The

plasmonic paper was soaked in 150  $\mu$ L of calibrator for 1 hour, thoroughly rinsed in DI water for 5 min, and air dried prior to collecting SERS spectrum from six different locations across the substrate.

**In-vivo study and pharmacokinetic analysis:** Procedures were performed on six hairless rats (335-375 gm, female, Charles River Laboratories, Wilmington, MA) continuously anesthetized by isoflurane (Isothesia, Henry Schein Animal Health, Dublin, OH) in 100% oxygen inhalation during drug administration and sample collection. A silicone rubber tube was placed in the right jugular vein and kept locked with sodium heparin (100 U/ml) solution in physiological saline. Care was taken to avoid administration of air bubbles, and blood samples were replaced with an approximately equal volume of heparinized saline. Each rat was infused with 10 mg/ml R6G in sterile water via a 24-gauge angiocatheter in the tail vein at a rate of 0.1 ml/min over 30 min by means of an infusion pump (Harvard Apparatus, Holliston, MA). Blood samples ( $\leq 500 \mu$ l) were collected in microtainer collection tubes with clot activator (BD Diagnostics, Franklin Lakes, NJ) from the jugular tube once prior to and at 2, 7, 15, 20, 30 and 35 min after the start of R6G infusion. Companion ISF samples were also collected using MN patches with plasmonic paper or bare filter paper (without AuNRs) from the lateral side of the rat at the same time points. At the end of the study, a final blood sample ( $\leq 1$  ml) was collected from each rat before euthanizing by carbon dioxide gas asphyxiation without recovery from isoflurane. These experiments were approved by the Georgia Institute of Technology Institutional Animal Care and Use Committee.

**Detection of R6G from ISF/serum samples using SERS:** Serum was separated from blood samples by centrifuging at 6000  $\times g$  for 1.5 min in a centrifuge tube (Eppendorf 5415R, Hamburg, Germany). For SERS-based testing, 1  $\mu$ l of each serum sample was added on a piece of plasmonic paper and allowed to air dry. The ISF samples collected on plasmonic paper MN patches were

tested directly. After rinsing in water, six spectra were collected from different locations across each plasmonic paper substrate to measure the intensity of the  $1364\text{ cm}^{-1}$  Raman band. The corresponding concentration of R6G was determined from a calibration curve.

**Detection of R6G from ISF/serum samples using fluorescence spectroscopy:** A 1:50 dilution of serum samples was performed by mixing  $2\text{ }\mu\text{l}$  of serum with  $100\text{ }\mu\text{l}$  of DI water and a 1:50 dilution of ISF samples was performed by extracting ISF from the MN patches by centrifuging at  $6000\times g$  for 1.5 min in  $100\text{ }\mu\text{l}$  DI water per MN patch. The R6G concentration in ISF and serum samples was measured against a standard calibration curve of R6G in a 384 well plate (Costar Black Polypropylene, Corning, Corning, NY) using a Synergy H4 hybrid reader (BioTek, Winooski, VT) at an emission wavelength of 516 nm and absorption wavelength of 557 nm.

Determination of R6G in protein-free serum: To determine the extent of binding of R6G to plasma protein,  $500\text{ }\mu\text{l}$  of serum sample collected prior to euthanizing the rats was centrifuged in a VivaSpin 500 centrifugal filter (MWCO 30,000; Vivaproducts, Littleton, MA) at  $15,000\times g$  for 5 min. The R6G concentration in the protein-free filtrate and in the serum prior to centrifugation were measured using the Synergy H4 hybrid reader, as described above.

**Statistical analysis:** Statistics were calculated using either Origin software (OriginLab, Northampton, MA) or Excel (Microsoft, Redmond, WA). All listed averages represent the arithmetic mean of the samples. Comparisons between individual samples were done using an unpaired t-test. Probability (p) values of  $<0.05$  were considered significant.

## 2.3 Plasmonic paper

We employed AuNRs as plasmonic nanostructures for the fabrication of plasmonic paper. AuNRs synthesized by seed-mediated method were found to be  $88 \pm 7\text{ nm}$  in length and  $33 \pm 2\text{ nm}$  in width, with an aspect ratio of nearly 3 (**Figure 2.1A**). AuNRs were coated with negatively charged

PSS to promote binding of positively charged R6G, which is the model compound used in this study. The optical extinction spectra of PSS-AuNRs showed two characteristic peaks at 513 nm and 683 nm, corresponding to the transverse and longitudinal plasmon resonances of the AuNRs (**Figure 2.1B**).

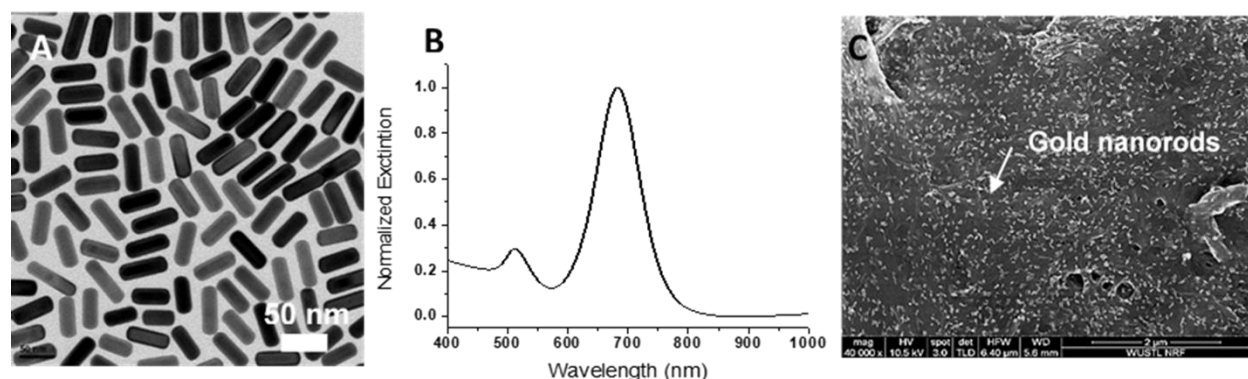


**Figure 2. 1:** Characterization of AuNRs and plasmonic paper. (A) Representative transmission electron microscopy image of AuNRs dispersed in nanopure water. (B) Representative ultraviolet-visible light extinction spectrum of PSS-AuNRs in nanopure water. (C) Representative scanning electron microscopy image of PSS-AuNRs adsorbed on filter paper after “drawing” by plasmonic calligraphy.

Two hundred-fold concentrated PSS-AuNRs solution was filled in a ball point pen refill and written onto a 1 mm x 7 mm filter paper adhered to a steel MN patch and rinsed with DI water to remove any loosely adhering AuNRs. SEM imaging depicts an evenly speckled surface morphology of the paper (**Figure 2.1C**), indicating uniform adsorption of AuNRs to the paper without significant aggregation.

## 2.4 ISF Collection Using Plasmonic Paper Microneedle Patch

We developed a MN patch to collect ISF from skin. The MN patch was comprised of a stainless-steel array of nine, 650 μm long MNs (used to create micropores in the skin surface) extending from a backing layer (for ease of handling). A strip of plasmonic paper was adhered to one side of the patch backing to create a reservoir calibrated to collect ~1 μl of ISF and bind

positively charged R6G (**Figure 2.2A**). ISF collection was performed by applying the MN patch to the skin so that the MNs penetrated the skin surface to create micropores and induce flow of ISF out of the skin and into the paper reservoirs (**Figure 2.2B**). MN insertion was repeated at a rate of  $\sim 1$  insertion per second until  $\sim 1 \mu\text{l}$  of ISF was collected. This process usually required up to 5 MN patch insertions. The MN insertion procedure was well tolerated (**Figure 2.2C**) with a very mild, transient erythema observed at the insertion site.

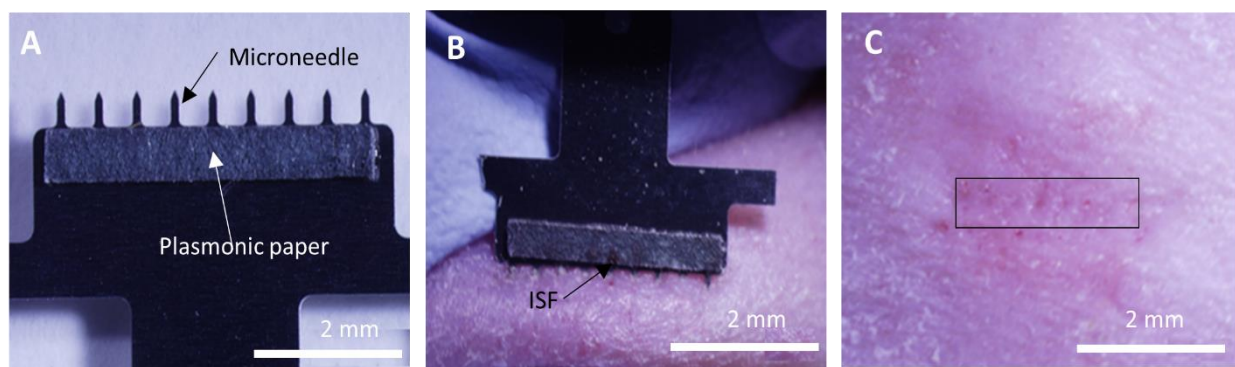


**Figure 2. 2:** Collection of ISF using a plasmonic paper microneedle patch. **(A)** Representative photographic image of a MN patch showing a row of nine MNs measuring  $650 \mu\text{m}$  in length extending from a patch backing with a thin rectangular strip of plasmonic paper adhered to one side. **(B)** Representative photographic image of the onset of ISF collection after two insertions of a MN patch into the skin of a hairless rat in vivo. The MNs, which are on the lower edge of the patch, are not visible because they are inserted into the skin. ISF is collected in the paper reservoir as observed by wetness of the paper (arrow). **(C)** Representative photographic image of rat skin 1 min after ISF collection by MN patch. The site of MN insertion has been marked with a rectangular box.

## 2.5 SERS Performance of Plasmonic Paper

We then turn our attention to the SERS performance of the plasmonic paper using R6G as a model analyte. To acquire a calibration curve, we performed SERS measurements on plasmonic paper incubated with ISF or serum (collected from rats) spiked with a range of concentrations of R6G (**Figures 2.3A and C**). All measurements were performed after air drying the plasmonic paper. With increasing R6G concentration, the Raman spectra show an increase in intensities of

characteristic Raman bands of R6G at 610, 1364 and 1512  $\text{cm}^{-1}$ , which are attributed to the C-C-C ring in-plane bending, C-O-C stretching and aromatic C-C stretching modes of R6G.<sup>180-181</sup>

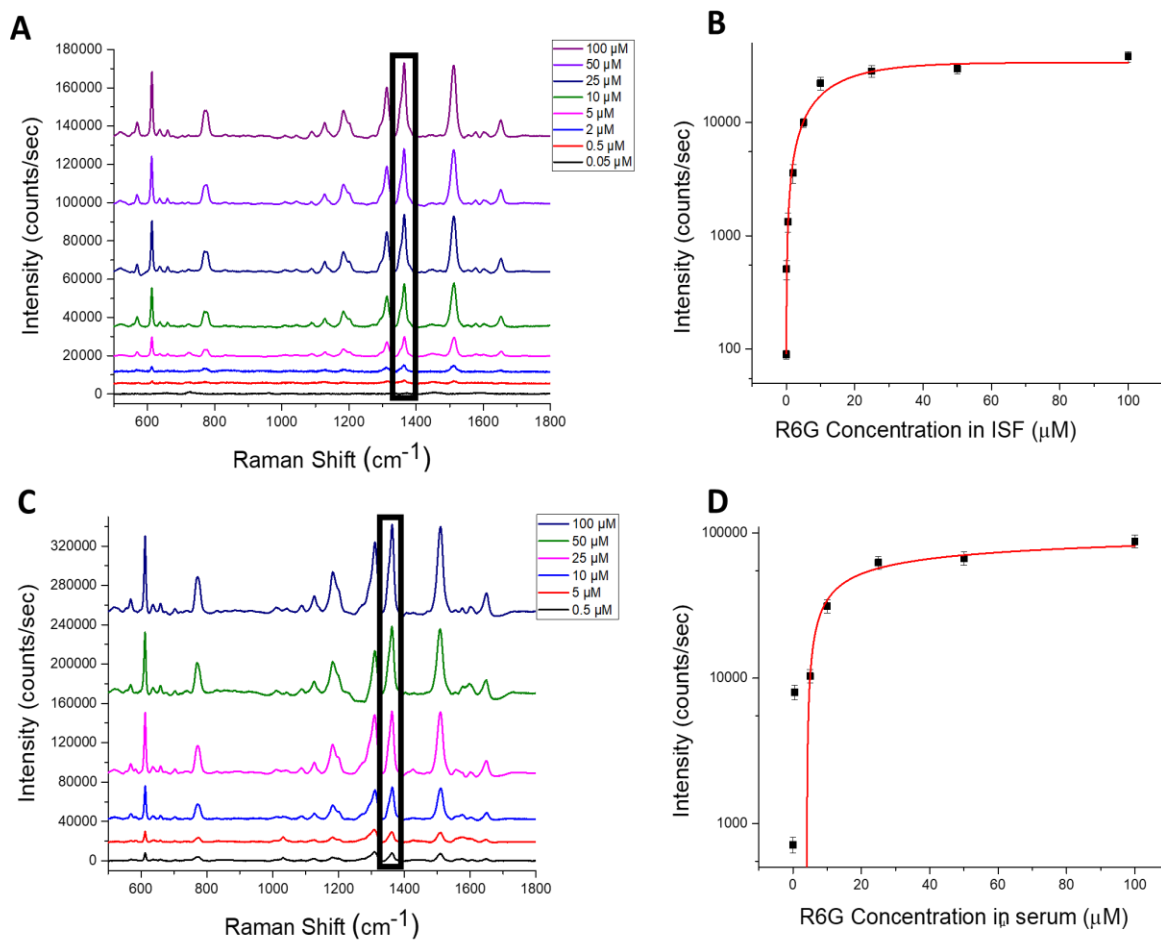


**Figure 2.3:** Measurement of R6G in plasmonic paper by SERS. Representative SERS spectra obtained from plasmonic paper soaked in different concentrations of R6G in (A) ISF and (C) serum. The Raman spectra show an increase in characteristic Raman peaks for R6G at 610, 1364 and 1512  $\text{cm}^{-1}$  with increase in concentration. The Raman band at 1364  $\text{cm}^{-1}$  (indicated with a black rectangular box) was used to generate calibration curves for R6G concentration in (B) ISF and (D) serum. Data points show mean  $\pm$  standard deviation from 6 spectra collected from each plasmonic paper substrate.

The intensity of Raman band at 1364  $\text{cm}^{-1}$ , which is the most intense Raman band for R6G, was plotted against R6G concentration to generate a calibration curve with good fit for both ISF and serum ( $R^2 = 0.97$  and  $0.98$ , respectively) (Figures 2.3B and D). The relative standard deviation is  $\sim 15\%$ , which is close to the values observed for commercially available

microfabricated SERS substrates<sup>182</sup>. Both the ISF and serum spectra in absence of R6G showed low Raman counts at  $1364\text{ cm}^{-1}$  suggesting no interference (**Figures 2.3B and D**). These results indicate that plasmonic paper can serve as a powerful tool to detect and quantify R6G in biological fluids. These calibration curves were used in the subsequent studies to determine the R6G concentration in ISF and serum samples collected in the R6G pharmacokinetic studies presented below.

## **2.6 R6G Pharmacokinetics in ISF Determined by On Patch SERS Measurement Using Plasmonic Paper Microneedle Patches**

To assess the utility of plasmonic paper MN patches, we studied the pharmacokinetics of R6G in ISF and serum in rats as measured by on-patch SERS after allowing the ISF to air dry. The Raman bands in the spectra obtained from ISF and serum look similar, although the intensity of the bands in ISF is about an order of magnitude lower than in serum, as discussed below (**Figure 2.4**).

We also performed ISF collection using conventional paper MN patches from which R6G was eluted and measured by fluorescence spectroscopy for comparison. When comparing R6G concentrations by on-patch SERS versus off-patch fluorescence spectroscopy, there were no statistically significant differences in the concentrations measured in ISF (ANOVA,  $p = 0.61$ ) or in serum samples (ANOVA,  $p = 0.68$ ) (**Figure 2.4**). Whether measured by SERS or fluorescence, there are significant differences in the pharmacokinetic profiles in ISF versus serum. In the experiment, R6G was slowly infused intravenously in each animal for 30 min. The resulting R6G



concentration profile in serum reflects this, showing an increase in R6G concentration for up to 30 min followed by a sharp decrease in concentration after 30 min in both the measurement techniques (**Figure 2.5**). The pharmacokinetic profile in ISF, in contrast, shows a steady increase, without the sudden drop in R6G concentration after 30 min. Moreover, the concentration profile in ISF is an order of magnitude lower than in serum in both the measurement techniques. As discussed below, these differences in the pharmacokinetic profiles may be explained by binding of R6G to plasma proteins, resulting in a steady increase in R6G concentration in ISF.

## 2.7 Binding of R6G to Plasma Proteins

To understand the lower concentration of R6G seen in ISF compared to serum, we isolated protein-free filtrate from serum samples from the pharmacokinetic study. R6G concentration in serum prior to filtration ( $9.6 \pm 4.2 \mu\text{M}$ ) was dramatically higher than in protein-free serum samples ( $0.05 \pm 0.03 \mu\text{M}$ ) (Student's t-test,  $p < 0.008$ ). This indicates that R6G strongly binds to plasma proteins and therefore may not partition well into ISF. This finding is consistent with prior literature, which also reported significant binding of R6G with human serum albumin<sup>183</sup>.

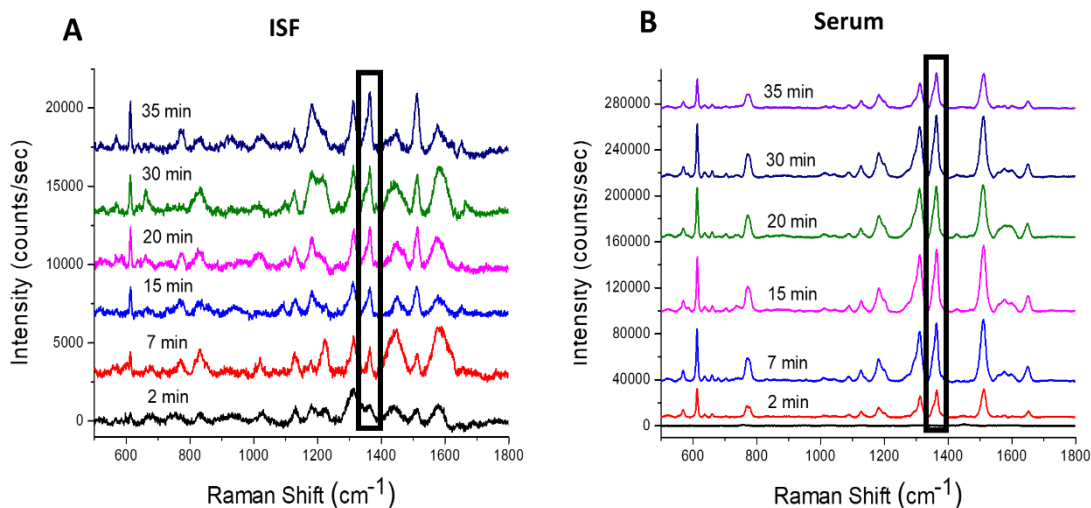


**Figure 2. 4:** Representative spectra from on-patch SERS measurement of samples collected in rats in vivo. (A) ISF was collected on plasmonic paper MN patches. (B) Blood was collected by intravenous catheter, from which serum was isolated and placed on plasmonic paper MN patches.

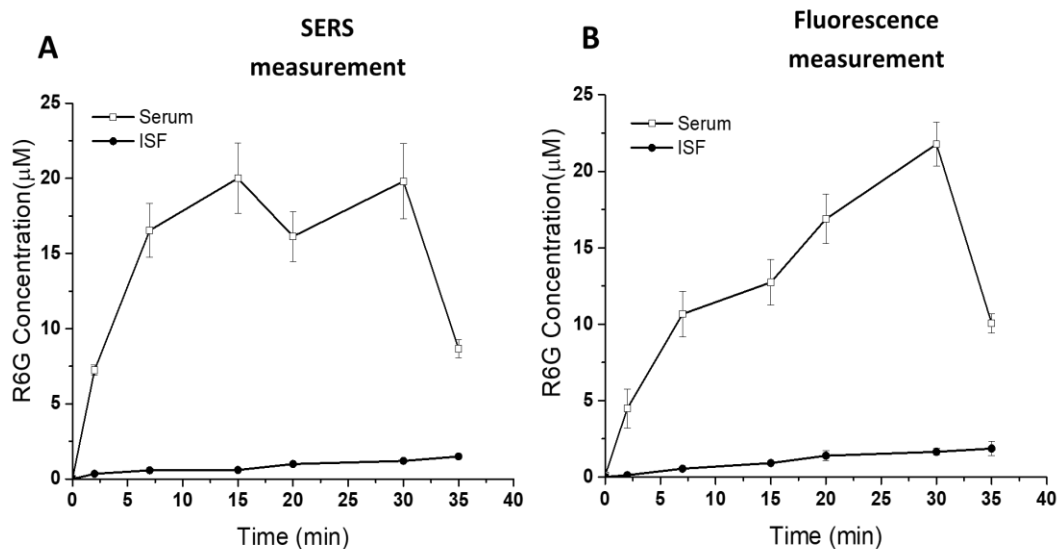


**Figure 2. 5:** Pharmacokinetics of R6G in ISF and serum. (A) On-patch SERS measurement using plasmonic paper MN patches or (B) fluorescence spectroscopy of R6G eluted from conventional paper MN patches. Data points show mean  $\pm$  standard deviation ( $n = 6$  rats).

## 2.8 Conclusions and Outlook

ISF is a rich source of biomarkers, but it has been relatively unexplored due to lack of good sampling methods. Current methods like suction blister, microdialysis and open flow microperfusion cause significant skin trauma, are time consuming and require expert personnel and equipment to perform<sup>8-11</sup>. They also require sample processing steps to prepare samples for analysis. This proof-of-concept study introduces a novel plasmonic paper MN patch for SERS-based detection of molecules in ISF using R6G as a model compound to simulate a biomarker. The plasmonic paper MN patch is minimally invasive, rapid, and simple-to-use. This MN patch also has the capability to perform on-patch SERS-based detection of molecules in ISF using a paper reservoir that captures molecules with functionalized AuNRs. Next steps in this research include optimization of the MN patch for usability, safety and efficacy and development of the

sensor for LSPR or SERS-based detection of biomolecules of clinical significance in ISF for future possible medical applications.

The plasmonic paper MN patch involves a simple, low-cost design using readily available materials. The MN array is fabricated from stainless steel sheets by chemical etching, which can be performed in mass production for pennies per array. The paper reservoir is made of conventional filter paper that has high surface area, is low-cost, is biodegradable, is compatible with conventional printing approaches and is commonly used in paper-based sensor devices<sup>184-186</sup>. The plasmonic calligraphy method controls test domain size in a simple manner by writing with a pen in the desired area. This method also offers the possibility for multiplexed biosensing of multiple biomarkers by simply ‘writing’ different test domains with plasmonic nanostructures functionalized to target different biomarkers of clinical significance. The manufacturing process is scalable due to possibility of inkjet printing of the plasmonic inks onto the paper.

SERS has become a mature analytical technique over the last decades with the development of low-cost, handheld Raman spectrometers. Moreover, development of SERS for medical diagnostic applications has been rapidly increasing<sup>187</sup>, and SERS has been shown to be useful for glucose sensing in vivo<sup>34-35</sup>, detection of diseases such as cholera<sup>188</sup> and detection for potential exposure to explosives<sup>189</sup>. Thus, a plasmonic paper MN patch could be a low-cost, portable, miniature diagnostic device suitable for point-of-care treatment in resource-limited environments.

# Chapter 3: Bioplasmonic Paper-based Assay for Non-invasive Detection of Perilipin-2 for Renal Cancer

*The results reported in this chapter have been published in – Hu, R., Gupta, R., et al, & Singamaneni, S. (2019). “Bioplasmonic paper-based assay for perilipin-2 non-invasively detects renal cancer.” Kidney International, 2019, 96(6), 1417-1421.*

## 3.1 Abstract

Renal cell carcinoma (RCC) has poor survival prognosis because it is asymptomatic at an early, more curative stage. Recently, urine perilipin-2 (PLIN-2) was demonstrated to be a sensitive and specific biomarker for the noninvasive, early detection of RCC and an indispensable indicator to distinguish cancer from a benign renal mass. However, current Western blot or ELISA PLIN-2 assays are complicated, expensive, time-consuming or insensitive, making them unsuitable for routine analysis in clinical settings. Here we developed a plasmonic biosensor based on the high refractive index sensitivity of gold nanorattles for the rapid detection of PLIN-2 in patient urine. The paper-based plasmonic assay is highly sensitive and has a dynamic range of 50 pg/ml to 5 µg/ml PLIN-2. The assay is not compromised by variations in urine pH or high concentrations of interfering proteins such as albumin and hemoglobin, making it an excellent candidate for routine clinical applications. The urine PLIN-2 assay readily distinguished patients with pathologically proven clear cell carcinomas of various size, stage and grade (55.9 [39.5, 75.8] ng/ml, median [1st and 3rd quartile]) from age-matched controls (0.3 [0.3, 0.5] ng/ml), patients with bladder

cancer (0.5 [0.4, 0.6] ng/ml) and patients with diabetic nephropathy (0.6 [0.4, 0.7] ng/ml). Urine PLIN-2 concentrations were roughly proportional to tumor size (Pearson coefficient 0.59). Thus, this cost-effective and label-free method represents a novel approach to conduct a non-invasive population screen or rapid differential diagnosis of imaged renal masses, significantly facilitating the early detection and diagnosis of RCC.

## 3.2 Materials and Methods

**Synthesis of Gold Nanorattles (AuNRTs):** Gold nanospheres were prepared by a seed-mediated approach as described previously.<sup>48, 190</sup> Two ml of gold nanospheres and 48 ml of 20 mM CTAC were mixed under mild stirring at 60 °C for 20 minutes. For the synthesis of Au@Ag nanocubes, 50 ml of 2 mM AgNO<sub>3</sub>, 25 ml of 80 mM CTAC, and 25 ml of 100 mM ascorbic acid were added successively, and the solution was stirred at 60 °C for 4 hours, protected from light by aluminum foil. Subsequently, the particles were centrifuged and re-dispersed into CTAC solution. The silver shell of Au@Ag nanocubes was transformed into a porous gold shell by means of galvanic replacement reaction, by titrating in 0.5 mM HAuCl<sub>4</sub> into the Au@Ag nanocube solution under stirring at 90 °C until the yellow-orange solution turned blue (LSPR wavelength about 660 nm). AuNRTs solution was centrifuged and redispersed into water for further use.

**AuNRTs – anti PLIN-2 conjugates preparation:** A solution of bifunctional SH-PEG-COOH (M<sub>w</sub> = 2000 g/mol, 50 µl, 20 µM, Jenkem Technology), 1-ethyl-3-(3-dimethylaminopropyl) (EDC, Thermo Scientific) and N-hydroxy succinimide (NHS, Thermo Scientific) was prepared with same molar ratio as SH-PEG-COOH followed by shaking for 1 hour. Ten-times concentrated phosphate buffered saline was added to adjust the pH to 7.4. Subsequently, 50 µl of anti-human PLIN-2 IgG<sub>2b</sub> monoclonal antibody (20 µM, R&D Systems) was added followed by gentle shaking for 2 hours. This solution was purified through 30 kDa cut off filters (Amicon-Ultra-0.5) and washed

twice with PBS pH 7.4 twice. To maximize the coverage of PLIN-2 antibody on the AuNRTs surface, 5  $\mu$ l increments of SH-PEG- anti-human PLIN-2 IgG<sub>2B</sub> conjugate solution was added to 1 ml AuNRTs solution until the LSPR wavelength no longer changed.

**Preparation and characterization of bioplasmonic paper substrates:** Whatman #1 filter paper (0.5 $\times$ 0.5 cm<sup>2</sup>) was incubated with AuNRTs - anti PLIN-2 conjugates for 15 hours to adsorb conjugates thus creating plasmonic paper substrates. These papers were then thoroughly rinsed in deionized water to remove weakly bounded nanostructures. The paper substrates were then air dried and protected from the light. Dried paper substrates were then treated with 2 mg/ml of SH-PEG (Mw = 5000, Jenkem Technology) for 1 hour at 4°C to mask nonspecific binding sites, rinsed with deionized water and dried. The extinction spectra were obtained and the LSPR wavelength was recorded, which served as the baseline for determining the LSPR shift and PLIN-2 concentration upon exposure to PLIN-2 standards in synthetic urine or to the urine samples of healthy volunteers or patients with RCC.

**Characterization Techniques:** The AuNRTs morphology was evaluated using transmission electron microscopy (TEM) on a JEM-2100F (JEOL) field emission instrument, operated at an acceleration voltage of 200 kV. The distribution of AuNRTs-anti PLIN-2 conjugates on the paper substrates was characterized using a FEI Nova 2300 Field Emission scanning electron microscope (SEM) at an acceleration voltage of 10 kV. Anti-human PLIN-2 IgG<sub>2B</sub> conjugation to plasmonic nanostructures was confirmed by surface enhanced Raman scattering (SERS) spectra obtained using Renishaw inVia confocal Raman spectrometer mounted on a Leica microscope with a 50X objective. A CRAIC QDI 302 micro-spectrophotometer (CRAIC Technologies, San Dimas, CA) coupled to a Leica DM4000M optical microscope (Leica Microsystems, Wetzlar, Germany) was employed to collect the extinction spectra of paper substrates. A 100 X objective with 10

accumulations and 1 sec exposure time was used to acquire the spectra at a resolution of 0.1 nm over 450 and 800 nm.

**Statistical Analysis:** Sample size calculations were based on the control group of a previous study of urine PLIN-2 concentrations.<sup>58</sup> To detect a 2-fold (conservative estimate) greater PLIN-2 concentration in patients with clear cell carcinoma versus controls, based on a two-sided t-test and 90% power, would require a minimum of 4 patients (0.01 significance). Analysis of 8- 20 patients in each group exceeded this minimum.

Non-normally distributed variables were expressed as median with interquartile range and normally distributed variables were as mean  $\pm$  standard deviation, as appropriate. Comparisons of age and sex were performed between all patient groups. Descriptive statistics compared age and urine PLIN-2 concentrations between groups using 2-tailed t-Test and Mann-Whitney calculations. Comparison of sex and ethnicity between groups was performed using the Pearson Chi-square test. To quantify agreement or lack thereof between different standard curves for PLIN-2, Deming analyses were performed. Statistical analysis was performed using R statistical software (<http://www.r-project.org>), Origin 2016 (OriginLab Corp) and Analyse-it for Excel 2010 (Analyse-it Software, Ltd, Leeds, United Kingdom). All P values were considered statistically significant at the 0.05 level or less.

**Preparation of calibrators and quality control samples and assay limit of detection:** For calibration and quality control standards six working stock concentrations of the recombinant PLIN-2 (Creative Biomart) in synthetic urine (Cerilliant Corporation) covering the anticipated biological range were prepared and aliquoted into 2 ml polypropylene vials followed by immediate storage at -80 °C until analysis. The calibrators and quality control samples (QCs) were tested by thawing six samples (50, 100, 500, 5000, 50,000, and 500,000 pg/ml) as calibration standards and

three separate typical samples representing low, medium and high concentrations (50, 5000, and 500,000 pg/ml, respectively) as the quality control samples. Initial standard curves covered PLIN-2 concentrations of 50 pg/ml to 5 µg/ml to determine the dynamic range of the assay. However, subsequent working curves eliminated the 5 µg/ml concentration as it greatly exceeded the range necessary to measure clinically relevant PLIN-2 concentrations. For a typical assay, calibration standards, QCs, and patient samples were thawed at room temperature, vortexed and transferred to individual wells of a 96-well plate (Nunc, Thermo Fisher, Pittsburgh, PA). To determine the limit of detection and quantification, the standard deviations of each PLIN-2 concentration for the three standard curves with seven PLIN-2 concentrations was subject to linear regression across the entire concentration range of PLIN-2. The resulting Y-intercept was then used to compute the limit of detection and limit of quantification.

**Patient Demographics:** Demographic data and medical history were recorded including age, sex and final diagnoses. Post-operative pathology reports made by an experience renal pathologist as part of the patient's standard of care for the patients with an imaged renal mass and a diagnosis of clear cell carcinoma included tumor size, tumor stage/node metastases/distant metastases (TNM), and the ISUP/WHO grading system. All groups were statistically homogeneous based on age (healthy controls were  $60 \pm 10$  yr, bladder cancer patients  $62 \pm 11$  yr, patients with diabetic nephropathy  $62 \pm 9$  yr, and patients with RCC were  $64 \pm 14$  yr (mean  $\pm$  standard deviation,  $P=0.8030$ , Kruskal-Wallis), sex (11 male/9 female healthy controls, vs 6 male/4 female for diabetic patients vs 6 male/2 female for patients with bladder cancer vs 12 male/8 female patients with RCC, ( $P=0.682$ , Chi-square test for proportions). The tumors ranged in size from 2.0 to 9.7 cm in longest dimension.



### 3.3 Bioplasmonic paper characterization and PLIN-2 dose-response

As mentioned earlier, we employed a seed-mediated synthesis approach in combination with galvanic replacement reaction to synthesize AuNRTs.<sup>48</sup> Transmission electron microscopy (TEM) images showed a narrow size distribution of the AuNRTs with an edge length of  $45.3 \pm 1.7$  nm and a side wall thickness of  $4.1 \pm 0.3$  nm ( $n > 50$  measured for each) (**Figure 3.1A**). These AuNRTs were conjugated with a commercially available human PLIN-2-specific monoclonal antibody as the biorecognition element. The successful conjugation of the PLIN-2 antibody was evidenced by a 6 nm red shift in the LSPR wavelength of the AuNRT (**Figure 3.1B**). Uniform adsorption of bioconjugated plasmonic nanostructures on the paper substrate, which ensures optical homogeneity of the plasmonic paper substrates, is of great importance in determining the limit and accuracy of detection. Scanning electron microscopy (SEM) images revealed that the AuNRTs were uniformly distributed on paper substrates without significant aggregation or patchiness (**Figure 3.1C**). Furthermore, surface enhanced Raman scattering (SERS) spectra confirm successful conjugation of anti-PLIN-2 IgG<sub>2B</sub> to the AuNRTs (**Figure 3.2D**). Characteristic Raman spectral bands at  $905\text{ cm}^{-1}$ ,  $960\text{ cm}^{-1}$ ,  $1233\text{ cm}^{-1}$ , and  $1307\text{ cm}^{-1}$  (correspond to symmetric C-C-N stretching and CH<sub>3</sub> rocking vibration and asymmetric C-C-N stretching of the IgG<sub>2B</sub>) confirm the successful biofunctionalization of the nanostructures with antibodies.

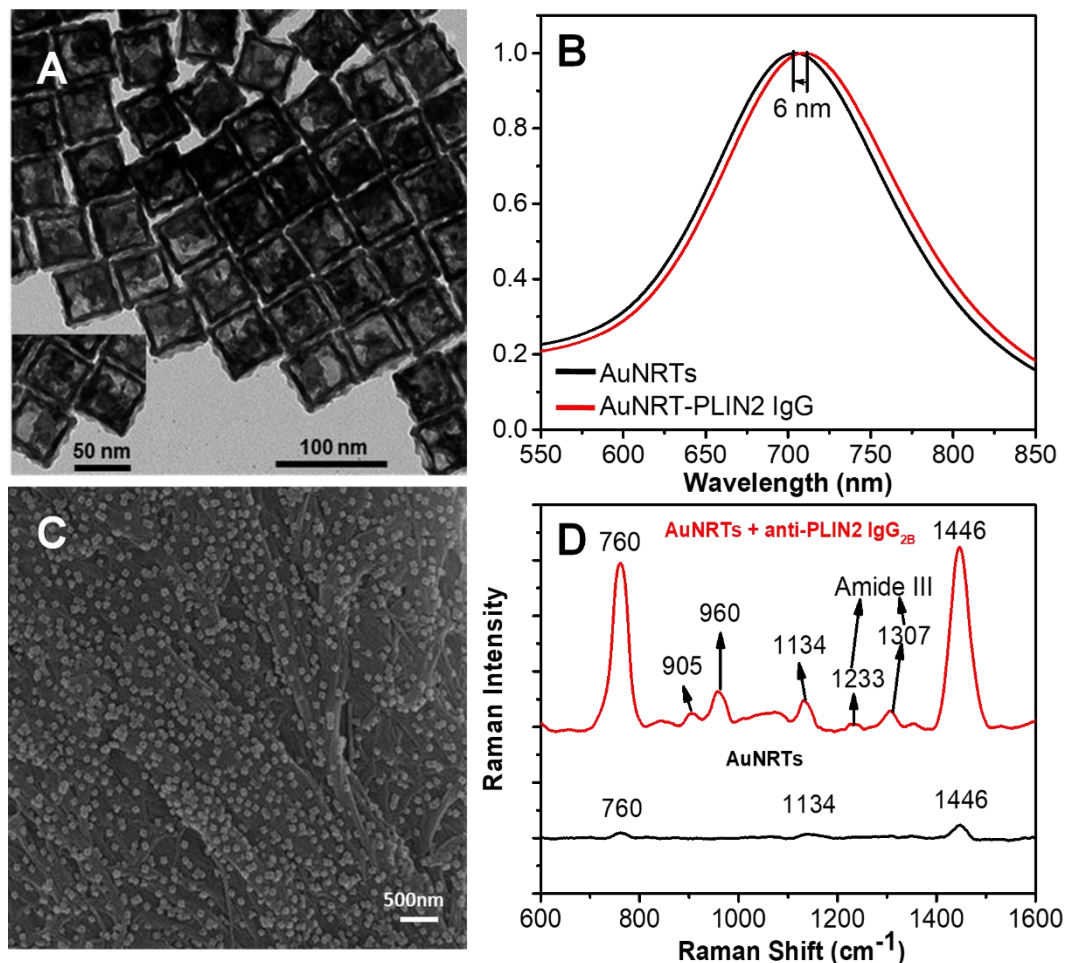


**Figure 3. 1:** (A) TEM image of gold nanorattles (AuNRTs). (B) vis-NIR extinction spectra demonstrating successful conjugation of SH-PEG-anti PLIN2 on AuNRTs. After incubating with SH-PEG-IgG, the  $\lambda_{\max}$  shifts by 6 nm (AuNRTs-anti PLIN2, red). (C) SEM images of paper adsorbed with AuNRTs-anti PLIN2 conjugates. (D) Surface enhanced Raman scattering spectra with on AuNRTs reveals the Raman bands corresponding to anti human PLIN2 IgG<sub>2B</sub>.

### 3.4 PLIN-2 dose-response curve and repeatability

To investigate linearity and dynamic range, plasmonic paper substrates were exposed to different concentrations of human recombinant PLIN-2 spiked in synthetic urine. A monotonic increase in wavelength shift was observed with the increase of PLIN-2 concentration on a semi-log plot of the LSPR shift (**Figure 3.2**) summarizing five separate standard curves. The dynamic range of the plasmonic biosensors spanned four orders of magnitude ranging from 50 pg/ml to 5 x

10<sup>5</sup> pg/ml. Three curves were run extending the concentration ranges five orders of magnitude to 5 x 10<sup>6</sup> pg/ml. Based on linear regression of the standard deviations of the seven PLIN-2 concentrations curves, the limit of detection (LOD) of the assay was computed to be 3.6 ± 0.4 pg/ml and the limit of quantitation (LOQ) computed to be 12.0 ± 1.3 pg/ml. This sensitivity was not possible with our previous Western blot technique, which had a LOQ over 1 ng/ml.<sup>56-60</sup> Additionally, dilution curves of the PLIN-2 standard in pooled urine from normal individuals paralleled the dilution in synthetic urine. The remarkable reproducibility of the bioplasmonic paper assay for PLIN-2 is illustrated in **Figure 3.2A**, which shows that more than 2 years apart the standard curves are indistinguishable. We also measured standard curve of human recombinant PLIN-2 in synthetic urine and pooled human urine of normal individuals, shown in **Figure 3.2B**.

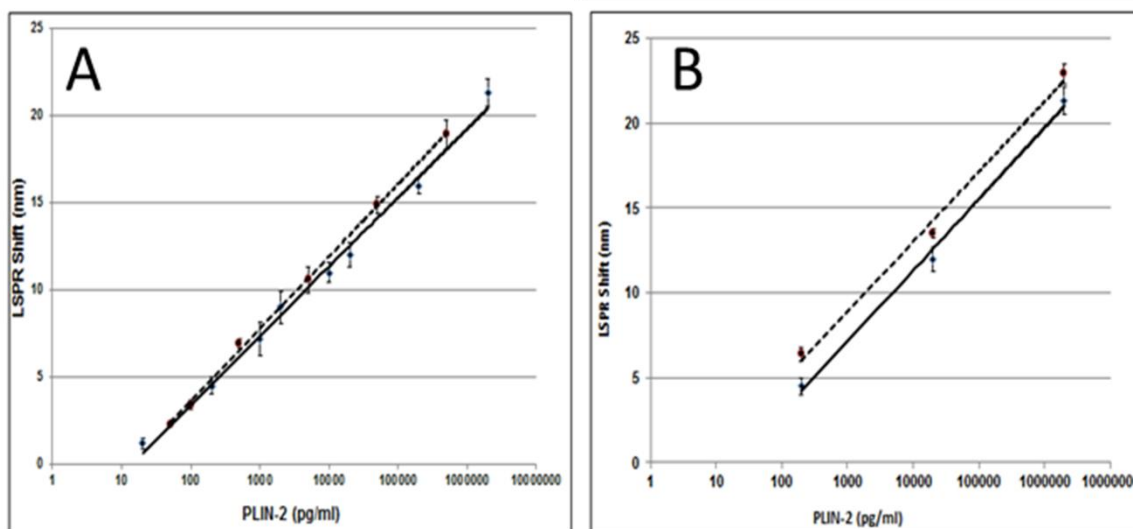


**Figure 3. 2:** (A) Comparison of PLIN-2 standard curves from November 2016 (solid line and diamonds) and March 2019 (dashed line and triangles). The mean and standard deviation of five standard curves from November 2016 and three replicates at each concentration in March 2019 are depicted. (B) Dilution of PLIN-2 standard in synthetic urine (solid line) or pooled human urine of normal individuals (dashed line). Mean and standard deviation of three replicates at each concentration is depicted.

### 3.5 Clinical study

The LSPR wavelength shift of the bio- plasmonic paper on exposure to kidney cancer patient urine samples was found to be significantly higher compared with that of healthy volunteers (Figure 12A). Results were also compared with PLIN-2 concentrations previously determined by Western blot analysis.<sup>191-192</sup> Median urine PLIN-2 concentrations from the 20 patients with RCC were 43 (interquartile range [IQR]: 29, 68) ng/ml and were significantly higher ( $P < 0.001$ , Kruskal-Wallis) than those of 20 controls at 0.3 (IQR: 0.3, 0.5) ng/ml, those of 8 patients with bladder cancer at 0.5 (IQR: 0.4, 0.6) ng/ml, or those of 10 patients with diabetic nephropathy at 0.6 (IQR: 0.4, 0.7) ng/ml (Figure 12B). There was no overlap in PLIN-2 concentration ranges between RCC and all other groups. Equally important, the urine PLIN-2 concentrations were related to tumor size (Figure 12C) with a Spearman correlation coefficient of 0.59 (95% confidence interval: 0.16 to 0.81;  $P < 0.009$ ). A Spearman plot of the urine PLIN-2 concentrations of the patients with RCC measured by the plasmonic papers and previously by Western blotting (Figure 12D) indicates an excellent correlation ( $R^2 = 0.94$ ;  $P < 0.001$ ). However, it should be noted that the Western blot analysis appears to tail off at low PLIN-2 concentrations.

### 3.6 Conclusions and Outlook

Plasmonic paper serves as a simple and versatile platform for implementing plasmonic biosensors. Due to the high sensitivity of the assay, and lack of potential interference by albuminuria or hematuria, urine PLIN-2 concentrations in normal individuals could be accurately measured, and there was a clear difference in urine PLIN-2 concentrations among normal individuals, patients with bladder cancer, patients with diabetic nephropathy, and patients with a pathologically proven clear cell carcinoma. A limitation of the study is the small number of patients

in this proof-of-concept analysis. A larger multicenter blinded study incorporating patients with a wide variety of noncancerous kidney diseases, more patients with cancerous urologic diseases, and many more control individuals would be necessary to validate this assay.

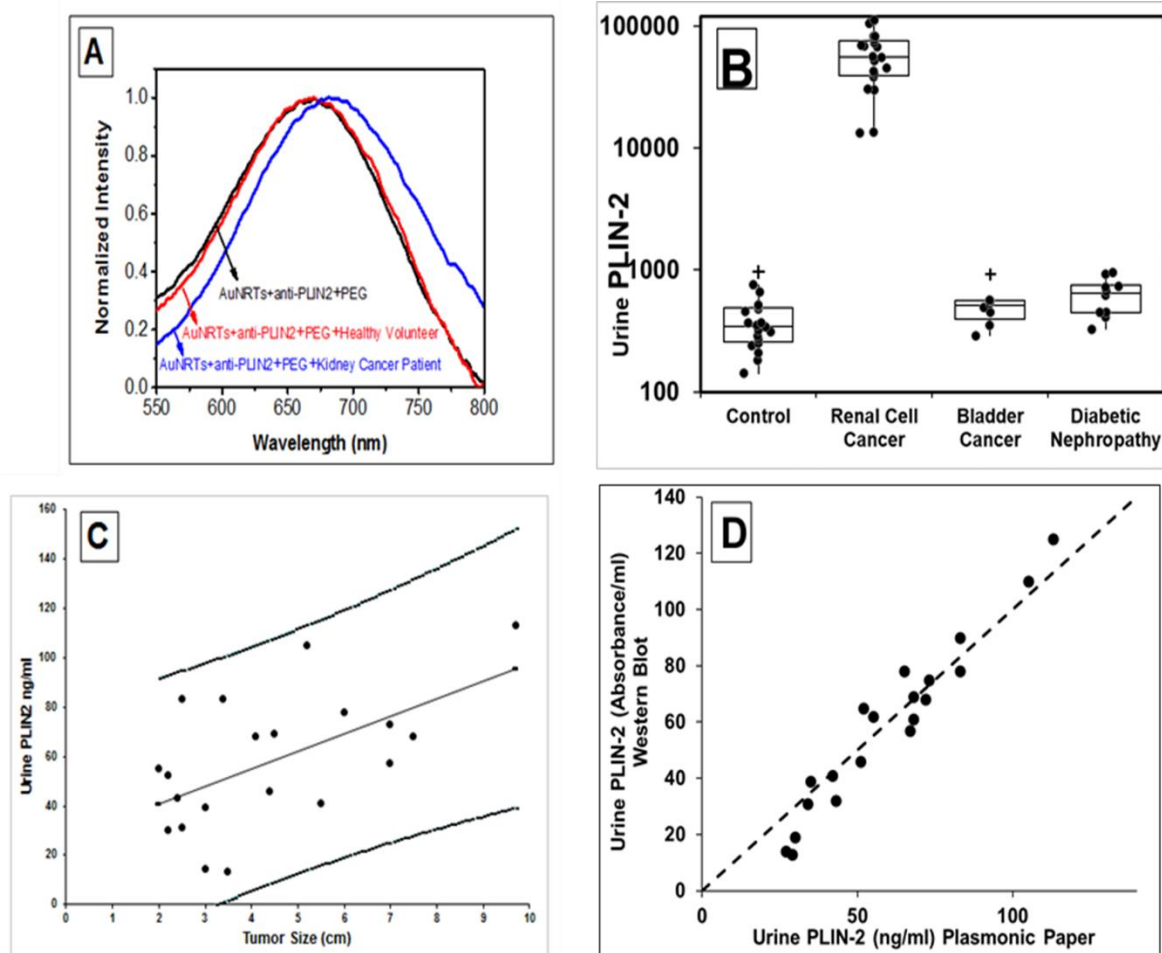


**Figure 3. 3:** (A) Representative localized surface plasmon resonance spectra of anti-perilipin-2 (anti-PLIN-2) functionalized gold nanorattles (AuNRTs) (black), functionalized AuNRTs incubated with urine from a healthy volunteer (red), and functionalized AuNRTs incubated with urine from a patient with renal clear cell carcinoma (blue). (B) Box and whisker plot of the urine PLIN-2 concentrations of 20 control patients, 20 patients with renal cell cancer, 8 patients with bladder cancer, and 10 patients with diabetic nephropathy. The median with whiskers and boxes depicting the interquartile range is shown. The concentration of each patient is depicted as a solid dot or a plus sign. The plus signs are outliers more than 1.5 times but less than 3.0 times the interquartile range. Patients with renal cell cancer have significantly higher urine PLIN-2 concentrations than that of other cohorts ( $P < 0.001$  by Kruskal-Wallis). (C) Urine PLIN-2 concentration of patients with renal cell cancer as a function of tumor size. The Spearman correlation coefficient is 0.59 ( $P = 0.009$ ). Regression line, solid line; 95% prediction

interval, dashed lines. **(D)** Urine PLIN-2 concentration determined by plasmonic paper versus relative absorbance by Western blot. Dashed line of identity. Spearman correlation = 0.94 ( $P < 0.001$ ). PEG, polyethylene glycol.

The assay enables fast, sensitive, cost-effective, and non-invasive diagnosis of kidney cancer, especially in at-risk groups. For example, the Veterans Health Administration now targets kidney cancer as a specific condition based on the exposure of soldiers, their families, and base personnel to contaminated drinking water.<sup>193</sup> There is also a significantly increased incidence of RCC among autoworkers exposed to metal-working fluids.<sup>194</sup> There are no current cost-effective high-throughput means of identifying individuals with RCC. Our assay could be of importance in identifying those with RCC in military bases or autoworker cohorts or other populations. Additionally, this assay would enable the differential diagnosis of imaged renal masses and could be useful in point-of-care settings such as hospital radiology departments and stand-alone imaging clinics. The need for differential diagnosis of imaged renal mass is compelling. Nationally, about 45,000 partial and radical nephrectomies were performed in the United States alone in 2015.<sup>195</sup> It is estimated that 18% of these would have undergone surgery for removal of a benign mass (extrapolation of the Surveillance, Epidemiology, and End Results [SEER] 18 database). A non-invasive biomarker assay to differentiate a benign mass from a renal cell cancer could potentially have prevented unnecessary surgery in these cases. Future prospective studies are needed to validate this bioplasmonic paper-based assay in population screening and to differentially diagnose imaged renal masses on a larger scale.

# Chapter 4: Refreshable Nanobiosensor-based on Organosilica Encapsulation of Biorecognition Elements

*The results reported in this chapter have been published in – Gupta, R., et al, & Singamaneni, S. (2019). “Refreshable Nanobiosensor Based on Organosilica Encapsulation of Biorecognition Elements” ACS Applied Materials and Interface, 2020, 12(5), 5420-5428.*

## 4.1 Abstract

Implantable and wearable biosensors that enable monitoring of biophysical and biochemical parameters over long durations are highly attractive for early and presymptomatic diagnosis of pathological conditions and timely clinical intervention. Poor stability of antibodies used as biorecognition elements and the lack of effective methods to refresh the biosensors upon demand without severely compromising the functionality of the biosensor remain significant challenges in realizing protein biosensors for long-term monitoring. Here, we introduce a novel method involving organosilica encapsulation of antibodies for preserving their biorecognition capability under harsh conditions, typically encountered during the sensor refreshing process, and elevated temperature. Specifically, a simple aqueous rinsing step using sodium dodecyl sulfate (SDS) solution refreshes the biosensor by dissociating the antibody–antigen interactions. Encapsulation of the antibodies with an organosilica layer is shown to preserve the biorecognition capability of otherwise unstable antibodies during the SDS treatment, thus ultimately facilitating the

refreshability of the biosensor over multiple cycles. Harnessing this method, we demonstrate the refreshability of plasmonic biosensors for anti-IgG (model bioanalyte) and neutrophil gelatinase-associated lipocalin (NGAL) (a biomarker for acute and chronic kidney injury). The novel encapsulation approach demonstrated can be easily extended to other transduction platforms to realize refreshable biosensors for monitoring of protein biomarkers over long durations.

## 4.2 Materials and Methods

**Materials:** Gold(III) chloride trihydrate ( $\text{HAuCl}_4 \cdot 3\text{H}_2\text{O}$ ,  $\geq 99.9\%$ ), ascorbic acid (AA,  $\geq 99.0\%$ ), silver nitrate ( $>99\%$ ), sodium borohydride ( $\text{NaBH}_4$ , 98%), cetyltrimethylammonium bromide (CTAB,  $\geq 99\%$ ), 3-(mercaptopropyl)trimethoxysilane (MPTES), (3-aminopropyl)trimethoxysilane (APTMS) and trimethoxy(propyl)silane (TMPS), sodium dodecyl sulfate ( $>99\%$ ) (SDS), albumin from human serum ( $M_w = 65 \text{ kDa}$ ) were obtained from Sigma-Aldrich. 1-Ethyl-3-(3-dimethylaminopropyl) carbodiimide (EDC) and N-hydroxysuccinimide (NHS), Rabbit IgG, and Goat anti-Rabbit IgG ( $M_w = 150 \text{ kDa}$ ) were purchased from Thermo scientific. SH-PEG-COOH ( $M_w = 5000 \text{ g/mol}$ ) and methoxy PEG silane was purchased from Jenkem Technology. The phosphate buffer saline (PBS) (10X) buffer was obtained from ThermoFisher. Neutrophil gelatinase-associated lipocalin (NGAL) and anti-NGAL were purchased from R&D Systems. All chemicals were used as received without further modifications.

**Synthesis of Gold nanorods (AuNR):** Gold nanorods were synthesized using a seed mediated approach. The seed solution was prepared by mixing 7.5 mL aqueous CTAB solution (0.1 M) and 2.5 mL of  $\text{HAuCl}_4$  (1 mM) in a 20 mL scintillation vial, followed by the rapid addition of 0.6 mL of ice-cold  $\text{NaBH}_4$  (10 mM) under vigorous stirring to yield a brown colored seed solution. Growth solution was prepared by mixing 95 mL of CTAB (0.1 M), 0.5 mL of silver nitrate (10 mM), 5 mL of  $\text{HAuCl}_4$  (10 mM), and 0.55 mL of ascorbic acid (0.1 M) in the same order. The solution was



homogenized by gentle stirring. To the resulting colorless solution, 0.12 mL of freshly prepared seed solution was added and set aside in dark for 14 h. Prior to use, the AuNR solution was centrifuged at 10000 rpm for 30 mins to remove excess CTAB and redispersed in nanopure water (18.2 M $\Omega$ .cm).

**Synthesis of Gold Nanorattles (AuNRT):** Same as mentioned in materials and methods section of previous chapter.

**AuNR-IgG and AuNRT-NGAL antibody bioconjugates preparation:** To a solution of SH-PEG-COOH in water (37.5  $\mu$ l, 20  $\mu$ M), EDC and NHS, with the same molar ratio as SH-PEG-COOH, were added followed by shaking for 1 h. The pH of the above reaction mixture was adjusted to 7.4 by adding concentrated phosphate buffered saline (10X PBS). Subsequently, rabbit IgG (10  $\mu$ l, 75  $\mu$ M) was added to the reaction mixture and was incubated for 2 h. Then the mixture was filtered to remove any byproduct during the reaction using centrifuge tube with 50 kDa filter. The final SH-PEG-IgG conjugates solution (0.75  $\mu$ M) was obtained after washing with PBS buffer (pH 7.4) twice. AuNR-IgG bioconjugates were prepared by adding 8  $\mu$ l of the SH-PEG-IgG (concentration  $\sim$ 1.3 mM in water), 2  $\mu$ l at a time to a 1 ml solution of twice centrifuged nanorods. The amount of SH-PEG-IgG was optimized to obtain maximum coverage of IgG on AuNR surface. The solution was left for 1 hour on a shaker to homogenize the conjugation. Similar procedure was employed to prepare AuNRT-NGAL antibody bioconjugates where SH-PEG-anti-NGAL antibody bioconjugates were prepared using anti-NGAL instead of IgG.

**Adsorption of AuNR-IgG and AuNRT-NGAL antibody on glass surface:** First, 1 $\times$ 2 cm rectangular slides of glass were cleaned with piranha solution (3:1 (v/v) mixture of H<sub>2</sub>SO<sub>4</sub> and 30% H<sub>2</sub>O<sub>2</sub>) followed by extensive rinsing with nanopure water (Caution: Piranha solution is

extremely dangerous and proper care needs to be executed in handling and disposal). Then the cleaned glass slides were modified with MPTES to render thiol functionality by immersing the glass substrate into 1% (w/v) MPTES solution in ethanol for 1 h followed by immersion in ethanol for 20 min and thoroughly rinsing with nanopure water. AuNR-IgG conjugates were immobilized onto MPTES-functionalized glass substrates by exposing them to AuNR-IgG conjugates solution for 3 h, and then rinsing with water to remove the loosely bound AuNRs. To make sure that the amount of IgG conjugated on the AuNR is consistent for each batch, we used the same amount and concentration of IgG solution (8  $\mu$ L, 1.3 mM) and AuNR solution (1 mL, optical density of 2.0). Also, we used LSPR shift to monitor bioconjugation of each batch to ensure similar LSPR red shift (8 nm). Moreover, by controlling the absorption time (3 hours) and optical density of the substrates after incubation (0.8), we make sure that the same amount of AuNRs deposited on the substrates. Similar procedure was employed to immobilize AuNRT-NGAL antibody bioconjugates on glass substrates.

**Polymer encapsulation and PEGylation:** Glass substrates with AuNR-IgG bioconjugates were immersed in 4 mL of 1x PBS (pH 7.4) containing similar concentration of TMPS and APTMS for 10 minutes, followed by rinsing with water and drying under a stream of nitrogen. Subsequently, to PEGylate the polymer surface to avoid nonspecific binding the substrates were exposed to 2 mg/ml mPEG-silane solution for 2 hours and then rinsed with water and dried with nitrogen.

**SDS treatment:** After polymerization and PEGylation the substrates were exposed to different concentration of Anti-IgG or NGAL in 1x PBS. To release analyte (anti-IgG or NGAL) the substrates were washed by immersion in 3 mL of 0.4% aqueous SDS solution in 1x PBS for 5

minutes. Prior to recapture of analyte on bioconjugates by exposure to different concentration of Anti-IgG, the substrates were rinsed with water and dried in nitrogen.

**Characterization:** Transmission electron microscopy (TEM) micrographs were recorded on a JEM-2100F (JEOL) field emission instrument operating at an accelerating voltage of 200 kV. Samples were prepared by drying a drop of the solution on a carbon-coated grid, which had been previously made hydrophilic by glow discharge. Atomic force microscopy (AFM) images were obtained using Dimension 3000 (Digital instruments) AFM in light tapping mode.

**Extinction Spectra and Raman Spectra Measurements:** Shimadzu UV-1800 spectrophotometer was employed for collecting UV–vis extinction spectra from solution and glass substrates. Raman spectra were obtained using a Renishaw inVia confocal Raman spectrometer mounted on a Leica microscope with 20x objective (NA = 0.4) and 785 nm wavelength diode laser (0.5 mW). The spectra were obtained in the range of 600–1800  $\text{cm}^{-1}$  with three accumulations and 10 s exposure time.

### 4.3 LSPR-based biosensor for detection of IgG

We employed rabbit IgG and goat anti-rabbit IgG as model antibody-antigen pair and gold nanorods (AuNRs) as plasmonic nanotransducers. We synthesized AuNRs using the seed-mediated method.<sup>196</sup> Transmission electron micrograph (TEM) images revealed the length and diameter of the AuNRs as  $57.5 \pm 2.1$  nm and  $19.7 \pm 2.6$  nm respectively (**Figure 4.1A**). The antibodies were conjugated to a bifunctional polyethylene glycol (COOH-PEG-SH) chain to obtain IgG-PEG-SH.<sup>77, 197-198</sup> Subsequently, IgG-PEG-SH was anchored to the AuNR surface via an Au-S linkage. Polyethylene glycol (PEG) chains offer two important advantages: (i) increased accessibility of IgG to target biomolecules by acting as a flexible linker<sup>198</sup>; and (ii) minimization of nonspecific binding owing to their high hydrophilicity.<sup>77</sup> The immobilization of IgG-PEG-SH

on AuNRs in solution resulted in ~8 nm red shift in the longitudinal LSPR wavelength of AuNRs, corresponding to an increase in the refractive index of the medium surrounding AuNRs (**Figure 4.1B**). To realize plasmonic biosensors, the AuNR-IgG bioconjugates were uniformly adsorbed onto the 3-mercaptopropyl-trimethoxysilane (MPTMS) functionalized glass substrates. Atomic force microscopy (AMF) images of the modified glass substrates revealed uniform distribution of AuNR-IgG bioconjugates with no signs of aggregation or patchiness. Atomic force microscopy (AFM) image of the substrate uniform distribution of AuNR-IgG bioconjugates on glass substrate (**Figure 4.1C**). To minimize nonspecific binding, glass substrates with AuNR-IgG bioconjugates were exposed to thiol-terminated polyethylene glycol (SH-PEG), which is expected to graft to the exposed regions of AuNRs and serve as a blocking layer. To investigate their biosensing performance, we exposed these plasmonic biochips to different concentrations of anti-IgG, which binds specifically to the IgG immobilized on the AuNRs. Consistent with our previous studies, the LSPR wavelength of AuNR exhibited a monotonic red shift with an increase in the concentration of anti-IgG.<sup>77, 198</sup> The limit of detection (LOD defined as: mean+3 $\sigma$  of the blank) of these biochips was found to be 240pg/ml.

## 4.4 Refreshability of AuNR-IgG biosensor

As mentioned above, antigens (anti-IgG in this case) are recognized and captured by antibodies (IgG conjugated to AuNRs in the present case) through non-covalent interactions, which can be disrupted by subjecting them to extreme pH or high concentrations of salt or surfactants.<sup>83, 199</sup> We used sodium dodecyl sulfate (SDS), an anionic surfactant frequently used in cleaning and hygiene products (*e.g.*, toothpaste, mouthwash), as a chemical agent to disrupt the antigen-antibody interactions. SDS, known to disrupt protein conformation, binds relatively uniformly along the protein chain with its hydrophobic tail conferring net charge on proteins and thus exposing

(unfolding) the otherwise buried regions of protein.<sup>83, 200-202</sup> We posited that exposure of the bound antibody-antigen pair to SDS results in electrostatic repulsion between antibody and antigen, thus overcoming the noncovalent interactions between them. Dissociation of the antibody-antigen pair essentially refreshes the binding sites and enables the reuse of the biosensor. We have harnessed the refractive index sensitivity of the AuNRs to monitor each step along this process (**Figure 4.1D**). Extinction spectra (**Figure 4.1E**) and LSPR wavelength of AuNR (**Figure 4.1F**) were obtained following each step in the procedure: immobilization of AuNR-IgG bioconjugates on glass substrates (step 1); PEGylation of AuNR-IgG bioconjugates to minimize non-specific binding (step 2); binding of anti-IgG to IgG (step 3); exposure to SDS solution (step 5); rebinding of anti-IgG to IgG (step 5).

The LSPR wavelength of AuNR exhibited ~20 nm redshift after exposure to 24  $\mu\text{g/ml}$  of anti-IgG (**Figure 4.1E and F**). After exposure to SDS, we observed ~21 nm blue shift suggesting complete removal of anti-IgG and thus leaving behind AuNR-IgG bioconjugates on the plasmonic biochip, ready for another cycle of antigen detection (**Figure 4.1E and F**). However, when SDS-treated plasmonic biochips were exposed to the same concentration of anti-IgG, we observed that the biochip lost ~50% sensitivity as evident from only ~10 nm red shift as opposed to ~20 nm observed in the pristine biochip (**Figure 4.1E and F**). The nearly 50% loss in biorecognition capability after SDS treatment was consistent over a broad range of anti-IgG concentration (**Figure 4.1G**). This is not surprising because in the process of dissociating anti-IgG:IgG complex, SDS partially denatures the immobilized IgG and thus results in the loss of its biorecognition capability. Consequently, with every cycle of SDS washing, we noted a progressive degradation in the biorecognition capability and by fourth cycle the plasmonic biochips exhibited only ~10% sensitivity compared to that in the pristine condition.

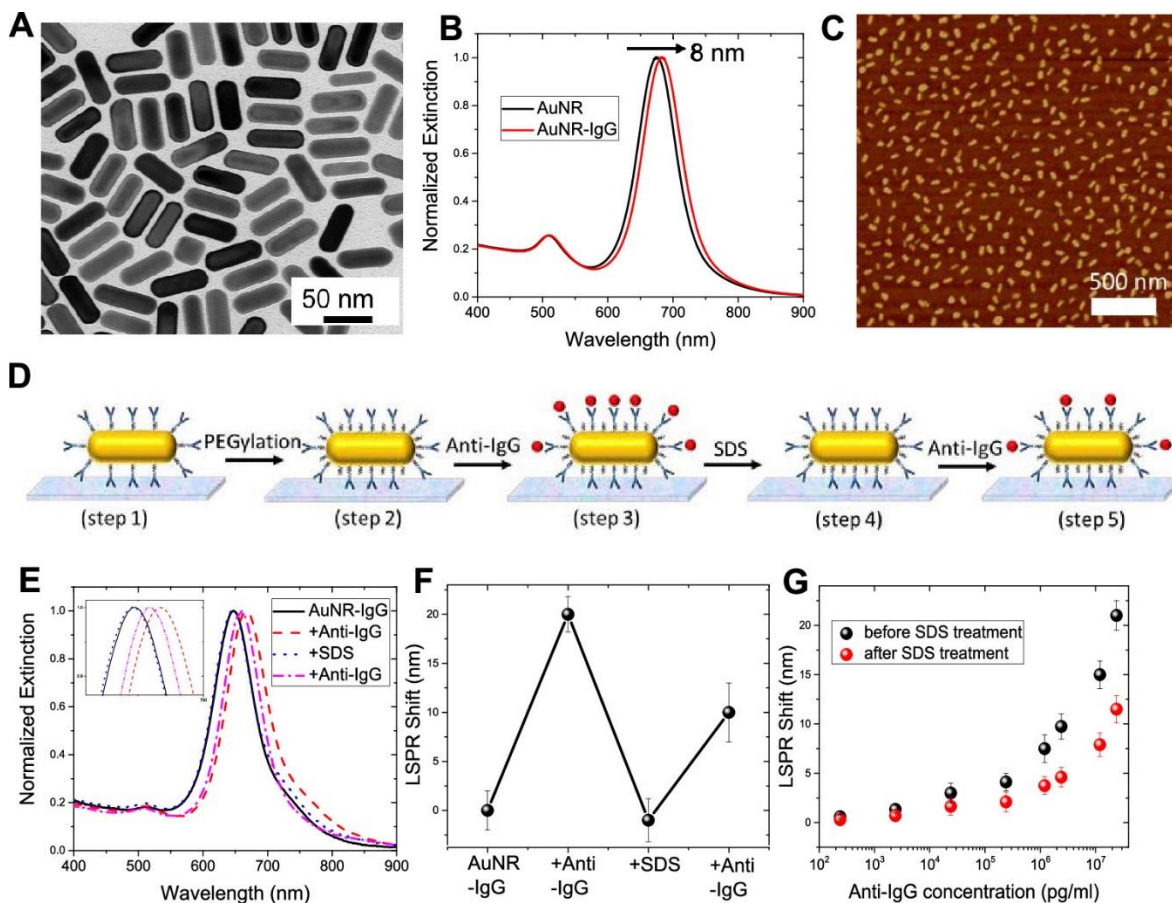


**Figure 4. 1:** (A) Representative TEM image of AuNRs used as plasmonic nanotransducers. (B) Normalized vis-NIR extinction spectra of AuNR and AuNR conjugated with IgG, depicting ~8 nm redshift in LSPR wavelength. (C) Representative AFM image showing uniform distribution of AuNR-IgG bioconjugates on glass substrate. (D) Schematic illustration of steps involved in the fabrication of refreshable sensor. (E) Extinction spectra of AuNR-IgG bioconjugates obtained after each fabrication step shown in (D). Inset shows zoomed in spectra highlighting the shifts in the LSPR wavelength. (F) LSPR shifts corresponding to biodetection and sensor refreshing. (G) LSPR shift upon exposure of plasmonic biochips to different concentrations of anti-IgG before (black) and after SDS (red) treatment. Error bars represent standard deviations from three different samples.

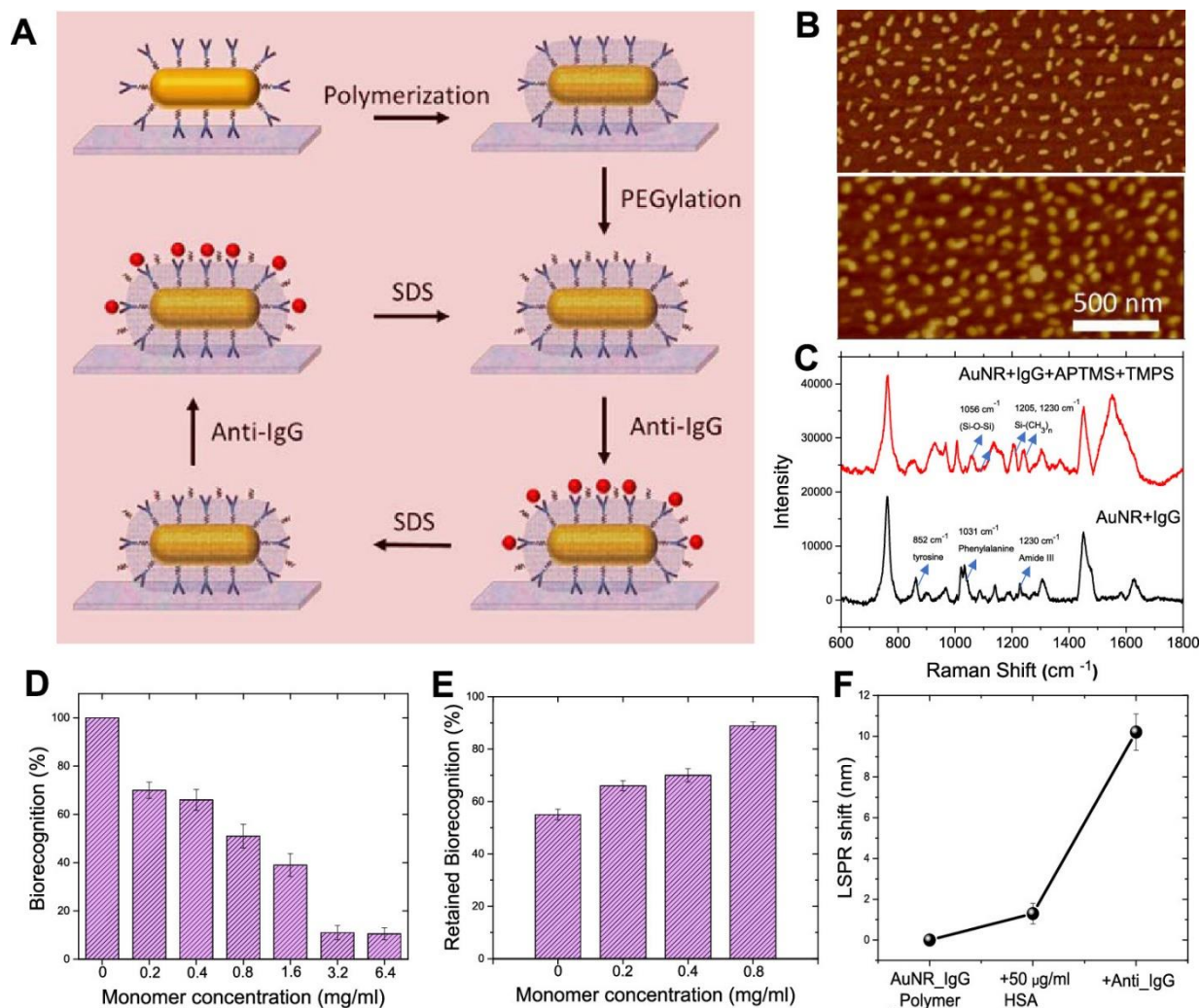


**Figure 4. 2:** (A) Schematic illustration of the steps involved in the organosilica-based biopreservation of bioconjugates to realize refreshable biosensors. (B) Representative AFM image of AuNR-IgG bioconjugates on glass substrate before (top) and after (bottom) polymer encapsulation with optimum monomer concentration (0.8 mg/ml). (C) Surface enhanced Raman scattering spectra of AuNR-IgG bioconjugates before and after polymerization. (D) Biorecognition capability corresponding to different monomer concentrations, which determines the polymer thickness. (E) Retained biorecognition capability of AuNR-IgG bioconjugates corresponding to different monomer concentrations, after SDS treatment. (F) LSPR shift of the polymer encapsulated biosensor after treatment with HSA and anti-IgG. Error bars represent standard deviations from three different samples.

Thus, this challenge of antibody denaturation and subsequent loss in biorecognition capability needs to be overcome to realize refreshable sensor. Towards this goal, we explored antibody encapsulation as a strategy hypothesized to render protection against harsh and potentially denaturing conditions and ultimately leads to refreshable biosensors.

## 4.5 Polymer encapsulation strategy to achieve refreshability

In a previous report, we have demonstrated an *in situ* polymerization technique for preserving the activity of enzyme, immobilized on plasmonic nanostructures, subjected to harsh conditions such as proteases and high temperature.<sup>203</sup> Inspired by this biopreservation method, we posited that encapsulation of immobilized antibodies with an *in situ* formed polymer layer can preserve its biorecognition capability against SDS washing (**Figure 4.2A**). Following the immobilization of AuNR-IgG bioconjugates on glass substrates, a polymer encapsulation layer is formed through copolymerization of (3-aminopropyl) trimethoxysilane (APTMS) and trimethoxy(propyl)silane (TMPS) on AuNR and around immobilized IgG. The methoxy group of TMPS and APTMS undergoes rapid hydrolysis to form methanol and trisilanols.<sup>204-205</sup> Hydrolysis is followed by condensation of the silanols, which results in the formation of amorphous aminopropyl functional polymer layer consisting of Si-O-Si bonds and functional end groups such as hydroxyl (-OH), amine (-NH<sub>3</sub><sup>+</sup>) and methyl (-CH<sub>3</sub>).<sup>206-207</sup> These end groups interact noncovalently via hydrogen bonding, hydrophobic and electrostatic interactions with AuNR-IgG bioconjugates resulting in the formation of a stable organosilica layer around them. Next, bifunctional PEG (methoxy-PEG-silane) was covalently grafted on to the free regions of the organosilica layer. The methoxysilane group of PEG undergoes hydrolysis followed by condensation with the reactive silanol group present on the polymer surface, resulting in the formation of a stable covalent siloxane bond (Si-O-Si). PEG chains shield the functional groups present on the polymer layer, thus minimizing nonspecific binding.<sup>203, 205, 207</sup> Biosensors with the organosilica protective layer were then exposed to a range of concentration of anti-IgG (240 pg to 24 μg) to allow antigen-antibody binding. The plasmonic biochips were subsequently exposed to an aqueous solution of SDS to overcome the noncovalent interactions, dissociate the antibody-



antigen pair and refresh the biochip. The restored biosensor was repeatedly exposed to anti-IgG to assess the refreshability of the biosensor.

## 4.6 Characterization and optimization of organosilica silica layer thickness

Formation of the polymer encapsulation layer on AuNR-IgG bioconjugates was confirmed by redshift in LSPR wavelength and AFM imaging **Figure 4.2B**. The AFM image of the polymer encapsulated bioconjugates revealed a change in the morphology corresponding to the formation of the organosilica polymer layer. The presence of an organosilica polymer layer on the AuNR-IgG bioconjugates was further confirmed by surface-enhanced Raman scattering (SERS) spectroscopy (**Figure 4.2C**). Pristine AuNR-IgG bioconjugates exhibited Raman bands at  $852\text{ cm}^{-1}$ ,  $1031\text{ cm}^{-1}$ ,  $1230\text{ cm}^{-1}$ , and  $1620\text{-}40\text{ cm}^{-1}$  corresponding to tyrosine, phenylalanine, amide III, and amide I, respectively, of IgG.<sup>198</sup> After the formation of an organosilica layer, we observed Raman bands at  $1024\text{ cm}^{-1}$ ,  $1056\text{ cm}^{-1}$ ,  $1205\text{ cm}^{-1}$  and  $1230\text{ cm}^{-1}$  corresponding to Si–O–R stretching, Si–O–Si stretching, and  $-\text{CH}_2$  bending.<sup>203, 207-208</sup>

It is important to note that if the entire antibody, including its antigen binding sites, is encapsulated within the polymer layer, it will severely compromise the biorecognition capability of IgG. On the other hand, if the encapsulation is insufficient then the protection against SDS and long-term stability of antibody will be limited. Therefore, the thickness of the encapsulating polymer layer is critical to provide both access for analyte binding and protection against harsh conditions.

The thickness of the organosilica layer can be controlled either by varying the polymerization time or by changing the concentration of the APTMS and TMPS monomers. We

varied the concentration of monomers while keeping the polymerization time constant (10 mins), as it offers better control and repeatability over multiple batches. The red shift in LSPR wavelength of the AuNR corresponding to the formation of organosilica layer increased with an increase in the concentration of monomers, indicating a gradual increase in the thickness of the polymer layer. Pristine plasmonic biochips with no polymer encapsulation, which corresponds to maximum availability of antibody binding sites, displayed ~20 nm redshift (treated as 100% biorecognition capability). As the thickness of the polymer layer was gradually increased, the plasmonic biochips exhibited a progressive decrease in biorecognition capability (**Figure 4.2D**). Here, biorecognition capability is defined as the percentage of the redshift upon specific binding of anti-IgG to IgG after encapsulation with a polymer layer compared with the redshift obtained from the same batch of biochips before encapsulation. An increase in thickness of the polymer layer rendered biosensors increasingly stable against SDS washing, thus enabling their reusability.

We used the percentage of retained biorecognition capability to quantitatively evaluate the preservation efficacy of the polymer encapsulation strategy. It was calculated as the percentage of the redshift upon specific binding of goat anti-rabbit IgG to the rabbit IgG on a restored biochip after one or more cycles of SDS treatment compared with the redshift obtained from the same batch of biosensor before SDS treatment. For example, samples with no polymer encapsulation and before SDS treatment exhibited ~20 nm redshift, showing 100% biorecognition capability (**Figure 4.2D**), and after SDS treatment displayed ~10 nm redshift corresponding to only 50% retained biorecognition capability (**Figure 4.2E**). On the other hand, plasmonic biochips with polymer encapsulation corresponding to monomer concentration of 0.8 mg/ml exhibited a red shift of 11.5 nm before SDS treatment and red shift of 10.5 nm following SDS treatment, corresponding to ~90% retained biorecognition capability (**Figure 4.2E**). This significant improvement in the

biorecognition capability against SDS underscores the importance of polymer encapsulation of antibody for successful refreshability of the biosensors. By gradually changing the monomer concentration/thickness of the polymer layer, we found a balance between the loss of biorecognition capability and increase in preservation efficacy of polymer encapsulation of AuNR-IgG conjugates to achieve refreshability. Considering the retained biorecognition capability of ~90% for monomer concentration of 0.8 mg/ml, we have employed this condition in subsequent experiments.

## **4.7 Specificity of polymer encapsulated AuNR-IgG biosensor**

To determine the specificity of bioconjugates after polymer encapsulation, we measured the shifts in LSPR wavelength of AuNR after the exposure of plasmonic biochips to high concentration (50  $\mu\text{g/ml}$ ) of interfering protein such as human serum albumin (HSA) (**Figure 4.2F**). We found that the LSPR shift corresponding to the exposure of polymerized biosensor to 50  $\mu\text{g/ml}$  of HSA was only ~1 nm, which is significantly lower than the ~10.5 nm redshift obtained upon exposure to 24  $\mu\text{g/ml}$  anti-IgG. We attribute this low nonspecific binding to the covalently grafted PEG chains on the free surface of the organosilica polymer layer, which are known to resist non-specific protein adsorption. Further, we probed the sensing capability of the polymer encapsulated plasmonic biosensors by exposing them to different concentrations of anti-IgG and monitoring the LSPR shift of the AuNR. As expected, we observed a monotonic increase in the LSPR wavelength with an increase in the anti-IgG concentration. Limit of detection (defined as:  $\text{mean}+3\sigma$  of the blank) of these biochips was found to be 3.7 ng/ml.

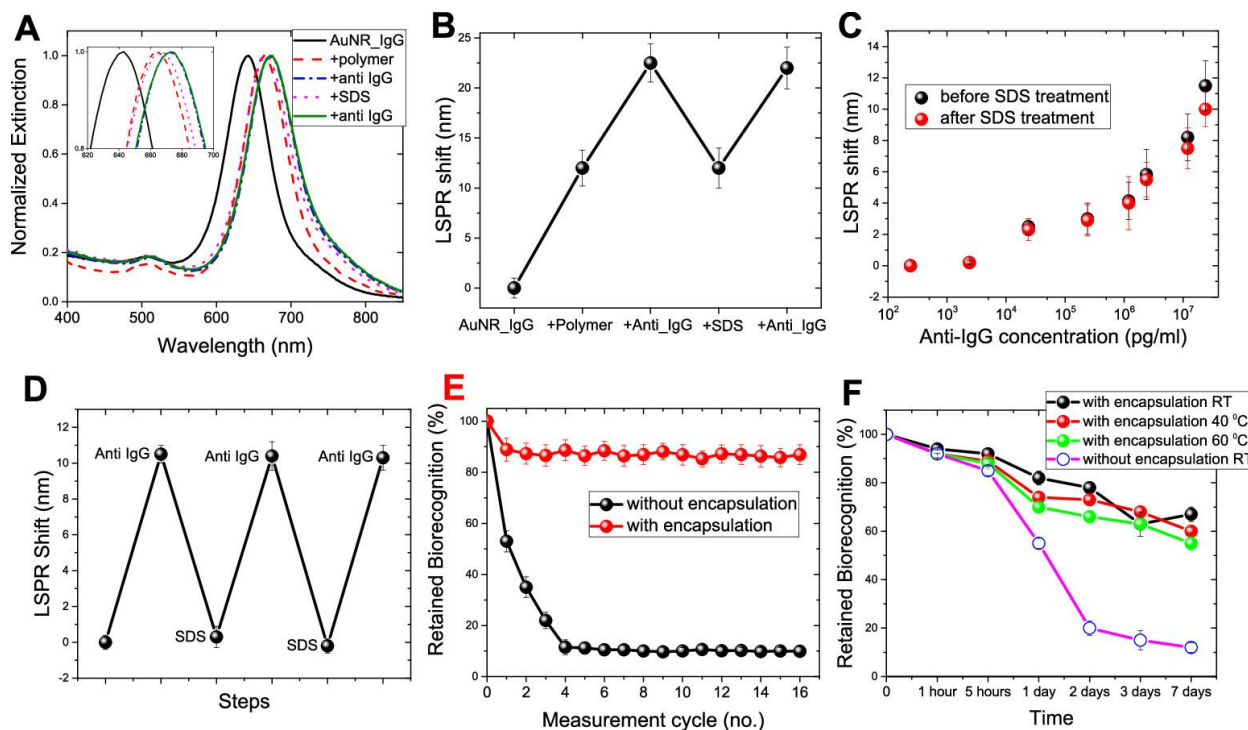


**Figure 4. 3:** (A) AuNR extinction spectra corresponding to each step involved in the polymer encapsulation strategy. Inset shows zoomed in spectra highlighting the shifts in the LSPR wavelength. (B) LSPR shift corresponding to each step involved in the polymer encapsulation strategy. (C) LSPR shift upon exposure of polymer-encapsulated biosensors to different concentrations of anti-IgG before (black) and after SDS (red) treatment. (D) LSPR wavelength shift after alternate exposure to anti-IgG and SDS. (E) Retained biorecognition capability of biosensors with and without polymer encapsulation over multiple capture/release cycles of the analyte. (F) Retained biorecognition capability of AuNR-IgG bioconjugates with and without polymer encapsulation stored at room temperature, 40 and 60°C for different durations. Error bars represent standard deviations from three different samples.

## 4.8 Refreshability of polymer encapsulated AuNR-IgG biosensor

Next, we set out to investigate the refreshability of the polymer-encapsulated biosensors. Figure 15A shows the extinction spectra obtained after: immobilization of AuNR-IgG; formation of organosilica layer; specific binding of anti-IgG (24  $\mu\text{g/ml}$ ) to IgG, which resulted in  $\sim 10.5$  nm red shift; refreshing the plasmonic biochip by SDS washing, which resulted in  $\sim 10.5$  nm blue shift

suggesting the dissociation of anti-IgG:IgG pair; reuse of refreshed biosensor by exposing it again to 24  $\mu\text{g/ml}$  of anti-IgG resulting in  $\sim 10$  nm redshift, thus depicting refreshability of biosensors. All the biosensors after polymerization and prior to exposure to analyte were PEGylated. The PEGylation step after polymer encapsulation resulted in a small ( $\sim 0.5$  nm) redshift, which is not shown in **Figure 4.3A**. **Figure 4.3B** depicts sequential LSPR shifts obtained following each of the aforementioned steps suggesting that the polymer encapsulation strategy provides the ability to reuse the biosensors without significantly compromising the biorecognition capability. Similar results were observed for different concentrations of anti-IgG suggesting stability and refreshability of the biosensors over a large range of concentrations (**Figure 4.3C**).

We investigated the reusability of polymer-encapsulated plasmonic biochips over multiple cycles by subjecting the plasmonic biochips to repeated cycles of capture (exposure to anti-IgG) and release (exposure to SDS). Anti-IgG captured by the polymer encapsulated AuNR-IgG conjugates was completely released with SDS treatment as confirmed by the LSPR blue shift, identical to the red shift observed during capture (**Figure 4.3D**). The refreshed biosensor was exposed to a fresh batch of anti-IgG (24  $\mu\text{g/ml}$ ) each time, resulting in  $\sim 10$  nm redshift suggesting the near complete preservation of biorecognition capability of bioconjugates. The polymer-encapsulated AuNR-IgG preserved  $\sim 80\%$  of biorecognition capability even after 16 cycles of SDS treatment (**Figure 4.3E**). On the other hand, biosensors without polymer encapsulation exhibited  $<40\%$  of biorecognition capability after the second cycle and  $\sim 10\%$  after the fourth cycle (**Figure 4.3E**). These results underscore the importance of a polymer encapsulation strategy to achieve refreshability without significantly compromising the biorecognition capability.

## 4.9 Long-term usability of polymer encapsulated AuNR-IgG biosensor

Another important aspect in deploying a refreshable biosensor over long duration of time is the long-term stability of the biorecognition element under ambient and even harsh conditions. Therefore, we tested the efficacy of polymer encapsulation to preserve the biorecognition capability of AuNR-IgG bioconjugates against harsh conditions that, without polymer encapsulation, would lead to protein denaturation and consequent loss in biorecognition capability.<sup>84-87</sup> The plasmonic biosensors with and without polymer encapsulation were stored at room temperature, 40 and 60 °C for different times (1 and 5 hours and 1, 2, 3 and 7 days) to monitor the changes in the biorecognition capabilities of the antibodies (**Figure 4.3F**). After storage, plasmonic biochips were exposed to anti-IgG (24 µg/ml). Biochips with polymer encapsulation exhibited ~70% retention of biorecognition capability after storage at room temperature (25 °C) for one week compared to almost complete loss in biorecognition capability for biochips without polymer encapsulation. Significantly, the biochips with polymer encapsulation retained ~60% of biorecognition capability even after storage at higher temperatures (40 and 60 °C) for a week. In contrast, pristine biochips lost more than 50% of biorecognition capability within one day and ~90% after one week. The remarkable stability of the polymer-encapsulated AuNR-IgG bioconjugates possibly stems from the restricted mobility of the biomolecules thus impeding protein denaturation even under extreme conditions.<sup>88, 206</sup> In other words, the noncovalent interactions between bioconjugates and organosilica layer imposes steric hindrance on the antibodies thus restricting them from undergoing changes in secondary and tertiary structure (unfold).<sup>203</sup>

## 4.10 Biological stability of AuNR-IgG biosensor

In addition to the remarkable thermal stability, which allows long-term usability, biosensors are required to be stable against biological agents such as proteases in patient serum/urine samples, which can lead to proteolytic degradation of antibodies. Therefore, to probe the biological stability of polymer-encapsulated biosensors, we subjected AuNR-IgG based pristine and organosilica-stabilized biosensors to different concentration of protease dissolved in synthetic urine for different time periods at room temperature. We observed that the biorecognition capability AuNR-IgG bioconjugates decreased to ~8% for all conditions, while the polymer-encapsulated bioconjugates retained ~90%, ~83% and ~70% of the biorecognition capability when subjected to 100 ng/ml, 1  $\mu$ g/ml and 10  $\mu$ g/ml for 24 hours, respectively (**Figure 4.4A**). These results suggest that the organosilica layer significantly lowers the accessibility of the immobilized antibody to the protease, rendering excellent biological stability against proteolytic digestion.

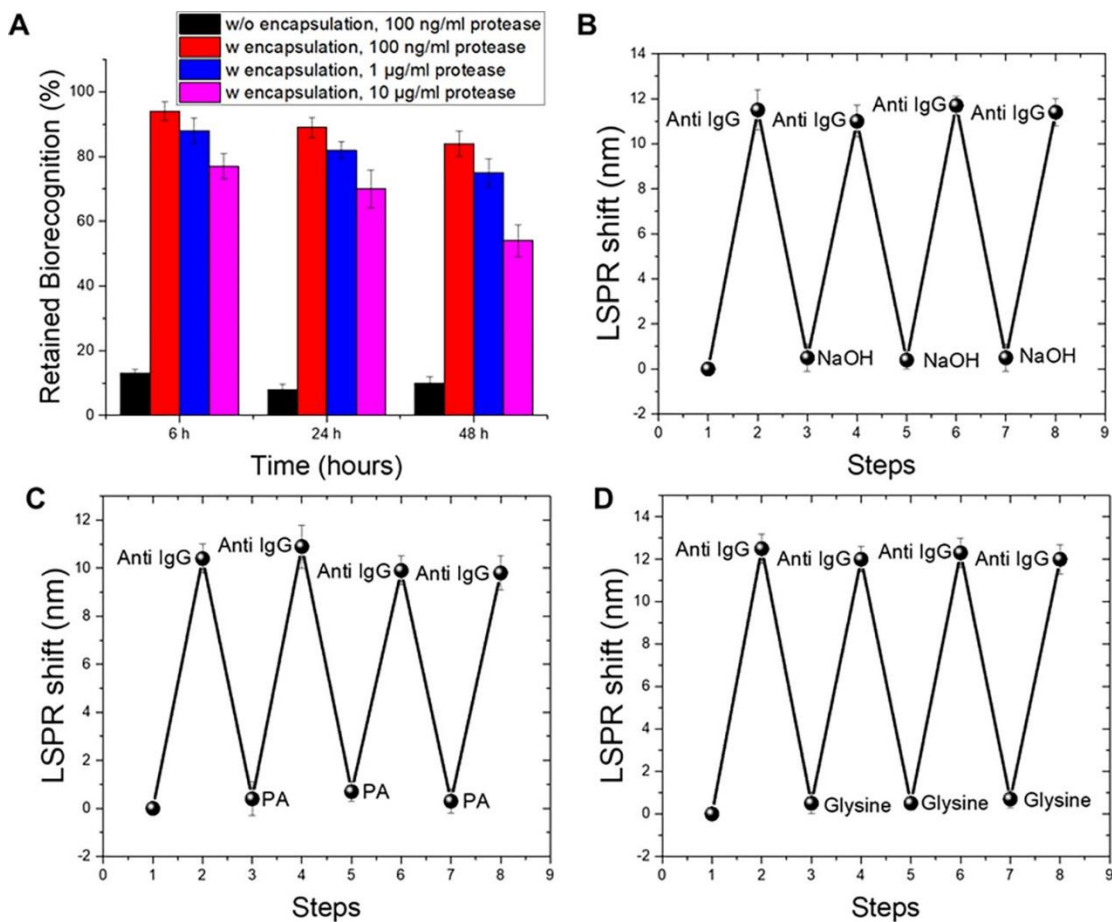


**Figure 4. 4:** (A) (%) Retained biorecognition capability of pristine and polymer encapsulated AuNR-IgG based biosensors after it had been subjected to different conditions of proteolytic degradation at room temperature. LSPR wavelength shift after alternate exposure of polymer encapsulated biosensors to anti-IgG and NaOH (B), PA (C) and glycine buffer (D). Error bar represents standard deviation from three independent samples.

## 4.11 Other chemical regeneration agents to Refresh polymer encapsulated biosensors

To further ascertain the universality of polymer encapsulation strategy, we explored the compatibility of the polymer encapsulation with different regeneration techniques. We performed multiple capture/release cycles using the following chemical regeneration agents: (i) acid-mediated regeneration using 0.1 M phosphoric acid (PA) solution;<sup>209</sup> (ii) base-mediated



regeneration using 50 mM sodium hydroxide (NaOH);<sup>210</sup> and (iii) 10 mM Glycine/HCl buffer (pH 2.8).<sup>211</sup> We investigated these chemical regeneration approaches by subjecting the polymer-encapsulated plasmonic biochips to repeated cycles of capture (exposure to analyte) and release (10 mins exposure to aforementioned regeneration agents). **Figure 4.4B, C and D** depicts the LSPR wavelength shift obtained after alternate exposures of analyte and regeneration agent. The polymer-encapsulated biosensors exhibited ~85% of biorecognition capability after treatment with different regeneration agents, including SDS, even after multiple wash cycles. We also exposed pristine plasmonic biosensors (*i.e.* unencapsulated) to these regeneration agents. As expected, these biosensors exhibited significant loss in biorecognition capability after treatment with aforementioned regeneration agents. These results underscore the universality of polymer encapsulation of the immobilized antibodies rendering stability against various regeneration agents for achieving refreshability.

## 4.12 Universality of polymer encapsulation strategy

Finally, to verify the generality of polymer encapsulation strategy for achieving refreshable biosensor, we employed gold nanorattles (AuNRT) as plasmonic nanotransducers and neutrophil gelatinase-associated lipocalin (NGAL), a urinary biomarker for acute and chronic kidney injury, as target analyte.<sup>77</sup> **Figure 4.5A** shows the TEM image of AuNRTs with an edge length of  $34.2 \pm 1.3$  nm. Similar to IgG, anti-NGAL was conjugated to AuNRT and the conjugation was confirmed by an ~10 nm redshift in the LSPR wavelength of AuNRT. Subsequently, AuNRT-anti-NGAL bioconjugates were immobilized on MPTMS-functionalized glass substrates. After PEGylation, the plasmonic biochips were exposed to NGAL (5  $\mu\text{g/ml}$ ) resulting in ~20 nm red shift in LSPR wavelength of AuNRT (**Figure 4.5B**).

To determine the refreshability, the biochips were treated with SDS to release the captured NGAL from AuNRT-anti-NGAL bioconjugates. The complete removal of NGAL was evidenced by ~20 nm blue shift in the LSPR wavelength. However, SDS treatment resulted in an ~56% loss in biorecognition capability. Following the SDS treatment, AuNRT exhibited LSPR shift of only ~9.5 nm upon exposure to NGAL (5  $\mu\text{g/ml}$ ), as opposed to ~20 nm observed before the SDS treatment. This loss in biorecognition capability was observed over a broad range of NGAL concentrations, which is consistent with that observed in the case of AuNR-IgG bioconjugates (**Figure 4.5B**). To overcome this loss in the biorecognition ability, we employed polymer encapsulation as a strategy to protect immobilized biorecognition elements against SDS treatment.

The monomer concentration was optimized to attain a balance between biopreservation and antibody availability for target antigen capture. The polymer encapsulated AuNRT-NGAL antibody bioconjugates were exposed to different concentrations of NGAL. Although the LSPR shift exhibited by polymer encapsulated biosensors was ~50% compared to those without polymer encapsulation, the polymer encapsulated biosensors exhibited excellent preservation of biorecognition capability after SDS treatment (**Figure 4.5C**). For instance, polymer encapsulated AuNRT-NGAL antibody bioconjugates exhibited nearly similar LSPR redshift (~10 nm) upon exposure to NGAL (5  $\mu\text{g/ml}$ ), both before and after SDS treatment, suggesting excellent stability and refreshability.

Similar results were observed for different concentrations of NGAL suggesting refreshability of the biosensors over a large range of concentrations (**Figure 4.5D**). The polymer encapsulated bioconjugates retained nearly 80% of the biorecognition ability after eight capture/release cycles, which is in stark contrast with less than 20% retained recognition capability of unencapsulated bioconjugates after just three capture/release cycles (**Figure 4.5E**). Finally, as

for IgG, we probed the thermal stability of these biosensors by storing the biosensors at different temperatures (room temperature, 40 and 60 °C) for different durations (1, 2, 3 and 7 days). As expected, polymer-encapsulated biosensors retained >60% of biorecognition capability even after storage for 7 days at 60 °C, whereas, pristine biochips lost more than 80% of biorecognition capability within one day (**Figure 4.5F**). These results attest to the generality of polymer encapsulation method in preserving and refreshing the biorecognition capabilities of immobilized antibodies.

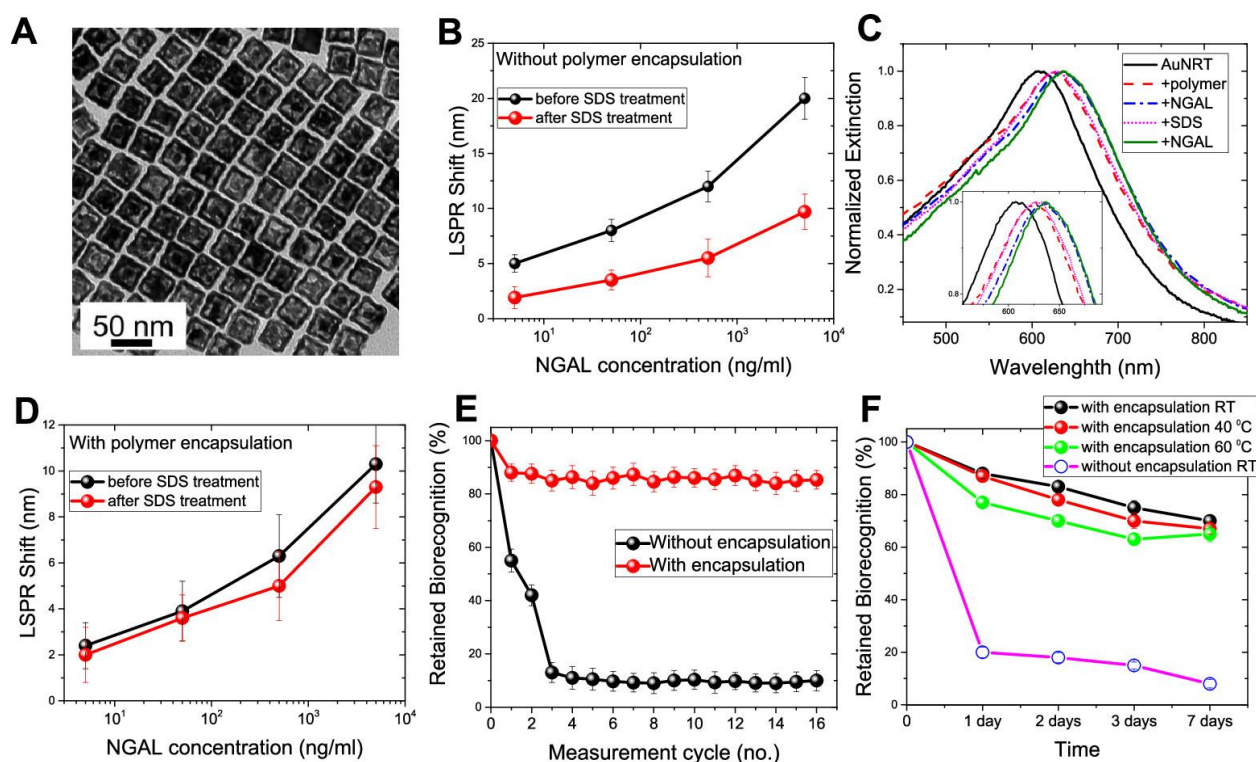


**Figure 4. 5:** (A) Representative TEM image of Au nanorattles (AuNRT) used as nanotransducers. (B) LSPR shift upon exposure of AuNRT-NGAL antibody bioconjugates to different concentrations of NGAL before (black) and after SDS (red) treatment. (C) Extinction spectra corresponding to each step involved in the polymer encapsulation strategy of AuNRT-NGAL antibody bioconjugates. Inset shows zoomed in spectra highlighting the shifts in the LSPR wavelength. (D) LSPR shift upon exposure of polymer encapsulated AuNRT-NGAL antibody bioconjugates to different concentrations of NGAL before (black) and after SDS (red) treatment. (E) Retained biorecognition capability of biosensors with and without polymer encapsulation over multiple capture/release cycles of NGAL. (F) Retained biorecognition capability of AuNR-IgG bioconjugates with and without polymer encapsulation stored at room temperature, 40 and 60°C for different durations. Error bar represents standard deviations from three different samples.

## 4.13 Conclusions and Outlook

In summary, we have introduced a facile and universal method based on *in situ* polymerization of an organosilica layer for preserving the biorecognition capabilities of immobilized antibodies. Polymer encapsulated antibodies on plasmonic nanostructures exhibited remarkable stability over multiple capture/release cycles, thus enabling refreshability of the biochips. The thickness of the polymer layer, controlled by the concentration of the monomers and the polymerization time, plays a critical role in determining the balance between the preservation of the recognition ability of the antibody and the availability of the antibody binding sites for antigen capture. Although, in this study, we have employed a plasmonic biosensor as a transduction platform and SDS treatment as a method to overcome the antibody-antigen interaction, the encapsulation approach can be easily extended to other transduction platforms and other possible sensor refreshing methods. More specifically, although the SDS-based sensor refreshing strategy offers a rather narrow application window, primarily limited to implantables in the oral cavity, the polymer-based preservation method demonstrated here is universal. The encapsulation-based preservation method demonstrated overcomes a critical challenge in wearable and implantable biosensors and is expected to advance the design and implementation of wearable biosensors for long-term monitoring of protein biomarkers.

# **Chapter 5: Plasmonically-active Tissue Analogues for Rapid and Ultrasensitive Quantification of Inflammatory Disease Burden**

*The results reported in this chapter are part of unpublished manuscript – Gupta, R., et al, & Singamaneni, S. “Plasmonically-active Tissue Analogues for Rapid and Ultrasensitive Quantification of Inflammatory Disease Burden”. Manuscript under preparation.*

## **5.1 Abstract**

Collagenases are the group enzymes which are responsible for the degradation of most of the extracellular matrix proteins such as collagen. They also play important roles in many pathological situations.<sup>92-93</sup> For example, collagenase can degrade collagen, which is the major component of gingival fluid. Moreover, several studies have shown that collagenases are biomarkers of various diseases, particularly tumor invasion, metastasis,<sup>96-97</sup> periodontitis, osteoarthritis and rheumatoid arthritis.<sup>98</sup> Therefore, development of new rapid and sensitive and selective detection of collagenase is of great significance in the diagnosis of collagenase relevant diseases. Collagenase activity measurements based on the use of ninhydrin mediated reaction require multiple steps, and the fluctuating formation of purple color makes the assay somewhat unreliable. Physical changes resulting from the enzymatic reaction of collagen with collagenases, e.g., turbidity and viscosity

measurements have also been used in assays.<sup>101</sup> Other methods for measuring collagenase activity are mentioned above in the background section. All of these methods have their own limitations of being lengthy, or uneconomical, or potentially unsafe to handle (in case of radiolabels), or they suffer from a lack of sensitivity. Most of them cannot be extended to use with other proteases. Therefore, it is imperative to develop a cost effective assay for rapid and sensitive detection of collagenase activity. Therefore, in the research task we aim to develop a collagen plasmonic foam based collagenase sensor for rapid and ultrasensitive detection of collagenase.

## 5.2 Materials and Methods

**Materials:** Gold(III) chloride trihydrate ( $\text{HAuCl}_4 \cdot 3\text{H}_2\text{O}$ ,  $\geq 99.9\%$ ), ascorbic acid (AA,  $\geq 99.0\%$ ), silver nitrate ( $>99\%$ ), sodium borohydride ( $\text{NaBH}_4$ , 98%), cetyltrimethylammonium bromide (CTAB,  $\geq 99\%$ ), 3-(mercaptopropyl)trimethoxysilane (MPTES), (3-aminopropyl)trimethoxysilane (APTMS), 10X phosphate buffer saline (PBS), collagenase, collagenase colorimetric assay, calcium chloride, N-[Tris (hydroxymethyl)methyl]-2-aminoethanesulfonic acid (TES) and trimethoxy(propyl)silane (TMPS), sodium dodecyl sulfate ( $>99\%$ ) (SDS), albumin from human serum (Mw = 65 kDa) were obtained from Sigma-Aldrich. Collagen wound dress was purchased from HeliTape. NHS-800 CW was purchased from LI-COR. Desalting column and NHS-PEG-Biotin were purchased from Thermo Scientific.

**Synthesis of AuNRs:** AuNR of LSPR wavelength of 760 nm was prepared by a seed mediated method.<sup>212-213</sup> Au seed was synthesized by adding 0.6 ml of ice-cold  $\text{NaBH}_4$  solution (10 mM) into a solution containing 0.25 ml 10 mM of  $\text{HAuCl}_4$  and 9.75 ml CTAB (0.1 M) under vigorous stirring at room temperature for 10 min. The color of the solution changed from yellow to brown indicating the formation of Au seed. For the synthesis of AuNR, the growth solution was prepared by the sequential addition of aqueous  $\text{HAuCl}_4$  (0.01 M, 2 ml), CTAB (0.1 M, 38 ml),  $\text{AgNO}_3$

(0.01 M, 0.5 ml), HCl (1M, 0.8 ml) and ascorbic acid (0.1 M, 0.22ml) followed by gentle inversion to homogenize the solution. The AgNO<sub>3</sub> and HCl volume ratio may vary to obtain the right wavelength. Subsequently, 5 µl of the seed solution was added into the growth solution and left undisturbed in the dark for 24 hours. AuNR solution was centrifuged at 7000 rpm for 40 minutes to remove the supernatant and the AuNR was re-dispersed into nanopure water to achieve a final peak extinction ~2.0.

**Conjugation of Biotin and 800CW:** Biotin and 800CW were sequentially conjugated to BSA through EDC/NHS chemistry. In pH 7-9 buffers, NHS esters react efficiently with primary amino groups (-NH<sub>2</sub>) by nucleophilic attack, forming an amide bond and releasing the NHS. Specifically, 2 mg of NHS activated biotin (NHS-PEG4-Biotin) was added to 2.2 ml of BSA solution (5 mg/ml in 1X PBS). The mixture was incubated at room temperature (~22°C) for 1 hour to complete the reaction. Excess NHS-PEG4-Biotin was removed from the solution using a desalting column (5mL, 7000 MWCO) pre-equilibrated with 1X PBS. Next, 800CW was conjugated to BSA-biotin. 0.1 ml of 1M potassium phosphate buffer (K<sub>2</sub>HPO<sub>4</sub>, pH=9) was added into 1ml of purified BSA-biotin solution to raise the pH. Next, 25 µl of 4 mg/ml NHS-800CW was added to the mixture and the solution was incubated at 23°C for 2.5 hours. Free NHS-800CW was then separated from the conjugate using a Zeba desalting column pre-equilibrated with nanopure water.

**Synthesis of plasmonic-fluor:** To synthesize plasmonic-fluor with high fluorescence enhancement efficacy, it is extremely important to choose an “on-resonant” plasmonic nanostructure for a given fluorophore. For 800CW, AuNR-760 (length and diameter of 83 and 24 nm, respectively) was employed as the nanoantenna. 1 µl of MPTMS was added to 1 ml AuNR with extinction ~2.0 and the mixtures was shaken for 1 hour allowing the formation of an interfacial layer on the AuNR. MPTMS modified AuNR was further mixed with different volumes

of APTMS and TMPS (from 0.5  $\mu$ l to 2  $\mu$ l) to form the polymer spacer layer on AuNR. Finally, AuNR/polymer solution was centrifuged twice each at 6000 rpm for 10 minutes to remove the free monomer. After second centrifugation, AuNR/polymer was concentrated into a final volume of 10  $\mu$ l. Next, BSA-biotin-800CW conjugate was coated around AuNR/polymer. We have adopted previously reported method to coat BSA around metal nanostructures with a few modifications.<sup>214</sup> Specifically, 1  $\mu$ l of 20 mg/ml citric acid was added into 100  $\mu$ l of BSA-biotin-800CW (~4 mg/ml) to lower the pH. Concentrated AuNR/polymer solution was subsequently added into this mixture and sonicated for 20 minutes under dark condition. The nanostructures were then collected using mild centrifugation (5000 rpm for 3 minutes). Subsequently, the AuNRs were incubated with 0.5 ml BSA-biotin-800CW (~0.4 mg/ml, pH=10) for 3 days under dark condition in 4°C. Finally, the nanostructures were washed four times using nanopure water (pH=10) by centrifugation at 6000 rpm. After the last washing step, the particles were re-dispersed into 1% BSA (buffered with 1X PBS).

**Material characterization:** Transmission electron microscopy (TEM) images were obtained using a JEOL JEM-2100F field emission (FE) instrument. A drop of aqueous solution was dried on a carbon-coated grid, which had been made hydrophilic by glow discharge. SEM images were obtained using a FEI Nova 2300 field-emission scanning electron microscope at an acceleration voltage of 10 kV. The extinction spectra of plasmonic nanostructures were obtained using a Shimadzu UV-1800 spectrophotometer. Fluorescence imaging were recorded using LI-COR Odyssey CLx imaging system. Confocal Fluorescence images were collected using Olympus FV1000 LSM confocal laser scanning microscopy under 10X water-immersion objective.

**Synthesis of Collagen foam with plasmonic fluor:** Collagen wound dresser obtained from Helitape was first washed thoroughly with water, then freeze dried to form collagen aerogel. Then



the collagen aerogel was incubated in 1  $\mu\text{g}/\text{ml}$  solution of streptavidin conjugated 800CW fluorophore in 1X PBS for 1 hour. The thus obtained collagen foam is then thoroughly rinsed with water to remove free fluorophore. Collagen foam obtained after this step is called CF\_Strep-800CW. Next, the collagen foam is incubated in plasmonic fluor (PF) solution to allow bonding between streptavidin, which is on the collagen foam and biotin, which is on the PF. After 1 hour incubation the foam is washed again to remove free PF from the foam. The thus modified collagen foam is called CF\_PF.

**Measurement of collagenase concentration dose response:** To measure the concentration of collagenase, CF\_PF or CF\_Strep-800CW foams are added to the TESCA buffer. The TESCA buffer was prepared using 0.36 mM calcium chloride and 50 mM TES. Before addition of these foams in TESCA buffer solution it was ensured that the foams are thoroughly washed and there is no leakage of the PF or fluorophore in the solution. This is ensured by subjecting these foams to multiple washing cycles. Then the required concentration of collagenase is added to 10 ml of TESCA buffer solution containing CF\_PF or CF\_Strep-800CW foam. Then at regular interval of 2 mins (until 10 mins) 100  $\mu\text{l}$  of solution is taken out to the 96 well plate to measure the fluorescence intensity using fluorescence imaging system. The rate of increase of fluorescence intensity vs time was measured for different concentration of collagenase to generate the dose response curve.

**Measurement of collagenase concentration in saliva samples:** To measure the concentration of collagenase in saliva samples, first, the saliva samples are diluted 10 times in TESCA buffer solution. Then to this diluted saliva solution CF\_PF is added. The TESCA buffer was prepared using 0.36 mM calcium chloride and 50 mM TES. Before addition of CF\_PF in TESCA buffer solution it was ensured that CF\_PF is thoroughly washed and there is no leakage of the PF in the

solution. This is ensured by subjecting CF\_PF to multiple washing cycles. Then at regular interval of 2 mins (until 10 mins) 100  $\mu$ l of solution is taken out to the 96 well plate to measure the fluorescence intensity using fluorescence imaging system. The rate of increase of fluorescence intensity vs time was measured and by using the dose response curve generated earlier the concentration of collagenase in saliva was determined.

### 5.3 Plasmonic-fluor as reporter element

Collagenases are important proteolytic tools for extracellular matrix remodeling during tissue regeneration and organ development<sup>215</sup>. However, an excess production of collagenase can destroy extracellular matrix and lead to pathological conditions, particularly periodontal disease<sup>216</sup>, tumor invasion and metastasis, *etc.*<sup>96-97</sup> Therefore, rapid, sensitive and selective detection of collagenase is of great significance in the diagnosis of collagenase-relevant diseases. Traditional techniques involve resource extensive and multistep detection process which makes the whole procedure time consuming and tedious. For instance, current detection methods of periodontal disease rely on mechanical assessment of pocket depth and radiographic detection of bone deterioration.<sup>217</sup> By the time the disease is diagnosed, it is often too late to reverse the condition making the process both laborious and not sensitive enough. We hypothesized that the collagen foam loaded with optically readable reporter element offers not only much simpler and faster detection technique but also high sensitivity.

**Figure 5.1D** displays the schematic illustration plasmonic of collagen foam based detection of collagenase present in any biospecimen. Upon exposure to biospecimen solution containing collagenase, the foam degrades resulting in release of reporter elements in the solution. Subsequently, the fluorescence signal of the solution increases which can be measured to

quantitatively determine collagenase concentration as the degradation of foam or the release of reporter element depends on the collagenase concentration. To enable ultrasensitive detection of collagenase, we employ plasmonically enhanced ultrabright fluorescent nanoscale labels called plasmonic-fluor<sup>167</sup> as optically readable reporter element (**Figure 5.1A, B and C**). Collagen plasmonic foam was synthesized by first incubating freeze dried collagen foam in streptavidin-800CW solution which binds non-specifically to collagen fibers via non-covalent interactions. The thus realized collagen hydrogel is then incubated in biotinylated PFs solution, enabling loading of PFs on collagen foam owing to high affinity of the biotin-streptavidin complex.<sup>218</sup> The morphology and the porous structure of the collagen foam (**Figure 5.1E**) was not compromised after loading of PF (**Figure 5.1F**). Scanning electron microscope (SEM) image depicted in **Figure 5.1G** reveals dense and uniform loading of PFs on collagen foam. **Figure 5.1H** shows individual collagen fibers decorated with PFs.

## 5.4 Collagen plasmonic foam characterization

To demonstrate the efficacy and importance of fluorescence measurement over absorbance of plasmonic-fluor, we measured the limit-of-detection (LOD) of plasmonic-fluor with different readout (**Figure 5.2A**). It was observed that the LOD of plasmonic-fluor detected by a fluorescence scanner is ~1000 fold better than when it is detected via absorbance. Further, the fluorescence intensity of collagen plasmonic foam (collagen foam decorated with plasmonic-fluor) is ~ 1000 times higher than the fluorescence intensity of the collagen foam loaded with conventional fluorophore (**Figure 5.2B**). The fluorescence signal from the PF or conventional fluorophore remains stable even when exposed to high concentration of collagenase, thus, suggesting stability of reporter elements (**Figure 5.2C**). The confocal fluorescence image of collagen foam loaded with conventional fluorophore (**Figure 5.2D**) and plasmonic-fluor (**Figure 5.2E and F**)

demonstrates clear difference between their fluorescence intensities thus justifying the significance of plasmonic-fluors.

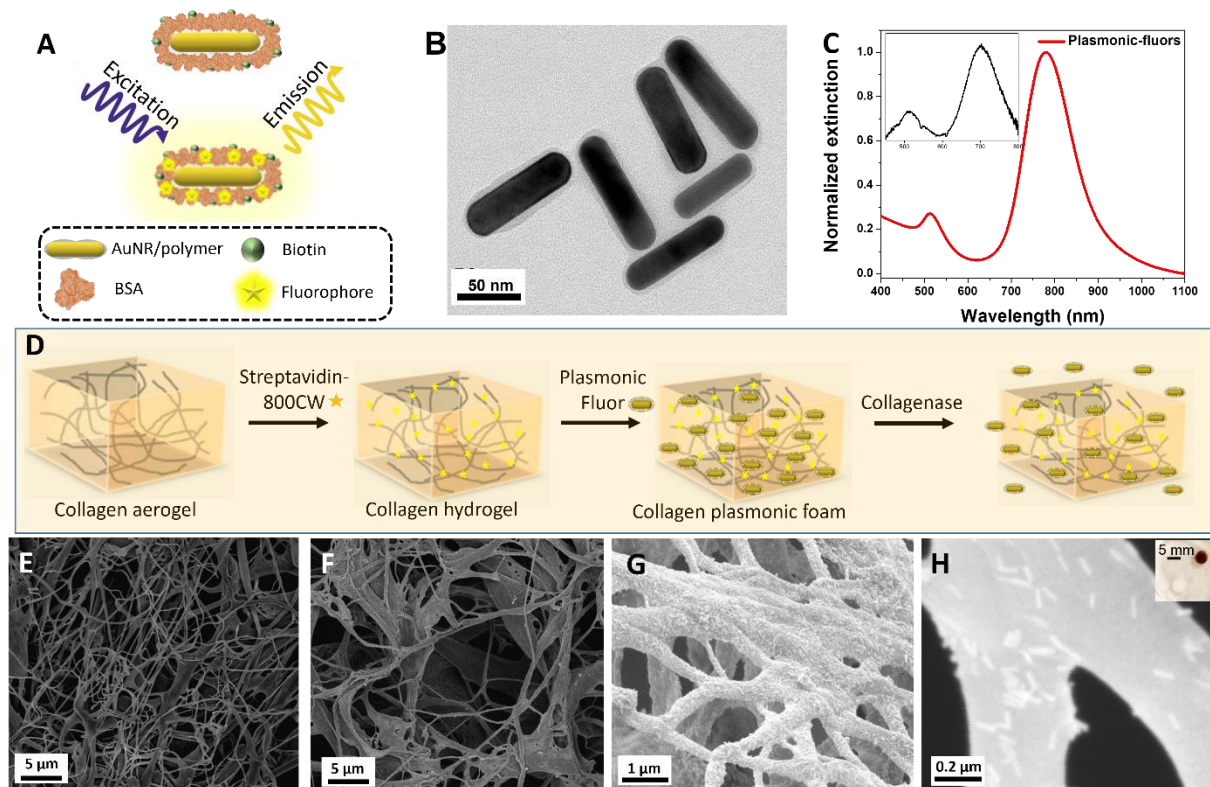


**Figure 5. 1:** (A) Schematic illustration of plasmonic-fluor, employed as the reporter element, comprising of gold nanorod as plasmonic core, polymer layer as spacer, molecular fluorophores (800CW), and biotin as recognition element. (B) Transmission electron microscopy image of plasmonic-fluors. (C) UV-vis absorbance spectra of plasmonic-fluor in solution. Inset depicts the UV-vis absorbance of the collagen foam loaded with plasmonic-fluors. (D) Schematic illustration of collagen foam based approach for quantitative detection of collagenase. SEM images of (E) freeze dried collagen foam, (F) collagen foam after pre-treatment, (G) collagen plasmonic foam and (H) individual collagen fibers decorated with PFs (inset shows photograph of collagen foam with (right) and without (left) plasmonic-fluors).

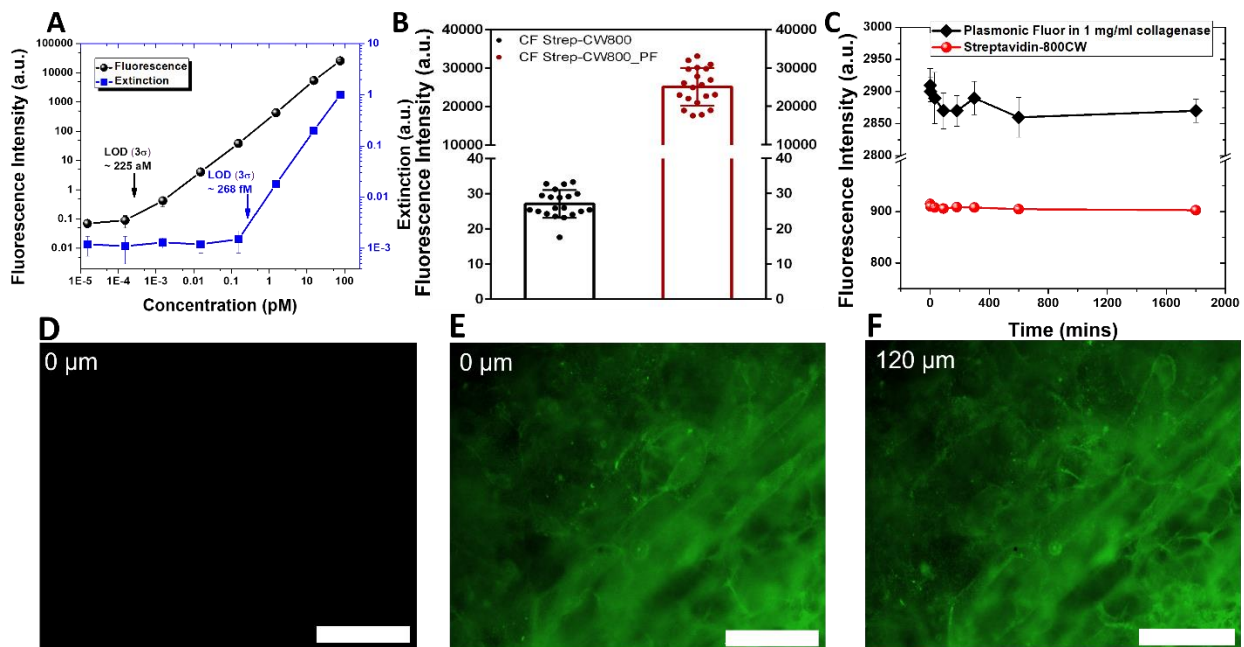


**Figure 5. 2:** (A) Dose-dependence of plasmonic-fluor with respect to its fluorescence intensity (black) and extinction (blue). (B) Fluorescence intensities of collagen foams (n=20) with conventional fluorophore (CF\_strep-800CW) and PF (CF\_strep-800CW\_PF). (C) The fluorescence intensity from both plasmonic-fluors and conventional fluorophore over period of time when exposed to high concentration of collagenase (1mg/ml). Confocal fluorescence image of collagen foam loaded with (D) conventional fluorophores and (E and F) plasmonic-fluors.

## 5.5 Specificity and kinetics of collagen plasmonic foam

Next, we investigated the release kinetics of PF from collagen plasmonic foam into the solution by immersing collagen plasmonic foam in the reservoir of TESCA buffer solution (15 ml), spiked with known concentration of collagenase. After regular intervals, small volume (100  $\mu$ l) of solution is taken out in 96 well plate to measure fluorescence intensity of the solution. It was observed, as shown in **Figure 5.3A**, that with time the fluorescence intensity of solutions containing collagen plasmonic foam and spiked with collagenase increased before saturating and the rate of increase of fluorescence intensity was dependent on collagenase concentration. In contrast, the increase in fluorescence intensity corresponding to collagen foam loaded with conventional fluorophore and spiked with similar collagenase concentration was not significant,

further emphasizing the importance of PF over conventional fluorophore. Further it should be noted that the fluorescence intensity of the solution not spiked with collagenase did not change over a period of time suggesting no release/leakage of PF in absence of collagenase (**Figure 5.3A**). We also sampled the resultant solution after exposure to collagenase via for the presence of plasmonic-fluors (**Figure 5.3B**).

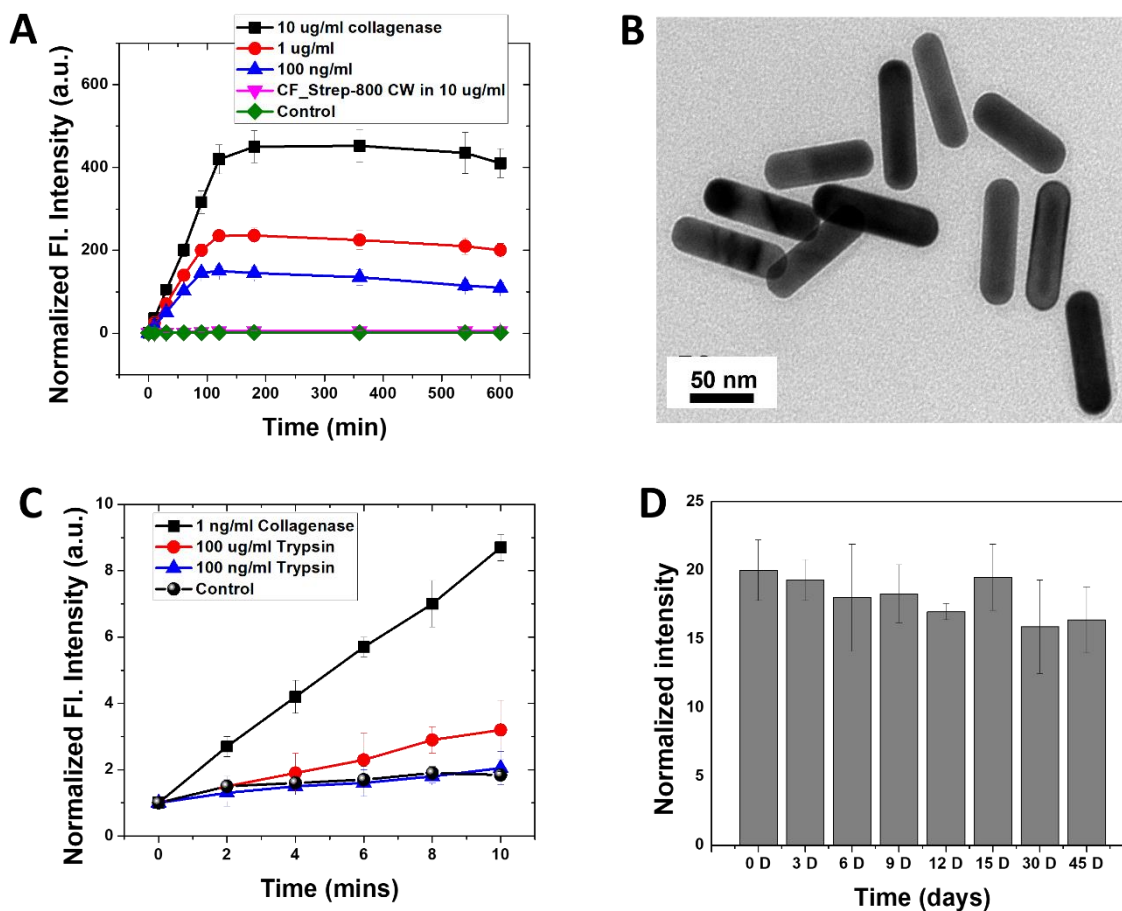


**Figure 5. 3:** (A) Kinetics study of action of collagenase on different collagen foams. Change in fluorescence intensities with respect to time at different concentration of collagenase. (B) TEM image of the solution obtained after degradation of collagen plasmonic foam in collagenase solution. (C) Change in fluorescence intensity with respect to time at different concentration of trypsin and collagenase, corroborating specificity of collagenase action on collagen foam. (D) Fluorescence intensity obtained from the solution containing collagen plasmonic foam and same concentration of collagenase over a period of time. n=3.

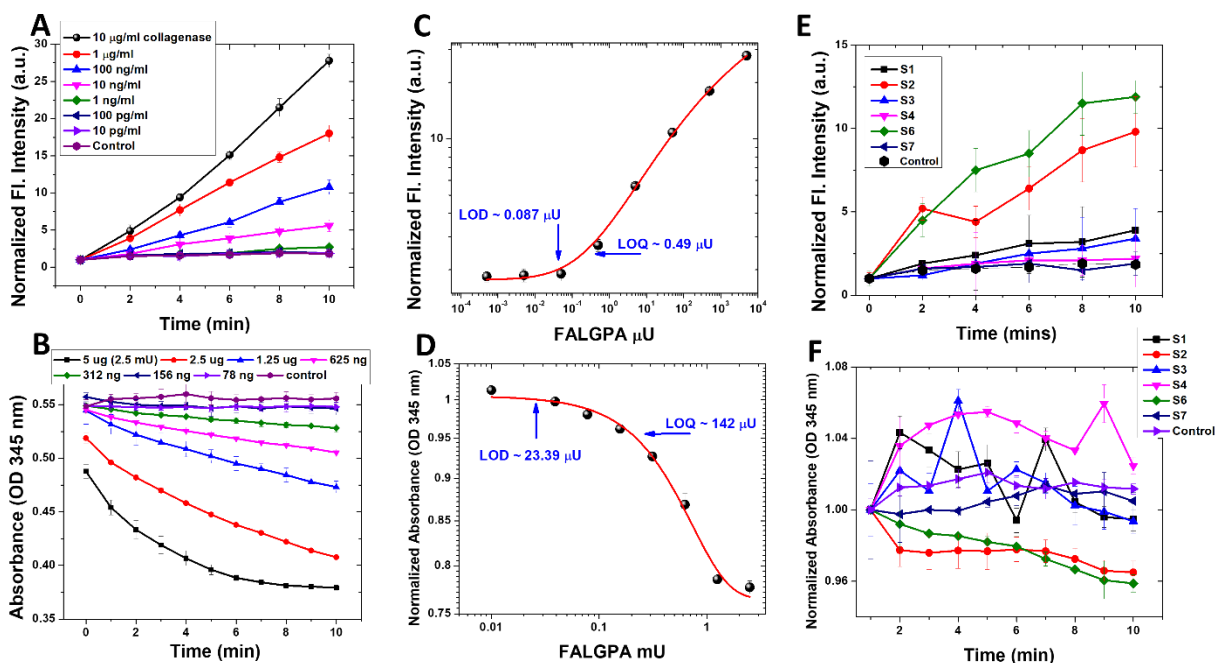


**Figure 5. 4:** (A) Change in fluorescence intensities with respect to time at different concentration of collagenase when measured using collagen plasmonic foam. (B) Change in absorbance with respect to time at different concentration of collagenase when measured using commercially available collagenase colorimetric kit. (C) Dose response curve to determine collagenase concentration, depicting increase fluorescence intensity in 10 minutes with respect to different concentration of collagenase. (D) Dose response curve to determine collagenase concentration, depicting change in absorbance in 10 minutes with respect to different concentration of collagenase. (E) Change in fluorescence intensities with respect to time and different human saliva samples when measured using collagen plasmonic foam. (F) Change in absorbance with respect to time and different human saliva samples when measured using commercially available collagenase colorimetric kit.

It is known that the undenatured, insoluble soft tissue collagens are not degraded by trypsin. Indeed, this property has been employed to establish the integrity of substrates intended for use in the study of collagenase activity.<sup>219-221</sup> We also investigated the specificity of the collagen foam towards the action of collagenase. The collagen plasmonic foams were subject to relatively higher concentration of trypsin. It was observed, as depicted in **Figure 5.3C**, that the upon exposure of trypsin to collagen foams the rate of increase in fluorescence intensity is very low as compared to that observed in case of collagenase even at much lower concentration of collagenase. This suggests the specificity of collagen plasmonic foam towards collagenase. Next, to determine the

stability and shelf life of collagen plasmonic foam, we prepared 24 collagen plasmonic foam and exposed them with similar concentrations of collagenase but at different time points, as shown in **Figure 5.3D**. We observed that the fluorescence intensity of the solution after exposure to similar concentration remained consistent over a long period of time, suggesting long-term stability and shelf life of collagen plasmonic foam.

**Table 5. 1:** Comparison of bioanalytical parameters of commercial colorimetric assay and collagen plasmonic foam-based assay.

Bioanalytical parameter	Commercial colorimetric assay	Collagen plasmonic foam-based assay
Limit-of-detection	~ 25 $\mu$ U	0.087 $\mu$ U
Dynamic range	25 $\mu$ U-5 mU	0.087 $\mu$ U-10 mU

## 5.6 Comparison with commercial kit and real-world applicability

Significantly, the difference in the rate of increase of fluorescence intensity corresponding to different concentrations of collagenase is discernable even within few minutes (**Figure 5.4A**), thus, enabling rapid and quantitative detection of collagenase. The limit of detection (LOD defined as: mean + 3  $\sigma$  of blank) of the aforementioned assay was found to be ~4 pg/ml (**Figure 5.4C**). We compared the LOD of collagenase detection with commercially available colorimetric collagenase kit (**Figure 5.4B**). We observed that the LOD attained by commercial kit is ~ 300 fold inferior than that obtained by our collagen plasmonic foam (**Figure 5.4D**). The bioanalytical



parameters obtained for collagen plasmonic foam and commercial colorimetric kit is tabulated in

**Table 5.1.**

**Table 5. 2:** Collagenase activity of healthy volunteer samples determined using commercial colorimetric assay and collagen plasmonic foam-based assay.

Sample no.	Measured collagenase activity	
	Colorimetric assay	Collagen plasmonic-foam based assay
1	Not detectable	<b>1.51 <math>\mu</math>U</b>
2	<b>164.28 <math>\mu</math>U</b>	<b>38 <math>\mu</math>U</b>
3	Not detectable	<b>0.89 <math>\mu</math>U</b>
4	Not detectable	<b>0.09 <math>\mu</math>U</b>
6	<b>187 <math>\mu</math>U</b>	<b>80.5 <math>\mu</math>U</b>
7	Not detectable	<b>0.019 <math>\mu</math>U (&lt;LOD)</b>

We anticipate that the discussed methodology could be employed not only in clinical diagnostic field but also for fields related to food analysis and environment. Therefore, next we tested the performance of our collagen plasmonic foam and commercially available collagenase colorimetric kit with human saliva samples. It was observed that with collagen plasmonic foam collagenase concentration of all of the samples were detectable (**Figure 5.4E and Table 5.2**), whereas with commercial kit only two of them were detectable (**Figure 5.4F and Table 5.2**).

## 5.7 Conclusions and Outlook

Collagenase can degrade collagen, which is the major component of gingival fluid. Moreover, several studies have shown that collagenases are biomarkers of various diseases, particularly tumor invasion, metastasis,<sup>96-97</sup> periodontitis, osteoarthritis and rheumatoid arthritis.<sup>98</sup> Therefore, development of new rapid and sensitive and selective detection of collagenase is of great significance in the diagnosis of collagenase relevant diseases. Collagenase activity measurements based on the use of ninhydrin mediated reaction require multiple steps, and the fluctuating formation of purple color makes the assay somewhat unreliable. Physical changes resulting from the enzymatic reaction of collagen with collagenases, e.g., turbidity and viscosity measurements have also been used in assays.<sup>101</sup> Other methods for measuring collagenase activity are mentioned above in the background section. All these methods have their own limitations of being lengthy, or uneconomical, or potentially unsafe to handle (in case of radiolabels), or they suffer from a lack of sensitivity. Most of them cannot be extended to use with other proteases. Thus, it is imperative to develop a cost-effective assay for rapid and sensitive detection of collagenase activity.

The collagen plasmonic foam suggested in this chapter offers highly sensitive and rapid detection of collagenase present in biospecimen and can help in determination of early progression of pathological conditions. We anticipate that the discussed methodology could be employed not only in clinical diagnostic field but also for fields related to food analysis and environment.

# Chapter 6: Digital fluoroimmunoassay for Sub-Femtomolar Detection of Protein Biomarkers

*The results reported in this chapter are part of unpublished manuscript – Seth, A., Gupta, R.\*, Wang, Z.\*, et al, & Singamaneni, S. “Disease Burden Chapter 6: Digital fluoroimmunoassay for Sub-Femtomolar Detection of Protein Biomarkers”. Manuscript under preparation.*

## 6.1 Abstract

Current antigen rapid detection tests for diagnosing COVID-19 are scalable and convenient but less sensitive than molecular tests. For this reason, current COVID-19 guidelines recommend the use of RNA tests over antigen tests for diagnostic purposes. Harnessing an ultrabright fluorescent nanoconstruct, plasmonic-fluor, as digital nanolabel, we demonstrate a partition-free digital fluoroimmunoassay for ultrasensitive, multiplexed, quantitative detection of SARS-CoV-2 proteins in nasopharyngeal swab and saliva samples from COVID-19 patients. The digital plasmon-enhanced fluorescence-based immunoassay (p-FLISA) enabled the simultaneous detection SARS-CoV-2 nucleocapsid protein, spike protein in free form and on the surface of live intact virions. Compared to the “gold standard” enzyme-linked immunosorbent assay (ELISA), the digital p-FLISA exhibited nearly 7000-fold lower limit-of-detection with virtually no change in the biorecognition elements or assay workflow. The digital assay outperformed a commercial antigen test with more than 5000-fold improvement in analytical sensitivity and was also able to

detect nucleocapsid protein from SARS-CoV-2 variants-of-concern. This ability to detect and quantify extremely low concentrations of target proteins can have a transformative impact in diagnosing infectious diseases such as COVID-19 and is broadly applicable to various other viral infections and future pandemics.

## 6.2 Materials and Methods

**Plasmonic-fluor procurement and characterization:** Streptavidin-conjugated Cy3-plasmonic-fluor (PF550<sup>TM</sup> ultrabright fluor) and streptavidin-conjugated Cy5-plasmonic-fluor (PF650<sup>TM</sup> ultrabright fluor) was purchased from Auragent Bioscience LLC (St. Louis, USA). The extinction was measured using a Shimadzu UV-1800 spectrophotometer. SEM images were obtained using a FEI Nova 2300 field-emission scanning electron microscope at an acceleration voltage of 10 kV. Fluorescence intensity was recorded using Azure Biomolecular Imager: Sapphire RGBNIR (Azure Biosystems, Inc. Dublin, USA) and the images were analyzed using Licor Image Studio Lite.

**Human IL-6 plasmon-enhanced fluorescence immunoassay (p-FLISA):** Human IL-6 DuoSet ELISA kit (R&D systems, catalog number DY406, lot number P256911), was used to perform the assays. Glass-bottom 96-well black plate (P96-1.5H-N, Cellvis, Mountain View, USA) was first coated with capture antibodies as per manufacturer's instructions (100  $\mu$ l/well) and incubated overnight at 4°C. The plate was washed three times with 1x PBST (1x PBS with 0.05% Tween-20) and then blocked with 200  $\mu$ l of reagent diluent (1x PBS in 1% BSA, 0.2 $\mu$ m filtered). After blocking the plates were washed three times with PBST, and serial dilutions of standard protein was added to different wells in duplicates and incubated for 2 hours at room temperature. The plates were washed three times with PBST and then incubated for 2 hours with 100  $\mu$ l of biotinylated detection antibody as per the manufacturer's instructions. The plates were washed

three times with PBST and streptavidin Cy5-plasmonic-fluor (extinction 0.5) for 30 minutes at room temperature in dark. Finally, the plates were washed three times in PBST and imaged using Nikon TsR2 epifluorescence microscope.

**N protein and S protein plasmon-enhanced fluorescence immunoassay (p-FLISA):**

Nucleocapsid recombinant protein: 40588-V08B, and antibodies: capture- 40143-MM08 and detection- 40143-R004 (SinoBiologicals, Wayne, USA) were used to perform the digital p-FLISA. For S protein recombinant protein (R&D systems, catalog number 10561-CV-100) was used as a standard. Capture (B04) and detection (E06) antibody for S protein were kindly provided by Ali Ellebedy's group. ACE-2 mimic was kindly provided by Rohit Pappu's group. The detection antibody for N protein and S protein were biotinylated using the commercial kit (ThermoFisher, catalog number: A39259). Glass-bottom 96-well black plate (P96-1.5H-N, Cellvis, Mountain View, USA) was first coated with capture antibodies (100  $\mu$ l/well) at the following concentrations for different assays: ACE-2 mimic: 700 ng/ml, B04: 4000 ng/ml and N protein: 100 ng/ml and incubated overnight at 4°C. The plate was washed three times with 1x PBST (1x PBS with 0.05% Tween-20) and then blocked with 200  $\mu$ l of reagent diluent (1x PBS in 1% BSA, 0.2 $\mu$ m filtered). After blocking the plates were washed three times with PBST, and serial dilutions of standard protein was added to different wells in duplicates and incubated for 2 hours at room temperature. The plates were washed three times with PBST and then incubated for 2 hours with 100  $\mu$ l of biotinylated detection antibody at the following concentrations for different assays: E06: 100 ng/ml and N protein detection: 200 ng/ml. The plates were washed three times with PBST and streptavidin Cy5-plasmonic-fluor (extinction 0.5) for 30 minutes at room temperature in dark. Finally, the plates were washed three times in PBST and imaged using Nikon TsR2 epifluorescence microscope. The N protein and S protein specific to HCoV-HKU1

(SinoBiologicals, catalog number 40642-V07E, 40606-V08B) and MERS-CoV (Abclonal, Woburn, USA, catalog number RP01297LQ, RP01303) were used as a standard to test the specificity. Recombinant N protein from D3L, S235F variant (SinoBiologicals, catalog number 40588-V07E8) and T205I variant (SinoBiologicals, catalog number 40588-V07E9) as used to assess the detection of antigens from variants. For spatial multiplexing NanoPlotter 2.0 (GeSim, Radeberg, Germany) was used to coat 2.7 nl of capture antibody (50 µg/ml) in predefined 7x7 microarray. ACE-2 mimic was used a capture element for S protein, SinoBiologicals antibody (40143-MM08) was used as capture for N protein and biotinylated human TNF $\alpha$  antibody (Biolegend, 502903) was used as a positive control. The other steps of multiplexing assay were performed as described above. At the end of the assay the plate was read using Auragent Bioscience Fluorescence plate reader and digital images were collected using an epifluorescence microscope.

**Epifluorescence Microscopic imaging:** All images were acquired on a Nikon Eclipse Ts2R-FL epifluorescence illumination microscope with a 20x, 0.75–numerical aperture (NA) lens and 60x, 1.4-NA. The microscope is attached to Hamamatsu digital camera (ORCA-Flash 4.0) with aura light engine. We used NIS-Elements AR 5.11.01 64-bit software to acquire images. Fluorescence images were collected in channels corresponding to Cy5 and TRITC. 200 ms exposure time was used. All images were saved as .jpeg files and further processed using particle counting algorithm.

**Enzyme-linked immunosorbent immunoassay:** ELISA corresponding to the above p-FLISA was performed in a similar manner as described above, except in the last step instead of Strep-plasmonic fluor, Streptavidin liked horse radish peroxidase (Strep-HRP) was added followed by TMB and stop solution as per manufacturer’s instructions.

**SARS-CoV-2 Virion p-FLISA:** SARS-CoV-2 strain 2019 n-CoV/USA\_WA1/2020 was obtained from the Department of Internal Medicine, Washington University in St. Louis (a gift from Dr. Mike Diamond). Virus was passaged in Vero CCL81 cells grown in DMEM supplemented with 10% fetal bovine serum and 1% Pen/Strep and titrated by plaque assay on Vero E6 cells. Virus was propagated in Vero E6 cells after inoculating at an MOI (multiplicity of infection) of 0.01 and incubating for 72 hours. Virus titer was determined by plaque assay and stored at -80°C. Briefly, virus was diluted serially in UTM and used in place of recombinant standard for different assays. For N protein assay the virus was diluted in UTM containing 0.05% Tween-20 to disrupt the virus and release the N protein. All work with infectious SARS-CoV-2 was approved by the Washington University School of Medicine and conducted in approved BSL3 facilities using appropriate powered air purifying respirators and personal protective equipment.

**Cloning, purifying, and conjugating the capture element for spike protein of SARS-CoV2 detection (ACE2-mimic):** The ACE2-mimic protein is a conjugate of one-to-several copies of the protein LCB1 and BSA. To generate LCB1, DNA encoding the LCB1 (modified to include a C-terminal cysteine) was synthesized (International DNA Technologies – IDT; custom gBlock synthesis) and subcloned into a pET28b vector (in-house) using Gibson cloning and custom primers (IDT).<sup>222</sup> The plasmid was confirmed to be accurate by sequencing (Genewiz). Expression of the LCB1 protein was carried out in *e. coli* (BL21 cells, New England Biolabs - C2530H) grown in 1-liter quantities in 1xLB Broth (Sigma: L3522) at 37°C. When cells reached an optical density at 0.6 (600nm) they were subjected to 20min cold shock, then induced with 0.5mM Isopropyl- $\beta$ -D-thiogalactoside (IPTG) and grown for an additional 4 hours. Cell lysates were prepared via sonication (Lysis buffer: 25 mM HEPES, 300mM NaCl, 20 mM imidazole, 6mM 2-mercaptoethanol, 1mM PMSF, pH 8) and LCB1 was affinity purified using a gravity column with

Ni-NTA HiPur® resin (Fisher: PI88222) - Wash Buffer: 25 mM HEPES, 600mM NaCl, 20 mM imidazole, pH 8; Elution buffer: 25 mM HEPES, 150mM NaCl, 500 mM imidazole, pH 8. Eluted LCB1 was further cleaned and buffer-exchanged by size exclusion chromatography (Superdex 75pg – 16/600 on an ÄKTA Pure FPLC) – storage buffer: 20mM NaPO<sub>4</sub>, 150mM NaCl, pH = 7.4. A 1-liter growth typically yielded 5 to 10 milligrams of >95% pure LCB1 (purity calculated by SDS-PAGE densitometry). Freshly purified LCB1 proteins were conjugated to BSA (Sigma: A7030) using sulfosuccinimidyl 4-(N-maleimidomethyl) cyclohexane-1-carboxylate (Sulfo-SMCC) (Thermo Scientific: A39268), according to manufacturer instructions. LCB1 proteins were included at 20-fold molar excess of BSA in the conjugation reaction. The resulting ACE2-mimic (i.e., LCB1 proteins conjugated to BSA) was purified by size exclusion chromatography (Superdex 75pg – 16/600) - storage buffer: 20mM NaPO<sub>4</sub>, 150mM NaCl, 0.02% v/v NaN<sub>3</sub>, pH = 7.4. SDS-PAGE analysis of the purified product revealed 4 to 5 discrete bands of uniformly spaced ≈15 kDa intervals, ranging in apparent MW from about 80 to 170 kDa. We infer that these bands correspond to one or multiple LCB1 proteins conjugated to a single BSA protein (LCB1 MW = 11 kDa (apparent MW ≈15 kDa), BSA MW = 66 kDa). No unconjugated BSA was observed. ACE2-mimic solutions were concentrated to ≥1mg/mL using Amicon® spin-concentrators (Sigma: UFC900396) and stored at 4°C until use.

LCB1 Synthesized Gene:

```
GTGAGCGGATAACAATCCCCTCTAGAAATAATTTTGTTTAACTTTAAGAAGGAGAT
ATACCATGTCTCATCATCATCACCATCACCACCACTCGGAAAACCTTGATTTCCAAA
GCGGCTCGGCATCTCACATGGGTGGGTCTGGGGGGTTTGGACAAAGAATGGATCTTA
CAAAAGATCTACGAGATTATGCGTTTGCTTGACGAACTTGGACATGCCGAAGCGAG
```



CATGCGCGTGTCCGACTTAATCTATGAGTTTATGAAGAAAGGCGACGAACGTCTGTT  
AGAAGAAGCCGAGCGCTTGCTGGAGGAGGTAGAAGGTAGCGGCGGCTCGGGTTTGG  
AAGGTGGCGGTTTCCTGCTAACTCGAGCACCACCACCACCACCACTGAG

LCB1 Protein:

MSHHHHHHHSENLYFQSGSASHMGGSGGLDKEWILQKIYEIMRLLDELGHAEASMRV  
SDLIYEFMKKGDERLLEEAERLLEEVEGSGGSGLEGGGSC

**Analysis of Patient samples:** The clinical samples used in the study was from a repository of nasopharyngeal and saliva samples collected from individuals with suspected and or confirmed COVID-19 disease at Washington University School of Medicine in St Louis, and remnant COVID-19 positive NP swab samples from the Barnes Jewish Clinical Microbiology Laboratory. Control specimens were obtained by written consent and collection of NP swab samples from asymptomatic healthy adults / volunteers. For evaluating cross reactivity with seasonal coronaviruses we obtained samples from adult patients at Barnes-Jewish Hospital who are found to have any of the four seasonal coronaviruses in through routine clinically warranted testing of NP samples in the clinical laboratory. This study was approved by the Washington University School of Medicine Human Research Protection Office (HRPO). A waiver of consent was obtained for data on COVID-19 PCR results, and for the clinical information collected from medical records. All clinical data pre-existed at the time of data collection; no COVID-19 PCR tests on patients were performed for the purposes of this study.

**Antibody conjugation on plasmonic-fluor:** Streptavidin-conjugated Cy3-plasmonic-fluor (40  $\mu$ l, extinction 32) and streptavidin-conjugated Cy5-plasmonic-fluor (40  $\mu$ l, extinction 30) was added to 50  $\mu$ l of 4.5  $\mu$ g/ml biotinylated detection antibody for N protein and biotinylated detection

antibody for S protein, respectively. The mixture was incubated for 30 minutes at room temperature and then washed twice with pH 10 water. For washing, Cy3-plasmonic-fluor was centrifuged at 4,000 revolutions per minute (rpm) for 10 minutes, and Cy5-plasmonic-fluor was centrifuged at 6,000 rpm for 10 minutes. Finally, the pellet was resuspended in 1% BSA in 1x PBS and stored in 4°C until further use.

**Commercial antigen assay:** BD Veritor kit was used to analyze the patient samples and serial dilutions of recombinant N protein. Veritor System – For Rapid Detection of SARS-CoV-2. BD Veritor System for Rapid Detection of SARS-CoV-2 assay, in conjunction with the BD Veritor Plus Analyzer, for swabs in Universal Transport Media (UTM) and Aimes (ESwab) transport medium was used. The Barnes Jewish Clinical Microbiology Laboratory did an internal validation, and the assay precision was deemed acceptable for testing on clinical samples.

**Code availability:** A Python code was used to count the number of particles and number of clusters. The latest version of the code is available at <https://github.com/singamaneni/Counting-single-plasmonic-nanoparticles>.

**Statistical Analysis:** All values are expressed as mean  $\pm$  standard deviation. GraphPad Prism 6 was used for all statistical analysis. 4-parameter logistic (4-PL) was used to calculate the  $R^2$  values and LOD in the standard curves of immuno-assays. The LOD is defined as the analyte concentration corresponding to the mean fluorescence intensity of blank plus three times of its standard deviation ( $\text{mean}+3\sigma$ ).

### **6.3 Digital plasmonic fluor-linked immunosorbent assay**

The ability to image individual reporter elements is critical for implementing a simple and partition-free digital immunoassay. The one-to-one correspondence between the individual

plasmonic-fluor-Cy5 observed in the scanning electron microscopy (SEM) images and fluorescence images confirm that the individual plasmonic-fluors can be imaged with high signal-to-background ratio ( $\sim 10$ ) using a standard epifluorescence microscope under a 20x objective (**Figure 6.1B**). We first set out to establish a simple theoretical model for the expected improvement in sensitivity of digital plasmonic-fluor linked immunosorbent assay (p-FLISA) in comparison to its analog counterpart. We assumed that all the analyte molecules incubated in sample wells are captured and each captured analyte molecule is labeled with one plasmonic-fluor to complete the sandwich assay. In an analog assay the signal intensity is determined by taking the average fluorescence signal from all the pixels. Two factors play a critical role in determining the analog signal intensity - spatial resolution of the image and the ratio of brightness of the label to a background pixel. We derived dose-response curves for labels with different brightness and for images acquired at different spatial resolution. For a given resolution, the LOD, defined as the concentration of the analyte at which signal-to-noise (SNR) is equal to 3, of the analog assay improved (*i.e.* concentration value decreases) as the brightness of the labels with respect to background pixel increased (**Figure A-1A**). Further, the LOD of the analog assay and the brightness of the labels with respect to the background pixel depend on the resolution of the image (**Figure A-1B**). While higher resolution improves the sensitivity of the analog assay, the finite contribution of background intensity in the mean pixel intensity still limits the LOD of the assay (**Figure 6.1C**). For lower resolution (higher pixel size) images, multiple labels or analyte molecules are required within one pixel to produce discernable signal ( $\text{SNR} \geq 3$ ), as illustrated in **Figure 6.1D**, thus precluding the detection of analytes at low concentrations. This limitation is mitigated in the digital assay as there is no contribution of background signal and the signal intensity is determined by simply counting the number of labels and disregarding the background

signal below a pre-set threshold. Thus, the digital assay signal exhibits a detectable increase proportionate to the analyte concentration, enabling detection of ultralow analyte concentrations (**Figure 6.1C**). Therefore, theoretically, the digital assay offers the capability to detect every single target analyte molecule over a broad dynamic range. It is important to note that the model presented above ignores the non-specific binding of the detection antibodies and labels on the assay surface, which determines the ultimate LOD of the digital assay. Nevertheless, the model predicts significantly improved LOD with the digital assay compared to the analog assay with identical non-specific binding.

Next, we set out to investigate the feasibility of implementing a partition-free digital immunoassay using plasmonic-fluors as digital nanolabels. Using human IL-6 (a pro-inflammatory cytokine) as a representative analyte, we compared the performance of ELISA, analog p-FLISA and digital p-FLISA. For the analog assays (ELISA and p-FLISA), conventional optical density or ensemble fluorescence intensity vs. concentration was analyzed using a four-parameter logistic (4PL) curve to determine the LOD and limit-of-quantification (LOQ). We tested a broad range of antigen concentrations (10 log orders) 5 ng/ml to 0.81 ag/ml to determine the analytical parameters (LOD, LOQ and dynamic range) of the digital p-FLISA. The LOD is defined as the signal from the blank well +  $3 \times$  standard deviation ( $3\sigma$ ) of the blank and was used as a parameter to compare the performance of the assays.

The digital assay protocol is essentially identical to analog p-FLISA except that the microtiter plate is imaged using an epifluorescence microscope and the images are analyzed using a custom-developed algorithm. The number of plasmonic-fluors at the bottom of the well monotonically increased with an increase in the concentration of IL-6 (**Figure 6.22A-D**). We found that the LOD of the digital p-FLISA (283 ag/ml) was more than 7000-fold lower than ELISA

and 60-fold lower than analog p-FLISA (**Figure 6.2D-G**). The significant improvement in sensitivity of the digital p-FLISA compared to the analog counterpart stems from the ultrahigh brightness of plasmonic-fluors, which enables single particle counting. When compared to analog p-FLISA, digital p-FLISA can sensitively detect changes in the concentration over a broader dynamic range, starting from sub-femtomolar concentration as compared to femtomolar concentration for analog p-FLISA (**Figure 6.2F**). We investigated if a similar digital assay can be performed using existing bright nanolabels such as semiconducting quantum dots (**Figure A-2**). Under a 20x objective lens, with quantum dots as nanolabels we did not observe any discernable dose-dependence for analog or digital assay. At higher magnification (60x objective), we observed individual particle-like features, which increased in number with an increase in concentration of the analyte. However, these features suffered from fluorescence intermittency (blinking) making them unsuitable for digital imaging (**Figure A-2**).<sup>223</sup> The LOD (~14 pg/ml) of the quantum dot-linked immunosorbent assay was nearly 1000-fold inferior compared to even analog p-FLISA. These findings underscore the importance of ultrabright nanolabels, such as plasmonic-fluors, for realizing a partition-free ultrasensitive digital assay, which is not feasible with moderately bright nanolabels such as quantum dots.

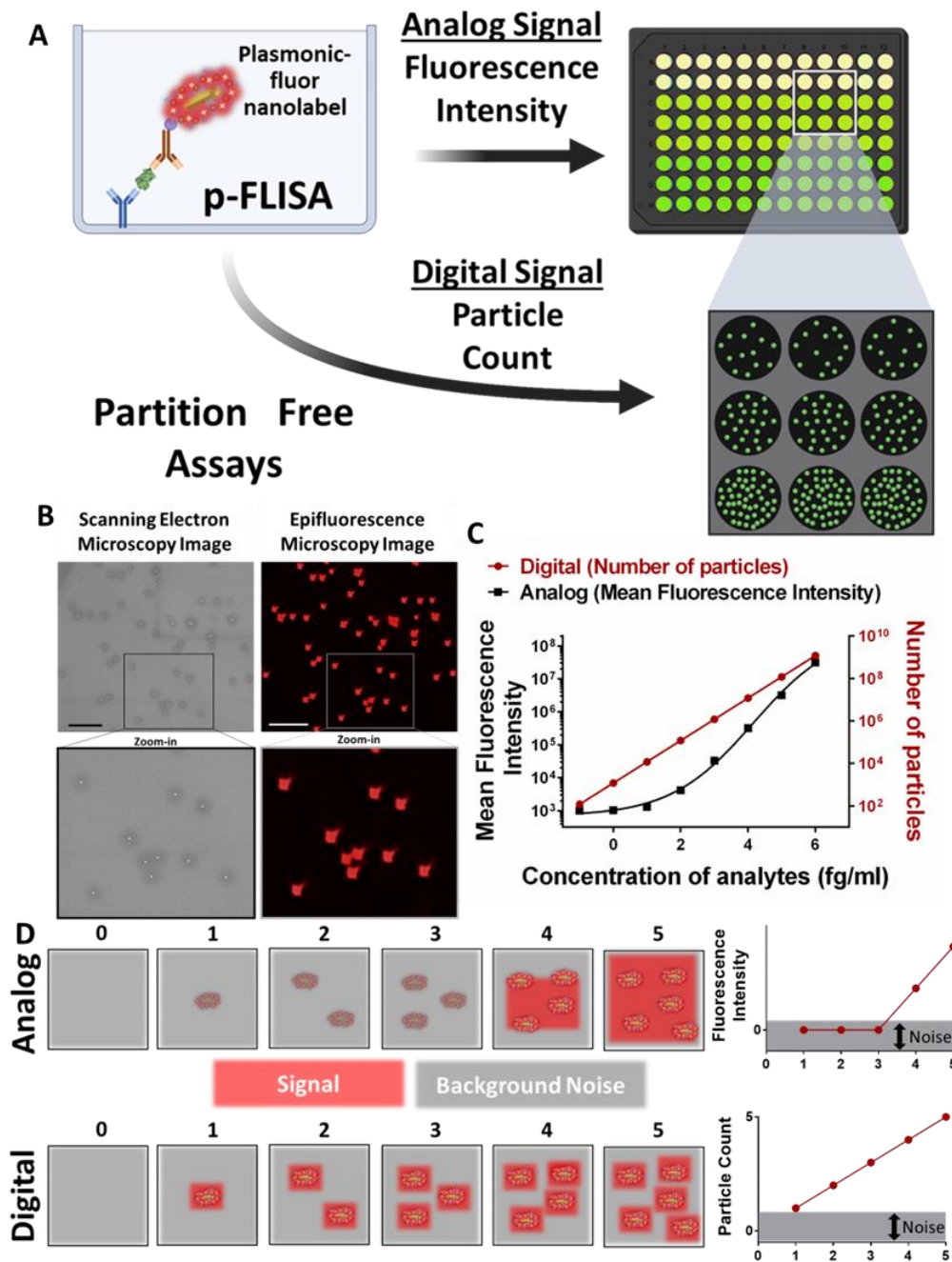


**Figure 6. 1:** (A) Schematic illustration comparing ELISA, Analog p-FLISA and Digital p-FLISA. (B) Confirmation of single particle fluorescence by correlating scanning electron microscopic images (left) and epifluorescence microscopy images (right) of the same plasmonic-fluor nanolabel. Scale bar: 5  $\mu\text{m}$ . (C) Theoretical model for comparing analog and digital p-FLISA and its effect on the slope of the standard curve for low concentration of analyte. (D) Schematic illustration representing the effect of background on the signal for analog and digital imaging. Confirmation of single particle fluorescence by correlating scanning electron microscopic images (left) and epifluorescence microscopy images (right) of the same plasmonic-fluor nanolabel. Scale bar: 5  $\mu\text{m}$ .

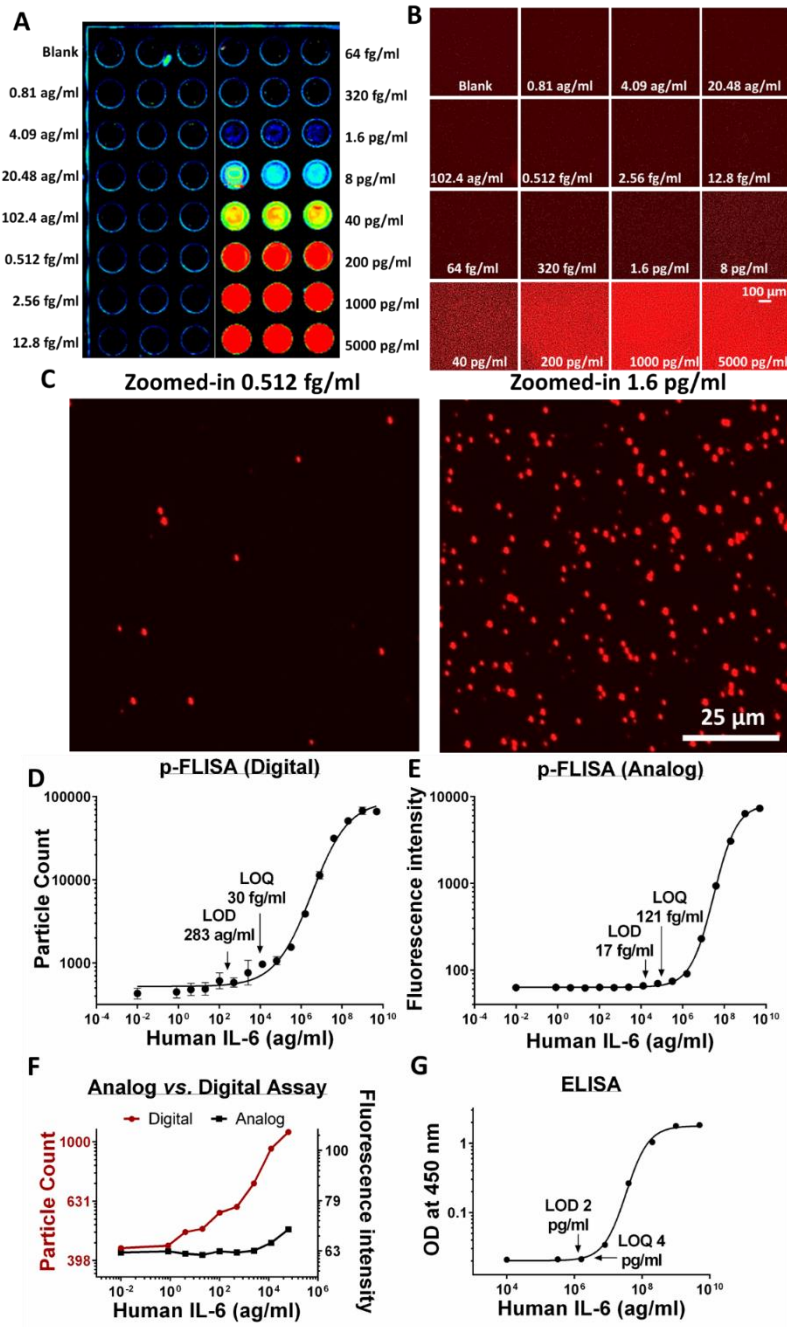


**Figure 6. 2:** Sensitivity of Human IL-6 digital p-FLISA is better than analog p-FLISA and ELISA (A) Fluorescence image of analog p-FLISA, (B) Epifluorescence microscopic images of digital p-FLISA, (C) zoomed-in epifluorescence images of digital p-FLISA for 0.512 fg/ml and 1.6 fg/ml of human IL-6. (D) Particle count vs. concentration plot of digital p-FLISA of human IL-6. n=2 (5 images per well). (E) Fluorescence intensity vs. concentration plot for analog p-FLISA. n=3. (F) Comparison of analog vs. digital. (G) ELISA (n=3). Digital R<sup>2</sup>= 0.9939, Analog R<sup>2</sup>= 0.9995, ELISA R<sup>2</sup>=0.9992.

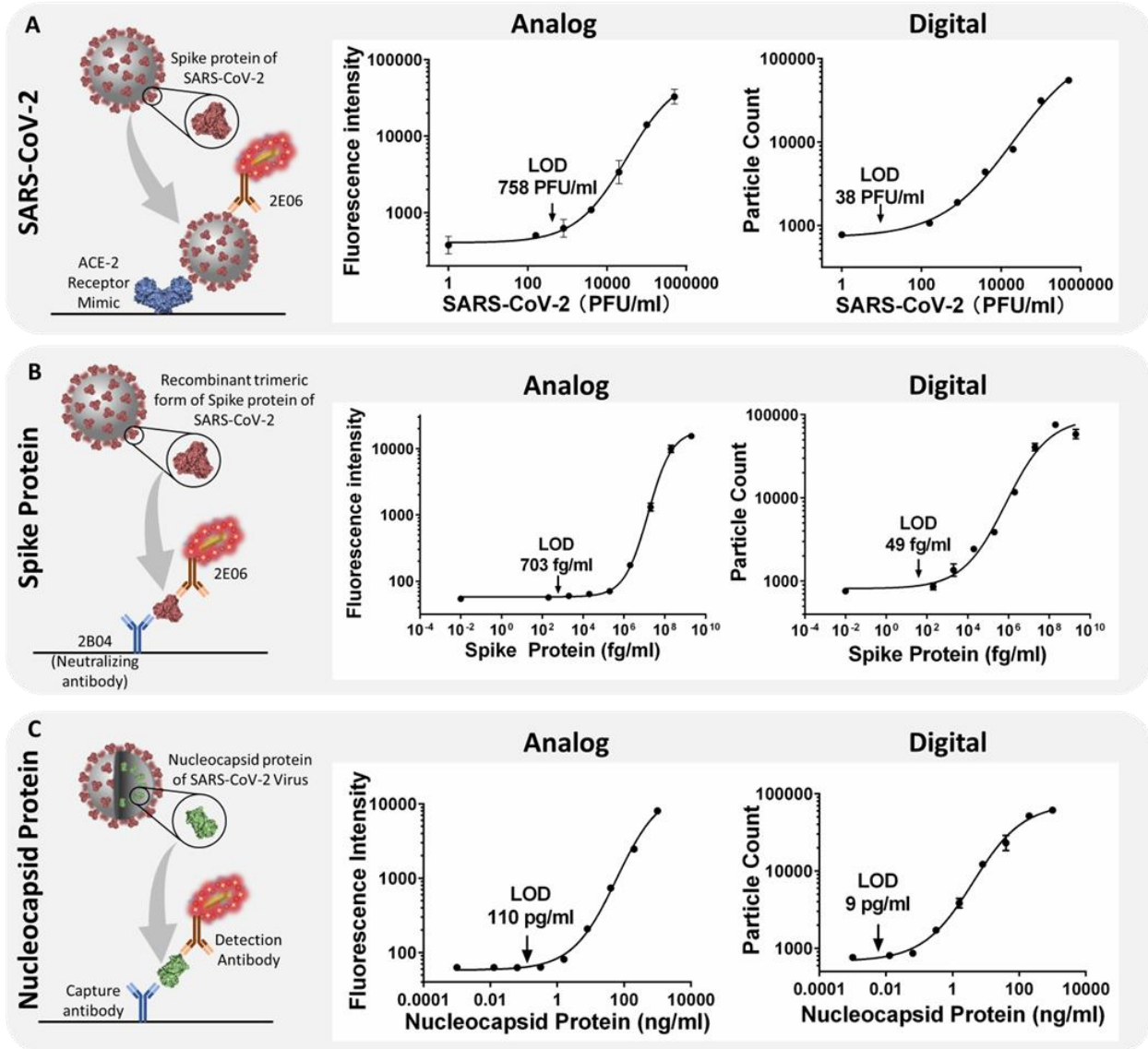


**Figure 6. 3:** Left panel (A), (B), (C) shows the schematic illustration representing different combinations of biorecognition elements used for detecting SARS-CoV-2 virus and protein. Middle panel: Fluorescence intensity vs. concentration plot (analog p-FLISA) for detection of (A) spike protein on the intact virus, (B) recombinant spike protein, (C) recombinant nucleocapsid protein.  $n=2$ . Right panel: Particle count vs. concentration plot (digital p-FLISA) of A spike protein on the intact virus, (B) recombinant spike protein, (C) recombinant nucleocapsid protein.  $n=2$  (5 images per well). Spike protein on virus: analog  $R^2=0.9901$ , digital  $R^2=0.9932$ , recombinant spike protein: analog  $R^2=0.9989$ , digital  $R^2=0.9875$ , recombinant nucleocapsid protein: analog  $R^2=0.9967$ , digital  $R^2=0.9953$ .



## 6.4 Ultrasensitive detection of SARS-CoV-2 antigens using plasmon-enhanced digital assay

Next, we set out to detect SARS-CoV-2 specific protein antigens (spike (S) protein and nucleocapsid (N) protein) and intact virion. We employed different combinations of affinity reagents to capture and detect antigens both in free form and on the whole virion. Ideally, the affinity reagents should have high specificity (low cross-reactivity), high affinity (low dissociation constant) with non-overlapping epitopes of the protein targeted by capture and detection antibodies. We determined the optimal concentration of capture and detection antibodies for attaining the highest sensitivity in p-FLISA.

The capture element of S protein is comprised of multiple copies of a rationally-designed protein that mimics the surface of angiotensin converting enzyme 2 (ACE2) and is termed LCB1.<sup>222</sup> LCB1 is conjugated to bovine serum albumin (BSA) and herein we refer to this conjugated protein as the ACE2-mimic. The LCB1 protein is a 56-amino-acid three-helix-bundle with additional N- and C- terminal flexible linkers that enable facile affinity purification (via an N-terminal 8xHis-tag) and maleimide-based covalent conjugation to BSA (via a sole cysteine residue genetically encoded to the C-terminal end). An individual LCB1 protein is comparable to a nano-body in terms of size ( $\approx 10$ kDa) and affinity (1's-100's of pM).<sup>224</sup> Furthermore, each ACE2-mimic contains several LCB1 proteins and this multivalency could provide high avidity. Lastly, the facile production and thermal stability of LCB1 ( $T_m \geq 95^\circ\text{K}$ ), and by extension, the ACE2-mimic (BSA  $T_m \sim 60^\circ\text{K}$ ), makes it an economical and resilient capture element.<sup>222, 225</sup> Monoclonal antibodies were generated in mice immunized with SARS-CoV-2 S protein and the neutralizing properties were confirmed using a focus reduction neutralization test (FRNT) and SARS-CoV-2

challenge.<sup>226</sup> Both E06 and B04 had strong binding to SARS-CoV-2 S protein and minimum or no cross-reactivity for S protein from SARS-CoV and MERS. B04 also exhibited strong neutralizing activity.

## **6.5 ACE-2 and E06 bind to non-overlapping epitopes of the spike protein**

Using these elements as capture and detection antibody respectively, we detected serially diluted intact SARS-CoV-2 virion (diluted in universal transport media, UTM) down to 38 PFU/ml using digital p-FLISA as compared to 758 PFU/ml using analog p-FLISA (**Figure 6.3A**). The fluorescence images revealed that the number of plasmonic-flours increased monotonically with the concentration of the virions (**Figure A-3**). For the detection of recombinant S protein and S protein on the SARS-CoV-2 virion, we employed B04, a neutralizing antibody, as the capture element and E06 as detection antibody. The LOD of digital p-FLISA (49 fg/ml) was nearly 15-fold lower compared to analog p-FLISA (703 fg/ml) (**Figure 6.3B**). Similarly, for the spike protein on the SARS-CoV-2 virion the LOD of digital p-FLISA (1.6 PFU/ml) was nearly 95-fold lower compared to that of the analog p-FLISA (152 PFU/ml) (**Figure A-4**). With an alternate pair of capture (LCB1) and detection (E06) elements, the LOD of recombinant S protein of digital p-FLISA improved to 10 pg/ml compared to 59 pg/ml of analog p-FLISA (**Figure A-5**).

A capture and detection antibody pair for detection of nucleocapsid (N) protein was procured from SinoBiologicals. We tested 9 combinations of capture and detection antibody concentrations to determine the optimal assay conditions (**Figure A-6**, see Experimental section). Under optimal assay conditions, the analog p-FLISA exhibited an LOD of 110 pg/ml, which was further improved by digital p-FLISA to 9 pg/ml, which is 870-fold lower than ELISA (LOD of 7.9

ng/ml) (**Figure 6.3C and A-7**). We also verified the detection of N protein in serial dilutions of SARS-CoV-2 virus stock (diluted in UTM with 0.05% Tween to disrupt the virus and release N protein). Digital p-FLISA enabled the detection of N protein in virus solutions diluted down to 100 PFU/ml compared to 1364 PFU/ml for analog p-FLISA (**Figure A-8**).

## 6.6 Testing clinical samples

Finally, we set out to investigate the applicability of the digital assay in analyzing nasopharyngeal (NP) swab and saliva samples obtained from COVID-19 patients (RT-PCR positive) and non-COVID-19 respiratory illness (RT-PCR negative) (**Figure 6.4A**). The NP swabs from patients were eluted in UTM, which is designed to transport and maintain the viral particles at room temperature. In order to mimic the patient sample, we tested the performance of N protein digital p-FLISA by diluting the recombinant standard N protein in UTM as opposed to reagent diluent (1% BSA) describe above. We observed a 4-fold improvement in LOD (2 pg/ml) with UTM as the standard diluent compared to 1% BSA (**Figure A-9**). We analyzed 60 PCR positive patient samples and 30 PCR negative patient samples. We observed that the digital p-FLISA for N protein exhibited analytical sensitivity of 82% and specificity of 100% (negative percent agreement) and the digital p-FLISA for S protein exhibited 68% sensitivity and 100% specificity (**Figure 6.4B, A-10**). The low analytical sensitivity of S protein digital p-FLISA is in agreement with the significantly lower concentration of S protein compared to N protein. It is worth noting that most of the commercial antigen tests detect the presence of N protein. The receiver operating characteristic (ROC) curve analysis for N protein showed that at a cut-off value of  $>2.363$  pg/ml the digital pFLISA assay exhibited 81.67% sensitivity and 100% specificity (Area under the curve (AUC)=0.983,  $p<0.0001$ ) (**Figure A-11**).

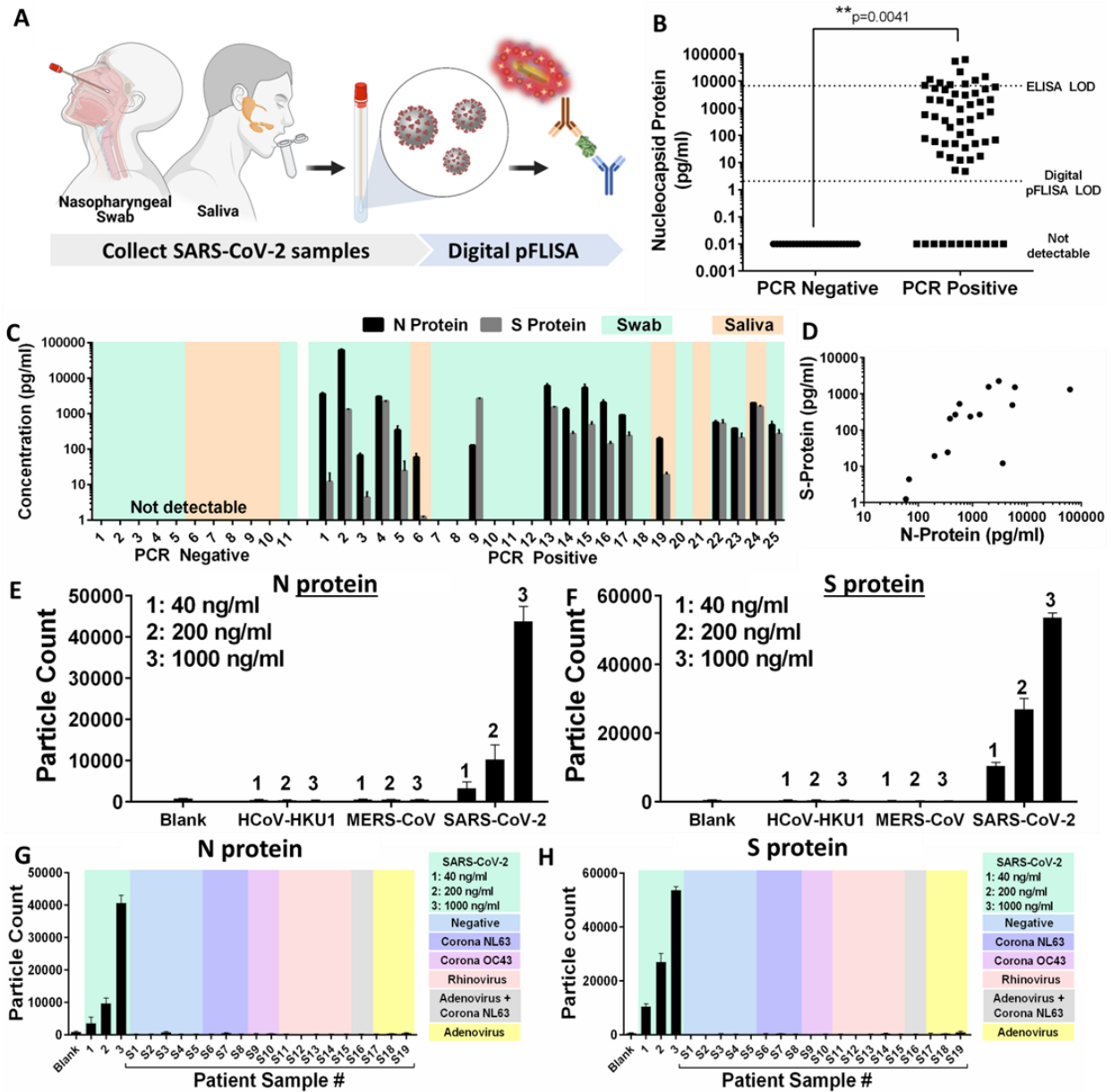


**Figure 6. 4:** (A) Schematic illustration representing the collection of human nasopharyngeal (NP) swabs and saliva samples followed by digital pFLISA. (B) Concentration of nucleocapsid protein in PCR-positive and PCR-negative human swabs and saliva,  $**p=0.0041$ , unpaired t test (two-tailed) with Welch's correction, (C) Concentration of nucleocapsid protein and spike protein in PCR-positive and PCR-negative human NP swabs and saliva. and (D) Correlation between the concentration of nucleocapsid protein and spike protein in PCR-positive patient samples (Pearson's correlation  $r=0.4254$ ). Lack of cross-reactivity of (E) nucleocapsid protein and (F) spike protein assay against recombinant protein from HCoV-HKU1 and MERS-CoV. Particle count corresponding to concentration of (G) nucleocapsid protein and (H) spike protein in patient samples tested positive for seasonal coronaviruses and other respiratory viruses.

We also analyzed SARS-CoV-2 positive patient samples (as determined by RT-PCR) for the presence and concentration of both antigens in the same sample. We observed detectable signals for both N protein and S protein for 17 out of the 25 PCR-positive samples (**Figure 6.4C**). Out of the 17 antigen-positive samples, 16 had higher concentration of N protein than concentration of S protein, which is consistent with previous findings.<sup>227</sup> Interestingly, we did not detect the presence of N protein or S protein in the remaining 8 samples (average Ct value  $36.8 \pm 6.4$ ), indicating either the absence of antigen in these samples or antigen levels below the LOD of the assay. We did not observe any detectable signal for both N and S protein from PCR negative (n=11) NP swabs and saliva, establishing the specificity of the digital p-FLISA. Although there is moderate correlation between the concentration of N protein and S protein (Pearson correlation r: 0.4254), for most of the samples (14 out of 17), the concentration of S protein increased with the concentration of N protein (**Figure 6.4D**).

The SARS-CoV-2 N and S protein digital assay did not exhibit detectable cross reactivity with N and S proteins from two other coronaviruses: MERS-CoV and HCoV-HKU1 virus (**Figure 6.4E and F**). The mean particle count in blank sample +  $3\sigma$  was set as the threshold for detectable signal. Samples positive for other common respiratory viruses (HCoV OC43, HCoV NL63, rhinovirus, and adenovirus) exhibited no detectable signal, establishing the high specificity of digital p-FLISA for SARS-CoV-2 N and S proteins (**Figure 6.4G and H**).

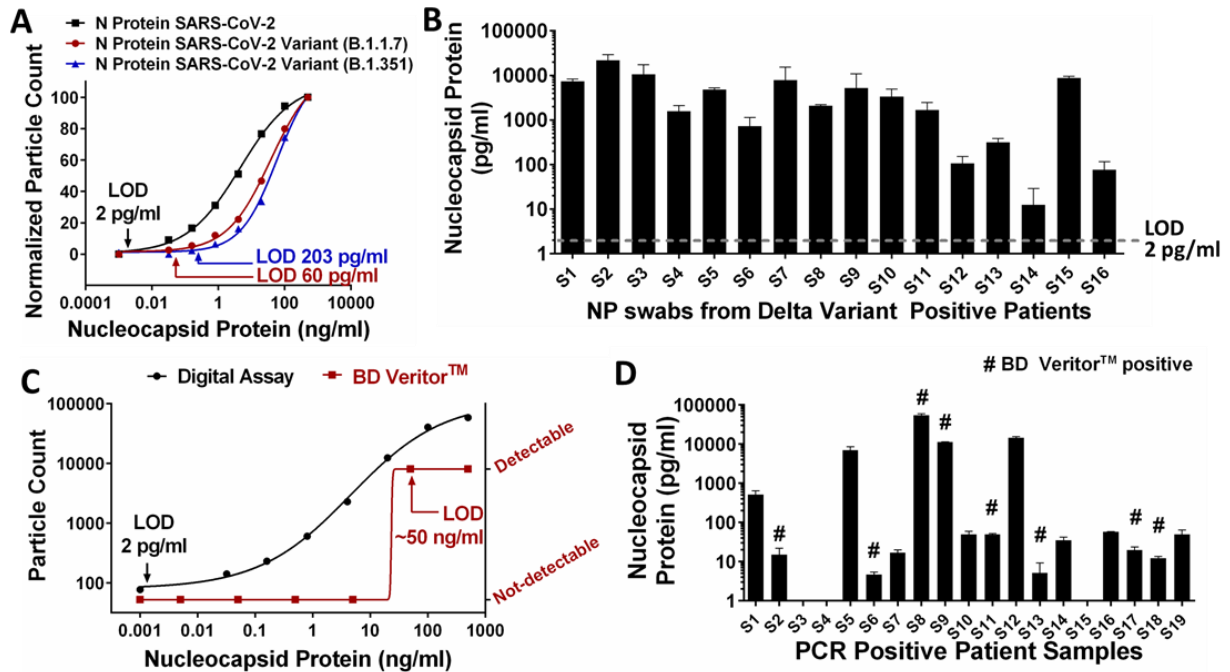


**Figure 6. 5:** (A) Digital assay for nucleocapsid protein derived from SARS-CoV-2 variants B.1.1.7 (alpha) and B.1.351 (beta). (B) Concentration of nucleocapsid protein in samples positive for SARS-CoV-2 variant B.1.617.2 (delta). (C) Comparison of the performance of commercial antigen kit (BD Veritor™) with that of nucleocapsid protein digital assay (n=2). (D) Detected nucleocapsid protein by digital assay (black bars) and BD Veritor kit™ (marked with #) in PCR positive patient samples (n=19).

## 6.7 Comparison with commercial antigen kit and the ability to detect variants:

Mutations in SARS-CoV-2 have led to emergence of variants of concern (VOCs) that are more transmissible, and with alterations to the protein or physical structure that could impact diagnostic accuracy of antigen tests.<sup>114, 228-230</sup> Most mutations in the VOCs involve the S-gene. Although fewer N-gene mutations exist, some can escape antigen detection tests.<sup>231-232</sup> A diagnostic test that misses variants can potentially lead to the spread of those variants by failing to identify individuals needing isolation and hindering contact tracing efforts. We determined the applicability of the digital p-FLISA in detecting antigens from two SARS-CoV-2 variants classified as VOCs: B.1.1.7 (Alpha, first detected in U.K), and B.1.351 (Beta, first detected in

South Africa).<sup>233</sup> The recombinant N protein from B.1.1.7 has mutation D3L and S235F and the recombinant protein from B.1.351 has mutation T205I. The D3L and T205I, S235F mutations in the N protein take place outside the RNA interaction and dimer interfaces, in the unstructured regions of the N-terminal domain (NTD) and linker regions, respectively.<sup>234</sup> The N protein antigen corresponding these variants were obtained from SinoBiologicals and were serially diluted and LOD was assessed using digital p-FLISA. The N protein assay for prototypic N protein was found to have preserved the sensitivity for detection of B.1.1.7 and B.1.351 variant with a small degradation in LOD to 60 pg/mL and 203 pg/ml, respectively (**Figure 6.5A**). We also tested 16 PCR-positive patient samples which were confirmed to be positive for B.1.617.2 (delta) variant using gene sequencing. All of the samples showed a positive signal for N protein using the digital pFLISA (**Figure 6.5B**). Thus, we conclude that the digital p-FLISA holds the potential to serve as a universal method for detection of prototypic SARS-CoV-2 as well as current and widely circulating variants.

The higher sensitivity of digital p-FLISA was further validated by analyzing serially diluted recombinant N protein using digital p-FLISA and a commercially available antigen kit BD Veritor™. BD Veritor™ is approved by FDA EUA for SARS-CoV2 antigen testing. Digital p-FLISA detected N protein down to 10 pg/ml, but the BD Veritor™ antigen kit indicated samples with concentrations below 50 ng/ml as “Presumptive Negative.” This indicates nearly 5000-fold better analytical sensitivity of p-FLISA compared to the commercial antigen test (**Figure 6.5C**). Digital p-FLISA outperformed the FDA-approved BD Veritor™ antigen kit when analyzing PCR-positive COVID-19 patient samples. BD Veritor™ detected antigen in only 8 of 19 PCR positive samples, while digital p-FLISA detected N protein in 16/19 (p=0.017, using two-tailed Fisher’s exact test). Among patients in the acute stage of illness (duration of symptoms <10 days), 13/14

samples tested positive by p-FLISA (93% sensitivity), compared to only 7/14 by BD Veritor™ (50% sensitivity) ( $p=0.032$ , using two-tailed Fisher's exact test) (**Figure 6.5D**). Among the remaining five, three patients were tested on day 14 of illness and two patients were asymptomatic. Among the three patients who were tested on day 14 of illness, the p-FLISA antigen test was negative in 2 patients who had moderate COVID-19 illness whereas it remained positive in one patient who has poorly controlled HIV and potentially had prolonged active viral replication because of immunocompromised status. Interestingly, this patient with poorly controlled HIV tested positive with BD Veritor™ and had a low RT-PCR cycle threshold ( $C_T$ ) value (21.8) which supports the possibility of active viral replication. Among the two asymptomatic patients, the p-FLISA antigen test was positive, but it is unclear if they have active viral replication. Previous studies reported that the majority of patients (>95%) with mild to moderate COVID-19 continue to shed SARS-CoV-2 RNA from the nasopharynx  $\geq 10$  days after symptom onset; however, no replication competent virus was identified beyond 9 days<sup>122, 123</sup>, whereas replicating virus was cultured through day 20 among critically ill and immunocompromised patients.<sup>124</sup> p-FLISA digital assay accurately tested positive in 13 out of 14 patients during acute phase of illness when they were expected to have replicating virus, tested negative as expected in two patients after 10 days of moderate COVID-19 illness and tested positive as expected in immunocompromised patient even after 10 days. These results warrant further evaluation of p-FLISA antigen test with larger patient samples to confirm its role in identifying infectious patients as there is urgent need for point-of-care non-culture-based tests for decision making regarding hospital infection prevention measures and removing quarantine on patients who are beyond transmissible stage of the illness. Future attempts to optimize the antigen concentration thresholds of the p-FLISA using ROC curve to accurately capture samples in the infectious stage of illness (samples with low cycle threshold



( $C_T$ ) values and positive viral cultures) while retaining sufficient sensitivity would help in development of p-FLISA antigen test as a surrogate to identify replication-competent virus.

## **6.8 Conclusions and Outlook**

We introduced a simple and ultrasensitive digital fluoro-immunoassay for the detection of SARS-CoV-2 antigens. The partition-free digital assay that is implemented in standard microtiter wells relies on an ultrabright fluorescent nanolabel, plasmonic-fluor, that can be imaged and counted using standard fluorescence microscopes. The digital assay with a workflow that is identical to that of ELISA exhibited over 5000-fold lower limit-of-detection across multiple protein analytes. As such, digital p-FLISA designed to detect SARS-CoV-2 antigens has the potential to alleviate the bottlenecks of molecular tests, including expensive equipment, technological expertise, and inherent difficulty to scale up. The digital assay demonstrated here represents an ultra-sensitive detection of SARS-CoV-2 antigens and live virion reported to date. The assay is capable of detecting both S and N proteins in single-plex and multiplex formats without any cross-reactivity to seasonal coronaviruses and other respiratory viruses. It outperformed a commercial antigen test in terms of sensitivity, and proved to be highly effective in detecting SARS-CoV-2 variants of concern. We believe this ultrasensitive antigen test can potentially distinguish individuals with actively replicating virus (who are thus more likely to be contagious) from patients who are past the infectious stage of illness. This simple, ultrasensitive, and widely deployable test can expand testing capacity and improve disease surveillance and control COVID-19 and other infectious disease outbreaks.

## **6.9 Supplementary information**

Supplementary information for chapter 6 is provided in appendix A.

# **Chapter 7: Plasmon-enhanced, Quantitative Lateral Flow Assay for Femtomolar Detection of Protein Biomarkers in Point-of- care Settings**

*The results reported in this chapter have been accepted in – Gupta, R., et al, & Singamaneni, S. (2019). “Plasmon-enhanced, Quantitative Lateral Flow Assay for Femtomolar Detection of Protein Biomarkers in Point-of-care Settings” Nature Biomedical Engineering, 2022, accepted.*

## **7.1 Abstract**

Lateral flow assays (LFAs) are the cornerstone of point-of-care diagnostics. Although rapid and inexpensive, they are nearly 1000-fold less sensitive than laboratory-based tests and cannot be used for definitive negative diagnosis. Here, we overcome this fundamental limitation by employing plasmonically-enhanced nanoscale fluorescent labels. Plasmon-enhanced LFAs (p-LFAs) enabled standard-free, ultrasensitive quantitative detection of low abundance analytes, without compromising the direct visual detection capability of conventional LFAs. Fluorometric p-LFA, completed in 20 min, attained 30-fold improvement in dynamic range and limits of detection over the 4 hour-long, “gold standard” enzyme-linked immunosorbent assay (ELISA), and achieved 95% clinical sensitivity and 100% specificity for SARS-CoV-2 antibodies and antigens. This improvement over ELISA could be achieved with either a standard benchtop fluorescence scanner or an inexpensive, portable scanner that we developed. Concentrations of

interleukin-6 (IL-6) in human serum samples and SARS-CoV-2 nucleocapsid (N) protein in nasopharyngeal swab samples determined using our portable scanner exhibited strong correlation with those determined using a benchtop scanner. p-LFAs offer potential as a broadly adaptable point-of-care diagnostic platform that outperforms standard laboratory tests in sensitivity, speed, dynamic range, ease of use, and cost.

## 7.2 Materials and Methods

**Synthesis of plasmonic-fluors:** Plasmonic-fluors consists of plasmonically active core, gold nanorod synthesized by seed-mediated method,<sup>235</sup> a polymer spacer layer, fluorophores and universal biorecognition element (biotin). Plasmonic-fluors were synthesized following the similar procedure described in our previous study.<sup>167</sup> Detailed stepwise procedure is discussed in the supplementary information.

**Synthesis of gold nanoparticles (AuNPs):** Citrate-stabilized AuNPs were synthesized using seed-mediated synthesis method and using citrate as reducing agent. Au seeds (~15 nm) were synthesized as described previously by Frens et al.<sup>236</sup> Briefly, 20 ml 0.25 mM of HAuCl<sub>4</sub> (Sigma Aldrich, 520918) was brought to boil under vigorous stirring, 800 rpm. Immediately after the solution started boiling, 0.2 ml of 3% (w/v) sodium citrate (Sigma Aldrich, 1613859) aqueous solution was added and maintained under boiling condition until the solution color changed to wine red, indicating the formation of Au seeds. Next ~100 nm AuNPs were synthesized using hydroquinone (Sigma Aldrich, H9003) as reducing agent for reduction of ionic gold.

**Materials characterization:** TEM images were obtained using a JEOL JEM-2100F field emission instrument. The extinction spectra of plasmonic nanostructures were obtained using a Shimadzu UV-1800 spectrophotometer. Fluorescence mappings were recorded using LI-COR Odyssey CLx imaging system. Digital camera (Sony cybershot DSC HX300) and imaging software, ImageJ were

employed to characterize mean gray intensities. SpectraMax iD3 (Molecular Devices) plate reader was used to measure the optical density in ELISA.

**Functionalization of nanolabels:** To functionalize nanolabels with streptavidin (Sigma Aldrich, SA101), 1  $\mu$ l 10 mg ml<sup>-1</sup> of streptavidin (or BSA-Biotin or detection antibody) was added to 1 ml OD1 of nanolabels and incubated for 1 h on a shaker at room temperature. To stabilize the particles, 1  $\mu$ l 10 mg ml<sup>-1</sup> of BSA (Sigma Aldrich, A7030) was added to the solution and further incubated for 20 min. Unbound protein was removed by washing the solution four times with pH 10 nanopure water (1  $\mu$ l NaOH in 10 ml of water). Finally, nanolabels were redispersed in 1% BSA in 1X PBS solution for use in the LFAs. To functionalize nanolabels with antibodies (IL-6 and N protein detection antibody and anti-human IgG), similar process was employed.

**Lateral flow immunoassay assembly and preparation procedures:** Nitrocellulose test membrane and absorbent pads with adhesive backing material (GE healthcare, FF120HP) were employed for fabricating the LFA strips. The test membrane and absorbent pad was cut into 4 mm wide strips using a paper trimmer. For preparing the LFA strip, biorecognition element (e.g., capture antibody) solution was pipetted onto the test membrane and dried at room temperature for 30 min. Subsequently, the test membrane was blocked using 3% BSA in 1X PBS solution. Next, strips were washed with PBST (1X PBS and 0.5% Tween20 (Sigma Aldrich, P9416), followed by drying at room temperature in a vacuum desiccator for 1 h. After drying, absorbent pads (GE healthcare, CF5) were assembled onto the polystyrene adhesive backing next to nitrocellulose test membrane. To ensure efficient transfer of the solution from the test membrane to the absorbent pad, we ensured an overlap of 1-2 mm between both strips. Experiments were performed by dipping LFAs into 96-well plates filled with 100  $\mu$ l of sample/standard solutions for 20 min. The visual signals of LFAs were obtained by a digital camera. The images were converted to 8-bit gray

scale image using ImageJ. Mean gray values of the test spot were calculated by averaging the test spot grayscale intensities obtained from ImageJ. The fluorescence signals were obtained by averaging test dot fluorescence intensities obtained using LI-COR Odyssey CLx fluorescence scanner using the following scan parameters: laser power~L2; resolution 21  $\mu\text{m}$ ; channel 800 nm; height 0 mm.

**Optimization of lateral flow immunoassay parameters:** To determine the optimum concentration of biotinylated BSA on the test spot, different LFA strips with varying concentrations of biotinylated BSA ( $100 \mu\text{g ml}^{-1}$  to  $5 \text{ mg ml}^{-1}$ ) were prepared in duplicates. LFAs were then subjected to the same concentration of streptavidin ( $1000 \text{ ng ml}^{-1}$  for AuNP-LFA and  $1 \text{ ng ml}^{-1}$  for p-LFA) and biotinylated nanolabels. To determine the optimal concentration of the nanolabels, LFA strips with the same concentration of biotinylated BSA ( $5 \text{ mg ml}^{-1}$ ) were prepared in duplicates. These LFA strips were then subjected to the same concentration of streptavidin ( $1000 \text{ ng ml}^{-1}$  for AuNPs and  $1 \text{ ng ml}^{-1}$  for plasmonic-fluors) but different numbers of biotin-functionalized nanolabels ( $4.45 \times 10^6$  to  $3.56 \times 10^{10}$  for AuNPs and  $1.2 \times 10^4$  to  $6 \times 10^6$  for plasmonic-fluors). The optimum number of nanolabels for colorimetric AuNPs-LFA and p-LFA, and fluorometric p-LFA was determined by subtracting the background signal from the test spot signal.

**Biotin-streptavidin lateral flow immunoassay:** Test spots were formed by pipetting  $0.5 \mu\text{l}$  of  $5 \text{ mg ml}^{-1}$  biotinylated-BSA onto the nitrocellulose membrane. The LFA strips were assembled as described above. For AuNP-based and plasmonic fluor-based Biotin-streptavidin LFA,  $1 \mu\text{l}$  of biotinylated AuNPs and  $1 \mu\text{l}$  of biotinylated plasmonic-fluors, respectively, were mixed with  $99 \mu\text{l}$  of different concentrations of streptavidin standard solutions ( $0.1 \text{ pg ml}^{-1}$  to  $1000 \mu\text{g ml}^{-1}$ ) in 96-well plates to allow the binding of streptavidin with the biotinylated nanolabels. LFA strips in duplicates were then exposed to the sample/standard solution for 20 min.

**Human IL-6 immunoassays:** Human IL-6 DuoSet ELISA kit (R&D systems, DY206) was utilized in the study. For AuNP-based IL-6 LFA, AuNPs were conjugated with IL-6 detection antibody for the test spot and with anti-sheep IgG (R&D systems, BAF016) for the control spot. For p-LFA, plasmonic-fluors were conjugated with IL-6 detection antibody for the test spot and AuNPs were conjugated with anti-sheep IgG for the control spot, respectively. To prepare LFA strips for IL-6 immunoassay, 0.5  $\mu\text{l}$  of 2  $\text{mg ml}^{-1}$  IL-6 capture antibody and 0.5  $\mu\text{l}$  of 2  $\text{mg ml}^{-1}$  sheep IgG (R&D systems, 5-001-A) was pipetted onto the nitrocellulose membrane at different spots to create test and control spot, respectively. Subsequently similar steps, mentioned above, were followed for LFA preparation and assembly. For AuNP-based IL-6 LFA, 1  $\mu\text{l}$  of IL-6 detection antibody-conjugated AuNPs and 1  $\mu\text{l}$  of anti-sheep IgG conjugated-AuNPs for test and control spot, respectively, were mixed with 98  $\mu\text{l}$  of different concentrations of human IL-6 standard solutions (64  $\text{fg ml}^{-1}$  to 5  $\text{ng ml}^{-1}$ ) in 96-well plates to allow the binding of the analyte with the detection antibody-conjugated nanolabels. LFA strips in duplicates were then exposed to the sample/standard solution for 20 min. For IL-6 p-LFA, 1  $\mu\text{l}$  of IL-6 detection antibody-conjugated plasmonic-fluors and 1  $\mu\text{l}$  of anti-sheep IgG conjugated AuNPs were mixed with 98  $\mu\text{l}$  of human IL-6 standard solutions (1  $\text{fg ml}^{-1}$  to 1  $\text{ng ml}^{-1}$ ) in 96-well plates. The visual signals and the fluorescence signals were obtained according to the procedure described above.

Human IL-6 ELISA was carried out according to the procedure described in DuoSet ELISA kit manual and is discussed in detail in supplementary information. Plasmonic fluor-linked immunosorbent assay (p-FLISA) was performed by adopting a similar approach, expect that the HRP-labeled streptavidin was replaced by streptavidin-functionalized plasmonic-fluor. Instead of streptavidin-HRP, 100  $\mu\text{l}$  of streptavidin-plasmonic-fluors (OD 1) was incubated for 30 min, and then the plate was washed three times with PBST. Both ELISA and p-FLISA were conducted in

duplicates. The fluorescence signal was obtained by averaging the fluorescence intensities from the microtiter wells obtained using LI-COR Odyssey CLx with the following scan parameters: laser power~L2; resolution 169  $\mu\text{m}$ ; channel 800 nm; height 4 mm.

**Lateral flow immunoassay quantitation study:** Four p-LFA IL-6 standard curves (1  $\text{fg ml}^{-1}$  to 1  $\text{ng ml}^{-1}$ ) were generated over a span of 6 months and samples with varying IL-6 concentrations (0.5  $\text{pg ml}^{-1}$  to 62.5  $\text{pg ml}^{-1}$ ) were tested in duplicates in a standard-free manner. Their experimental concentrations were determined using each standard curve, and deviation from actual concentrations were calculated.

**SARS-CoV-2 S1 antibody immunoassays:** We pipetted 0.5  $\mu\text{l}$  of 2  $\text{mg ml}^{-1}$  recombinant SARS-CoV-2 S1 protein (R&D systems, 10522-CV) and 0.5  $\mu\text{l}$  of 2  $\text{mg ml}^{-1}$  sheep IgG onto the nitrocellulose membrane as test and control spot, respectively. Subsequently, we followed the same steps described above to prepare the LFA strips. For detecting SARS-CoV-2 S1 antibodies, AuNP-LFA and p-LFA, AuNPs and plasmonic-fluors were conjugated with biotinylated anti-human IgG (Rockland, 609-4617) for test spots, respectively. In both cases, AuNPs were conjugated with anti-sheep IgG for control spot. For AuNP-based SARS-CoV-2 S1 antibody LFA, 1  $\mu\text{l}$  of anti-human IgG conjugated-AuNPs and 1  $\mu\text{l}$  of anti-sheep IgG conjugated-AuNPs were mixed with different concentrations of standard solutions (16  $\text{pg ml}^{-1}$  to 25  $\mu\text{g ml}^{-1}$ ) in 96-well plates, prior to exposure to LFA strip for 20 min. For plasmonic-fluor-based SARS-CoV-2 S1 antibody LFA, 1  $\mu\text{l}$  of anti-human IgG conjugated-plasmonic-fluors and 1  $\mu\text{l}$  of anti-sheep IgG conjugated-AuNPs were mixed with different concentrations of standard solutions (16  $\text{pg ml}^{-1}$  to 1  $\mu\text{g ml}^{-1}$ ) in 96-well plates, prior to exposure to LFA strip for 20 min. Plasma samples were diluted 500-fold in reagent diluent (1X PBS containing 3% BSA, 0.2  $\mu\text{m}$  filtered) before use. All

experiments were done in duplicates. The visual signals and the fluorescence signals were obtained by employing the same procedure mentioned above.

SARS-CoV-2 S1 antibody ELISA was carried out according to the following procedure. Microtiter wells in duplicates were coated with 100  $\mu\text{l}$  of 5  $\mu\text{g ml}^{-1}$  (in 1X PBS) recombinant SARS-CoV-2 S1 protein via overnight incubation at room temperature. For blocking, 300  $\mu\text{l}$  of reagent diluent was added to the wells for a minimum of 1 h. Next, 100  $\mu\text{l}$  of serially-diluted standard samples were incubated for 2 h, followed by incubation of 100  $\mu\text{l}$  of 100  $\text{ng ml}^{-1}$  biotinylated anti-human IgG for 2 h. Next, 100  $\mu\text{l}$  of 500  $\text{ng ml}^{-1}$  streptavidin-labelled HRP (Thermo Fisher scientific, N100) was incubated for 20 min, followed by the addition of 100  $\mu\text{l}$  of substrate solution for 20 min. The reaction was stopped by addition of 50  $\mu\text{l}$  of 2N  $\text{H}_2\text{SO}_4$  (R&D Systems, DY994) and immediately the optical density at 450 nm was measured using a microplate reader. p-FLISA was carried out by adopting a similar procedure, expect that the HRP-labelled streptavidin was replaced by streptavidin functionalized-plasmonic-fluor. Instead of HRP, 100  $\mu\text{l}$  of plasmonic-fluors (OD 1) were incubated for 30 min, and then the plate was washed three times with PBST. The fluorescence signal was obtained by averaging the fluorescence intensities from the microtiter wells obtained using LI-COR Odyssey CLx.

**SARS-CoV-2 antigen (nucleocapsid protein) immunoassays:** We pipetted 0.5  $\mu\text{l}$  of 2  $\text{mg ml}^{-1}$  nucleocapsid protein capture antibodies (SinoBiologicals, 40143-MM08) and 0.5  $\mu\text{l}$  of 2  $\text{mg ml}^{-1}$  sheep IgG onto the nitrocellulose membrane as test and control spots, respectively. For N protein p-LFA, plasmonic-fluors were conjugated with biotinylated N protein detection antibody (SinoBiologicals, 40143-R004) for the test spots. AuNPs conjugated with anti-sheep IgG were employed for control spot. Subsequently, similar steps mentioned above were followed to prepare and assemble the LFA strips. For plasmonic-fluor-based N protein LFA, 1  $\mu\text{l}$  of detection



antibodies conjugated-plasmonic-fluors and 1  $\mu\text{l}$  of anti-sheep IgG conjugated-AuNPs were incubated with different concentrations of standard solution (12  $\text{pg ml}^{-1}$  and 1  $\mu\text{g ml}^{-1}$ ; SinoBiologicals, 40588-V08B) spiked in universal transport media in 96-well plates prior to exposure to LFA strips for 20 min. p-LFAs were employed for the detection of N protein present in patient NP swab samples. The NP swab samples were in universal transport media and were used without any dilution or processing. All experiments were performed in duplicates. The visual signals and the fluorescence signals were obtained employing the similar process described above.

N protein ELISA was carried out by first coating the microtiter wells in duplicates with 100  $\mu\text{l}$  of 100  $\text{ng ml}^{-1}$  N protein capture antibodies (in 1X PBS) via overnight incubation at room temperature. For blocking, 300  $\mu\text{l}$  of reagent diluent was added to the wells for a minimum of 1 h. Next, 100  $\mu\text{l}$  of serially-diluted standard samples were incubated for 2 h, followed by incubation of 100  $\mu\text{l}$  of 200  $\text{ng ml}^{-1}$  biotinylated N protein detection antibody for 2 h. Next, 100  $\mu\text{l}$  of 500  $\text{ng ml}^{-1}$  streptavidin-labelled HRP (Thermo Fisher scientific, N100) was incubated for 20 min, followed by the addition of 100  $\mu\text{l}$  of substrate solution for 20 min. The reaction was stopped by addition of 50  $\mu\text{l}$  of 2N  $\text{H}_2\text{SO}_4$  (R&D Systems, DY994) and immediately the optical density at 450 nm was measured using a microplate reader. p-FLISA was carried out by adopting a similar procedure, expect that the HRP-labelled streptavidin was replaced by streptavidin-functionalized plasmonic-fluor. Instead of HRP, 100  $\mu\text{l}$  of plasmonic-fluors (OD 1) were incubated for 30 min, and then the plate was washed three times with PBST. The fluorescence signal was obtained by averaging the fluorescence intensities from the microtiter wells obtained using LI-COR Odyssey CLx.

**Commercial antigen test:** BD Veritor kit, Veritor System – For Rapid Detection of SARS-CoV-2, was used to analyze the presence of N protein in the patient samples. BD Veritor System was

used in conjunction with the BD Veritor Plus Analyzer. NP swabs were eluted in Universal Transport Media (UTM) and Aimes (ESwab) transport medium. Internal validation and the assay precision was conducted and deemed acceptable for testing on clinical samples by the Barnes Jewish Clinical Microbiology Laboratory.

**Patient sample acquisition:** The clinical samples used in the study were acquired from the repository of saliva, serum, plasma and nasopharyngeal swab samples from individuals confirmed/suspected with COVID-19 disease, located at Washington University School of Medicine in St Louis, and from the Barnes Jewish Clinical Microbiology Laboratory, and supported by: the Barnes-Jewish Hospital Foundation; the Siteman Cancer Center grant P30 CA091842 from the National Cancer Institute of the National Institutes of Health; and the Washington University Institute of Clinical and Translational Sciences grant UL1TR002345 from the National Center for Advancing Translational Sciences (NCATS) of the National Institutes of Health (NIH). This repository was developed and is maintained by Jane O'Halloran, MD, PhD; Charles Goss, PhD, and Phillip Mudd, MD, PhD. Control NP swab samples from asymptomatic healthy volunteers were obtained with prior written consent. For evaluation of cross reactivity with seasonal coronaviruses, samples were obtained from adults at Barnes-Jewish Hospital who were tested positive with either of the four seasonal coronaviruses or respiratory diseases via clinically warranted NP samples tests. Washington University School of Medicine Human Research Protection Office (HRPO) approved the study. All clinical data pre-existed at the time of data collection. A prior waiver of consent was obtained for the clinical information and data on COVID-19 PCR results.

**Preparation and assembly of full-strip LFAs:** Full strip p-LFA components include - NC membrane: FF80HP on polystyrene backing (cat: 10547020, from Whatman, Cytiva) Sample pad:

Fusion 5 (cat: 8151-9915, from Whatman, Cytiva) Conjugate pad: Whatman STANDARD 14 (8133-2250, Cytiva) Absorption pad: CF5 (cat: 8115-2250, Cytiva). Sample and conjugate pads were subjected to following pre-treatment process. Sample pad was soaked in 5% BSA, 0.5% Tween 20, 1X PBS and then dried in 37 °C oven for 2 h. Conjugate pad was soaked in 5% BSA, 10% sucrose, 0.5% Tween 20, 1X PBS and then dried in 37 °C oven for 2 h. After pre-treatment, sample and conjugate pad were cut into a strip of 15 mm \* 25 mm and 13 mm \* 25 mm dimensions, respectively. Absorption pads were used as received and were cut into 18 mm \* 25 mm dimensions.

To prepare nanolabels for test line, 1-3  $\mu\text{l}$  of biotinylated SARS-CoV-2 N protein or human IL-6 detection antibody of 1  $\text{mg ml}^{-1}$  concentration were added to 1 ml of streptavidin functionalized plasmonic-fluors of extinction 2. After 30 min incubation, 100  $\mu\text{l}$  of 10% BSA in 1X PBS was added to this antibody-conjugated plasmonic fluor solution. After another 30 min incubation, the conjugated nanolabel solution was centrifuged three times to remove unbound detection antibodies and the subsequent solution was dispersed back to 2 mM sodium borate, pH 8.5 with 10% sucrose. For preparation of nanolabels for control line 1-5  $\mu\text{l}$  of biotinylated anti-goat IgG of 2  $\text{mg ml}^{-1}$  concentration was added to 1 ml of streptavidin plasmonic-fluors of extinction 2. After 30min incubation, 100  $\mu\text{l}$  of 10% BSA in 1X PBS was added to this antibody-plasmonic fluors conjugate solution. After another 30 min incubation, the conjugated nanolabel solution was centrifuged three times and dispersed back to 2 mM sodium borate of pH 8.5 consisting of 10% sucrose.

Next, the nanolabel for test and control line were mixed in 1:1 ratio. Thereafter, the resulting solution was sprayed on to the pre-treated conjugate pad. The nanolabel solution was air-jet sprayed with a dispense rate of 5  $\mu\text{l cm}^{-1}$  employing a reagent dispenser (XYZ Platform Dispenser HM3030, Kinbio, Shanghai). After spraying conjugate pads were dried in 37 °C oven

for 2 h. Next, the test membrane were prepared by printing the capture antibodies specific to test and control lines. For test line SARS-CoV-2 Ag and human IL-6 capture antibody of 1mg ml<sup>-1</sup> concentration, and for control line goat IgG of 2 mg ml<sup>-1</sup> concentration were simultaneously printed on FF80HP nitrocellulose test membrane at a dispense rate of 0.5  $\mu$ l cm<sup>-1</sup> and speed of 50 mm s<sup>-1</sup> by a reagent dispenser (XYZ Platform Dispenser HM3030, Kinbio, Shanghai). Thereafter, the membranes were dried in 37 °C oven for 2 h.

Finally, the pre-treated sample pad, the conjugate pad after spraying of nanolabels, and the membrane pad after printing of capture antibodies were assembled with a 2 mm overlap between each pad and cut to strips with a width of 3 mm using a strip cutter (Programmable Strip Cutter ZQ2002, Kinbio, Shanghai). For the schematic illustration of the design of p-LFA please refer to **Figure B-48**.

**Portable fluorescence scanner:** An 80 mW 785 nm diode laser (Zlaser , Z80M18S3-F-785-pe) was used as an excitation source. The laser beam was attenuated with an ND 2.0 neutral density filter and shaped into a 4 mm wide line using the combination of the laser focus control and a 30 mm focal length cylinder PCX lens. Fluorescence was collected with a 30 mm focal length PCX lens (12.5 mm diameter) and passed through an 832/37 nm emission filter (Edmund Optics, 84-107). A 45 mm focal length achromatic doublet lens (Edmund Optics, 49-355) was used to form a 1.5x magnified image of the lateral flow strip on the sensor of the camera (ZWO ASI462MC). Fluorescence was measured at a 45° angle relative to excitation. Measurements from lateral flow cassettes were carried out by translating the sample (using Actuonix L16-R 50 mm travel actuator) through the optical system at 1 mm/s while streaming the camera video. Video was collected with 100 ms exposure (10 images per second). The average pixel value from each 10 images was used

for analysis and corresponded to one point in the trace produced by this instrument. A Raspberry Pi 4 single board computer was used for controlling all hardware components of the instrument.

### **7.3 Plasmonic-fluors increases sensitivity over AuNPs by 10000-fold in LFAs**

Plasmonic-fluors were first applied to overcome three fundamental limitations of the 30-40 nm AuNPs used as conventional colorimetric labels in LFAs. AuNPs have low capture rate (<5%), low signal-to-background ratio, and thus relatively low sensitivity.<sup>237-238</sup> Even with use of 100 nm AuNPs, shown recently to improve LFA sensitivity,<sup>239</sup> these problems persist. Because of these three limitations, color changes in AuNP-based LFAs are limited to qualitative analysis or simply a binary output, indicating the presence or absence of the target analyte.

To assess whether plasmonic-fluors (length  $98 \pm 8.7$  nm; diameter  $29.2 \pm 3.1$  nm) could overcome these limitations, we compared their performance to AuNPs (diameter  $104 \pm 13.4$  nm) on a nitrocellulose membrane. The localized surface plasmon resonance (LSPR) wavelength of plasmonic-fluors (and the gold nanorod (AuNR) core) was tuned to match the excitation and emission wavelengths of the molecular fluorophores<sup>167</sup> by modifying their aspect ratios<sup>240-241</sup>, and the optimal dimensions of the nanostructures were chosen to maximize fluorescence enhancement, based on our previous study<sup>242</sup>. We set out to determine the minimum number of AuNPs and plasmonic-fluors required to produce a detectable visible or fluorescence signal. When serially diluted AuNPs (**Figure 7.1B, B-1**) and plasmonic-fluors (**Figure 7.1C, B-1**) of known concentration were drop-casted onto nitrocellulose membrane, accumulations of  $\sim 10^6$  AuNPs and plasmonic-fluors were needed to produce a discernable visible signal (**Figure 7.1D, B-2, B-3**). However, only  $\sim 10^2$  plasmonic-fluors were required to produce a detectable fluorescence signal

(**Figure 7.1E, B-3**). Further, accumulations of  $\sim 0.6 \times 10^6$  molecular fluorophores (800CW, the fluorescent unit of plasmonic-fluors) were required to produce detectable fluorescence signal (**Figure 7.1F**), indicating  $\sim 6000$ -fold lower concentration threshold for a detectable fluorescence signal with plasmonic-fluors compared to molecular fluorophores.

Plasmonic-fluors exhibited colorimetric signal nearly identical to that of AuNPs (**Figure B-4**). The colorimetric signal enabled qualitative visual detection (by naked eye), obviating the need for specialized read-out equipment at a relatively high concentration of the target analyte, while the fluorescence signal enabled ultrasensitive detection and quantification of low abundance analytes. Thus, plasmonic-fluor function as a bimodal nanolabels (colorimetric+fluorescent) and offers ultrasensitive detection in a biological assay representative of LFAs.

Next, to compare the performance of plasmonic-fluors and AuNPs in LFA format, we employed the well-characterized biotin-streptavidin conjugate pairing, known to exhibit extremely high binding affinity.<sup>243</sup> Both AuNPs and plasmonic-fluors were functionalized with streptavidin and biotinylated bovine serum albumin (BSA) was used as a capture-ligand. LFA strips were then subjected to different known concentrations of streptavidin-conjugated AuNPs and plasmonic-fluors for 20 min (**Figure B-5**). Nanolabels flows along the nitrocellulose membrane by capillary force and gets captured by the capture-ligand, leading to the accumulation of nanoparticles at the test spot. Accumulation of sufficient number of nanolabels converts the color at the test site to red, indicating a positive result and the presence of the target analyte. The average grayscale intensity of the colorimetric signal at the test site with AuNPs and the fluorescence signal with plasmonic-fluors monotonically increased with the concentration of the nanolabels (**Figure 7.1G and H**). Significantly, for both AuNPs and plasmonic-fluors, approximately  $\sim 10^7$  nanoparticles are needed to produce a discernable visible signal, however, only  $\sim 10^3$  plasmonic-fluors are enough to

produce a detectable fluorescence signal. The four-order magnitude lower concentration threshold for a detectable signal with plasmonic-fluors compared to AuNPs in the LFA format is consistent with the drop-casting approach discussed above. These results manifest the fundamental basis that plasmonic-fluors can serve as ultrabright nanolabels for ultrasensitive detection of target analytes in an LFA.

## 7.4 Bioanalytical parameters of p-LFA compared to LFA

We optimized the bioanalytical performance of LFA by tuning concentration of capture ligand and nanolabels. We employed biotin-streptavidin as a model system. Both AuNPs and plasmonic-fluors were biotin functionalized, streptavidin and biotinylated BSA were utilized as target analyte and capture ligand, respectively (**Figure B-6**). It was observed that as the concentration of capture-ligand (*i.e.*, biotinylated BSA) increased, both mean grayscale intensity and fluorescence intensity of the test spot corresponding to AuNPs (**Figure B-7**) and plasmonic-fluors (**Figure B-8**), respectively, increased. These results suggest that higher concentrations of capture-ligand results in better signal intensity. Further, as the number of nanolabels increased, both mean grayscale intensity and fluorescence intensity of the test spot corresponding to AuNPs (**Figure B-9**) and plasmonic-fluors (**Figure B-10**), respectively, increased, implying better signal intensity with higher number of nanolabels. However, in both cases, the background signal (signal from the LFA strip outside the capture spot) also increased with the number of nanolabels. Therefore, the optimum number of nanolabels for both AuNPs-based LFA and p-LFA was determined by subtracting the background signal from the test spot signal. As expected, the optimum number of plasmonic-fluors ( $1.2 \times 10^6$ ) was four-orders magnitude lower than the AuNPs ( $1.78 \times 10^{10}$ ).

Next, we compared the bioanalytical parameters (limit-of-detection (LOD), limit-of-quantitation (LOQ) and dynamic range) of biotin-streptavidin AuNPs-based LFA and p-LFA. It is worth noting that colorimetric signal, obtained from the 8-bit ImageJ processed images of LFA strips, from both AuNPs and plasmonic-fluors exhibit similar LOD, suggesting no loss in visual detection capabilities in p-LFAs (**Figure B-11**). The LOD (defined as mean +  $3\sigma$  of the blank) of colorimetric LFA was calculated to be  $4.8 \text{ ng ml}^{-1}$  (**Figure B-12**, five-parameter logistic). In contrast, the fluorometric p-LFA enabled the detection down to  $2.3 \text{ pg ml}^{-1}$  (**Figure B-13**, five-parameter logistic fit), representing  $\sim 2000$ -fold improvement in the LOD. The LOQ (defined as mean +  $10\sigma$  of the blank) of fluorometric p-LFA is  $\sim 2500$ -fold better than the LOQ of colorimetric LFA. Further, the fluorescent component of plasmonic-fluor augmented the dynamic range of the assay by three orders of magnitude. Therefore, owing to the ultrabright fluorescence signal of the plasmonic-fluors, the p-LFAs enable ultrasensitive detection of target analyte over a much broader range of analyte concentration.



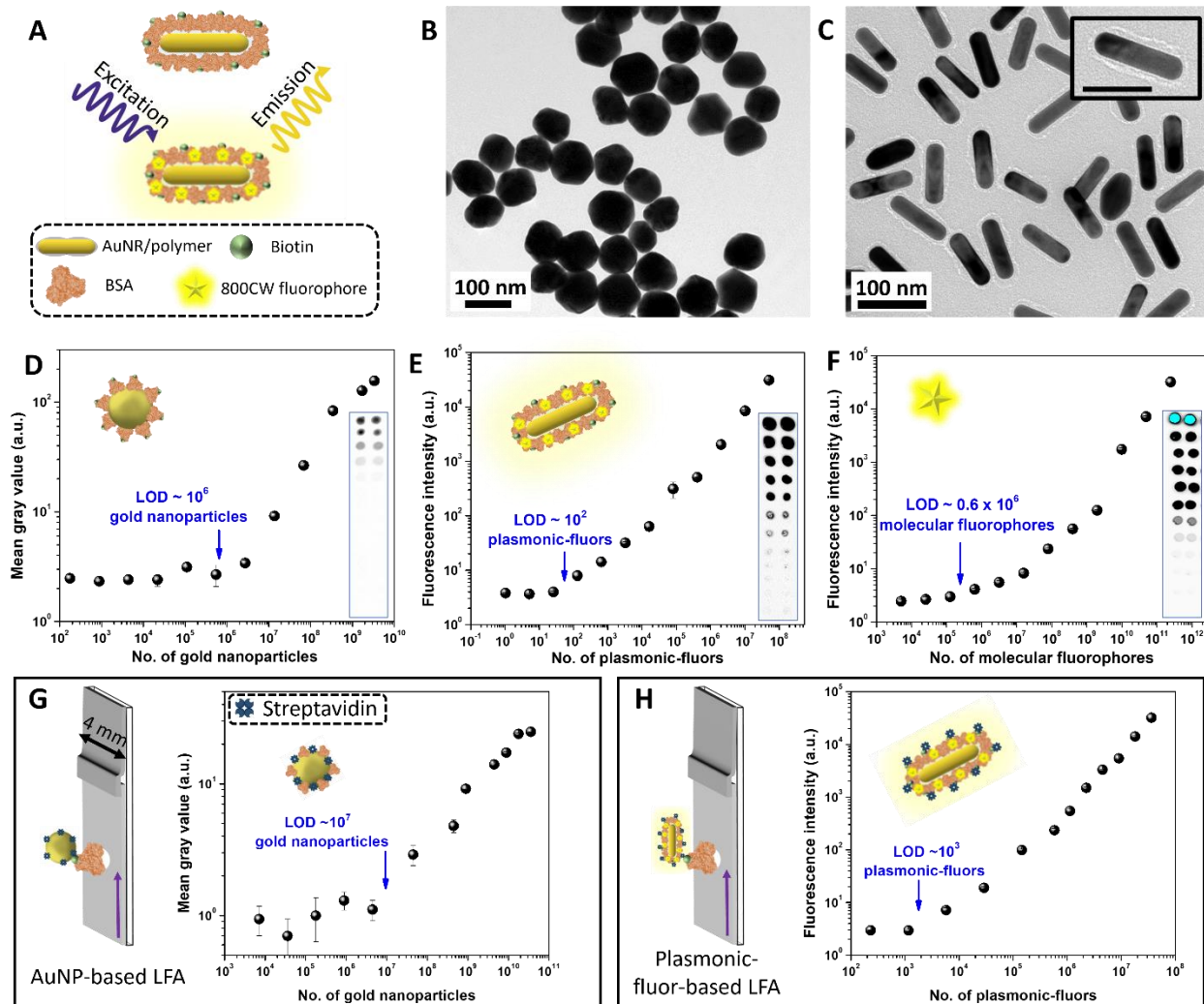


**Figure 7. 1:** Gold nanoparticles and plasmonic-fluors as nanolabels for LFA. (A) Schematic illustration of plasmonic-fluor, employed as a bimodal nanolabel (colorimetric+fluorescent) in LFAs, comprising of gold nanorod as plasmonic core, polymer layer as spacer, molecular fluorophores (800CW), and biotin as recognition element. Transmission electron microscopy image of (B) AuNPs and (C) plasmonic-fluors. (D) Mean gray values obtained from nitrocellulose membrane drop-casted with different concentrations of AuNPs. Inset shows the 8-bit ImageJ-processed image of the nitrocellulose membrane. Fluorescence intensities obtained from nitrocellulose membrane drop-casted with different concentrations of (E) plasmonic-fluors and (F) molecular fluorophores. Inset shows the corresponding fluorescence image of the nitrocellulose membrane. (G) Mean gray values obtained from nitrocellulose membranes, with biotinylated-BSA used as capture-ligand at test sites, after exposure to different concentrations of streptavidin-conjugated AuNPs. Inset shows the schematic illustration of streptavidin-conjugated AuNPs. (H) Fluorescence intensities obtained from nitrocellulose membranes, with biotinylated-BSA as recognition elements at test sites, after exposure to different concentrations of streptavidin-conjugated plasmonic-fluors. Inset shows the schematic illustration of streptavidin-conjugated

plasmonic-fluors. Purple arrows indicate the direction of flow of the nanoconjugates. Error bars represent standard deviations from four different samples (n=4).

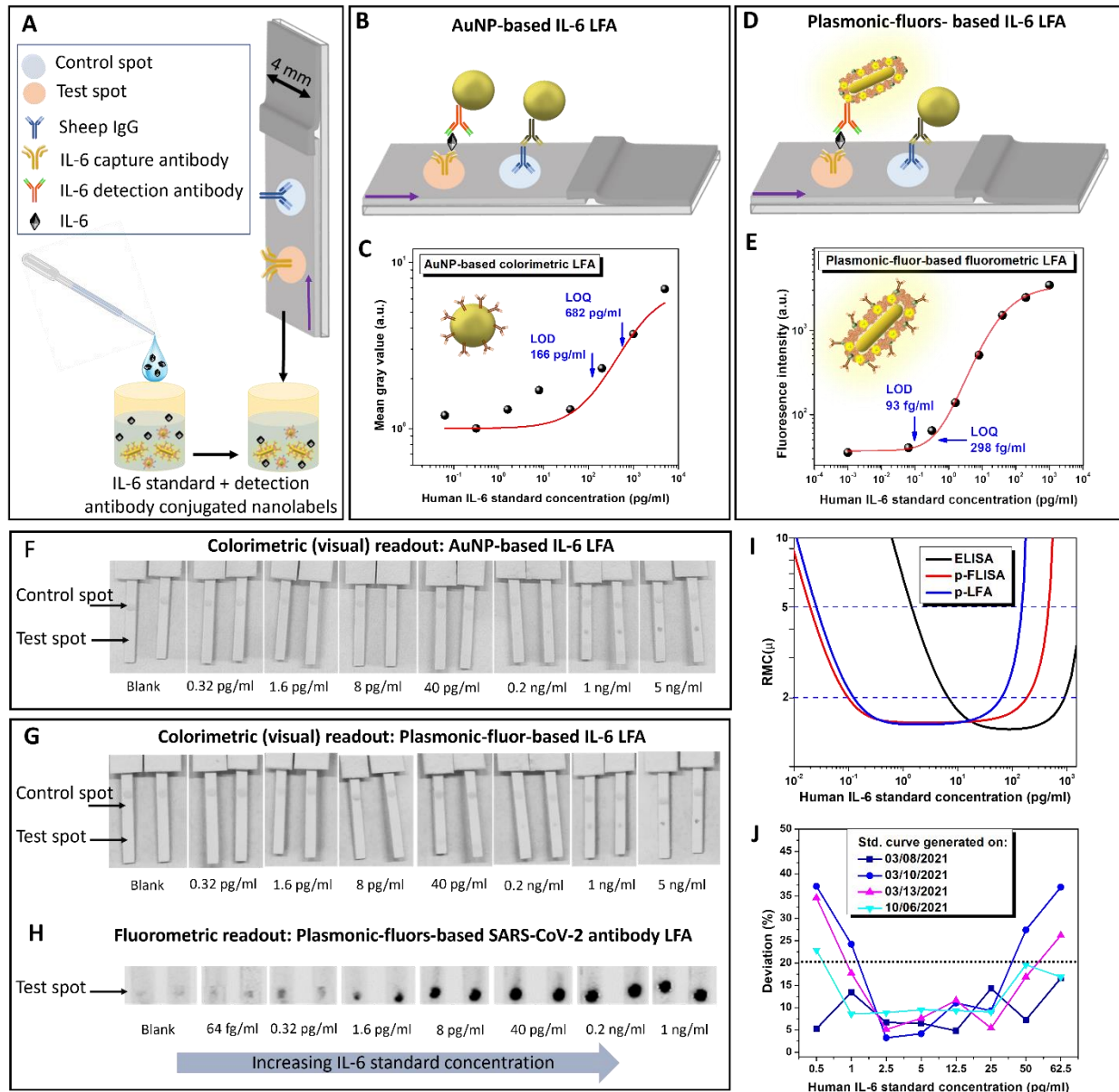


**Figure 7. 2:** Quantitative p-LFA of human IL-6. (A) Schematic illustration of IL-6 LFA strips comprising an IL-6 capture antibody test spot and a sheep IgG control spot. (B) Schematic illustration of AuNP-based IL-6 LFA, and (C) dose-dependent mean gray values, corresponding to different IL-6 concentrations, acquired from these AuNP-based LFAs. (D) Schematic illustration of IL-6 p-LFA and (E) dose-dependent fluorescence intensities of IL-6 p-LFA. 8-bit, ImageJ processed images of (F) AuNP-based IL-6 LFAs and (G) IL-6 p-LFAs, depicting the visual readout mode. (H) Fluorescence images of the IL-6 p-LFA strips depicting the fluorescence readout mode. (I) Resolution of molecular concentration (RMC) curves for ELISA, p-FLISA and p-LFA. The dashed lines indicate RMC cutoffs at  $\mu=2$  and  $\mu=5$ ; intersections of dashed lines and RMC curves indicate the range of concentrations over which a specific quantitative

performance of the assay is achieved. For IL-6 p-LFA,  $\mu < 2$  over a concentration range over of 0.13–86.0 pg/mL, suggesting that IL-6 p-LFA can distinguish signals corresponding to any two concentrations within that range that differ by at least 100% with at least 99% confidence. The relevant RMC parameters are listed in Table S1. **(J)** Stability of IL-6 p-LFA over 7 months, as evidenced by the error in concentration estimates of IL-6 concentration deduced using four different standard curves obtained over a span of seven months.

## 7.5 p-LFA for quantitative detection of human IL-6

Cytokines are small (5-26 kDa) proteins, involved in cell signaling and immunomodulation and are critical indicators of health and disease.<sup>244</sup> Several diseases including cancer, sepsis, HIV, chronic inflammation and auto-immune diseases are known to be associated with dysregulation of immune system, leading to disruption of the subtle balance between pro-inflammatory and anti-inflammatory cytokines.<sup>245-246</sup> The pro-inflammatory cytokines include IL-1 (interleukin-1), IL-6, IL-12, TNF $\alpha$  (tumor necrosis factor  $\alpha$ ) and IFN $\gamma$  (interferon  $\gamma$ ), while the anti-inflammatory cytokines include TGF $\beta$  (transforming growth factor  $\beta$ ), IL-10 and IL-4. Rapid monitoring of the immune status by analyzing serum cytokines and early diagnosis of these diseases is essential for prompt clinical intervention and for inhibiting disease progression. Though few LFAs for IL-6 detection have been introduced recently,<sup>247-248</sup> none provide sensitivity and quantitation comparable to gold-standard ELISA. Therefore, we employed IL-6 as a model target analyte to investigate the applicability of our p-LFA.

Human IL-6 capture antibodies and sheep anti-immunoglobulin G (IgG) antibodies were immobilized on a nitrocellulose membrane to form test and control spots, respectively (**Figure 7.2A, B-14**). The LOD of AuNP-based colorimetric LFA (**Figure 7.2B**) and of molecular fluorophore-based LFA was calculated to be 166 pg ml<sup>-1</sup> (**Figure 7.2C**, five-parameter logistic fit) and 362 pg ml<sup>-1</sup> (**Figure B-15**), respectively. In contrast, the fluorometric p-LFA (**Figure 7.2D**) enabled the detection down to 93 fg ml<sup>-1</sup> (**Figure 7.2E**, five-parameter logistic fit), which

represents a 1785-fold improvement in the LOD compared with conventional AuNP-based LFAs and at least an order magnitude higher than the previously reported LFAs<sup>247-250</sup>. The LOQ of fluorometric p-LFA (298 fg ml<sup>-1</sup>) is 2288-fold better than the LOQ of colorimetric LFA (682 pg ml<sup>-1</sup>). Further, the plasmonic-fluor improved the dynamic range of the LFA by nearly three-order magnitude. The colorimetric signal from both AuNPs and p-LFA exhibited similar LODs, suggesting no loss in visual detection capabilities in p-LFAs (**Figure 7.2F and G, B-16**). Additionally, the fluorescence signal from the plasmonic-fluors enabled ultrasensitive detection and quantitative analysis over a much broader range of analyte concentration (**Figure 7.2E and H**).

We also compared the sensitivity and LOD of fluorometric p-LFA with gold-standard ELISA and plasmonic-fluor linked immunosorbent assay (p-FLISA) implemented on a microtiter plate (**Figure B-17**). The LOD of p-LFA is nearly 30-fold lower compared to conventional sandwich ELISA (2.9 pg ml<sup>-1</sup>) and only 5-fold inferior to that of p-FLISA (16.8 fg ml<sup>-1</sup>) (**Figure B-18**). However, the sample-to-answer time for p-LFAs was 20 min whereas ELISA and p-FLISA require 4 h.

To evaluate the ability of fluorometric p-LFA to accurately resolve changes in concentration of human IL-6, we quantified the resolution of molecular concentration (RMC), a recently introduced metric that indicates whether changes in analyte concentration can be discriminated with statistical significance.<sup>251</sup> This metric is complementary to LOD: whereas the low LOD represents the smallest analyte concentration that can be distinguished from the background, RMC represents the smallest fold change in concentration that can be discriminated with 99% certainty.<sup>251</sup> We compared the RMC of ELISA, p-FLISA and p-LFA for resolution of two-fold changes in concentration of human IL-6 (RMC parameter  $\mu=2$ , meaning a two-fold

change in concentration could be resolved). The RMC curves for p-LFA exhibited  $\mu \leq 2$  over a concentration range of 0.13–86.1 pg/mL, two orders of magnitude lower than that of ELISA (**Figure 7.2I**), and nearly identical to that of p-FLISA. This suggests that IL-6 p-LFA can distinguish signals corresponding to two concentrations that differ by at least 100% within that range with at least 99% confidence. The RMC function and other bioanalytical parameters of p-FLISA and p-LFA, listed in **Table B-1**, indicate that the performance of the 20 min POC-compatible p-LFA is nearly identical to 4 h lab-based p-FLISA.

Next, to establish the stability of fluorometric p-LFA for quantitative detection without the use of standards, multiple IL-6 standard curves were acquired over a span of seven months (**Figure B-19**). All standard curves attained similar RMC (**Figure B-20**) and bioanalytical parameters, suggesting excellent repeatability and reproducibility. Using these standard curves, IL-6 concentrations ranging from 1 pg ml<sup>-1</sup> to 50 pg ml<sup>-1</sup> were quantified with less than 20% deviation (**Figure 7.2J and B-21**).

Overall, the POC assay showed performance comparable to that of the lab-based assay, and showed the ability to accurately quantify the analyte concentration in a standard-free manner. This has not been reported previously with LFA technology, ascertains that p-LFAs overcome the long-standing limitations of LFAs – limited sensitivity, low accuracy and smaller analytical range compared to laboratory tests, and limited quantitation ability.

## 7.6 Ultrasensitive p-LFA for SARS-CoV-2 serology

To assess the potential for clinical translation of our p-LFA, we next optimized it for detection of SARS-CoV-2 antibodies. A pressing need persists for sensitive, rapid and POC serological assays for SARS-CoV-2, both for epidemiological studies and for vaccine efficacy against SARS-CoV-2 studies.<sup>144, 161</sup> Several LFAs<sup>144-145, 252</sup> and other assay methods<sup>253</sup> exist that

employ SARS-CoV-2 spike protein as recognition element for detection of SARS-CoV-2 antibodies. Using p-LFA, our goal was to extend the sensitivity and limit of detection beyond the range possible with current assays, and into the range of ELISA.

Recombinant SARS-CoV-2 S1 subunit of spike protein was immobilized at the test spot and sheep IgG was used for control spot (**Figure 7.3A and B-22**). We first determined the bioanalytical parameters of AuNP-based LFA (**Figure 7.3B**) and p-LFA (**Figure 7.3D**) for detection of SARS-CoV-2 S1 antibody. Using the colorimetric signal obtained from LFA strips, the LOD of AuNP-based LFA was determined to be  $\sim 1.05 \mu\text{g ml}^{-1}$  (**Figure 7.3C**). In contrast, fluorometric p-LFA exhibited an LOD of  $185 \text{ pg ml}^{-1}$  (**Figure 7.3E**, five-parameter logistic fit), which represents a nearly 5675-fold improvement. Further, as expected, the mean grayscale intensities obtained from both AuNP and p-LFA exhibited similar sensitivity, suggesting no compromise in the visual detection capabilities (**Figure 7.3F and 3G, B-23**). However, the fluorescence signal from plasmonic-fluors enabled ultrasensitive detection and quantitative analysis over a much broader (four-orders of magnitude higher) range of analyte concentration (**Figure 7.3E and H**). Fluorometric p-LFA displayed 165-fold improvement in LOD as compared to conventional sandwich ELISA and comparable LOD to p-FLISA (**Figure 7.3I**).

To assess the translational potential of fluorometric p-LFAs, we tested 79 plasma samples obtained from COVID-19 positive individuals and 48 archived de-identified serum/plasma samples which were collected pre-COVID-19 (March-October 2019) under HRPO 201102546<sup>254</sup> for the presence of SARS-CoV-2 S1 antibodies. All 127 plasma samples were diluted 500-fold and tested using fluorometric p-LFA. Out of 79 IgG positive samples (tested positive by ELISA), 76 were tested positive (sample SNR  $\geq$  blank SNR +  $3\sigma$  of blank) with p-LFA, indicating 96.2% sensitivity. All pre-COVID-19 samples tested negative with LFA for SARS-CoV-2 S1 IgGs,

indicating 100% specificity (**Figure 7.3J**). Thus, the p-LFAs for SARS-CoV-2 antibodies detection offers POC applicability with accuracy comparable to gold standard ELISA and with potential applicability to vaccine efficacy and epidemiological studies.

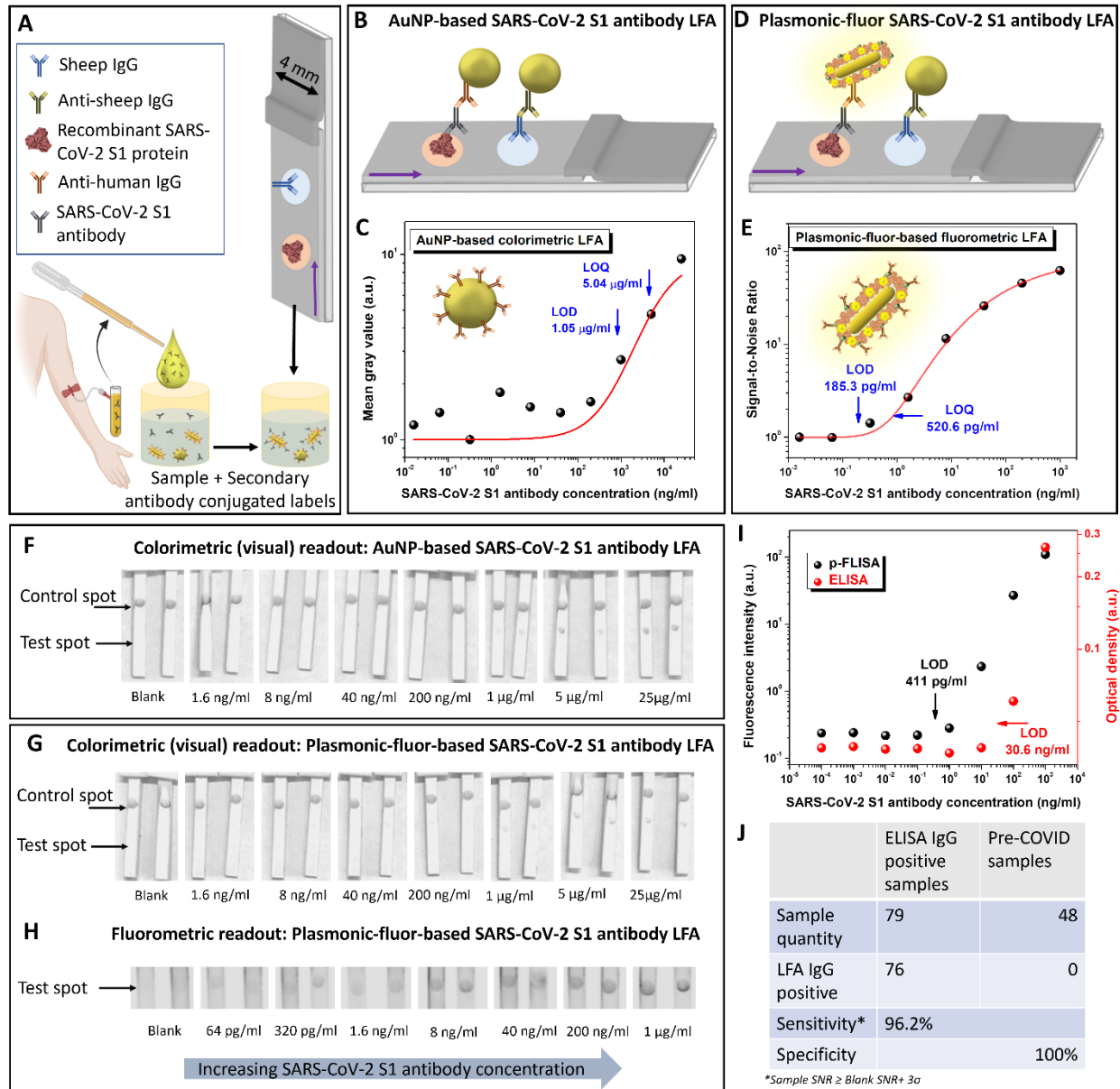


**Figure 7. 3:** SARS-CoV-2 serological p-LFA. (A) Schematic illustration of the SARS-CoV-2 S1 antibody LFA strips comprising recombinant SARS-CoV-2 S1 protein as capture element at the test spot and sheep IgG at the control spot. Schematic illustrations of (B) AuNP-based SARS-CoV-2 S1 antibody LFA and (D) p-LFA. (C) Dose-dependent mean gray values, corresponding to different concentrations of SARS-CoV-2 S1 antibody, acquired from AuNP-based LFA. (E) Dose-dependent signal-to-noise ratio of SARS-CoV-2 S1 antibody p-LFA performed in 20 min. 8-bit ImageJ processed images of (F) AuNP-based SARS-CoV-

2 S1 antibody LFA and (G) SARS-CoV-2 S1 antibody p-LFA, depicting the visual readout mode. (H) Fluorescence images of SARS-CoV-2 S1 antibody p-LFA strips, depicting the fluorescence readout mode. (I) Dose-dependent optical densities and fluorescence intensities, corresponding to different SARS-CoV-2 S1 antibody concentrations, obtained by standard ELISA (red) and p-FLISA (black) implemented on a microtiter plate, performed in 4 h. (J) Table depicting the clinical sensitivity and specificity of the SARS-CoV-2 S1 antibody p-LFA.

## 7.7 p-LFA for SARS-CoV-2 antigen detection

Next, we evaluated the potential of p-LFAs to fill the critical need for a highly sensitive and specific POC SARS-CoV-2 antigen test. In serological testing of virus-specific immunoglobulins, the antibody responses to viral antigens are usually detected in the late stage of infection (7–14 days after virus exposure), therefore serological antibody tests cannot achieve accurate screening of asymptomatic populations or early stages of infection.<sup>255</sup> Further, RT-PCR, the current gold standard in diagnosing COVID-19, has proven highly successful in identifying individuals who have contracted the SARS-CoV-2 virus, however, they may fail to distinguish between infectious patients and noninfectious individual, and may yield false positive results for months even after a patient has recovered from the disease.<sup>115, 117</sup>

Since antigens are expressed only when the virus is actively replicating, the antigen-based tests may have better correlation with infectiousness than RNA detection by RT-PCR. Current antigen detection tests for diagnosing COVID-19 are scalable and convenient but are limited by their low and wide-ranging accuracy.<sup>123, 125, 127-128</sup> LFAs for detection of SARS-CoV-2 antigens can be the most important tool in addressing the infection outbreaks owing to their ease of use, lower-cost and better correlation with infectivity. Currently, several LFA-based antigen<sup>147-148, 256</sup> assays have been reported and are widely used but none offers the optimal sensitivity,<sup>257</sup> thus, a negative result with such assays in a symptomatic patient requires a confirmatory RT-PCR test or



frequent retesting. Therefore, there is an urgent need for a more sensitive POC antigen assay that would be just as reliable and accurate as the RT-PCR method.

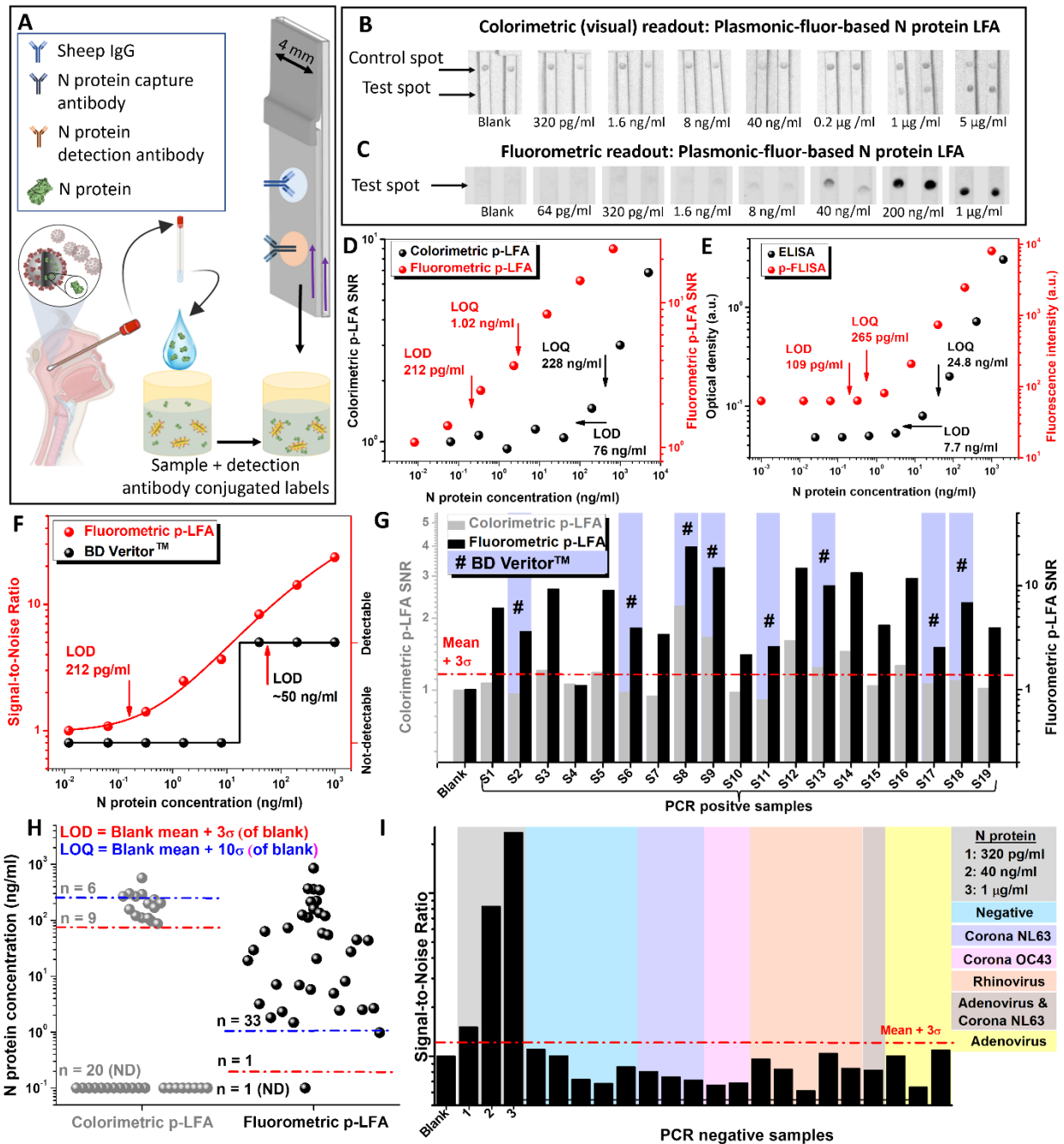


**Figure 7. 4:** p-LFA for SARS-CoV-2 N protein and variants-of-concern. (A) Schematic illustration of the nucleocapsid (N) protein p-LFA strips comprising of N protein capture antibody as test spot and sheep IgG as control spot. (B) Colorimetric and (C) fluorometric readout modes of p-LFA for N protein detection. (D) Dose-dependent mean gray values, corresponding to different concentrations of N protein, acquired from colorimetric p-LFA (black) and dose-dependent signal-to-noise ratio of N protein fluorometric p-LFA

performed in 20 min (red). **(E)** Dose-dependent optical densities and fluorescence intensities, corresponding to different N protein concentrations, obtained by standard ELISA (black) and p-FLISA (red) implemented on a microtiter plate, performed in 4 h. **(F)** Comparison of fluorometric p-LFA (red) and commercial point-of-care rapid antigen kit (BD Veritor™) (black). **(G)** N-protein signal-to-noise ratio in PCR-positive NP swab samples (wild type SARS-CoV-2) determined by colorimetric p-LFA (gray), fluorometric p-LFA (black) and BD Veritor™ (marked with #). **(H)** Comparison of colorimetric (gray) and fluorometric (black) p-LFA in terms of their ability to quantify N protein concentrations present in NP swab samples of 35 PCR-positive samples (19 wild type SARS-CoV-2 and 16 Delta variant). **(I)** N protein signal-to-noise ratio in NP swab samples tested negative for COVID-19 and positive for different seasonal coronaviruses and other respiratory viruses.

p-LFA provided the accuracy and sensitivity needed for this in samples from patients who simultaneously had PCR tests performed. Our test focused on the detection of SARS-CoV-2 nucleocapsid protein (N protein). Test and the control spots on the LFA strips were prepared by immobilizing N protein capture antibodies and sheep IgG, respectively (**Figure 7.4A, B-24**). Both colorimetric and fluorescence signals obtained from p-LFAs increased monotonically with an increase in the concentration of N protein standard (**Figure 7.4B and C**). However, the LOD and LOQ of fluorometric p-LFA were calculated to be nearly 400-fold better than colorimetric counterpart, ascertaining the importance of plasmonic-fluors as ultrabright fluorescent nanolabels (**Figure 7.4D**). Further, fluorometric p-LFA displayed 37-fold improvement in LOD as compared to conventional sandwich ELISA and comparable LOD to p-FLISA (**Figure 7.4E**).

Next, to demonstrate the advantage of p-LFAs over an existing commercial FDA EUA approved rapid, point-of-care antigen testing method, we compared the analytical sensitivity of p-LFAs with BD Veritor™ assay, which indicated samples with concentrations below 50 ng/ml as “Presumptive Negative” (**Figure 7.4F**). This implies that the fluorometric p-LFA offers nearly 235-fold better analytical sensitivity as compared to the commercial antigen test. p-LFA outperformed the FDA-approved BD Veritor™ antigen kit when analyzing PCR-positive COVID-19 patient samples (wild type SARS-CoV-2). BD Veritor™ antigen kit and colorimetric p-LFA correctly identified 8 out of 19 PCR-positive NP swab samples (analytical sensitivity: 42.1%),

whereas fluorometric p-LFA correctly identified 18/19 samples (analytical sensitivity: 94.7%) (**Figure 7.4G**). 13/14 patient samples in the early stage of illness (<10 days since symptoms onset) were tested positive by fluorometric p-LFA (93% sensitivity), while only 7 tested positive by BD Veritor™ (50% sensitivity) (**Table B-2**). Significantly, FDA-approved BD Veritor™ antigen kit can only be used in negative/positive format, however, fluorometric p-LFA enabled quantitative detection of target analyte in patient samples (**Table B-3**). We also compared the quantitative performance of colorimetric and fluorometric p-LFA. While only 3/19 samples were quantifiable (above LOQ) via colorimetric p-LFA, 18/19 samples were quantifiable via fluorometric p-LFA (**Figure 7.4H**).

To further substantiate the clinical translational potential of fluorometric p-LFAs for the detection of N protein, we tested 16 PCR-positive Delta B.1.617.2 variant (confirmed by gene sequencing) NP swab patient samples. Colorimetric p-LFA detected N protein in 7/16 Delta variant positive samples, of which only 3 were quantifiable. However, fluorometric p-LFA detected N protein in all 16 samples, of which 15 were quantifiable (above LOQ) (**Figure 7.4H, B-26, Table B-4**). We also tested 17 PCR-positive Omicron BA.1 (confirmed by gene sequencing) samples and observed that fluorometric p-LFA returned positive results for 16/17 Omicron (**Figure B-27, table B-5**) variant samples. All Omicron-positive patient samples were collected within a short duration from the onset of symptoms (1-2 days) and all, but one patient had very mild illness (**Table B-6**). These findings establish the efficacy of p-LFA in early detection of N protein.

A total of 52 PCR-positive samples was tested. While only 15/52 returned positive result with colorimetric p-LFA, indicating 28.8% clinical sensitivity, 50/52 tested positive with fluorometric p-LFA (SNR > mean + 3 $\sigma$ ), indicating 96.2% analytical sensitivity. The diagnostic

sensitivity of p-LFA for samples with low viral load (cycle threshold (CT) values  $\geq 25$ ) was 91.7% (11 out of 12) and for samples with high viral load (CT values  $< 25$ ) was 97.5% (39 out of 40). This diagnostic sensitivity was significantly higher than those previously reported for rapid antigen/POC SARS-CoV-2 tests (~80% for samples with CT values  $< 25$  and 20-40% for samples with CT values  $\geq 25$ ).<sup>148, 257-259</sup>

Finally, to evaluate the specificity of p-LFA to SARS-CoV-2 N protein, we tested 19 PCR-negative NP swab samples. The negative NP swab samples comprised a mix of healthy samples, and samples tested positive for seasonal coronaviruses and other respiratory viruses. All the 19 PCR-negative samples tested negative (SNR  $<$  mean of blank +  $3\sigma$ ) using p-LFA, suggesting 100% analytical specificity to COVID-19 N protein and no cross-reactivity with different seasonal coronaviruses and other viruses (**Figure 7.4I**). These results substantiate that p-LFAs enable ultrasensitive, accurate, rapid, inexpensive, and point-of-care diagnosis of COVID-19 antigen and antibodies and thus can be a potential tool for rapidly and quantitative diagnosis of symptomatic and asymptomatic infections.

## **7.8 Point-of-care p-LFA using an inexpensive, portable fluorescence scanner**

Finally, to determine the applicability of this biodiagnostic technology in POC settings, we validated the performance of p-LFA using a portable, inexpensive fluorescence scanner. Note that the Stokes shift corresponding to plasmonic-fluors is much smaller (~15 nm) than those corresponding to commonly employed fluorescent nanoparticles such as quantum dots and europium nanoparticles (100s of nm)<sup>260-261</sup>. To the best of our knowledge, no inexpensive, portable fluorescence scanner compatible with plasmonic-fluor is available commercially. Therefore, we

developed an inexpensive portable fluorescence scanner for reading p-LFA employing plasmonic-fluors as nanolabels. The scanner prototype, with dimensions 25 x 25 x 19 cm (LxBxH), was built using routinely available, off-the-shelf optical components (see Methods section for detailed description **Figure 5A, S28**). The total cost of the scanner is \$1429, and the most expensive component is the laser, which costs \$919. It is worth noting that for all the measurements described in this work, the laser (excitation source) power was set to 1% of the maximum power to avoid fluorescence signal saturation. Thus, these components can be miniaturized and replaced with less expensive components for commercialization. Also, the portable scanner can run from a battery and thus can be immediately deployed in resource-limited settings.

We fabricated full-strip LFAs with separate sample and conjugate pads along with test membranes and absorbent pads. The assembled strip was embedded into a standard LFA cassette (**Figure 5B, S29**). Fluorescence measurements were performed by translating the cassette using travel actuator along the optical system of the portable scanner in the direction of the blue arrow in **Figure 5B**. This produced trace of pixel value (signal intensity), averaged from 10 images, versus the travel length of the test membrane, taken in 100  $\mu\text{m}$  increments (**Figure 5C**). Consequently, a valid positive result has peaks at test and control lines, and a negative result has a peak only at the control line. A test without a peak at the control line is considered to be an invalid result (**Figure B-30**).

First, to compare the performance of the portable scanner with the benchtop scanner, we determined the minimum number of nanolabels that could be detected by each scanner. When serially diluted plasmonic-fluors (**Figure 5D, S31**) and 800CW molecular fluorophores (**Figure B-32, S33**) of known concentration were drop-casted on the test membranes, accumulations of  $\sim 100$  plasmonic-fluors were needed to produce detectable fluorescence intensity (mean of blank +

3 $\sigma$ ) when measured using the benchtop scanner, and ~200 plasmonic-fluors were needed for the portable scanner (**Figure 5D**). Accumulations of  $\sim 0.6 \times 10^6$  molecular fluorophores (not plasmonically enhanced) were needed to produce detectable fluorescence intensity when measured using either the benchtop or portable scanner. Data acquired by the portable scanner and subsequent data processing methodology is discussed in detail in the supplementary information (**Figure B-34, S35**). These observations indicate nearly identical performance of the benchtop and portable scanners in detecting the fluorescence signal from plasmonic-fluors.

Next, to demonstrate the POC-compatible workflow of p-LFA and compare the performance of the portable and benchtop scanners, we employed human IL-6 as a model analyte. Human IL-6 capture antibodies and sheep anti-immunoglobulin G (IgG) antibodies were printed on a nitrocellulose membrane to form test and control lines, respectively (**Figure B-36**). The LOD of the colorimetric IL-6 p-LFA in full strip format (**Figure 5E**) was calculated to be  $\sim 526 \text{ pg ml}^{-1}$  (**Figure B-37**). In contrast, the fluorometric p-LFA (**Figure 5F, S38**) enabled the detection down to  $813 \text{ fg ml}^{-1}$  (**Figure 5G in black**, five-parameter logistic fit), measured using the benchtop scanner. Significantly, with the portable scanner, the IL-6 p-LFA exhibited similar LOD,  $916 \text{ fg ml}^{-1}$  (**Figure 5G in red**, five-parameter logistic fit). The near identical performance of benchtop and portable scanners was further confirmed by comparing the N protein dose-response curve (**Figure B-39-41**). Note that the LOD of the full-strip LFAs is higher compared to the half-strip format discussed above due to the shorter time (15 min vs 20 min) and smaller analyte volume (70  $\mu\text{l}$  vs 100  $\mu\text{l}$ ) available for binding of the analytes to the capture antibody conjugated-nanotags in the full-strip format.

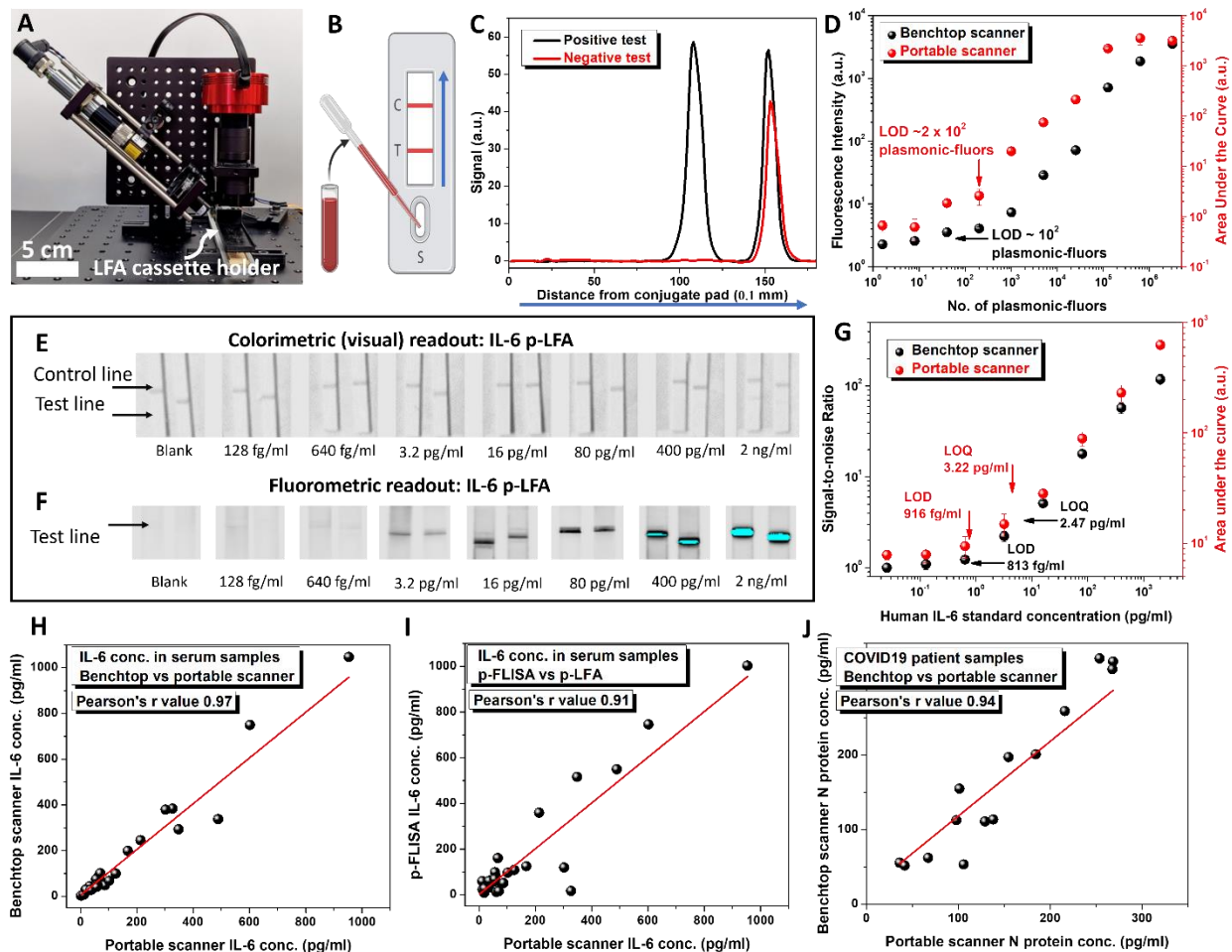


**Figure 7. 5:** Validation of p-LFA using an inexpensive, portable fluorescence scanner. **(A)** Photograph of the portable fluorescence scanner. **(B)** Fluorescence intensities (black spheres) and area under the curve values (red spheres) obtained from LFA strips, drop-casted with different concentrations of plasmonic-fluors, scanned using benchtop and portable scanners. **(C)** Schematic illustration of the LFA cassette employed in the study and the workflow of p-LFA. S, C and T correspond to the sample pad, test line and control line, respectively. The blue arrow represents the direction of the fluorescence measurements made on the LFA cassette using the portable scanner. **(D)** Representative positive (black) and negative (red) signals obtained using the portable scanner. **(E)** 8-bit ImageJ processed image of the full strip IL-6 colorimetric p-LFA depicting the visual readout mode. **(F)** Fluorescence image of the full strip IL-6 fluorometric p-LFA depicting the fluorescence readout mode. **(G)** Dose-dependent signal of 15 min IL-6 fluorometric p-LFA measured by benchtop (black) and portable scanners (red). **(H)** Linear regression plot of IL-6 concentration in serum samples determined by fluorometric p-LFA, and measured benchtop and portable scanners. **(I)** Linear regression plot of IL-6 concentration in serum samples determined by 4 h lab-based p-FLISA and a benchtop fluorescence scanner, compared to measurements made using 15 min fluorometric p-LFA and the portable scanner. **(J)** Linear regression plot of N protein concentration in NP swab samples determined by fluorometric p-LFA and measured using the benchtop and portable scanners.

Finally, to demonstrate the clinical translational potential and the possible POC application of p-LFA with the portable scanner, we tested 28 serum and 14 NP swab samples from COVID-19 PCR-positive individuals for detection of IL-6 (**Figure B-42, S43**) and N protein (**Figure B-44, S45**), respectively. These samples were tested by 15 min p-LFAs and measured using benchtop and portable scanners. Quantitative results from the benchtop and portable scanners exhibited excellent correlation with a Pearson's  $r$  value of 0.97 for IL-6 (**Figure 5H**) and 0.94 for N protein concentrations (**Figure 5J, Table S7**). Equally important, the IL-6 concentrations determined by 15 min p-LFA and measured by the portable scanner also exhibited excellent correlation with those determined by 4 h long lab-based p-FLISA (Pearson's  $r$  value of 0.91) (**Figure 5I, Table S8**).

This observation, along with the nearly identical bioanalytical parameters of the p-LFA standard curve generated using the benchtop and portable scanners for IL-6 and N protein, suggests that the sensitivity and quantitative detection ability of p-LFA is not compromised by the use of an inexpensive, portable fluorescence scanner. Results using this portable scanner were comparable to those obtained using the 4 h long, lab-based tests performed using the expensive, non-portable benchtop fluorescence scanner. These results highlight the simple workflow of p-LFA and its potential for biodiagnostics in POC settings.

## 7.9 Conclusions and Outlook

In summary, plasmonic-fluors were demonstrated as a bimodal (colorimetric+fluorescent) reporter element for overcoming long-standing limitations of LFAs. Specifically, p-LFA overcomes the limited sensitivity, low accuracy, small dynamic range, and limited quantitation ability of LFAs compared to laboratory tests. Plasmonic-fluors produced a discernable fluorescence signal at densities 10000-fold lower than those needed in conventional colorimetric AuNPs. p-LFAs for various analytes (IL-6, SARS-CoV-2 S1 antibodies, and SARS-CoV-2



antigen) exhibited ~1000-fold improvement in bioanalytical parameters (LOD, LOQ and dynamic range) over conventional LFAs. p-LFAs offered standard-free quantitative detection with over 10-fold better sensitivity than that of gold standard ELISA, with a much lower sample-to-answer time (20 min versus 4-6 hours) and similar ability to resolve molecular concentration as lab-based tests. p-LFAs for detection of COVID-19 antibodies and antigens present in plasma and nasopharyngeal swab samples achieved >95% sensitivity and 100% specificity, demonstrating clinical applicability. The inexpensive and portable fluorescence scanner we developed and optimized for reading p-LFA was as effective as the benchtop scanner we used. When applied to human specimens of COVID-19 positive individuals, concentrations of IL-6 and N protein measured for 15 min p-LFAs using the benchtop and portable scanners exhibited excellent correlation with each other, and also with concentrations determined by lab-based 4 h p-FLISA. We believe p-LFAs are highly attractive for realizing POC biodiagnostics that require accurate and quantitative detection of bioanalytes. The technology demonstrated here can be readily adapted for the detection of other infectious pathogens and disease biomarkers, and can complement or even replace laboratory-based tests for the diagnosis of pathogenic infections and other acute conditions.

## **7.10 Supplementary information**

Supplementary information for chapter 7 is provided in appendix b.

# Chapter 8: Conclusions and Outlook

## 8.1 Conclusion

This dissertation demonstrates strategies to solve the fundamental limitations associated with label-free and labelled biosensors in their applicability as POC biosensors. We demonstrate multiple ways to bridge the gap between laboratory-based and at-home or point-of-care (POC) diagnosis. At the heart of all solutions and strategies discussed lies plasmonic nanomaterials. For instance, in one of our proof-of-concept study, we introduces a novel plasmonic paper MN patch for SERS-based detection of molecules present in ISF. The plasmonic paper MN patch is minimally invasive, rapid, and simple-to-use. The MN patch also has the capability to perform on-patch SERS-based detection of molecules in ISF using a paper reservoir that captures molecules with functionalized AuNRs. This is significant as it offers a facile two-step process as opposed conventional approach such as suction blister, microdialysis and open flow microperfusion cause significant skin trauma, which are time consuming and require expert personnel and equipment to perform. Thus, a plasmonic paper MN patch could be a low-cost, portable, miniature diagnostic device suitable for point-of-care treatment in resource-limited environments.

Employing another unique optical property of plasmonic nanoparticles, LSPR, we demonstrate a simple paper-based biosensor for sensitive and quantitative detection of renal cancer. There are no current cost-effective high-throughput means of identifying individuals with RCC. Our assay could be of importance in identifying those with RCC in military bases or autoworker cohorts or other populations. Additionally, this assay would enable the differential diagnosis of imaged renal masses and could be useful in point-of-care settings such as hospital

radiology departments and stand-alone imaging clinics. Therefore, plasmonic paper serves as a simple and versatile platform for implementing plasmonic biosensors and fills critical gap in diagnosis of renal cancer.

Employing LSPR-based biosensor, we introduce a solution to overcome a long-standing problem associated with POC biosensors – poor long-term stability and usability. We introduced a facile and universal method based on *in situ* polymerization of an organosilica layer for preserving the biorecognition capabilities of immobilized antibodies of the biosensor. The encapsulation-based preservation method demonstrated overcomes a critical challenge in wearable and implantable biosensors and is expected to advance the design and implementation of wearable biosensors for long-term monitoring of protein biomarkers.

In another unique demonstration of application of plasmonic nanoparticles, we demonstrate a novel strategy to quantitatively detect inflammatory disease burden by determining the concentration of collagenase in biospecimen. Traditional techniques to determine collagenase concentration involve resource extensive and multistep detection process which makes the whole procedure time consuming and tedious. For instance, current detection methods of periodontal disease rely on mechanical assessment of pocket depth and radiographic detection of bone deterioration.<sup>217</sup> By the time the disease is diagnosed, it is often too late to reverse the condition making the process both laborious and not sensitive enough. We demonstrate that the collagen plasmonic foam offers much simpler, faster, and highly sensitive detection technique.

Finally, in the last two chapters of this dissertation we improve the bioanalytical parameters of the labelled (sandwich) immunoassays, again by employing plasmonic nanoparticles. We introduced a simple and ultrasensitive digital fluoro-immunoassay for the detection of protein biomarkers. The digital assay that is implemented in standard microtiter wells relies on an

ultrabright fluorescent nanolabel, plasmonic-fluor, that can be imaged and counted using standard fluorescence microscopes. The digital assay with a workflow that is identical to that of ELISA exhibited over 5000-fold lower limit-of-detection across multiple protein analytes. As such, digital p-FLISA has the potential to alleviate the bottlenecks of molecular tests, including expensive equipment, technological expertise, and inherent difficulty to scale up.

We demonstrate that by employing plasmonic nanomaterials we can overcome decade-long fundamental challenges associated with the lateral flow assays, which are the cornerstone of POC diagnosis. We introduced plasmon-enhanced lateral flow assays which exhibited ~1000-fold improvement in bioanalytical parameters over conventional LFAs. p-LFAs offered standard-free quantitative detection with over 10-fold better sensitivity than that of gold-standard ELISA, with a much lower sample-to-answer time (20 min versus 4-6 hours) and similar ability to resolve molecular concentration as lab-based tests. We also demonstrated a complete workflow of p-LFA in POC and resource-limited settings by use of an inexpensive portable fluorescence scanner. When tested with human specimens, our 15 min p-LFA technology exhibited strong correlation with lab-based 4 h p-FLISA. This ascertains that p-LFAs overcome the long-standing limitations of LFAs – limited sensitivity, low accuracy and smaller analytical range compared to laboratory tests, and limited quantitation ability.

Taken together, these advances are expected to overcome fundamental challenges associated with POC biosensors and offers POC diagnostic platform that outperforms standard laboratory tests in sensitivity, speed, dynamic range, ease of use, and cost.

## **8.2 Outlook**

The plasmonic paper MN patch involves a simple, low-cost design using readily available materials. The MN array is fabricated from stainless steel sheets by chemical etching, which can

be performed in mass production for pennies per array. The paper reservoir is made of conventional filter paper that has high surface area, is low-cost, is biodegradable, is compatible with conventional printing approaches and is commonly used in paper-based sensor devices. The plasmonic calligraphy method controls test domain size in a simple manner by writing with a pen in the desired area. This method also offers the possibility for multiplexed biosensing of multiple biomarkers by simply ‘writing’ different test domains with plasmonic nanostructures functionalized to target different biomarkers of clinical significance. The manufacturing process is scalable due to possibility of inkjet printing of the plasmonic inks onto the paper. The next steps in this research include optimization of the MN patch for usability, safety and efficacy and development of the sensor for LSPR or SERS-based detection of biomolecules of clinical significance in ISF for future possible medical applications.

Plasmonic paper serves as a simple and versatile platform for implementing plasmonic biosensors. Due to the high sensitivity of the assay, and lack of potential interference by albuminuria or hematuria, urine PLIN-2 concentrations in normal individuals could be accurately measured, and there was a clear difference in urine PLIN-2 concentrations among normal individuals, patients with bladder cancer, patients with diabetic nephropathy, and patients with a pathologically proven clear cell carcinoma. A limitation of the study is the small number of patients in this proof-of-concept analysis. A larger multicenter blinded study incorporating patients with a wide variety of noncancerous kidney diseases, more patients with cancerous urologic diseases, and many more control individuals would be necessary to validate this assay. Future prospective studies are needed to validate this bioplasmonic paper-based assay in population screening and to differentially diagnose imaged renal masses on a larger scale.

Polymer encapsulated antibodies on plasmonic nanostructures exhibited remarkable stability over multiple capture/release cycles, thus enabling refreshability of the biochips. In this study, we have employed a plasmonic biosensor as a transduction platform and SDS treatment as a method to overcome the antibody-antigen interaction. However, the encapsulation approach can be easily extended to other transduction platforms and other possible sensor refreshing methods. More specifically, although the SDS-based sensor refreshing strategy offers a rather narrow application window, primarily limited to implantable in the oral cavity, the polymer-based preservation method demonstrated here is universal and thus can be applied with other biosensors especially in case of wearable and implantable biosensors.

Finally, this dissertation offers a universal solution to improve the bioanalytical parameters of LFA by orders of magnitude. We believe that p-LFAs are highly attractive for realizing POC biodiagnostics for accurate and quantitative detection of bioanalytes. The technology demonstrated here can be readily adapted for the detection of other infectious pathogens and disease biomarkers, and can complement or even replace laboratory-based tests for the diagnosis of pathogenic infections and other acute conditions.

# References

1. Vashist, S. K.; Luppa, P. B.; Yeo, L. Y.; Ozcan, A.; Luong, J. H., Emerging technologies for next-generation point-of-care testing. *Trends in biotechnology* **2015**, *33* (11), 692-705.
2. Deacon, B.; Abramowitz, J., Fear of needles and vasovagal reactions among phlebotomy patients. *J. Anxiety Disord.* **2006**, *20* (7), 946-960.
3. Anderson, N. L.; Anderson, N. G., The human plasma proteome history, character, and diagnostic prospects. *Mol. Cell. Proteomics* **2002**, *1* (11), 845-867.
4. Niedzwiecki, M. M.; Samant, P.; Walker, D. I.; Tran, V.; Jones, D. P.; Prausnitz, M. R.; Miller, G. W., Human Suction Blister Fluid Composition Determined Using High-Resolution Metabolomics. *Anal. Chem.* **2018**, *90* (6), 3786-3792.
5. Tran, B. Q.; Miller, P. R.; Taylor, R. M.; Boyd, G.; Mach, P. M.; Rosenzweig, C. N.; Baca, J. T.; Polsky, R.; Glaros, T., Proteomic Characterization of Dermal Interstitial Fluid Extracted Using a Novel Microneedle-Assisted Technique. *J. Proteome Res.* **2017**, *17* (1), 479-485.
6. Celis, J. E.; Gromov, P.; Cabezón, T.; Moreira, J. M.; Ambartsumian, N.; Sandelin, K.; Rank, F.; Gromova, I., Proteomic characterization of the interstitial fluid perfusing the breast tumor microenvironment A novel resource for biomarker and therapeutic target discovery. *Mol. Cell. Proteomics* **2004**, *3* (4), 327-344.
7. Kastellorizios, M.; Burgess, D. J., Continuous metabolic monitoring based on multi-analyte biomarkers to predict exhaustion. *Sci. Rep.* **2015**, *5*, 10603.
8. Kiistala, U.; Mustakallio, K., Dermo-epidermal separation with suction: electron microscopic and histochemical study of initial events of blistering on human skin. *J. Invest. Dermatol.* **1967**, *48* (5), 466-477.
9. Sieg, A.; Guy, R. H.; Delgado-Charro, M. B., Noninvasive glucose monitoring by reverse iontophoresis in vivo: application of the internal standard concept. *Clin. Chem.* **2004**, *50* (8), 1383-1390.
10. Schmidt, S.; Banks, R.; Kumar, V.; Rand, K. H.; Derendorf, H., Clinical microdialysis in skin and soft tissues: an update. *J. Clin. Pharmacol.* **2008**, *48* (3), 351-364.
11. Ellmerer, M.; Schaupp, L.; Brunner, G. A.; Sendlhofer, G.; Wutte, A.; Wach, P.; Pieber, T. R., Measurement of interstitial albumin in human skeletal muscle and adipose tissue by open-flow microperfusion. *American Journal of Physiology-Endocrinology and Metabolism* **2000**, *278* (2), E352-E356.

12. Donnelly, R. F.; Mooney, K.; Caffarel-Salvador, E.; Torrasi, B. M.; Eltayib, E.; McElnay, J. C., Microneedle-mediated minimally invasive patient monitoring. *Ther. Drug Monit.* **2014**, *36* (1), 10-17.
13. El-Laboudi, A.; Oliver, N. S.; Cass, A.; Johnston, D., Use of microneedle array devices for continuous glucose monitoring: a review. *Diabetes Technol. Ther.* **2013**, *15* (1), 101-115.
14. Prausnitz, M. R., Engineering microneedle patches for vaccination and drug delivery to skin. *Annu. Rev. Chem. Biomol. Eng.* **2017**, *8*, 177-200.
15. Nguyen, T. T.; Park, J. H., Human studies with microneedles for evaluation of their efficacy and safety. *Expert Opin. Drug Delivery* **2018**, *15* (3), 235-245.
16. Marshall, S.; Sahn, L. J.; Moore, A. C., The success of microneedle-mediated vaccine delivery into skin. *Hum. Vaccines Immunother.* **2016**, *12* (11), 2975-2983.
17. Samant, P. P.; Prausnitz, M. R., Mechanisms of sampling interstitial fluid from skin using a microneedle patch. *Proc. Natl. Acad. Sci.* **2018**, *115*, 4583.
18. Wang, P. M.; Cornwell, M.; Prausnitz, M. R., Minimally invasive extraction of dermal interstitial fluid for glucose monitoring using microneedles. *Diabetes Technol. Ther.* **2005**, *7* (1), 131-141.
19. Chang, H.; Zheng, M.; Yu, X.; Than, A.; Seeni, R. Z.; Kang, R.; Tian, J.; Khanh, D. P.; Liu, L.; Chen, P., A Swellable Microneedle Patch to Rapidly Extract Skin Interstitial Fluid for Timely Metabolic Analysis. *Adv. Mater.* **2017**, *29* (37).
20. Caffarel-Salvador, E.; Brady, A. J.; Eltayib, E.; Meng, T.; Alonso-Vicente, A.; Gonzalez-Vazquez, P.; Torrasi, B. M.; Vicente-Perez, E. M.; Mooney, K.; Jones, D. S., Hydrogel-forming microneedle arrays allow detection of drugs and glucose in vivo: potential for use in diagnosis and therapeutic drug monitoring. *PLoS one* **2015**, *10* (12), e0145644.
21. Garg, S. K.; Potts, R. O.; Ackerman, N. R.; Fermi, S. J.; Tamada, J. A.; Chase, H. P., Correlation of fingerstick blood glucose measurements with GlucoWatch biographer glucose results in young subjects with type 1 diabetes. *Diabetes Care* **1999**, *22* (10), 1708-1714.
22. Taylor, R. M.; Miller, P. R.; Ebrahimi, P.; Polsky, R.; Baca, J. T., Minimally-invasive, microneedle-array extraction of interstitial fluid for comprehensive biomedical applications: transcriptomics, proteomics, metabolomics, exosome research, and biomarker identification. *Laboratory animals* **2018**, 0023677218758801.
23. Coffey, J. W.; Meliga, S. C.; Corrie, S. R.; Kendall, M. A., Dynamic application of microprojection arrays to skin induces circulating protein extravasation for enhanced biomarker capture and detection. *Biomater.* **2016**, *84*, 130-143.



24. Muller, D. A.; Corrie, S. R.; Coffey, J.; Young, P. R.; Kendall, M. A., Surface modified microprojection arrays for the selective extraction of the dengue virus NS1 protein as a marker for disease. *Anal. Chem.* **2012**, *84* (7), 3262-3268.
25. Miller, P. R.; Xiao, X.; Brener, I.; Burckel, D. B.; Narayan, R.; Polsky, R., Microneedle-Based Transdermal Sensor for On-Chip Potentiometric Determination of K<sup>+</sup>. *Adv. Healthcare Mater.* **2014**, *3* (6), 876-881.
26. Rebrin, K.; Sheppard Jr, N. F.; Steil, G. M., Use of subcutaneous interstitial fluid glucose to estimate blood glucose: revisiting delay and sensor offset. SAGE Publications Sage CA: Los Angeles, CA: 2010.
27. Venugopal, M.; Feuvrel, K. E.; Mongin, D.; Bambot, S.; Faupel, M.; Panangadan, A.; Talukder, A.; Pidva, R., Clinical evaluation of a novel interstitial fluid sensor system for remote continuous alcohol monitoring. *IEEE Sens. J.* **2008**, *8* (1), 71-80.
28. Stiles, P. L.; Dieringer, J. A.; Shah, N. C.; Van Duyne, R. P., Surface-enhanced Raman spectroscopy. *Annu. Rev. Anal. Chem.* **2008**, *1*, 601-626.
29. Kneipp, K.; Wang, Y.; Kneipp, H.; Perelman, L. T.; Itzkan, I.; Dasari, R. R.; Feld, M. S., Single molecule detection using surface-enhanced Raman scattering (SERS). *Physical review letters* **1997**, *78* (9), 1667.
30. Jain, P. K.; Lee, K. S.; El-Sayed, I. H.; El-Sayed, M. A., Calculated absorption and scattering properties of gold nanoparticles of different size, shape, and composition: applications in biological imaging and biomedicine. *The journal of physical chemistry B* **2006**, *110* (14), 7238-7248.
31. Kelly, K. L.; Coronado, E.; Zhao, L. L.; Schatz, G. C., The optical properties of metal nanoparticles: the influence of size, shape, and dielectric environment. ACS Publications: 2003.
32. Schlücker, S., Surface-Enhanced raman spectroscopy: Concepts and chemical applications. *Angewandte Chemie International Edition* **2014**, *53* (19), 4756-4795.
33. Rosi, N. L.; Mirkin, C. A., Nanostructures in biodiagnostics. *Chemical reviews* **2005**, *105* (4), 1547-1562.
34. Stuart, D. A.; Yuen, J. M.; Shah, N.; Lyandres, O.; Yonzon, C. R.; Glucksberg, M. R.; Walsh, J. T.; Van Duyne, R. P., In vivo glucose measurement by surface-enhanced Raman spectroscopy. *Analytical chemistry* **2006**, *78* (20), 7211-7215.
35. Ma, K.; Yuen, J. M.; Shah, N. C.; Walsh Jr, J. T.; Glucksberg, M. R.; Van Duyne, R. P., In vivo, transcutaneous glucose sensing using surface-enhanced spatially offset Raman spectroscopy: multiple rats, improved hypoglycemic accuracy, low incident power, and

- continuous monitoring for greater than 17 days. *Analytical chemistry* **2011**, 83 (23), 9146-9152.
36. Zhang, H.; Harpster, M. H.; Park, H. J.; Johnson, P. A.; Wilson, W. C., Surface-enhanced Raman scattering detection of DNA derived from the West Nile virus genome using magnetic capture of Raman-active gold nanoparticles. *Analytical chemistry* **2010**, 83 (1), 254-260.
  37. Wang, G.; Lipert, R. J.; Jain, M.; Kaur, S.; Chakraborty, S.; Torres, M. P.; Batra, S. K.; Brand, R. E.; Porter, M. D., Detection of the potential pancreatic cancer marker MUC4 in serum using surface-enhanced Raman scattering. *Analytical chemistry* **2011**, 83 (7), 2554-2561.
  38. Lee, C. H.; Tian, L.; Singamaneni, S., based SERS swab for rapid trace detection on real-world surfaces. *ACS applied materials & interfaces* **2010**, 2 (12), 3429-3435.
  39. Polavarapu, L.; Liz-Marzán, L. M., Towards low-cost flexible substrates for nanoplasmonic sensing. *Physical Chemistry Chemical Physics* **2013**, 15 (15), 5288-5300.
  40. Lee, C. H.; Hankus, M. E.; Tian, L.; Pellegrino, P. M.; Singamaneni, S., Highly Sensitive Surface Enhanced Raman Scattering Substrates Based on Filter Paper Loaded with Plasmonic Nanostructures. *Analytical Chemistry* **2011**, 83 (23), 8953-8958.
  41. Abbas, A.; Brimer, A.; Slocik, J. M.; Tian, L.; Naik, R. R.; Singamaneni, S., Multifunctional Analytical Platform on a Paper Strip: Separation, Preconcentration, and Subattomolar Detection. *Analytical Chemistry* **2013**, 85 (8), 3977-3983.
  42. Jiang, Q.; Chandar, Y. J.; Cao, S.; Kharasch, E. D.; Singamaneni, S.; Morrissey, J. J., Rapid, Point-of-Care, Paper-Based Plasmonic Biosensor for Zika Virus Diagnosis. *Advanced Biosystems* **2017**, 1 (9), 1700096.
  43. Tian, L.; Morrissey, J. J.; Kattumenu, R.; Gandra, N.; Kharasch, E. D.; Singamaneni, S., Bioplasmonic paper as a platform for detection of kidney cancer biomarkers. *Analytical chemistry* **2012**, 84 (22), 9928-9934.
  44. Li, T.; Vongehr, S.; Tang, S.; Dai, Y.; Huang, X.; Meng, X., Scalable Synthesis of Ag Networks with Optimized Sub-monolayer Au-Pd Nanoparticle Covering for Highly Enhanced SERS Detection and Catalysis. *Scientific reports* **2016**, 6, 37092.
  45. Novo, C.; Funston, A. M.; Mulvaney, P., Direct observation of chemical reactions on single gold nanocrystals using surface plasmon spectroscopy. *Nature nanotechnology* **2008**, 3 (10), 598-602.
  46. Shao, Q.; Wu, P.; Gu, P.; Xu, X.; Zhang, H.; Cai, C., Electrochemical and spectroscopic studies on the conformational structure of hemoglobin assembled on gold nanoparticles. *The journal of physical chemistry. B* **2011**, 115 (26), 8627-37.

47. Sun, Y.; Xia, Y., Gold and silver nanoparticles: a class of chromophores with colors tunable in the range from 400 to 750 nm. *The Analyst* **2003**, *128* (6), 686-91.
48. Luan, J.; Liu, K. K.; Tadepalli, S.; Jiang, Q.; Morrissey, J. J.; Kharasch, E. D.; Singamaneni, S., PEGylated Artificial Antibodies: Plasmonic Biosensors with Improved Selectivity. *ACS applied materials & interfaces* **2016**, *8* (36), 23509-16.
49. Miller, K. D.; Siegel, R. L.; Lin, C. C.; Mariotto, A. B.; Kramer, J. L.; Rowland, J. H.; Stein, K. D.; Alteri, R.; Jemal, A., Cancer treatment and survivorship statistics, 2016. *CA: a cancer journal for clinicians* **2016**, *66* (4), 271-89.
50. Petersen, A. C.; Sogaard, M.; Mehnert, F.; Larsen, E. H.; Donskov, F.; Azawi, N. H.; Kromann-Andersen, B., The database of the Danish Renal Cancer Group. *Clinical epidemiology* **2016**, *8*, 725-729.
51. Akdogan, B.; Gudeloglu, A.; Inci, K.; Gunay, L. M.; Koni, A.; Ozen, H., Prevalence and predictors of benign lesions in renal masses smaller than 7 cm presumed to be renal cell carcinoma. *Clinical genitourinary cancer* **2012**, *10* (2), 121-5.
52. Johnson, D. C.; Vukina, J.; Smith, A. B.; Meyer, A. M.; Wheeler, S. B.; Kuo, T. M.; Tan, H. J.; Woods, M. E.; Raynor, M. C.; Wallen, E. M.; Pruthi, R. S.; Nielsen, M. E., Preoperatively misclassified, surgically removed benign renal masses: a systematic review of surgical series and United States population level burden estimate. *The Journal of urology* **2015**, *193* (1), 30-5.
53. Leao, R. R.; Richard, P. O.; Jewett, M. A., The role of biopsy for small renal masses. *International journal of surgery* **2016**, *36* (Pt C), 513-517.
54. Sfoungaristos, S.; Giannitsas, K.; Perimenis, P., Present and future therapeutic options for locally advanced and metastatic renal cell carcinoma. *Expert opinion on pharmacotherapy* **2011**, *12* (4), 533-47.
55. Thorstenson, A.; Bergman, M.; Scherman-Plogell, A. H.; Hosseinnia, S.; Ljungberg, B.; Adolfsson, J.; Lundstam, S., Tumour characteristics and surgical treatment of renal cell carcinoma in Sweden 2005-2010: a population-based study from the national Swedish kidney cancer register. *Scandinavian journal of urology* **2014**, *48* (3), 231-8.
56. Morrissey, J. J.; Kharasch, E. D., The specificity of urinary aquaporin 1 and perilipin 2 to screen for renal cell carcinoma. *The Journal of urology* **2013**, *189* (5), 1913-20.
57. Morrissey, J. J.; London, A. N.; Luo, J.; Kharasch, E. D., Urinary biomarkers for the early diagnosis of kidney cancer. *Mayo Clinic proceedings* **2010**, *85* (5), 413-21.
58. Morrissey, J. J.; Mellnick, V. M.; Luo, J.; Siegel, M. J.; Figenschau, R. S.; Bhayani, S.; Kharasch, E. D., Evaluation of Urine Aquaporin-1 and Perilipin-2 Concentrations as

- Biomarkers to Screen for Renal Cell Carcinoma: A Prospective Cohort Study. *JAMA oncology* **2015**, *1* (2), 204-12.
59. Morrissey, J. J.; Mobley, J.; Figenshau, R. S.; Vetter, J.; Bhayani, S.; Kharasch, E. D., Urine aquaporin 1 and perilipin 2 differentiate renal carcinomas from other imaged renal masses and bladder and prostate cancer. *Mayo Clinic proceedings* **2015**, *90* (1), 35-42.
  60. Morrissey, J. J.; Mobley, J.; Song, J.; Vetter, J.; Luo, J.; Bhayani, S.; Figenshau, R. S.; Kharasch, E. D., Urinary concentrations of aquaporin-1 and perilipin-2 in patients with renal cell carcinoma correlate with tumor size and stage but not grade. *Urology* **2014**, *83* (1), 256 e9-14.
  61. Gao, W.; Emaminejad, S.; Nyein, H. Y. Y.; Challa, S.; Chen, K.; Peck, A.; Fahad, H. M.; Ota, H.; Shiraki, H.; Kiriya, D., Fully Integrated Wearable Sensor Arrays for Multiplexed In situ Perspiration Analysis. *Nature* **2016**, *529* (7587), 509-514.
  62. Bandodkar, A. J.; Jia, W.; Yardımcı, C.; Wang, X.; Ramirez, J.; Wang, J., Tattoo-based Noninvasive Glucose Monitoring: a proof-of-concept study. *Anal. Chem.* **2014**, *87* (1), 394-398.
  63. Koh, A.; Kang, D.; Xue, Y.; Lee, S.; Pielak, R. M.; Kim, J.; Hwang, T.; Min, S.; Banks, A.; Bastien, P., A soft, Wearable Microfluidic Device for the Capture, Storage, and Colorimetric Sensing of Sweat. *Sci. Transl. Med.* **2016**, *8* (366), 366ra165.
  64. Lee, H.; Choi, T. K.; Lee, Y. B.; Cho, H. R.; Ghaffari, R.; Wang, L.; Choi, H. J.; Chung, T. D.; Lu, N.; Hyeon, T., A graphene-based electrochemical device with thermoresponsive microneedles for diabetes monitoring and therapy. *Nat. Nanotech.* **2016**, *11* (6), 566-572.
  65. Mannoor, M. S.; Tao, H.; Clayton, J. D.; Sengupta, A.; Kaplan, D. L.; Naik, R. R.; Verma, N.; Omenetto, F. G.; McAlpine, M. C., Graphene-based Wireless Bacteria Detection on Tooth Enamel. *Nat. Comm.* **2012**, *3*, 763-770.
  66. Kim, J.; Campbell, A. S.; de Ávila, B. E.-F.; Wang, J., Wearable Biosensors for Healthcare Monitoring. *Nat. Biotech.* **2019**, *37* (4), 389-406.
  67. Kelly, K. L.; Coronado, E.; Zhao, L. L.; Schatz, G. C., The Optical Properties of Metal Nanoparticles: The Influence of Size, Shape, and Dielectric Environment. *J. Phys. Chem. B* **2003**, *107* (3), 668-677.
  68. Stewart, M. E.; Anderton, C. R.; Thompson, L. B.; Maria, J.; Gray, S. K.; Rogers, J. A.; Nuzzo, R. G., Nanostructured Plasmonic Sensors. *Chem. Rev.* **2008**, *108* (2), 494-521.
  69. Willets, K. A.; Van Duyne, R. P., Localized Surface Plasmon Resonance Spectroscopy and Sensing. *Annu. Rev. Phys. Chem.* **2007**, *58*, 267-297.

70. Mayer, K. M.; Hao, F.; Lee, S.; Nordlander, P.; Hafner, J. H., A Single Molecule Immunoassay by Localized Surface Plasmon Resonance. *Nanotechnology* **2010**, *21* (25), 255503.
71. Mayer, K. M.; Lee, S.; Liao, H.; Rostro, B. C.; Fuentes, A.; Scully, P. T.; Nehl, C. L.; Hafner, J. H., A Label-free Immunoassay Based Upon Localized Surface Plasmon Resonance of Gold Nanorods. *ACS Nano* **2008**, *2* (4), 687-692.
72. Olkhov, R. V.; Fowke, J. D.; Shaw, A. M., Whole Serum BSA Antibody Screening Using a Label-free Biophotonic Nanoparticle Array. *Anal. Biochem.* **2009**, *385* (2), 234-241.
73. Mayer, K. M.; Hafner, J. H., Localized Surface Plasmon Resonance Sensors. *Chem. Rev.* **2011**, *111* (6), 3828-3857.
74. Kolluru, C.; Gupta, R.; Jiang, Q.; Williams, M.; Gholami Derami, H.; Cao, S.; Noel, R.; Singamaneni, S.; Prausnitz, M. R., Plasmonic Paper Microneedle Patch for on-patch Detection of Molecules in Dermal Interstitial Fluid. *ACS Sens.* **2019**, *4* (6), 1569-1576.
75. Hu, R.; Gupta, R.; Wang, Z.; Wang, C.; Sun, H.; Singamaneni, S.; Kharasch, E. D.; Morrissey, J. J., Bioplasmonic Paper-based Assay for Perilipin-2 Non-invasively Detects Renal Cancer. *Kidney Int.* **2019**, *96* (6), 1417-1421.
76. Wang, C.; Sudlow, G.; Wang, Z.; Cao, S.; Jiang, Q.; Neiner, A.; Morrissey, J. J.; Kharasch, E. D.; Achilefu, S.; Singamaneni, S., Metal-Organic Framework Encapsulation Preserves the Bioactivity of Protein Therapeutics. *Adv. Healthcare Mater.* **2018**, *7* (22), 1800950.
77. Wang, C.; Tadepalli, S.; Luan, J.; Liu, K. K.; Morrissey, J. J.; Kharasch, E. D.; Naik, R. R.; Singamaneni, S., Metal-Organic Framework as a Protective Coating for Biodiagnostic Chips. *Adv. Mater.* **2017**, *29* (7), 1604433.
78. Wang, C.; Wang, L.; Tadepalli, S.; Morrissey, J. J.; Kharasch, E. D.; Naik, R. R.; Singamaneni, S., Ultrarobust Biochips with Metal-Organic Framework Coating for Point-of-Care Diagnosis. *ACS Sens.* **2018**, *3* (2), 342-351.
79. Joshi, G. K.; Blodgett, K. N.; Muhoberac, B. B.; Johnson, M. A.; Smith, K. A.; Sardar, R., Ultrasensitive Photoreversible Molecular Sensors of Azobenzene-Functionalized Plasmonic Nanoantennas. *Nano Lett.* **2014**, *14* (2), 532-540.
80. Perelson, A. S.; Oster, G. F., Theoretical Studies of Clonal Selection: Minimal Antibody Repertoire Size and Reliability of Self-non-self Discrimination. *J. Theor. Biol.* **1979**, *81* (4), 645-670.
81. Frieden, E., Non-covalent Interactions: key to Biological Flexibility and Specificity. *J. Chem. Educ.* **1975**, *52* (12), 754-762.

82. Yao, L.; Xu, S., Force-induced Selective Dissociation of Noncovalent Antibody–Antigen Bonds. *J. Phys. Chem. B* **2012**, *116* (33), 9944-9948.
83. Janeway Jr, C. A.; Travers, P.; Walport, M.; Shlomchik, M. J., Immunological Memory. In *Immunobiology: The Immune System in Health and Disease. 5th edition*, Garland Science: 2001.
84. Brandts, J. F.; Hunt, L., Thermodynamics of Protein Denaturation. III. Denaturation of Ribonuclease in Water and in Aqueous Urea and Aqueous Ethanol Mixtures. *J. Am. Chem. Soc.* **1967**, *89* (19), 4826-4838.
85. Turk, B. E.; Huang, L. L.; Piro, E. T.; Cantley, L. C., Determination of Protease Cleavage Site Motifs using Mixture-based Oriented Peptide Libraries. *Nat. Biotech.* **2001**, *19* (7), 661-667.
86. Nick Pace, C.; Trevino, S.; Prabhakaran, E.; Martin Scholtz, J., Protein structure, Stability and Solubility in Water and Other Solvents. *Philos. Trans. R. Soc. Lond. B Biol. Sci.* **2004**, *359* (1448), 1225-1235.
87. Vermeer, A. W.; Norde, W., The Thermal Stability of Immunoglobulin: Unfolding and Aggregation of a Multi-domain Protein. *Biophys. J.* **2000**, *78* (1), 394-404.
88. Wang, C.; Luan, J.; Tadepalli, S.; Liu, K.-K.; Morrissey, J. J.; Kharasch, E. D.; Naik, R. R.; Singamaneni, S., Silk-Encapsulated Plasmonic Biochips with Enhanced Thermal Stability. *ACS App. Mat. Inter.* **2016**, *8* (40), 26493-26500.
89. McKenzie, K. G.; Lafleur, L. K.; Lutz, B. R.; Yager, P., Rapid Protein Depletion from Complex Samples using a Bead-based Microfluidic Device for the Point of Care. *Lab Chip* **2009**, *9* (24), 3543-3548.
90. Crowe, J. H.; Carpenter, J. F.; Crowe, L. M., The Role of Vitrification in Anhydrobiosis. *Annu. Rev. Physiol.* **1998**, *60* (1), 73-103.
91. Gubala, V.; Harris, L. F.; Ricco, A. J.; Tan, M. X.; Williams, D. E., Point of Care Diagnostics: Status and Future. *Anal. Chem.* **2011**, *84* (2), 487-515.
92. Sano, M.; Nishino, I.; Ueno, K.; Kamimori, H., Assay of collagenase activity for native triple-helical collagen using capillary gel electrophoresis with laser-induced fluorescence detection. *Journal of Chromatography B* **2004**, *809* (2), 251-256.
93. Taradaj, J.; Urbanek, T.; Kloth, L. C.; Romanelli, M., Physical therapy in wound healing, edema, and urinary incontinence. *BioMed research international* **2014**, *2014*.
94. Kim, K. E.; Cho, D.; Park, H. J., Air pollution and skin diseases: Adverse effects of airborne particulate matter on various skin diseases. *Life sciences* **2016**, *152*, 126-134.

95. Osathanukul, M.; Buddhachat, K.; Chomdej, S., A modified colorimetric method of gelatinolytic assay using bacterial collagenase type II as a model. *Analytical biochemistry* **2013**, *433* (2), 168-170.
96. Efsen, E.; Særmark, T.; Hansen, A.; Bruun, E.; Brynskov, J., Ramiprilate inhibits functional matrix metalloproteinase activity in Crohn's disease fistulas. *Basic & clinical pharmacology & toxicology* **2011**, *109* (3), 208-216.
97. Seltzer, J.; Akers, K.; Weingarten, H.; Grant, G.; McCourt, D.; Eisen, A., Cleavage specificity of human skin type IV collagenase (gelatinase). Identification of cleavage sites in type I gelatin, with confirmation using synthetic peptides. *Journal of Biological Chemistry* **1990**, *265* (33), 20409-20413.
98. Reboul, P.; Pelletier, J.-P.; Tardif, G.; Cloutier, J.-M.; Martel-Pelletier, J., The new collagenase, collagenase-3, is expressed and synthesized by human chondrocytes but not by synoviocytes. A role in osteoarthritis. *The Journal of clinical investigation* **1996**, *97* (9), 2011-2019.
99. Moore, S.; Stein, W. H., A modified ninhydrin reagent for the photometric determination of amino acids and related compounds. *J. biol. Chem* **1954**, *211* (2), 907-913.
100. Zhang, Y.; Fu, Y.; Zhou, S.; Kang, L.; Li, C., A straightforward ninhydrin-based method for collagenase activity and inhibitor screening of collagenase using spectrophotometry. *Analytical biochemistry* **2013**, *437* (1), 46-48.
101. Bleeg, H. S., Collagenolytic enzymes assayed by spectrophotometry with suspensions of reconstituted collagen fibrils. *Connective tissue research* **1991**, *26* (4), 247-257.
102. Cooksley, S.; Hipkiss, J. B.; Tickle, S. P.; Holmes-Ievers, E.; Docherty, A. J.; Murphy, G.; Lawson, A. D., Immunoassays for the Detection of Human Collagenase, Stromelysin, Tissue Inhibitor of Metallo-proteinases (TIMP) and Enzyme-Inhibitor Complexes. *Matrix* **1990**, *10* (5), 285-291.
103. Yoshioka, H.; Oyamada, I.; Usuku, G., An assay of collagenase activity using enzyme-linked immunosorbent assay for mammalian collagenase. *Analytical biochemistry* **1987**, *166* (1), 172-177.
104. Morales, T. I.; Woessner, J. F.; Howell, D. S.; Marsh, J. M.; LeMaire, W. J., A microassay for the direct demonstration of collagenolytic activity in Graafian follicles of the rat. *Biochimica et Biophysica Acta (BBA)-Enzymology* **1978**, *524* (2), 428-434.
105. Cawston, T. E.; Barrett, A. J., A rapid and reproducible assay for collagenase using [1-14C] acetylated collagen. *Analytical biochemistry* **1979**, *99* (2), 340-345.
106. Dean, D. D.; Woessner Jr, J. F., A sensitive, specific assay for tissue collagenase using telopeptide-free [3H] acetylated collagen. *Analytical biochemistry* **1985**, *148* (1), 174-181.

107. Ishikawa, T.; Nimni, M. E., A modified collagenase assay method based on the use of p-dioxane. *Analytical biochemistry* **1979**, *92* (1), 136-143.
108. Komsa-Penkova, R. S.; Rashap, R. K.; Yomtova, V. M., Advantages of orange-labelled collagen and gelatine as substrates for rapid collagenase activity measurement. *Journal of biochemical and biophysical methods* **1997**, *34* (3), 237-249.
109. Van Wart, H. E.; Steinbrink, D. R., A continuous spectrophotometric assay for *Clostridium histolyticum* collagenase. *Analytical biochemistry* **1981**, *113* (2), 356-365.
110. Vencill, C. F.; Rasnick, D.; Crumley, K. V.; Nishino, N.; Powers, J. C., *Clostridium histolyticum* collagenase: development of new thio ester, fluorogenic, and depsipeptide substrates and new inhibitors. *Biochemistry* **1985**, *24* (13), 3149-3157.
111. Deshmukh, A. A.; Weist, J. L.; Leight, J. L., Detection of proteolytic activity by covalent tethering of fluorogenic substrates in zymogram gels. *BioTechniques* **2018**, *64* (5), 203-210.
112. Inanc, S.; Keles, D.; Oktay, G., An improved collagen zymography approach for evaluating the collagenases MMP-1, MMP-8, and MMP-13. *BioTechniques* **2017**, *63* (4), 174-180.
113. Mahase, E., Covid-19: Where are we on vaccines and variants? *BMJ* **2021**, *372*, n597.
114. <https://www.who.int/publications/m/item/weekly-epidemiological-update-on-covid-19---8-june-2021>.
115. Mina, M. J.; Parker, R.; Larremore, D. B., Rethinking Covid-19 Test Sensitivity — A Strategy for Containment. *New England Journal of Medicine* **2020**, *383* (22), e120.
116. Bullard, J.; Dust, K.; Funk, D.; Strong, J. E.; Alexander, D.; Garnett, L.; Boodman, C.; Bello, A.; Hedley, A.; Schiffman, Z.; Doan, K.; Bastien, N.; Li, Y.; Van Caesele, P. G.; Poliquin, G., Predicting infectious SARS-CoV-2 from diagnostic samples. *Clin Infect Dis* **2020**.
117. He, X.; Lau, E. H. Y.; Wu, P.; Deng, X.; Wang, J.; Hao, X.; Lau, Y. C.; Wong, J. Y.; Guan, Y.; Tan, X.; Mo, X.; Chen, Y.; Liao, B.; Chen, W.; Hu, F.; Zhang, Q.; Zhong, M.; Wu, Y.; Zhao, L.; Zhang, F.; Cowling, B. J.; Li, F.; Leung, G. M., Temporal dynamics in viral shedding and transmissibility of COVID-19. *Nat Med* **2020**, *26* (5), 672-675.
118. Sethuraman, N.; Jeremiah, S. S.; Ryo, A., Interpreting Diagnostic Tests for SARS-CoV-2. *JAMA* **2020**, *323* (22), 2249-2251.
119. Choi, B.; Choudhary, M. C.; Regan, J.; Sparks, J. A.; Padera, R. F.; Qiu, X.; Solomon, I. H.; Kuo, H.-H.; Boucau, J.; Bowman, K.; Adhikari, U. D.; Winkler, M. L.; Mueller, A. A.; Hsu, T. Y. T.; Desjardins, M.; Baden, L. R.; Chan, B. T.; Walker, B. D.; Lichterfeld, M.; Brigl, M.; Kwon, D. S.; Kanjilal, S.; Richardson, E. T.; Jonsson, A. H.; Alter, G.; Barczak, A. K.; Hanage, W. P.; Yu, X. G.; Gaiha, G. D.; Seaman, M. S.; Cernadas, M.; Li, J. Z.,



- Persistence and Evolution of SARS-CoV-2 in an Immunocompromised Host. *New England Journal of Medicine* **2020**, 383 (23), 2291-2293.
120. Taramasso, L.; Sepulcri, C.; Mikulska, M.; Magnasco, L.; Lai, A.; Bruzzone, B.; Dentone, C.; Bassetti, M., Duration of isolation and precautions in immunocompromised patients with COVID-19. *Journal of Hospital Infection* **2021**, 111, 202-204.
  121. Aydillo, T.; Gonzalez-Reiche, A. S.; Aslam, S.; van de Guchte, A.; Khan, Z.; Obla, A.; Dutta, J.; van Bakel, H.; Aberg, J.; García-Sastre, A.; Shah, G.; Hohl, T.; Papanicolaou, G.; Perales, M.-A.; Sepkowitz, K.; Babady, N. E.; Kamboj, M., Shedding of Viable SARS-CoV-2 after Immunosuppressive Therapy for Cancer. *New England Journal of Medicine* **2020**, 383 (26), 2586-2588.
  122. Owusu, D.; Pomeroy, M. A.; Lewis, N. M.; Wadhwa, A.; Yousaf, A. R.; Whitaker, B.; Dietrich, E.; Hall, A. J.; Chu, V.; Thornburg, N.; Christensen, K.; Kiphibane, T.; Willardson, S.; Westergaard, R.; Dasu, T.; Pray, I. W.; Bhattacharyya, S.; Dunn, A.; Tate, J. E.; Kirking, H. L.; Matanock, A., Persistent SARS-CoV-2 RNA Shedding without Evidence of Infectiousness: A Cohort Study of Individuals with COVID-19. *J Infect Dis* **2021**.
  123. Wölfel, R.; Corman, V. M.; Guggemos, W.; Seilmaier, M.; Zange, S.; Müller, M. A.; Niemeyer, D.; Jones, T. C.; Vollmar, P.; Rothe, C.; Hoelscher, M.; Bleicker, T.; Brünink, S.; Schneider, J.; Ehmann, R.; Zwirgmaier, K.; Drosten, C.; Wendtner, C., Virological assessment of hospitalized patients with COVID-2019. *Nature* **2020**, 581 (7809), 465-469.
  124. van Kampen, J. J. A.; van de Vijver, D. A. M. C.; Fraaij, P. L. A.; Haagmans, B. L.; Lamers, M. M.; Okba, N.; van den Akker, J. P. C.; Endeman, H.; Gommers, D. A. M. P. J.; Cornelissen, J. J.; Hoek, R. A. S.; van der Eerden, M. M.; Hesselink, D. A.; Metselaar, H. J.; Verbon, A.; de Steenwinkel, J. E. M.; Aron, G. I.; van Gorp, E. C. M.; van Boheemen, S.; Voermans, J. C.; Boucher, C. A. B.; Molenkamp, R.; Koopmans, M. P. G.; Geurtsvankessel, C.; van der Eijk, A. A., Duration and key determinants of infectious virus shedding in hospitalized patients with coronavirus disease-2019 (COVID-19). *Nature Communications* **2021**, 12 (1), 267.
  125. Peeling, R. W.; Olliaro, P. L.; Boeras, D. I.; Fongwen, N., Scaling up COVID-19 rapid antigen tests: promises and challenges. *The Lancet infectious diseases* **2021**.
  126. Bullard, J.; Dust, K.; Funk, D.; Strong, J. E.; Alexander, D.; Garnett, L.; Boodman, C.; Bello, A.; Hedley, A.; Schiffman, Z.; Doan, K.; Bastien, N.; Li, Y.; Van Caesele, P. G.; Poliquin, G., Predicting Infectious Severe Acute Respiratory Syndrome Coronavirus 2 From Diagnostic Samples. *Clin Infect Dis* **2020**, 71 (10), 2663-2666.
  127. La Scola, B.; Le Bideau, M.; Andreani, J.; Hoang, V. T.; Grimaldier, C.; Colson, P.; Gautret, P.; Raoult, D., Viral RNA load as determined by cell culture as a management tool for discharge of SARS-CoV-2 patients from infectious disease wards. *Eur J Clin Microbiol Infect Dis* **2020**, 39 (6), 1059-1061.

128. McKay, S. L.; Tobolowsky, F. A.; Moritz, E. D.; Hatfield, K. M.; Bhatnagar, A.; LaVoie, S. P.; Jackson, D. A.; Lecy, K. D.; Bryant-Geneviev, J.; Campbell, D.; Freeman, B.; Gilbert, S. E.; Folster, J. M.; Medrzycki, M.; Shewmaker, P. L.; Bankamp, B.; Radford, K. W.; Anderson, R.; Bowen, M. D.; Negley, J.; Reddy, S. C.; Jernigan, J. A.; Brown, A. C.; McDonald, L. C.; Kutty, P. K., Performance Evaluation of Serial SARS-CoV-2 Rapid Antigen Testing During a Nursing Home Outbreak. *Annals of Internal Medicine* **2021**.
129. Pekosz, A.; Parvu, V.; Li, M.; Andrews, J. C.; Manabe, Y. C.; Kodsí, S.; Gary, D. S.; Roger-Dalbert, C.; Leitch, J.; Cooper, C. K., Antigen-Based Testing but Not Real-Time Polymerase Chain Reaction Correlates With Severe Acute Respiratory Syndrome Coronavirus 2 Viral Culture. *Clinical Infectious Diseases* **2021**.
130. Pray, I. W.; Ford, L.; Cole, D.; Lee, C.; Bigouette, J. P.; Abedi, G. R.; Bushman, D.; Delahoy, M. J.; Currie, D.; Cherney, B.; Kirby, M.; Fajardo, G.; Caudill, M.; Langolf, K.; Kahrs, J.; Kelly, P.; Pitts, C.; Lim, A.; Aulik, N.; Tamin, A.; Harcourt, J. L.; Queen, K.; Zhang, J.; Whitaker, B.; Browne, H.; Medrzycki, M.; Shewmaker, P.; Folster, J.; Bankamp, B.; Bowen, M. D.; Thornburg, N. J.; Goffard, K.; Limbago, B.; Bateman, A.; Tate, J. E.; Gieryn, D.; Kirking, H. L.; Westergaard, R.; Killerby, M., Performance of an Antigen-Based Test for Asymptomatic and Symptomatic SARS-CoV-2 Testing at Two University Campuses - Wisconsin, September-October 2020. *MMWR Morb Mortal Wkly Rep* **2021**, *69* (5152), 1642-1647.
131. Toptan, T.; Eckermann, L.; Pfeiffer, A. E.; Hoehl, S.; Ciesek, S.; Drosten, C.; Corman, V. M., Evaluation of a SARS-CoV-2 rapid antigen test: Potential to help reduce community spread? *Journal of Clinical Virology* **2021**, *135*, 104713.
132. Mina, M. J.; Peto, T. E.; García-Fiñana, M.; Semple, M. G.; Buchan, I. E., Clarifying the evidence on SARS-CoV-2 antigen rapid tests in public health responses to COVID-19. *The Lancet* **2021**, *397* (10283), 1425-1427.
133. Fitzpatrick, M. C.; Pandey, A.; Wells, C. R.; Sah, P.; Galvani, A. P., Buyer beware: inflated claims of sensitivity for rapid COVID-19 tests. *The Lancet* **2021**, *397* (10268), 24-25.
134. Luan, J.; Seth, A.; Gupta, R.; Wang, Z.; Rathi, P.; Cao, S.; Gholami Derami, H.; Tang, R.; Xu, B.; Achilefu, S.; Morrissey, J. J.; Singamaneni, S., Ultrabright fluorescent nanoscale labels for the femtomolar detection of analytes with standard bioassays. *Nat Biomed Eng* **2020**, *4* (5), 518-530.
135. Cohen, L.; Cui, N.; Cai, Y.; Garden, P. M.; Li, X.; Weitz, D. A.; Walt, D. R., Single Molecule Protein Detection with Attomolar Sensitivity Using Droplet Digital Enzyme-Linked Immunosorbent Assay. *ACS Nano* **2020**, *14* (8), 9491-9501.
136. Dinh, T. L.; Ngan, K. C.; Shoemaker, C. B.; Walt, D. R., Using Antigen-antibody Binding Kinetic Parameters to Understand Single-Molecule Array Immunoassay Performance. *Analytical Chemistry* **2016**, *88* (23), 11335-11339.

137. Rissin, D. M.; Kan, C. W.; Campbell, T. G.; Howes, S. C.; Fournier, D. R.; Song, L.; Piech, T.; Patel, P. P.; Chang, L.; Rivnak, A. J.; Ferrell, E. P.; Randall, J. D.; Provuncher, G. K.; Walt, D. R.; Duffy, D. C., Single-molecule enzyme-linked immunosorbent assay detects serum proteins at subfemtomolar concentrations. *Nature Biotechnology* **2010**, *28* (6), 595-599.
138. Wilson, D. H.; Rissin, D. M.; Kan, C. W.; Fournier, D. R.; Piech, T.; Campbell, T. G.; Meyer, R. E.; Fishburn, M. W.; Cabrera, C.; Patel, P. P.; Frew, E.; Chen, Y.; Chang, L.; Ferrell, E. P.; von Einem, V.; McGuigan, W.; Reinhardt, M.; Sayer, H.; Vielsack, C.; Duffy, D. C., The Simoa HD-1 Analyzer: A Novel Fully Automated Digital Immunoassay Analyzer with Single-Molecule Sensitivity and Multiplexing. *Journal of Laboratory Automation* **2015**, *21* (4), 533-547.
139. Witters, D.; Knez, K.; Ceyskens, F.; Puers, R.; Lammertyn, J., Digital microfluidics-enabled single-molecule detection by printing and sealing single magnetic beads in femtoliter droplets. *Lab on a Chip* **2013**, *13* (11), 2047-2054.
140. Decrop, D.; Brans, T.; Gijzenbergh, P.; Lu, J.; Spasic, D.; Kokalj, T.; Beunis, F.; Goos, P.; Puers, R.; Lammertyn, J., Optical Manipulation of Single Magnetic Beads in a Microwell Array on a Digital Microfluidic Chip. *Analytical Chemistry* **2016**, *88* (17), 8596-8603.
141. Zhao, W.; Ali, M. M.; Brook, M. A.; Li, Y., Rolling Circle Amplification: Applications in Nanotechnology and Biodetection with Functional Nucleic Acids. *Angewandte Chemie International Edition* **2008**, *47* (34), 6330-6337.
142. Soh, J. H.; Chan, H.-M.; Ying, J. Y., Strategies for developing sensitive and specific nanoparticle-based lateral flow assays as point-of-care diagnostic device. *Nano Today* **2020**, *30*, 100831.
143. Nguyen, V.-T.; Song, S.; Park, S.; Joo, C., Recent advances in high-sensitivity detection methods for paper-based lateral-flow assay. *Biosensors and Bioelectronics* **2020**, *152*, 112015.
144. Li, Z.; Yi, Y.; Luo, X.; Xiong, N.; Liu, Y.; Li, S.; Sun, R.; Wang, Y.; Hu, B.; Chen, W., Development and clinical application of a rapid IgM-IgG combined antibody test for SARS-CoV-2 infection diagnosis. *Journal of medical virology* **2020**, *92* (9), 1518-1524.
145. Charlton, C. L.; Kanji, J. N.; Johal, K.; Bailey, A.; Plitt, S. S.; MacDonald, C.; Kunst, A.; Buss, E.; Burnes, L. E.; Fonseca, K., Evaluation of six commercial mid-to high-volume antibody and six point-of-care lateral flow assays for detection of SARS-CoV-2 antibodies. *Journal of clinical microbiology* **2020**, *58* (10), e01361-20.
146. Heggstad, J. T.; Kinnamon, D. S.; Olson, L. B.; Liu, J.; Kelly, G.; Wall, S. A.; Oshabahebwa, S.; Quinn, Z.; Fontes, C. M.; Joh, D. Y., Multiplexed, quantitative serological profiling of COVID-19 from blood by a point-of-care test. *Science advances* **2021**, *7* (26), eabg4901.

147. Mertens, P.; De Vos, N.; Martiny, D.; Jassoy, C.; Mirazimi, A.; Cuypers, L.; Van den Wijngaert, S.; Monteil, V.; Melin, P.; Stoffels, K., Development and potential usefulness of the COVID-19 Ag Respi-Strip diagnostic assay in a pandemic context. *Frontiers in medicine* **2020**, *7*, 225.
148. Porte, L.; Legarraga, P.; Vollrath, V.; Aguilera, X.; Munita, J. M.; Araos, R.; Pizarro, G.; Vial, P.; Iruretagoyena, M.; Dittrich, S., Evaluation of a novel antigen-based rapid detection test for the diagnosis of SARS-CoV-2 in respiratory samples. *International Journal of Infectious Diseases* **2020**, *99*, 328-333.
149. Pickering, S.; Betancor, G.; Galão, R. P.; Merrick, B.; Signell, A. W.; Wilson, H. D.; Kia Ik, M. T.; Seow, J.; Graham, C.; Acors, S., Comparative assessment of multiple COVID-19 serological technologies supports continued evaluation of point-of-care lateral flow assays in hospital and community healthcare settings. *PLoS pathogens* **2020**, *16* (9), e1008817.
150. Kontou, P. I.; Braliou, G. G.; Dimou, N. L.; Nikolopoulos, G.; Bagos, P. G., Antibody tests in detecting SARS-CoV-2 infection: a meta-analysis. *Diagnostics* **2020**, *10* (5), 319.
151. Hu, J.; Jiang, Y.-Z.; Tang, M.; Wu, L.-L.; Xie, H.-y.; Zhang, Z.-L.; Pang, D.-W., Colorimetric-fluorescent-magnetic nanosphere-based multimodal assay platform for Salmonella detection. *Analytical chemistry* **2018**, *91* (1), 1178-1184.
152. Posthuma-Trumpie, G. A.; Korf, J.; van Amerongen, A., Lateral flow (immuno) assay: its strengths, weaknesses, opportunities and threats. A literature survey. *Analytical and bioanalytical chemistry* **2009**, *393* (2), 569-582.
153. Hu, J.; Wang, S.; Wang, L.; Li, F.; Pingguan-Murphy, B.; Lu, T. J.; Xu, F., Advances in paper-based point-of-care diagnostics. *Biosensors and Bioelectronics* **2014**, *54*, 585-597.
154. Huang, L.; Jin, J.; Ao, L.; Jiang, C.; Zhang, Y.; Wen, H.-M.; Wang, J.; Wang, H.; Hu, J., Hierarchical Plasmonic-Fluorescent Labels for Highly Sensitive Lateral Flow Immunoassay with Flexible Dual-Modal Switching. *ACS Applied Materials & Interfaces* **2020**, *12* (52), 58149-58160.
155. García-Basteiro, A. L.; Chaccour, C.; Guinovart, C.; Llupià, A.; Brew, J.; Trilla, A.; Plasencia, A., Monitoring the COVID-19 epidemic in the context of widespread local transmission. *The Lancet Respiratory Medicine* **2020**, *8* (5), 440-442.
156. Organization, W. H., COVID-19 weekly epidemiological update, 25 May 2021. **2021**.
157. Pang, J.; Wang, M. X.; Ang, I. Y. H.; Tan, S. H. X.; Lewis, R. F.; Chen, J. I.-P.; Gutierrez, R. A.; Gwee, S. X. W.; Chua, P. E. Y.; Yang, Q., Potential rapid diagnostics, vaccine and therapeutics for 2019 novel coronavirus (2019-nCoV): a systematic review. *Journal of clinical medicine* **2020**, *9* (3), 623.

158. Yu, F.; Yan, L.; Wang, N.; Yang, S.; Wang, L.; Tang, Y.; Gao, G.; Wang, S.; Ma, C.; Xie, R., Quantitative detection and viral load analysis of SARS-CoV-2 in infected patients. *Clinical Infectious Diseases* **2020**, *71* (15), 793-798.
159. Che, X.-y.; Qiu, L.-w.; Pan, Y.-x.; Wen, K.; Hao, W.; Zhang, L.-y.; Wang, Y.-d.; Liao, Z.-y.; Hua, X.; Cheng, V. C., Sensitive and specific monoclonal antibody-based capture enzyme immunoassay for detection of nucleocapsid antigen in sera from patients with severe acute respiratory syndrome. *Journal of clinical microbiology* **2004**, *42* (6), 2629-2635.
160. Di, B.; Hao, W.; Gao, Y.; Wang, M.; Wang, Y.-d.; Qiu, L.-w.; Wen, K.; Zhou, D.-h.; Wu, X.-w.; Lu, E.-j., Monoclonal antibody-based antigen capture enzyme-linked immunosorbent assay reveals high sensitivity of the nucleocapsid protein in acute-phase sera of severe acute respiratory syndrome patients. *Clinical and Vaccine Immunology* **2005**, *12* (1), 135-140.
161. Long, Q.-X.; Liu, B.-Z.; Deng, H.-J.; Wu, G.-C.; Deng, K.; Chen, Y.-K.; Liao, P.; Qiu, J.-F.; Lin, Y.; Cai, X.-F., Antibody responses to SARS-CoV-2 in patients with COVID-19. *Nature medicine* **2020**, *26* (6), 845-848.
162. Peterhoff, D.; Glück, V.; Vogel, M.; Schuster, P.; Schütz, A.; Neubert, P.; Albert, V.; Frisch, S.; Kiessling, M.; Pervan, P., A highly specific and sensitive serological assay detects SARS-CoV-2 antibody levels in COVID-19 patients that correlate with neutralization. *Infection* **2021**, *49* (1), 75-82.
163. Tromberg, B. J.; Schwetz, T. A.; Pérez-Stable, E. J.; Hodes, R. J.; Woychik, R. P.; Bright, R. A.; Fleurence, R. L.; Collins, F. S., Rapid scaling up of Covid-19 diagnostic testing in the United States—the NIH RADx initiative. *New England Journal of Medicine* **2020**, *383* (11), 1071-1077.
164. Valera, E.; Jankelow, A.; Lim, J.; Kindratenko, V.; Ganguli, A.; White, K.; Kumar, J.; Bashir, R., COVID-19 Point-of-Care Diagnostics: Present and Future. *ACS nano* **2021**.
165. Hu, J.; Zhang, Z.-L.; Wen, C.-Y.; Tang, M.; Wu, L.-L.; Liu, C.; Zhu, L.; Pang, D.-W., Sensitive and quantitative detection of C-reaction protein based on immunofluorescent nanospheres coupled with lateral flow test strip. *Analytical chemistry* **2016**, *88* (12), 6577-6584.
166. Udugama, B.; Kadhiresan, P.; Kozlowski, H. N.; Malekjahani, A.; Osborne, M.; Li, V. Y.; Chen, H.; Mubareka, S.; Gubbay, J. B.; Chan, W. C., Diagnosing COVID-19: the disease and tools for detection. *ACS nano* **2020**, *14* (4), 3822-3835.
167. Luan, J.; Seth, A.; Gupta, R.; Wang, Z.; Rathi, P.; Cao, S.; Derami, H. G.; Tang, R.; Xu, B.; Achilefu, S., Ultrabright fluorescent nanoscale labels for the femtomolar detection of analytes with standard bioassays. *Nature biomedical engineering* **2020**, *4* (5), 518-530.

168. Tam, F.; Goodrich, G. P.; Johnson, B. R.; Halas, N. J., Plasmonic enhancement of molecular fluorescence. *Nano letters* **2007**, *7* (2), 496-501.
169. Kinkhabwala, A.; Yu, Z.; Fan, S.; Avlasevich, Y.; Müllen, K.; Moerner, W. E., Large single-molecule fluorescence enhancements produced by a bowtie nanoantenna. *Nature photonics* **2009**, *3* (11), 654-657.
170. Zhang, B.; Kumar, R. B.; Dai, H.; Feldman, B. J., A plasmonic chip for biomarker discovery and diagnosis of type 1 diabetes. *Nature medicine* **2014**, *20* (8), 948-953.
171. Bardhan, R.; Grady, N. K.; Cole, J. R.; Joshi, A.; Halas, N. J., Fluorescence enhancement by Au nanostructures: nanoshells and nanorods. *ACS nano* **2009**, *3* (3), 744-752.
172. Rycenga, M.; Cobley, C. M.; Zeng, J.; Li, W.; Moran, C. H.; Zhang, Q.; Qin, D.; Xia, Y., Controlling the synthesis and assembly of silver nanostructures for plasmonic applications. *Chemical reviews* **2011**, *111* (6), 3669-3712.
173. Orendorff, C. J.; Murphy, C. J., Quantitation of metal content in the silver-assisted growth of gold nanorods. *The Journal of Physical Chemistry B* **2006**, *110* (9), 3990-3994.
174. Huang, J.; Zhu, H.; Chen, Y.; Preston, C.; Rohrbach, K.; Cumings, J.; Hu, L., Highly transparent and flexible nanopaper transistors. *Acs Nano* **2013**, *7* (3), 2106-2113.
175. Pastoriza-Santos, I.; Pérez-Juste, J.; Liz-Marzán, L. M., Silica-coating and hydrophobation of CTAB-stabilized gold nanorods. *Chemistry of Materials* **2006**, *18* (10), 2465-2467.
176. Tian, L.; Tadepalli, S.; Park, S. H.; Liu, K.-K.; Morrissey, J. J.; Kharasch, E. D.; Naik, R. R.; Singamaneni, S., Bioplasmonic calligraphy for multiplexed label-free biodetection. *Biosensors and Bioelectronics* **2014**, *59*, 208-215.
177. Arya, J.; Henry, S.; Kalluri, H.; McAllister, D. V.; Pewin, W. P.; Prausnitz, M. R., Tolerability, usability and acceptability of dissolving microneedle patch administration in human subjects. *Biomaterials* **2017**, *128*, 1-7.
178. Rouphael, N. G.; Paine, M.; Mosley, R.; Henry, S.; McAllister, D. V.; Kalluri, H.; Pewin, W.; Frew, P. M.; Yu, T.; Thornburg, N. J., The safety, immunogenicity, and acceptability of inactivated influenza vaccine delivered by microneedle patch (TIV-MNP 2015): a randomised, partly blinded, placebo-controlled, phase 1 trial. *The Lancet* **2017**, *390* (10095), 649-658.
179. Kolluru, C.; Williams, M.; Chae, J.; Prausnitz, M. R., Recruitment and collection of dermal interstitial fluid using a microneedle patch. *Advanced healthcare materials* **2019**, *8* (3), 1801262.

180. Jensen, L.; Schatz, G. C., Resonance Raman scattering of rhodamine 6G as calculated using time-dependent density functional theory. *The Journal of Physical Chemistry A* **2006**, *110* (18), 5973-5977.
181. Hildebrandt, P.; Stockburger, M., Surface-enhanced resonance Raman spectroscopy of Rhodamine 6G adsorbed on colloidal silver. *The Journal of Physical Chemistry* **1984**, *88* (24), 5935-5944.
182. Hankus, M. E.; Stratis-Cullum, D. N.; Pellegrino, P. M. In *Characterization of next-generation commercial surface-enhanced Raman scattering (SERS) substrates*, Chemical, Biological, Radiological, Nuclear, and Explosives (CBRNE) Sensing XII, International Society for Optics and Photonics: 2011; p 80180P.
183. Das, D. K.; Mondal, T.; Mandal, A. K.; Bhattacharyya, K., Binding of Organic Dyes with Human Serum Albumin: A Single-Molecule Study. *Chemistry—An Asian Journal* **2011**, *6* (11), 3097-3103.
184. Martinez, A. W.; Phillips, S. T.; Nie, Z.; Cheng, C.-M.; Carrilho, E.; Wiley, B. J.; Whitesides, G. M., Programmable diagnostic devices made from paper and tape. *Lab Chip* **2010**, *10* (19), 2499-2504.
185. Carvalhal, R. F.; Simão Kfour, M.; de Oliveira Piazzetta, M. H.; Gobbi, A. L.; Kubota, L. T., Electrochemical detection in a paper-based separation device. *Anal. Chem.* **2010**, *82* (3), 1162-1165.
186. Bracher, P. J.; Gupta, M.; Whitesides, G. M., Patterned paper as a template for the delivery of reactants in the fabrication of planar materials. *Soft Matter* **2010**, *6* (18), 4303-4309.
187. Xie, W.; Schlücker, S., Medical applications of surface-enhanced Raman scattering. *Physical Chemistry Chemical Physics* **2013**, *15* (15), 5329-5344.
188. Schmit, V.; Martoglio, R.; Carron, K., Lab-on-a-bubble surface enhanced Raman indirect immunoassay for cholera. *Analytical chemistry* **2012**, *84* (9), 4233-4236.
189. Botti, S.; Almaviva, S.; Cantarini, L.; Palucci, A.; Puiu, A.; Rufoloni, A., Trace level detection and identification of nitro-based explosives by surface-enhanced Raman spectroscopy. *Journal of Raman Spectroscopy* **2013**, *44* (3), 463-468.
190. Lee, K. S.; El-Sayed, M. A., Gold and silver nanoparticles in sensing and imaging: sensitivity of plasmon response to size, shape, and metal composition. *The journal of physical chemistry. B* **2006**, *110* (39), 19220-5.
191. Morrissey, J. J.; Mellnick, V. M.; Luo, J.; Siegel, M. J.; Figenschau, R. S.; Bhayani, S.; Kharasch, E. D., Evaluation of urine aquaporin-1 and perilipin-2 concentrations as biomarkers to screen for renal cell carcinoma: a prospective cohort study. *JAMA oncology* **2015**, *1* (2), 204-212.

192. Morrissey, J. J.; Mobley, J.; Figenshau, R. S.; Vetter, J.; Bhayani, S.; Kharasch, E. D. In *Urine aquaporin 1 and perilipin 2 differentiate renal carcinomas from other imaged renal masses and bladder and prostate cancer*, Mayo Clinic Proceedings, Elsevier: 2015; pp 35-42.
193. Affairs, D. o. V., Diseases Associated With Exposure to Contaminants in the Water Supply at Camp Lejeune. Final rule. *Federal register* **2017**, 82 (9), 4173.
194. Shrestha, D.; Liu, S.; Hammond, S. K.; LaValley, M. P.; Weiner, D. E.; Eisen, E. A.; Applebaum, K. M., Risk of renal cell carcinoma following exposure to metalworking fluids among autoworkers. *Occupational and environmental medicine* **2016**, 73 (10), 656-662.
195. Johnson, D. C.; Vukina, J.; Smith, A. B.; Meyer, A.-M.; Wheeler, S. B.; Kuo, T.-M.; Tan, H.-J.; Woods, M. E.; Raynor, M. C.; Wallen, E. M., Preoperatively misclassified, surgically removed benign renal masses: a systematic review of surgical series and United States population level burden estimate. *The Journal of urology* **2015**, 193 (1), 30-35.
196. Orendorff, C. J.; Gearheart, L.; Jana, N. R.; Murphy, C. J., Aspect Ratio Dependence on Surface Enhanced Raman Scattering using Silver and Gold Nanorod Substrates. *Phys. Chem. Chem. Phys.* **2006**, 8 (1), 165-170.
197. Tadepalli, S.; Kuang, Z.; Jiang, Q.; Liu, K.-K.; Fisher, M. A.; Morrissey, J. J.; Kharasch, E. D.; Slocik, J. M.; Naik, R. R.; Singamaneni, S., Peptide Functionalized Gold Nanorods for the Sensitive Detection of a Cardiac Biomarker using Plasmonic Paper Devices. *Sci. Rep.* **2015**, 5, 16206.
198. Tian, L.; Morrissey, J. J.; Kattumenu, R.; Gandra, N.; Kharasch, E. D.; Singamaneni, S., Bioplasmonic Paper as a Platform for Detection of Kidney Cancer Biomarkers. *Anal. Chem.* **2012**, 84 (22), 9928-9934.
199. Goode, J. A.; Rushworth, J. V. H.; Millner, P. A., Biosensor Regeneration: A Review of Common Techniques and Outcomes. *Langmuir* **2015**, 31 (23), 6267-6276.
200. Bhuyan, A. K., On the Mechanism of SDS-induced Protein Denaturation. *Biopolymers* **2010**, 93 (2), 186-199.
201. Michaux, C.; Pomroy, N. C.; Privé, G. G., Refolding SDS-denatured Proteins by the Addition of Amphipathic Cosolvents. *J. Mol. Biol.* **2008**, 375 (5), 1477-1488.
202. Xu, Q.; Keiderling, T. A., Stop-flow Kinetics Studies of the Interaction of Surfactant, Sodium Dodecyl Sulfate, with Acid-denatured Cytochrome C. *Proteins* **2006**, 63 (3), 571-580.
203. Tadepalli, S.; Yim, J.; Madireddi, K.; Luan, J.; Naik, R. R.; Singamaneni, S., Gold Nanorod-Mediated Photothermal Enhancement of the Biocatalytic Activity of a Polymer-Encapsulated Enzyme. *Chem. Mater.* **2017**, 29 (15), 6308-6314.



204. Abbas, A.; Tian, L.; Morrissey, J. J.; Kharasch, E. D.; Singamaneni, S., Hot Spot-localized Artificial Antibodies for Label-free Plasmonic Biosensing. *Adv. Func. Mat.* **2013**, *23* (14), 1789-1797.
205. Luan, J.; Xu, T.; Cashin, J.; Morrissey, J. J.; Kharasch, E. D.; Singamaneni, S., Environmental Stability of Plasmonic Biosensors Based on Natural versus Artificial Antibody. *Anal. Chem.* **2018**, *90* (13), 7880-7887.
206. Correro, M. R.; Moridi, N.; Schützinger, H.; Sykora, S.; Ammann, E. M.; Peters, E. H.; Dudal, Y.; Corvini, P. F. X.; Shahgaldian, P., Enzyme Shielding in an Enzyme-thin and Soft Organosilica Layer. *Ange. Chem.* **2016**, *128* (21), 6393-6397.
207. Luan, J.; Liu, K.-K.; Tadepalli, S.; Jiang, Q.; Morrissey, J. J.; Kharasch, E. D.; Singamaneni, S., PEGylated Artificial Antibodies: Plasmonic Biosensors with Improved Selectivity. *ACS App. Mat. Inter.* **2016**, *8* (36), 23509-23516.
208. Huang, X.; Aguilar, Z. P.; Xu, H.; Lai, W.; Xiong, Y., Membrane-based lateral flow immunochromatographic strip with nanoparticles as reporters for detection: A review. *Biosensors and Bioelectronics* **2016**, *75*, 166-180.
209. Steegborn, C.; Skládal, P., Construction and Characterization of the Direct Piezoelectric Immunosensor for Atrazine Operating in Solution. *Biosens. Bioelectron.* **1997**, *12* (1), 19-27.
210. Bright, F. V.; Betts, T. A.; Litwiler, K. S., Regenerable Fiber-optic-based Immunosensor. *Anal. Chem.* **1990**, *62* (10), 1065-1069.
211. Hong, S.-R.; Choi, S.-J.; Do Jeong, H.; Hong, S., Development of QCM Biosensor to Detect a Marine Derived Pathogenic Bacteria *Edwardsiella Tarda* using a Novel Immobilisation Method. *Biosens. Bioelectron.* **2009**, *24* (6), 1635-1640.
212. Lee, K.-S.; El-Sayed, M. A., Dependence of the enhanced optical scattering efficiency relative to that of absorption for gold metal nanorods on aspect ratio, size, end-cap shape, and medium refractive index. *The Journal of Physical Chemistry B* **2005**, *109* (43), 20331-20338.
213. Gole, A.; Murphy, C. J., Azide-derivatized gold nanorods: functional materials for “click” chemistry. *Langmuir* **2008**, *24* (1), 266-272.
214. Tebbe, M.; Kuttner, C.; Männel, M.; Fery, A.; Chanana, M., Colloidally stable and surfactant-free protein-coated gold nanorods in biological media. *ACS applied materials & interfaces* **2015**, *7* (10), 5984-5991.
215. Dong, Z.-M.; Jin, X.; Zhao, G.-C., Amplified QCM biosensor for type IV collagenase based on collagenase-cleavage of gold nanoparticles functionalized peptide. *Biosensors and Bioelectronics* **2018**, *106*, 111-116.

216. Koss, M. A.; Castro, C. E.; Gramajo, A. M.; López, M. E., sIgA, peroxidase and collagenase in saliva of smokers aggressive periodontal patients. *Journal of oral biology and craniofacial research* **2016**, *6*, S24-S28.
217. Preshaw, P. M. In *Detection and diagnosis of periodontal conditions amenable to prevention*, BMC oral health, BioMed Central: 2015; p S5.
218. Holmberg, A.; Blomstergren, A.; Nord, O.; Lukacs, M.; Lundeberg, J.; Uhlén, M., The biotin-streptavidin interaction can be reversibly broken using water at elevated temperatures. *Electrophoresis* **2005**, *26* (3), 501-510.
219. Scott, P.; Leaver, A., The degradation of human dentine collagen by trypsin. *Connective tissue research* **1974**, *2* (4), 299-307.
220. Etherington, D., The nature of the collagenolytic cathepsin of rat liver and its distribution in other rat tissues. *Biochemical Journal* **1972**, *127* (4), 685-692.
221. Anderson, A., Effects of lysosomal collagenolytic enzymes, anti-inflammatory drugs and other substances on some properties of insoluble collagen. *Biochemical Journal* **1969**, *113* (3), 457-463.
222. Cao, L.; Goresnik, I.; Coventry, B.; Case, J. B.; Miller, L.; Kozodoy, L.; Chen, R. E.; Carter, L.; Walls, A. C.; Park, Y.-J.; Strauch, E.-M.; Stewart, L.; Diamond, M. S.; Veessler, D.; Baker, D., De novo design of picomolar SARS-CoV-2 miniprotein inhibitors. *Science* **2020**, *370* (6515), 426.
223. Bruhn, B.; Qejvanaj, F.; Gregorkiewicz, T.; Linnros, J., Temporal correlation of blinking events in CdSe/ZnS and Si/SiO<sub>2</sub> nanocrystals. *Physica B: Condensed Matter* **2014**, *453*, 63-67.
224. Landry, J. P.; Ke, Y.; Yu, G.-L.; Zhu, X. D., Measuring affinity constants of 1450 monoclonal antibodies to peptide targets with a microarray-based label-free assay platform. *Journal of Immunological Methods* **2015**, *417*, 86-96.
225. Michnik, A., Thermal stability of bovine serum albumin DSC study. *Journal of Thermal Analysis and Calorimetry* **2003**, *71* (2), 509-519.
226. Alsoussi, W. B.; Turner, J. S.; Case, J. B.; Zhao, H.; Schmitz, A. J.; Zhou, J. Q.; Chen, R. E.; Lei, T.; Rizk, A. A.; McIntire, K. M.; Winkler, E. S.; Fox, J. M.; Kafai, N. M.; Thackray, L. B.; Hassan, A. O.; Amanat, F.; Krammer, F.; Watson, C. T.; Kleinstein, S. H.; Fremont, D. H.; Diamond, M. S.; Ellebedy, A. H., A Potently Neutralizing Antibody Protects Mice against SARS-CoV-2 Infection. *The Journal of Immunology* **2020**, *205* (4), 915.
227. Zeng, R.; Ruan, H.-Q.; Jiang, X.-S.; Zhou, H.; Shi, L.; Zhang, L.; Sheng, Q.-H.; Tu, Q.; Xia, Q.-C.; Wu, J.-R., Proteomic Analysis of SARS Associated Coronavirus Using Two-Dimensional Liquid Chromatography Mass Spectrometry and One-Dimensional Sodium

- Dodecyl Sulfate-Polyacrylamide Gel Electrophoresis Followed by Mass Spectroemtric Analysis. *Journal of Proteome Research* **2004**, 3 (3), 549-555.
228. CDC <https://www.cdc.gov/coronavirus/2019-ncov/cases-updates/variant-surveillance/variant-info.html>.
229. The impact of novel variants of SARS-CoV-2 on diagnostic testing - FIND. 2021.
230. PATH. <https://www.path.org/programs/diagnostics/covid-dashboard-implication-variants-covid-19-antigen-test-detection/>. (accessed 6/1/2021).
231. Bourassa, L.; Perchetti, G. A.; Phung, Q.; Lin, M. J.; Mills, M. G.; Roychoudhury, P.; Harmon, K. G.; Reed, J. C.; Greninger, A. L., A SARS-CoV-2 Nucleocapsid Variant that Affects Antigen Test Performance. *medRxiv* **2021**, 2021.05.05.21256527.
232. Del Vecchio, C.; Brancaccio, G.; Brazzale, A. R.; Lavezzo, E.; Onelia, F.; Franchin, E.; Manuto, L.; Bianca, F.; Cianci, V.; Cattelan, A.; Toppo, S.; Crisanti, A., Emergence of N antigen SARS-CoV-2 genetic variants escaping detection of antigenic tests. *medRxiv* **2021**, 2021.03.25.21253802.
233. Galloway, S. E.; Paul, P.; MacCannell, D. R.; Johansson, M. A.; Brooks, J. T.; MacNeil, A.; Slayton, R. B.; Tong, S.; Silk, B. J.; Armstrong, G. L.; Biggerstaff, M.; Dugan, V. G., Emergence of SARS-CoV-2 B.1.1.7 Lineage - United States, December 29, 2020-January 12, 2021. *MMWR Morb Mortal Wkly Rep* **2021**, 70 (3), 95-99.
234. Singh, J.; Samal, J.; Kumar, V.; Sharma, J.; Agrawal, U.; Ehtesham, N. Z.; Sundar, D.; Rahman, S. A.; Hira, S.; Hasnain, S. E., Structure-Function Analyses of New SARS-CoV-2 Variants B.1.1.7, B.1.351 and B.1.1.28.1: Clinical, Diagnostic, Therapeutic and Public Health Implications. *Viruses* **2021**, 13 (3).
235. Gupta, R.; Luan, J.; Chakrabarty, S.; Scheller, E. L.; Morrissey, J.; Singamaneni, S., Refreshable Nanobiosensor Based on Organosilica Encapsulation of Biorecognition Elements. *ACS applied materials & interfaces* **2020**, 12 (5), 5420-5428.
236. Frens, G., Controlled nucleation for the regulation of the particle size in monodisperse gold suspensions. *Nature physical science* **1973**, 241 (105), 20-22.
237. Moghadam, B. Y.; Connelly, K. T.; Posner, J. D., Two orders of magnitude improvement in detection limit of lateral flow assays using isotachopheresis. *Analytical chemistry* **2015**, 87 (2), 1009-1017.
238. Mosley, G. L.; Nguyen, P.; Wu, B. M.; Kamei, D. T., Development of quantitative radioactive methodologies on paper to determine important lateral-flow immunoassay parameters. *Lab on a Chip* **2016**, 16 (15), 2871-2881.

239. Zhan, L.; Guo, S.-z.; Song, F.; Gong, Y.; Xu, F.; Boulware, D. R.; McAlpine, M. C.; Chan, W. C.; Bischof, J. C., The role of nanoparticle design in determining analytical performance of lateral flow immunoassays. *Nano letters* **2017**, *17* (12), 7207-7212.
240. Chen, H.; Shao, L.; Li, Q.; Wang, J., Gold nanorods and their plasmonic properties. *Chemical Society Reviews* **2013**, *42* (7), 2679-2724.
241. Dreaden, E. C.; Alkilany, A. M.; Huang, X.; Murphy, C. J.; El-Sayed, M. A., The golden age: gold nanoparticles for biomedicine. *Chemical Society Reviews* **2012**, *41* (7), 2740-2779.
242. Liang, C.; Luan, J.; Wang, Z.; Jiang, Q.; Gupta, R.; Cao, S.; Liu, K.-K.; Morrissey, J. J.; Kharasch, E. D.; Naik, R. R., Gold nanorod size-dependent fluorescence enhancement for ultrasensitive fluoroimmunoassays. *ACS Applied Materials & Interfaces* **2021**, *13* (9), 11414-11423.
243. Weber, P. C.; Ohlendorf, D. H.; Wendoloski, J.; Salemme, F., Structural origins of high-affinity biotin binding to streptavidin. *Science* **1989**, *243* (4887), 85-88.
244. Schett, G.; Elewaut, D.; McInnes, I. B.; Dayer, J.-M.; Neurath, M. F., How Cytokine Networks Fuel Inflammation: Toward a cytokine-based disease taxonomy. *Nature Medicine* **2013**, *19*, 822.
245. Coussens, L. M.; Werb, Z., Inflammation and cancer. *Nature* **2002**, *420* (6917), 860-867.
246. McInnes, I. B.; Schett, G., Cytokines in the pathogenesis of rheumatoid arthritis. *Nature Reviews Immunology* **2007**, *7*, 429.
247. de Souza Sene, I.; Costa, V.; Brás, D. C.; de Oliveira Farias, E. A.; Nunes, G. E.; Bechtold, I. H., A point of care lateral flow assay for rapid and colorimetric detection of interleukin 6 and perspectives in bedside diagnostics. *J Clin Med Res* **2020**, *2* (2), 1-16.
248. Huang, D.; Ying, H.; Jiang, D.; Liu, F.; Tian, Y.; Du, C.; Zhang, L.; Pu, X., Rapid and sensitive detection of interleukin-6 in serum via time-resolved lateral flow immunoassay. *Analytical biochemistry* **2020**, *588*, 113468.
249. Swanson, C.; D'Andrea, A., Lateral flow assay with near-infrared dye for multiplex detection. *Clinical chemistry* **2013**, *59* (4), 641-648.
250. Tang, J.; Wu, L.; Lin, J.; Zhang, E.; Luo, Y., Development of quantum dot-based fluorescence lateral flow immunoassay strip for rapid and quantitative detection of serum interleukin-6. *Journal of Clinical Laboratory Analysis* **2021**, *35* (5), e23752.
251. Wilson, B. D.; Eisenstein, M.; Soh, H. T., Comparing assays via the resolution of molecular concentration. *Nature Biomedical Engineering* **2022**, *6* (3), 227-231.

252. Huang, C.; Wen, T.; Shi, F.-J.; Zeng, X.-Y.; Jiao, Y.-J., Rapid detection of IgM antibodies against the SARS-CoV-2 virus via colloidal gold nanoparticle-based lateral-flow assay. *ACS omega* **2020**, *5* (21), 12550-12556.
253. Amanat, F.; Stadlbauer, D.; Strohmeier, S.; Nguyen, T. H.; Chromikova, V.; McMahon, M.; Jiang, K.; Arunkumar, G. A.; Jurczynszak, D.; Polanco, J., A serological assay to detect SARS-CoV-2 seroconversion in humans. *Nature medicine* **2020**, *26* (7), 1033-1036.
254. Fischer, P. U.; Fischer, K.; Curtis, K. C.; Huang, Y.; Fetcho, N.; Goss, C. W.; Weil, G. J., Evaluation of commercial rapid lateral flow tests, alone or in combination, for SARS-CoV-2 antibody testing. *The American Journal of Tropical Medicine and Hygiene* **2021**, *105* (2), 378.
255. Grant, B. D.; Anderson, C. E.; Williford, J. R.; Alonzo, L. F.; Glukhova, V. A.; Boyle, D. S.; Weigl, B. H.; Nichols, K. P., SARS-CoV-2 coronavirus nucleocapsid antigen-detecting half-strip lateral flow assay toward the development of point of care tests using commercially available reagents. *Analytical chemistry* **2020**, *92* (16), 11305-11309.
256. Krueger, L. J.; Gaeddert, M.; Koepfel, L.; Bruemmer, L.; Gottschalk, C.; Miranda, I. B.; Schnitzler, P.; Kraeusslich, H.-G.; Lindner, A.; Nikolai, O., Evaluation of the accuracy, ease of use and limit of detection of novel, rapid, antigen-detecting point-of-care diagnostics for SARS-CoV-2. *medRxiv* **2020**.
257. Mattiuzzi, C.; Henry, B. M.; Lippi, G., Making sense of rapid antigen testing in severe acute respiratory syndrome coronavirus 2 (SARS-CoV-2) diagnostics. *Diagnosis* **2021**, *8* (1), 27-31.
258. Dinnes, J.; Deeks, J. J.; Berhane, S.; Taylor, M.; Adriano, A.; Davenport, C.; Dittrich, S.; Emperador, D.; Takwoingi, Y.; Cunningham, J., Rapid, point-of-care antigen and molecular-based tests for diagnosis of SARS-CoV-2 infection. *Cochrane Database of Systematic Reviews* **2021**, (3).
259. Liotti, F. M.; Menchinelli, G.; Lalle, E.; Palucci, I.; Marchetti, S.; Colavita, F.; La Sorda, M.; Sberna, G.; Bordi, L.; Sanguinetti, M., Performance of a novel diagnostic assay for rapid SARS-CoV-2 antigen detection in nasopharynx samples. *Clinical Microbiology and Infection* **2020**.
260. Syamchand, S.; Sony, G., Europium enabled luminescent nanoparticles for biomedical applications. *Journal of Luminescence* **2015**, *165*, 190-215.
261. Kundu, J.; Ghosh, Y.; Dennis, A. M.; Htoon, H.; Hollingsworth, J. A., Giant nanocrystal quantum dots: stable down-conversion phosphors that exploit a large stokes shift and efficient shell-to-core energy relaxation. *Nano letters* **2012**, *12* (6), 3031-3037.

262. Harris, C. R.; Millman, K. J.; Van Der Walt, S. J.; Gommers, R.; Virtanen, P.; Cournapeau, D.; Wieser, E.; Taylor, J.; Berg, S.; Smith, N. J., Array programming with NumPy. *Nature* **2020**, 585 (7825), 357-362.
263. Hunter, J. D., Matplotlib: A 2D graphics environment. *Computing in science & engineering* **2007**, 9 (03), 90-95.
264. Zhao, J.; Lui, H.; McLean, D. I.; Zeng, H., Automated autofluorescence background subtraction algorithm for biomedical Raman spectroscopy. *Applied spectroscopy* **2007**, 61 (11), 1225-1232.
265. de Rooi, J. J.; Eilers, P. H., Mixture models for baseline estimation. *Chemometrics and Intelligent Laboratory Systems* **2012**, 117, 56-60.
266. Virtanen, P.; Gommers, R.; Oliphant, T. E.; Haberland, M.; Reddy, T.; Cournapeau, D.; Burovski, E.; Peterson, P.; Weckesser, W.; Bright, J., SciPy 1.0: fundamental algorithms for scientific computing in Python. *Nature methods* **2020**, 17 (3), 261-272.

# Appendix A: Supporting Information for Chapter 6

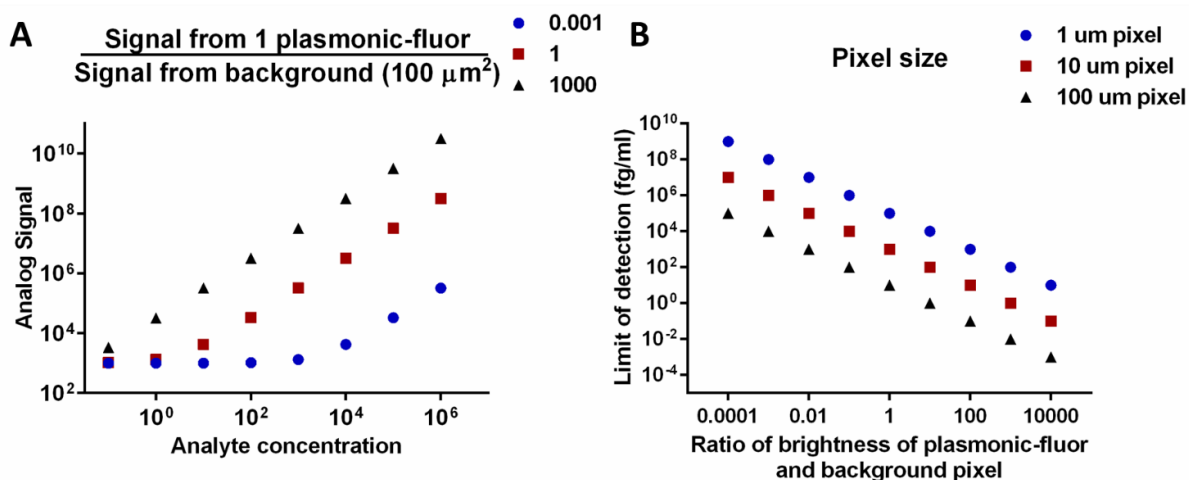


**Figure A- 1:** Image of a single plasmonic-fluor collected using an epifluorescence microscope using a 20x objective along with line-scan to measure the change in the mean intensity of plasmonic-fluor with respect to that of background.

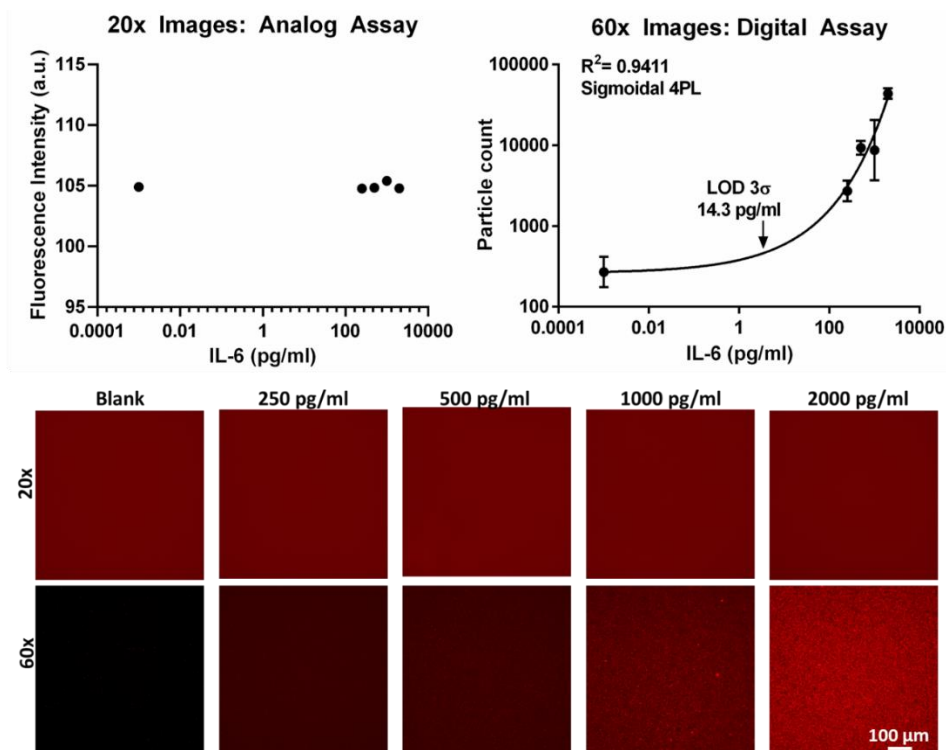


**Figure A- 2:** FLISA of human IL-6 performed using quantum dots (QDs). Fluorescence intensity vs. concentration plot for FLISA calculated from (A) 20x images and (B) 60x images, n=2. C) 20x and 60x epifluorescence microscopic images of FLISA using quantum dots.

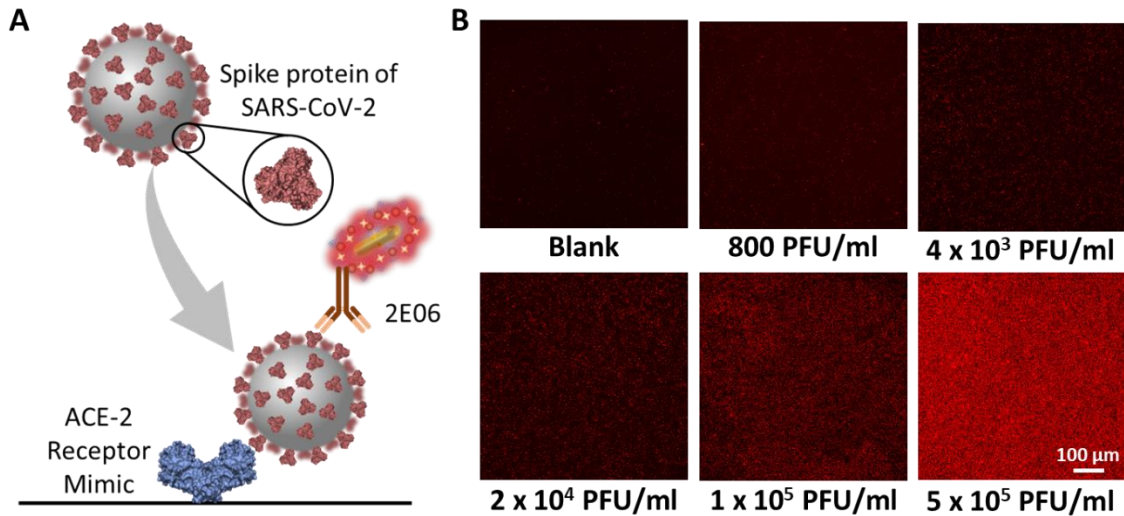


**Figure A- 3:** (A) Schematic illustration of the digital p-FLISA of spike protein in SARS-CoV-2 virion. (B) Epifluorescence microscopic images of digital p-FLISA of SARS-CoV-2 virion. n=2 (5 images per well).

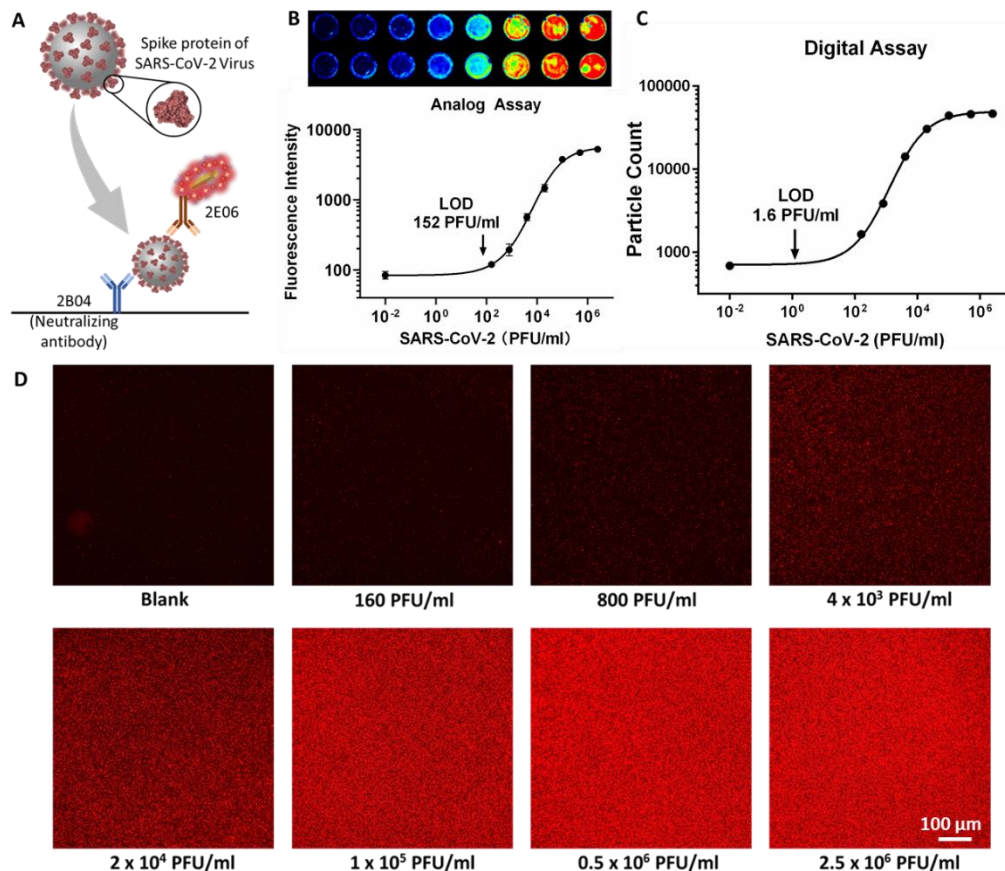




**Figure A- 4:** Analog vs. digital plasmonic-FLISA (p-FLISA) of SARS-CoV-2 virion. **(A)** Schematic illustration of the experiment. **(B)** Fluorescence image and fluorescence intensity vs. concentration plot for p-FLISA. n=2. **(C)** Particle count vs. concentration plot of digital p-FLISA and **(D)** epifluorescence microscopic images of digital p-FLISA of SARS-CoV-2 virion. n=2 (5 images per well). Analog p-FLISA  $R^2=0.9964$ , digital p-FLISA  $R^2=0.9986$ .

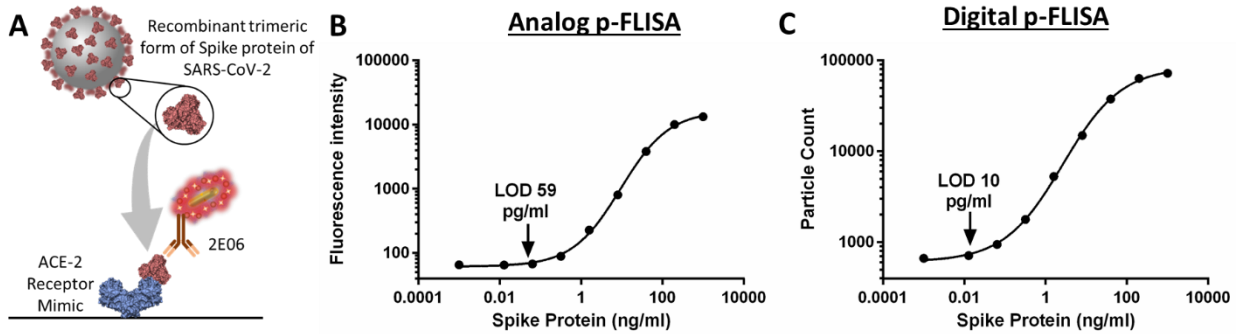


**Figure A- 5:** Analog vs. digital plasmonic-FLISA (p-FLISA) of recombinant spike protein (S-protein). **(A)** Schematic illustration of the experiment S protein. **(B)** Fluorescence intensity vs. concentration plot for S protein analog p-FLISA. n=2. **(C)** Particle count vs. concentration plot of S protein digital p-FLISA. n=2 (5 images per well). Analog p-FLISA  $R^2=0.9991$ , digital p-FLISA  $R^2=0.9994$ .

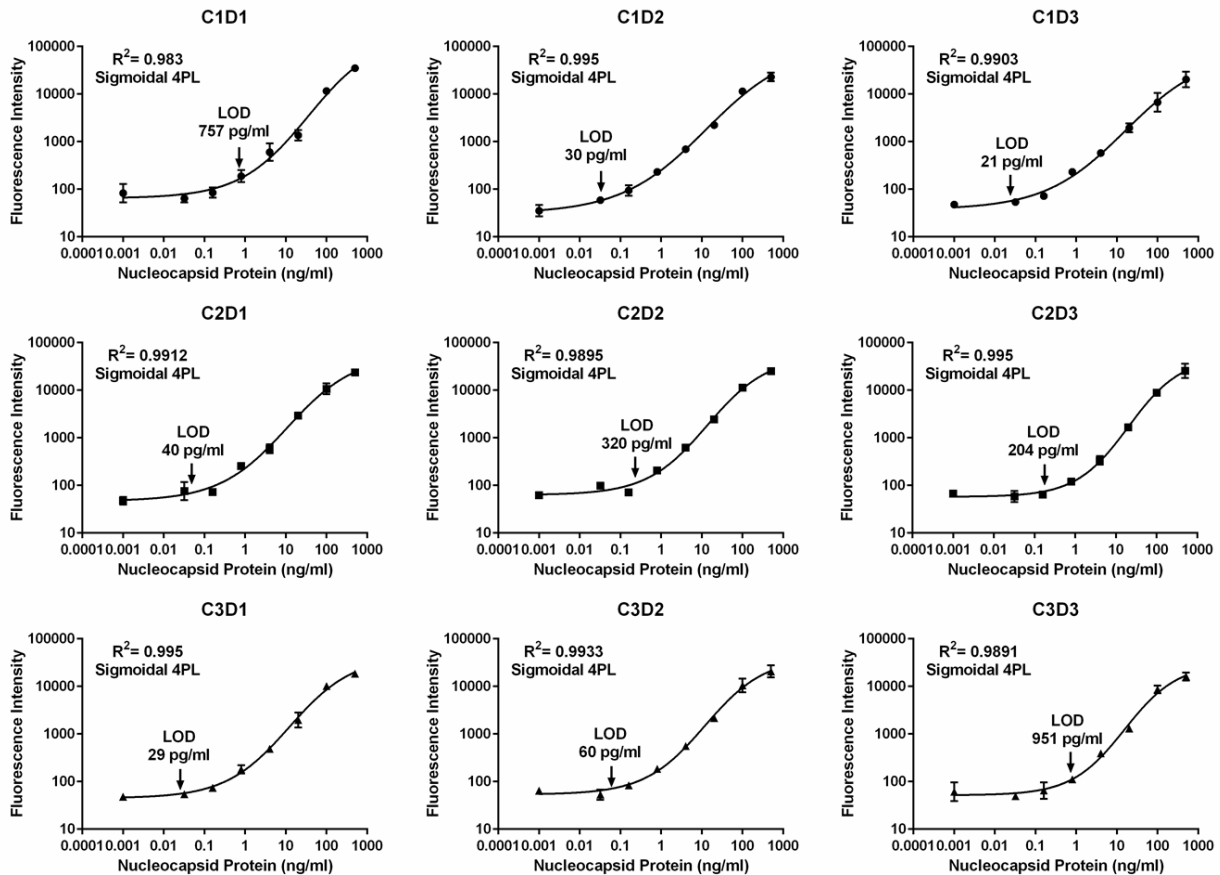


**Figure A- 6:** Optimization of N protein capture and detection for implementation in p-FLISA. (n=2) Dilution factors tested are mentioned in the table.

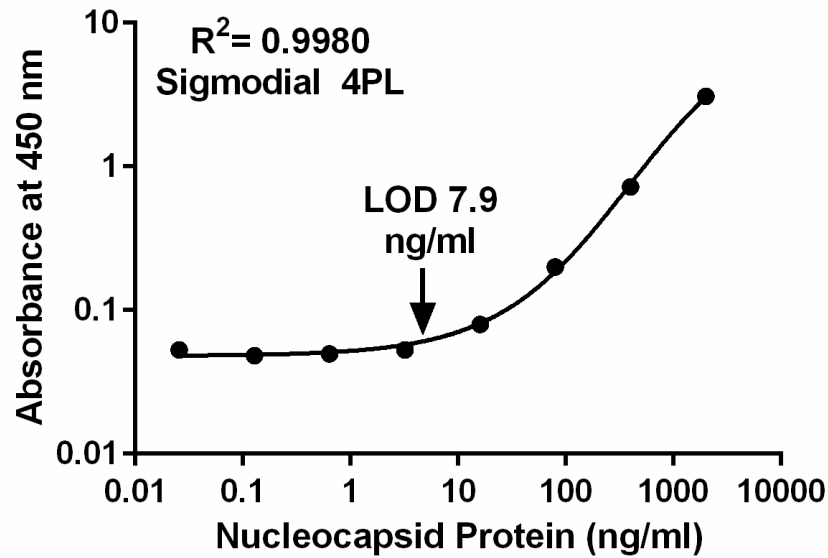


**Figure A- 7:** ELISA of recombinant nucleocapsid protein in SARS-CoV-2

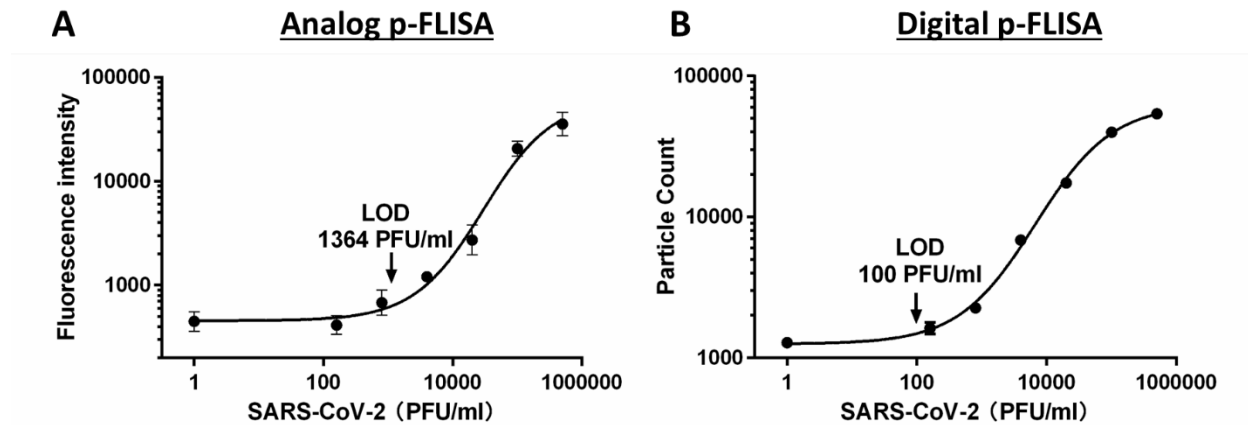


**Figure A- 8:** Analog vs. digital plasmonic-FLISA (p-FLISA) of nucleocapsid protein in SARS-CoV-2 virion. (A) Fluorescence intensity vs. concentration plot for p-FLISA. n=2. (B) Particle count vs. concentration plot of digital p-FLISA. n=2 (5 images per well). Analog p-FLISA R<sup>2</sup>= 0.9795, digital p-FLISA R<sup>2</sup>= 0.9976.

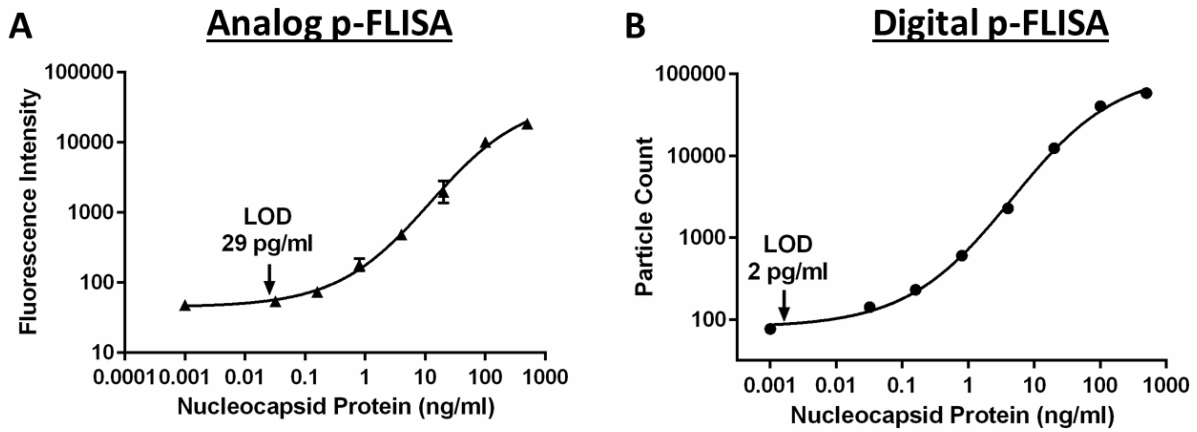


**Figure A- 9:** Analog vs. digital plasmonic-FLISA (p-FLISA) of recombinant nucleocapsid protein in UTM. A) Fluorescence intensity vs. concentration plot for p-FLISA. n=2. B) Particle count vs. concentration plot of digital p-FLISA. n=2 (5 images per well). Analog p-FLISA  $R^2= 0.9950$ , digital p-FLISA  $R^2= 0.9978$ .

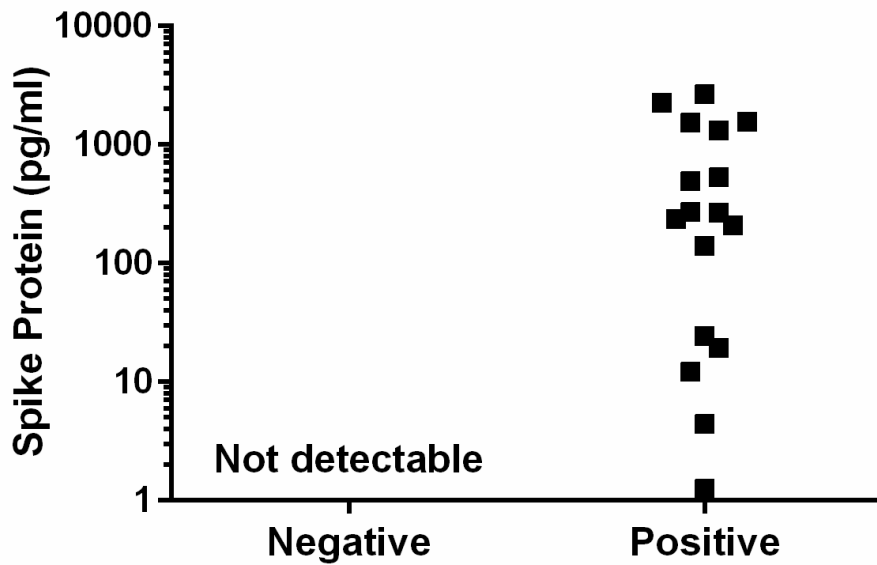


**Figure A- 10:** S protein in PCR-positive and PCR-negative human swabs and saliva.

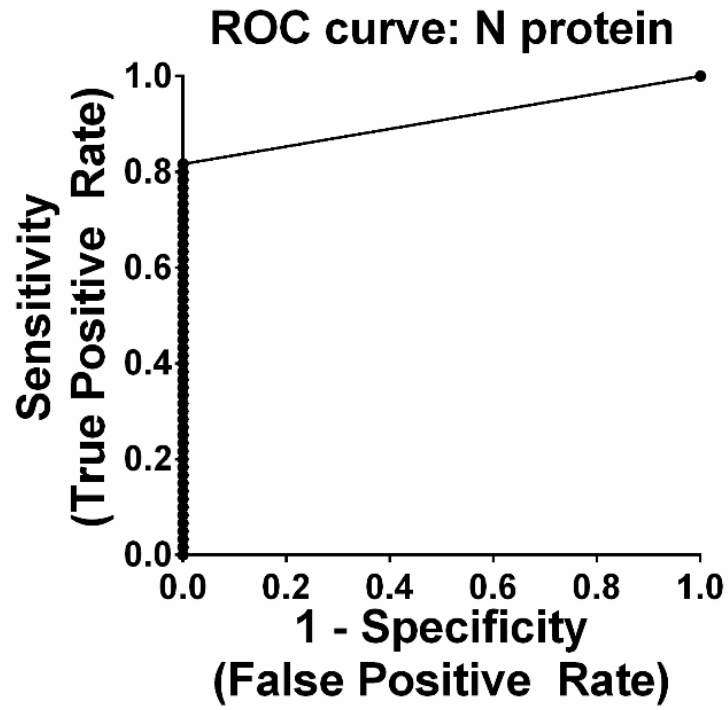


**Figure A- 11:** Receiver operating characteristic curve for N protein digital pFLISA.

# Appendix B: Supporting Information for

## Chapter 7

### Human IL-6 enzyme-linked immunosorbent immunoassay

Human IL-6 ELISA was carried out according to the procedure mentioned in DuoSet ELISA kit manual. Specifically, wells were first coated with 100  $\mu\text{l}$  2  $\mu\text{g ml}^{-1}$  (in 1X PBS) of capture antibodies via overnight incubation at room temperature. Next for blocking, 300  $\mu\text{l}$  of reagent diluent (1X PBS containing 3% BSA, 0.2  $\mu\text{m}$  filtered) was incubated in wells for minimum of 1 h. Next, 100  $\mu\text{l}$  of serially diluted standard samples were incubated for 2 h, followed by incubation of 100  $\mu\text{l}$  50  $\text{ng ml}^{-1}$  biotinylated detection antibodies for 2 h. Next, 100  $\mu\text{l}$  of streptavidin labelled horseradish peroxidase (200-fold diluted using reagent diluent) was incubated for 20 min, followed by incubation of 100  $\mu\text{l}$  of substrate solution, 1:1 mixture of color reagent A ( $\text{H}_2\text{O}_2$ ) and B (tetramethylbenzidine) (R&D Systems, DY999) for 20 min. The reaction was stopped by addition of 50  $\mu\text{l}$  2N  $\text{H}_2\text{SO}_4$  (R&D Systems, DY994) and immediately after the optical density at 450 nm was measured using a microplate reader.

### Biotinylation of anti-human IgG

Using EDC–NHS chemistry, antibodies were conjugated with biotin. First NHS-PEG4-biotin solution was prepared by addition of 170  $\mu\text{l}$  of nanopure water in 2 mg of NHS-PEG4-biotin (Thermo Scientific, 21329). Next, mixture of 1 ml 2  $\text{mg ml}^{-1}$  of anti-human IgG (Rockland, 609-4617) in 1X PBS and 30  $\mu\text{l}$  NHS-PEG4-biotin solution were incubated at room temperature for

1 h. Biotinylated anti-human IgG was purified by 7,000 MWCO desalting column (Thermo Scientific, 21329).

## **Biotinylation of N protein detection antibody**

Using EDC–NHS chemistry, N protein detection antibodies were conjugated with biotin. First NHS-PEG4-biotin solution was prepared by addition of 170  $\mu$ l of nanopure water in 2 mg of NHS-PEG4-biotin (Thermo Scientific, 21329). Next, mixture of 400  $\mu$ l of as received N protein detection antibody (SinoBiologicals, 40143-R004) in 1X PBS and 5  $\mu$ l NHS-PEG4-biotin solution were incubated at room temperature for 1 h. Biotinylated N protein detection antibody was purified by 7,000 MWCO desalting column.

## **Antibody conjugation on plasmonic-fluor**

Streptavidin-conjugated plasmonic-fluor (40  $\mu$ l, extinction 32) was added to 50  $\mu$ l of 4.5  $\mu$ g/ml biotinylated anti-human IgG and biotinylated detection antibody for N protein at room temperature. The solution was incubated for 0.5 h and washed thrice with pH 10 water. For washing conjugated plasmonic-fluor was centrifuged at 6,000 rpm (2800 g) for 10 minutes. Finally, the pellet was resuspended in 1% BSA in 1x PBS and stored in 4 C for further use in immunoassays.

## **RMC calculations**

The RMC is a recently introduced bioanalytical parameter that helps in determining whether the signal of an unknown concentration  $\mu_x$  can be distinguished from the signal of a certain concentration,  $x$ , at a certain confidence level for a 2-sided t-test.<sup>251</sup> A molecular assay can be considered ‘good’ if it can resolve <100% changes in the concentration of analyte along a

clinically meaningful concentration range. In other words, the RMC ( $\mu$ ) should be below 2 over the desired concentration range.<sup>251</sup> In our case, we defaulted to the 99% confidence interval to determine the range of concentration for which  $\mu$  is below 2. This stringent criteria in determining the RMC of p-LFA helps us in identifying the working concentration of the p-LFA in a standard-free manner with 99% certainty.

For example, a  $\mu$  value of 1.4511 at  $x = 2.47$  pg/mL (**Figure B-47**) would mean that at 2.47 pg/mL, p-LFA can distinguish 45.11% change (*i.e.* 2.47 to 3.58 pg/mL) in concentration with 99% confidence. Furthermore, since the concentration range over which  $\mu < 2$  is 0.1292–86.08 pg/mL, IL-6 p-LFA can distinguish the signal corresponding to any two concentrations that differ by at least 100% within that range with at least 99% confidence. We also evaluated the  $\mu < 5$  range (0.0281–180.979 pg/mL) because our dose responses were performed with 5-fold serial dilutions and this measurement gives another point of evaluation for comparison of assay performance of p-LFA, p-FLISA, and ELISA (**Figure B-47**).

To calculate the RMC, we first fitted our dose response data with the following Langmuir Binding Isotherm function for a signal-on assay using OriginPro's function builder:

$$S(x) = (S_{max} - S_0) \frac{x}{x + K_D} + S_0$$

Next, we calculated the RMC values and parameters according to the equations mentioned below:<sup>251</sup>

$$\frac{Z}{\sqrt{3}} = \frac{|S(\mu x) - S(x)|}{\sqrt{(\sigma_{S(x)})^2 + (\sigma_{S(\mu x)})^2}}$$

where is determined via following error propagation equation:

$$\sigma_s = \sqrt{\sum_{i=1}^n \left(\frac{\partial S}{\partial c_i} \sigma_{c_i}\right)^2} \quad \text{where } c_i = \{S_{\max}, S_0, KD\}$$

Z is the critical value and is equal to 4.604 for a 2-sided t-test with 4 degrees of freedom corresponding to a 99% confidence interval.

RMC calculations were then performed via Python3. Our code outputs an excel file with x (concentration in the same units as original dose response) values, their corresponding  $\mu$  values with an insignificant  $\pm 0.0008$  units of uncertainty. The minimum  $\mu$  value and the range where  $\mu$  is under 2 and 5, are printed in the Python3 shell. The uncertainty in  $\mu$  comes from how our code solves the RMC equation implicitly by incrementing  $\mu$  by 0.0004 units to estimate what  $\mu$  value equals the constant on the left side of the equation. NumPy<sup>262</sup> and Matplotlib<sup>263</sup> packages were used to aid these calculations. The Python3 Code for RMC can be found at <https://github.com/seanwangsalad/PythonRMC>.

## **Data processing on the data acquired by portable scanner:**

The portable fluorescence scanner outputs each data point in the form of the average pixel value (signal intensity) versus the travel length of LFA strip through the scanner by 100  $\mu\text{m}$  increments. Subsequently, Python3 was used to perform baseline correction, a process that normalizes the data and separates the true fluorescence signals from the background noise. This correction was performed by using the iModPoly algorithm<sup>264</sup> followed by another correction with the Mixture Model algorithm<sup>265</sup>, which were both provided in the pybaselines package (*GitHub Repository: <https://github.com/derb12/pybaselines>*). For ease of data processing, the first 25 data points were truncated as the test/control lines were printed from x=60 to 150 (6 to 15 mm).



Truncated regions are represented with 0 signal intensity. For example, in **Figure B-32**, the region of 0-2.5 or 0-25 data points were set to 0.

After baseline correction, relevant/key local minima and maxima were calculated. Since the test line was printed at around 11 mm along the LFA strip, the largest maxima nearest to this point is chosen as the signal's apex. Subsequently, 2 local minima based on the mean of the pairs that were closest to that maximum were chosen. The centroid of these 3 points estimates the center of the test line's signal area. These calculations were aided by NumPy<sup>262</sup> and SciPy packages<sup>266</sup>. In addition, Matplotlib was used to generate all representations.<sup>263</sup>

**Data processing for LFA strip drop-casted with known concentrations of nanolabels:** To find the total signal produced by the test line, integration of the signal intensity curve within a range of  $\pm 2.5$  mm (plasmonic-fluor) or  $\pm 2.0$  mm (molecular fluorophore, 800CW) from the centroid was implemented. These ranges were determined by the range that the highest concentration of drop-casted nanolabels encompassed (**Figure B-32 and 33**). For all further tests we used the same range for signal integration. As representative examples of data processing in **Figure B-32 and 33** we show the original and corrected processed data for low and high concentrations, ( $\sim 10^6$  and  $\sim 10^3$  for plasmonic-fluors and  $\sim 10^{11}$  and  $\sim 10^6$  for molecular fluorophores) and blank data points corresponding to plasmonic-fluor and molecular fluorophore nanolabels, respectively.

**Data processing for p-LFA strip subjected to standard target analyte:** p-LFA strips contain both test line and fluorometric control line are expected to exhibit either one or two peaks: a positive reading will result in two peaks and a negative result would result in one peak occurring at the control line. In both cases, our code automatically truncates the data corresponding to the region where the control line is printed ( $x > 125$  data points or  $> 12.5$  mm) before baseline

correction and integration. However, if a test were to have no signal at the control line, our code will report it as an invalid test result. As an example, please refer to **Figure B-38 and 40** which show the above-described truncation process of the data acquired from p-LFA strip exposed to known concentration of IL-6 and N protein, respectively.

**Data processing for p-LFA strip subjected to patient samples:** Data processing for p-LFA strips subjected to patient samples use the same methods described above. However, due to the varying amount of non-specific proteins or debris in the patient samples, there may be varying background signal that can interfere with baseline correction. For example, in case of **Figure B-45**, if there is signal downstream of the test line that is greater than 50% of the test line, the code will truncate the region after the printed test line ( $x > 125$  data points or  $> 12.5$  mm) before baseline correction and integration as shown in **Figure B-45**.

The code for the software can be found at:

<https://github.com/seanwangsalad/AreaUnderCurveForLFARreader>.

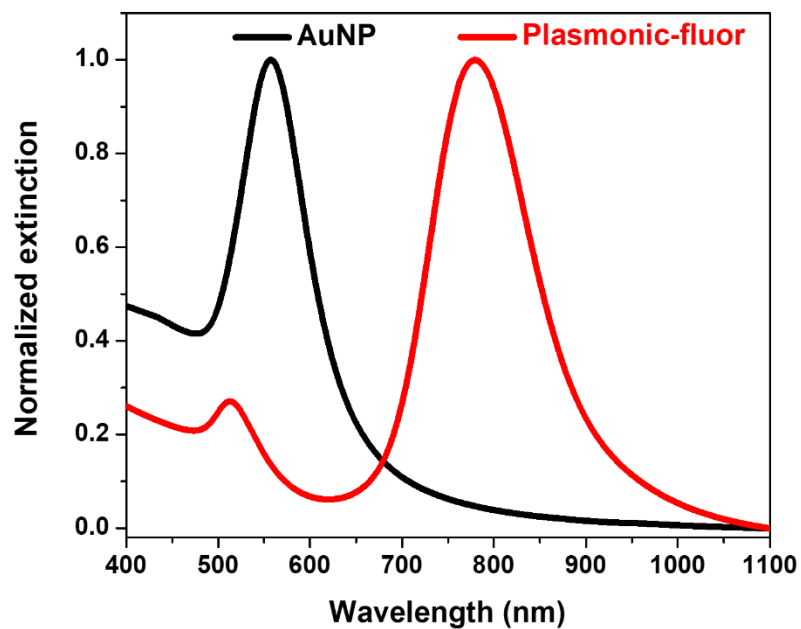


**Figure B- 1:** Visible-NIR extinction spectra of streptavidin functionalized AuNPs (black) and plasmonic-fluors (red).

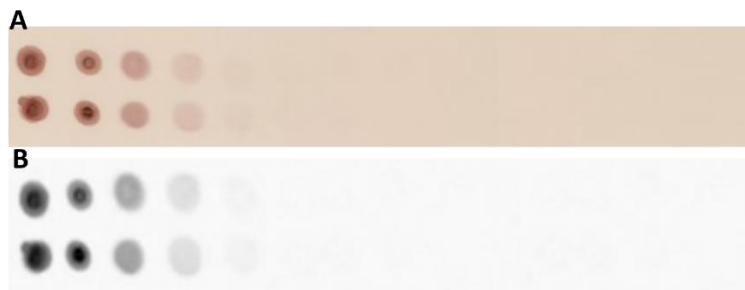


**Figure B- 2:** (A) Digital photograph of a strip drop-casted with different concentrations of AuNPs. (B) 8-bit ImageJ processed image.

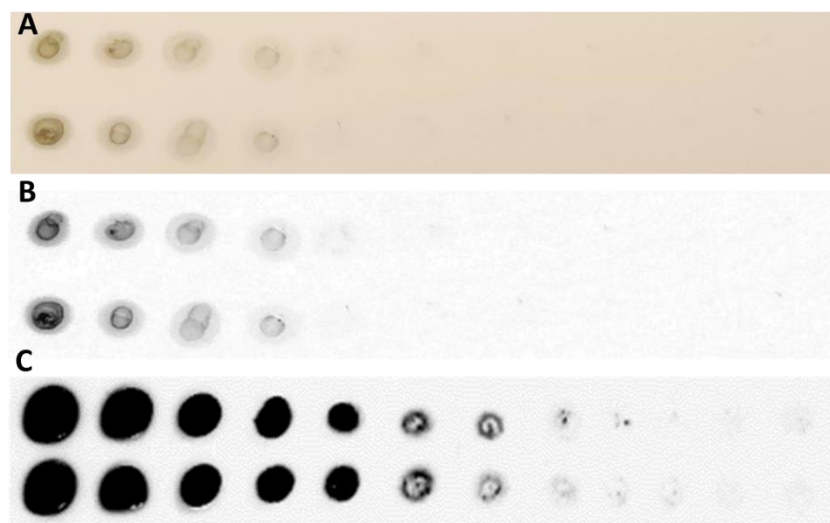


**Figure B- 3:** (A) Digital photograph of the strip drop-casted with different concentrations of plasmonic-fluors. (B) 8-bit ImageJ processed image. (C) Corresponding fluorescence image of the nitrocellulose membrane.

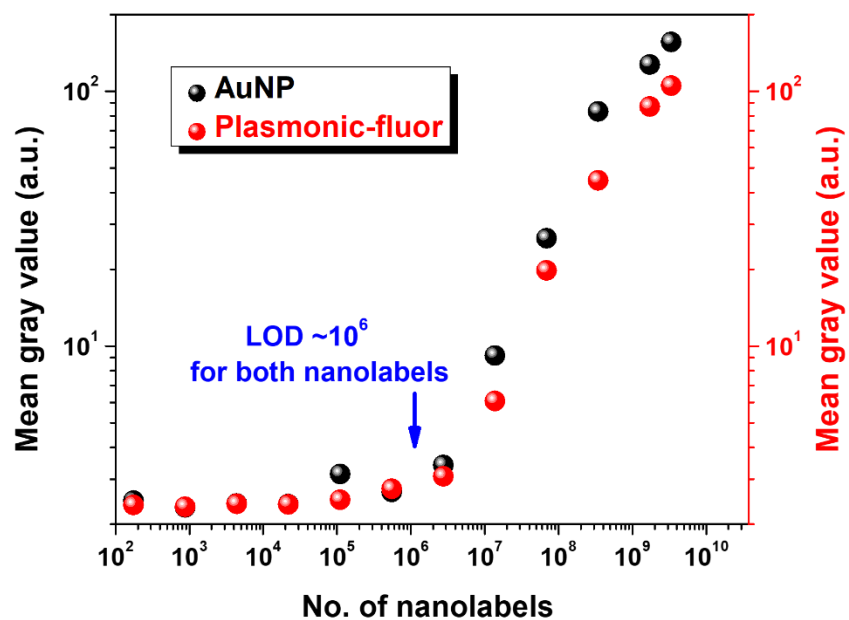


**Figure B- 4:** Mean gray values obtained from nitrocellulose membrane drop-casted with different concentrations of AuNPs (black) and plasmonic-fluors (red).

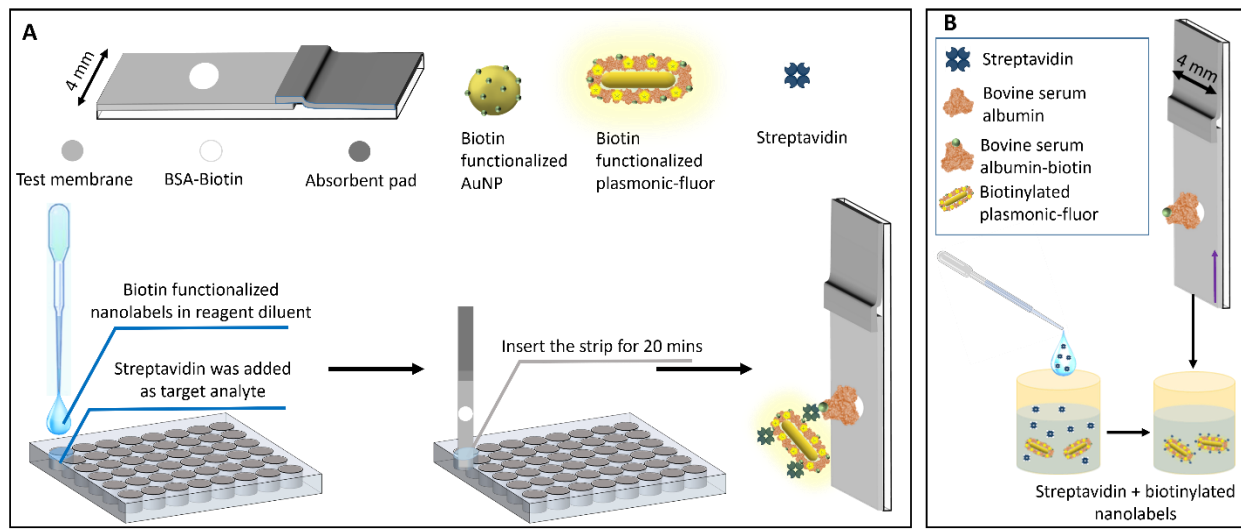


**Figure B- 5:** Schematic representation of **(A)** biotin-streptavidin lateral flow assay and **(B)** corresponding work-flow of p-LFA.

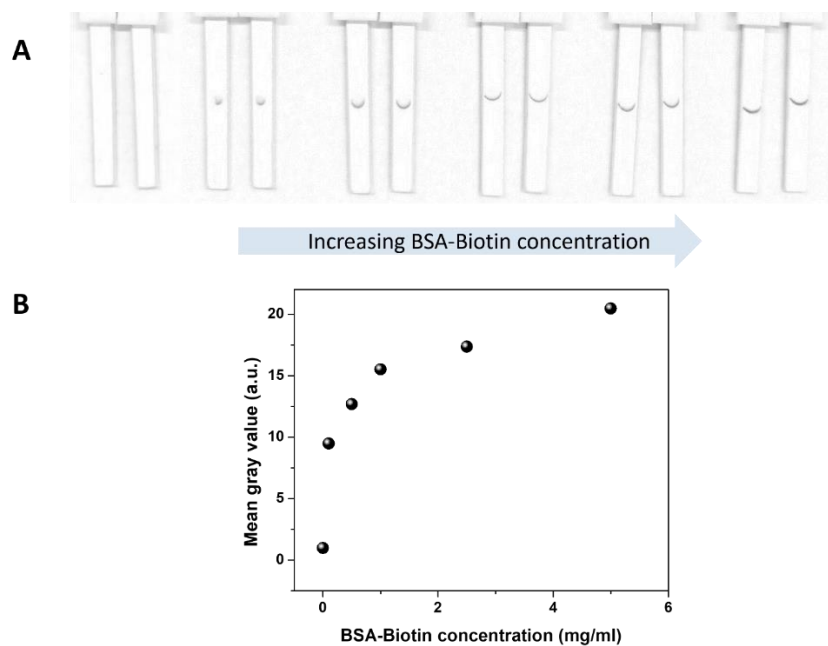


**Figure B- 6:** **(A)** Image of the LFA strips (after Image J processing), with different concentrations of BSA-Biotin as capture spot, after exposure to the same concentration of streptavidin as target analyte and biotin-functionalized AuNPs. **(B)** Corresponding mean gray values as a function of BSA-Biotin concentration.

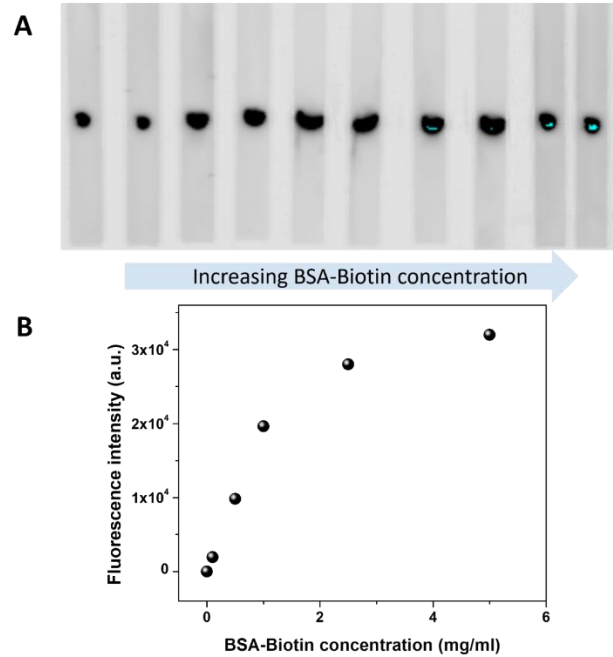


**Figure B- 7:** (A) Fluorescence image of the LFA strips, with different concentrations of BSA-Biotin as capture spot, after exposure to the same concentration of streptavidin as target analyte and biotin-functionalized plasmonic-fluors. (B) Corresponding fluorescence intensity as a function of BSA-Biotin concentration.

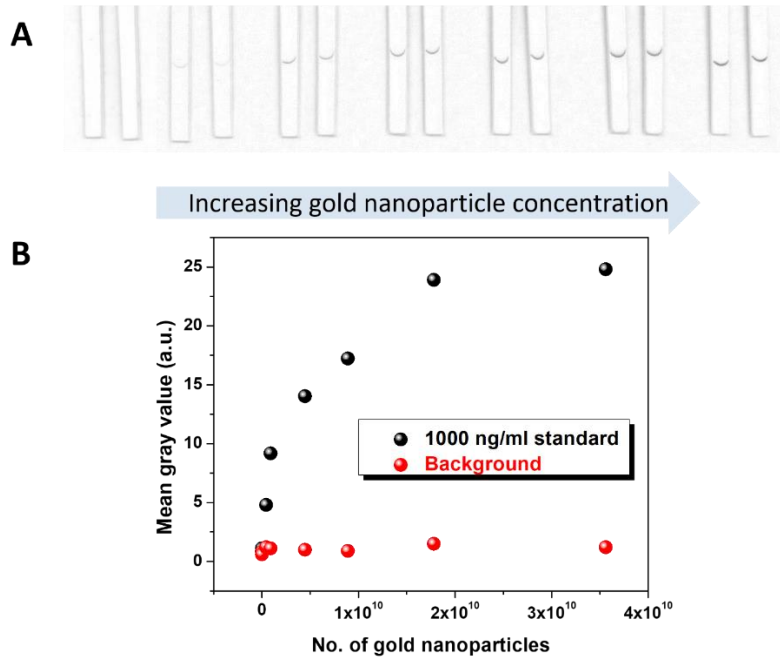


**Figure B- 8:** (A) 8-bit ImageJ-processed image of the nitrocellulose membranes with the same concentration of BSA-Biotin concentration after exposure to different concentrations of biotin

functionalized AuNPs, and identical concentrations of streptavidin as target analyte. **(B)** Corresponding mean gray values as a function of AuNP concentrations.

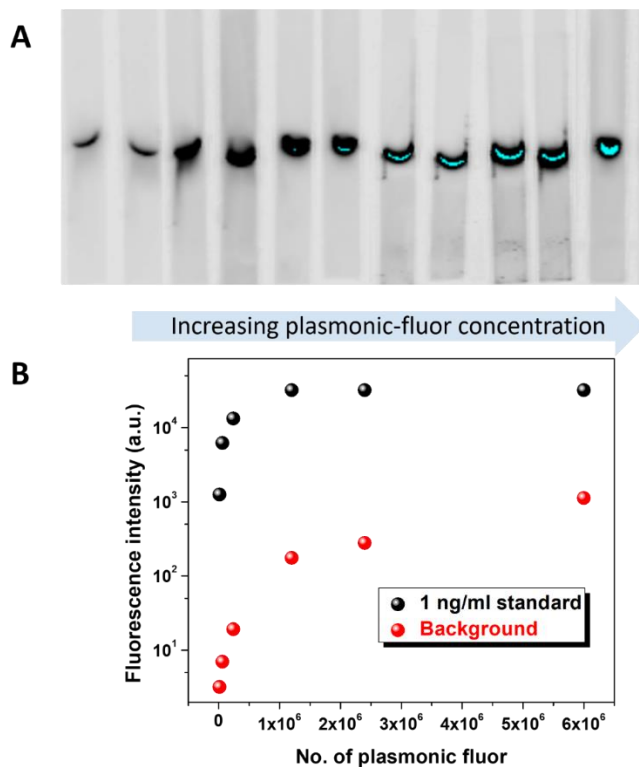


**Figure B- 9:** **(A)** Fluorescence image of LFAs with the same concentration of BSA-Biotin concentration after exposure to different concentrations of biotin functionalized plasmonic-fluors, and identical concentrations of streptavidin as target analyte. **(B)** Corresponding fluorescence intensity as a function of plasmonic-fluors concentration.

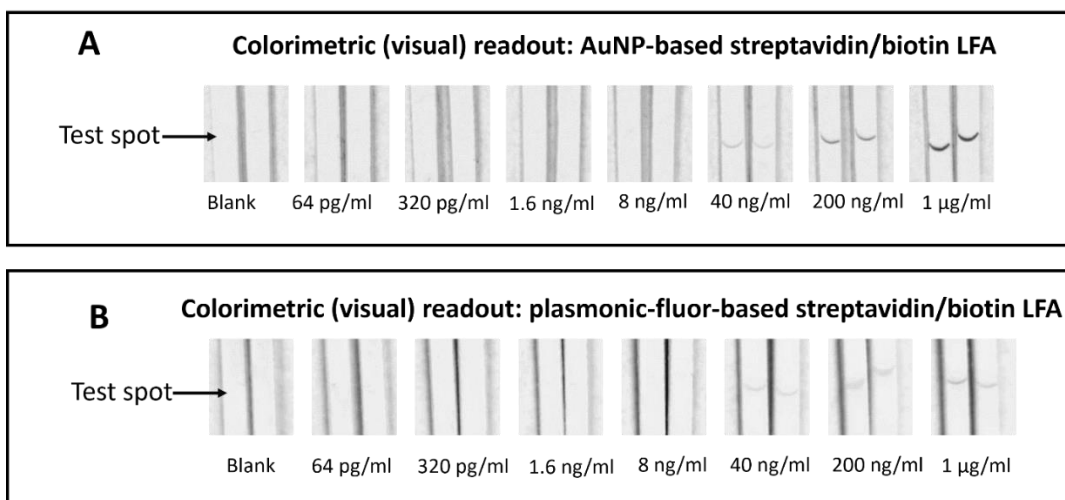


**Figure B- 10:** 8-bit ImageJ processed images of nitrocellulose membranes corresponding to (A) AuNPs-based streptavidin-biotin LFA and (B) streptavidin-biotin p-LFA depicting the visual or colorimetric readout mode.

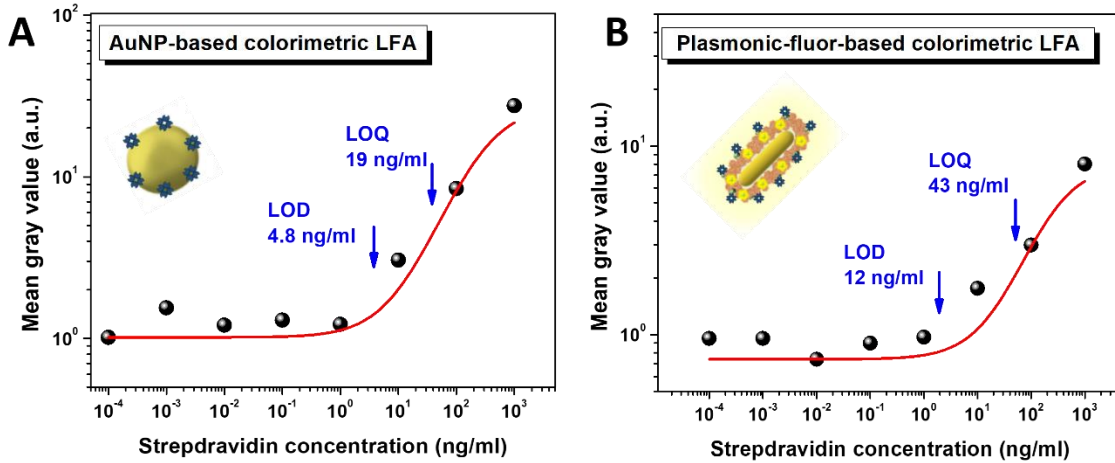


**Figure B- 11:** Dose-dependent mean gray values obtained from nitrocellulose membrane corresponding to different concentrations of streptavidin acquired from (A) AuNP-based and (B) plasmonic-fluor-based biotin-streptavidin LFA.

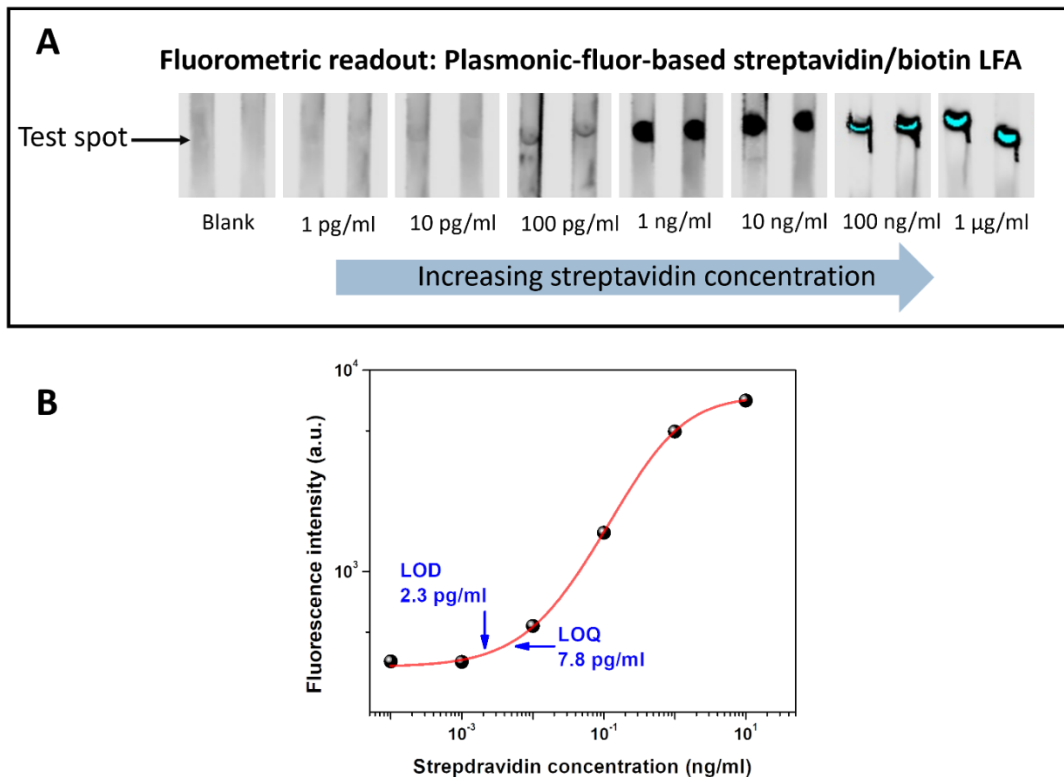




**Figure B- 12:** (A) Fluorescence image of the nitrocellulose membranes corresponding to streptavidin-biotin p-LFA strips depicting fluorometric readout mode. (B) Dose-dependent mean gray values obtained from nitrocellulose membrane corresponding to different concentrations of streptavidin acquired from streptavidin-biotin p-LFA.

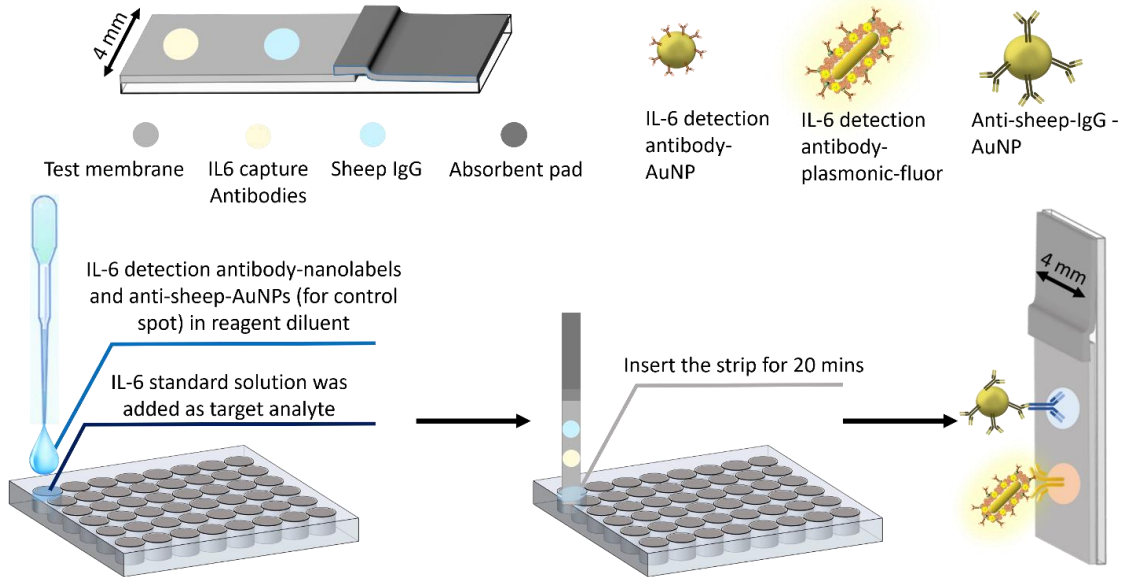


**Figure B- 13:** Schematic representation of IL-6 plasmonic-fluor-based lateral flow assay.

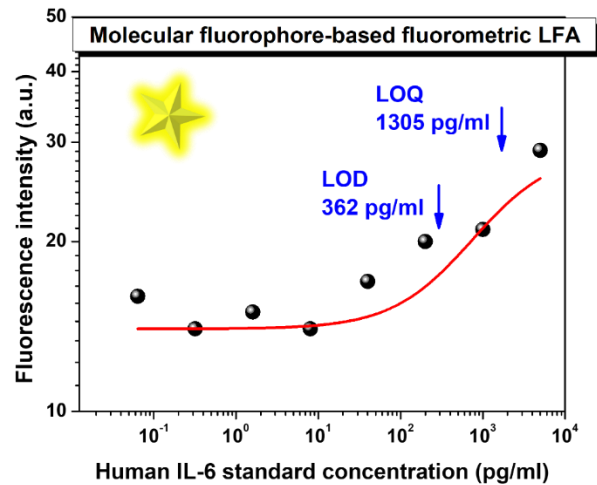


**Figure B- 14:** Dose-dependent fluorescence intensity values obtained from nitrocellulose membrane corresponding to different concentrations of IL-6 standards acquired from molecular fluorophore-based LFA.

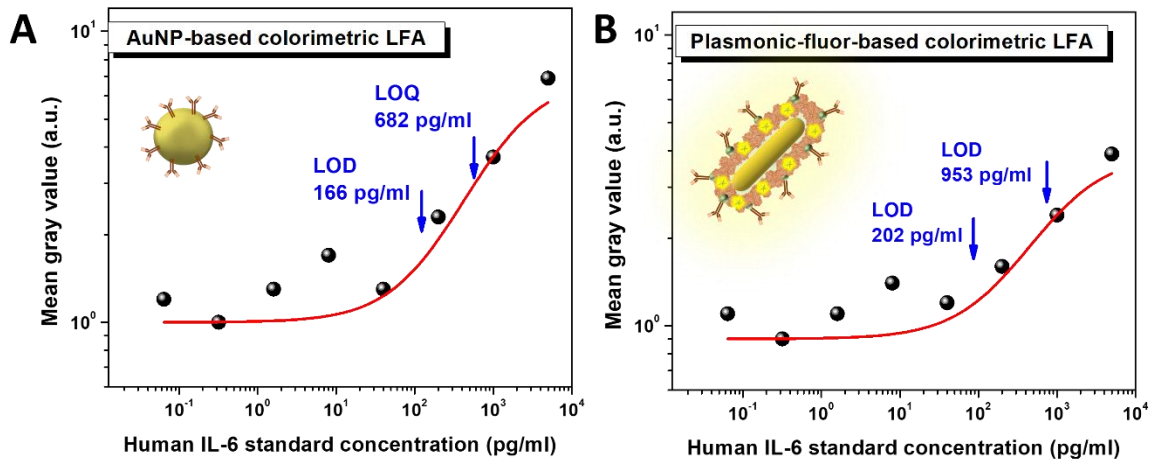


**Figure B- 15:** Dose-dependent mean gray values obtained from nitrocellulose membrane corresponding to different concentrations of IL-6 standards acquired from (A) AuNP-based and (B) plasmonic-fluor-based IL-6 LFA.

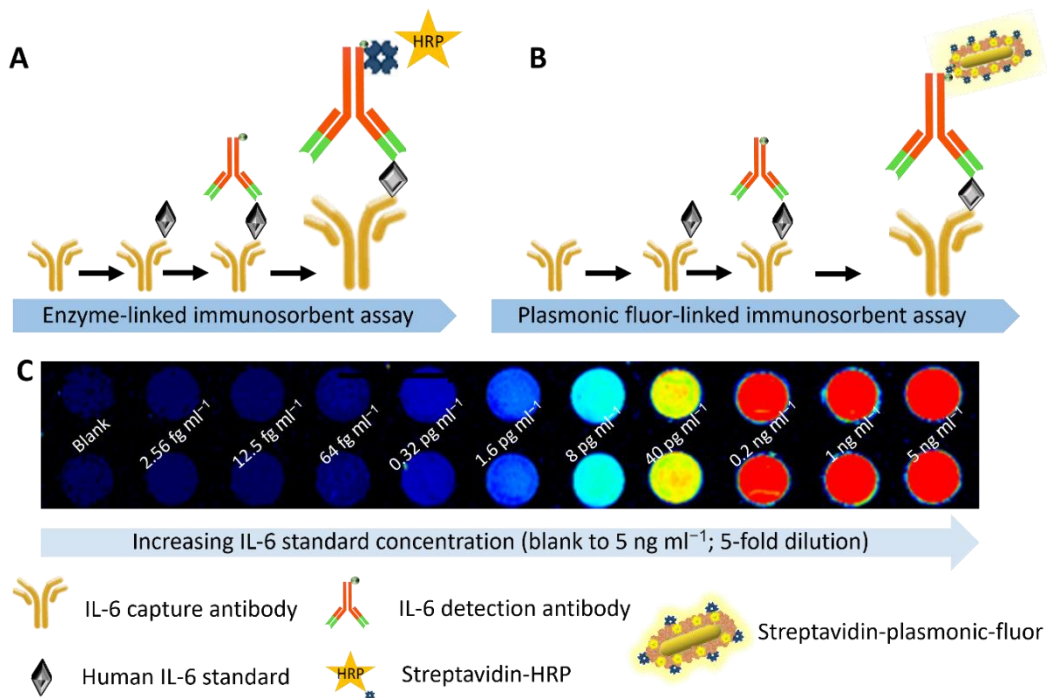


**Figure B- 16:** Schematic representation of (A) ELISA and (B) p-FLISA. (Bottom) Dose-dependent fluorescence intensity maps acquired by p-FLISA for different IL-6 concentrations.

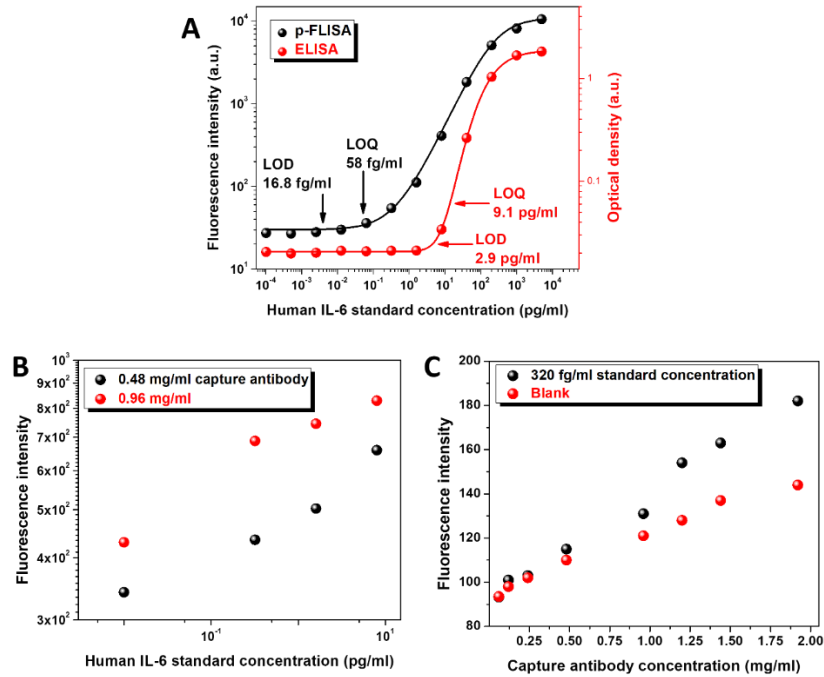


**Figure B- 17:** (A) Dose-dependent fluorescence intensities and optical densities, corresponding to different IL-6 concentrations in plasmonic fluor-linked immunosorbent assay (p-FLISA, black circles) and standard ELISA (red circles), respectively, implemented on a microtiter plate, performed in 4 h. (B) Dose-dependent mean gray values obtained from nitrocellulose membrane corresponding to different concentrations of IL-6 standards acquired from IL-6 p-LFA strips drop-casted with different capture antibody concentrations. (C) Fluorescence intensity obtained for blank and 320 fg/ml human IL-6 standard concentrations from p-LFA strips as a function of capture antibody concentration.

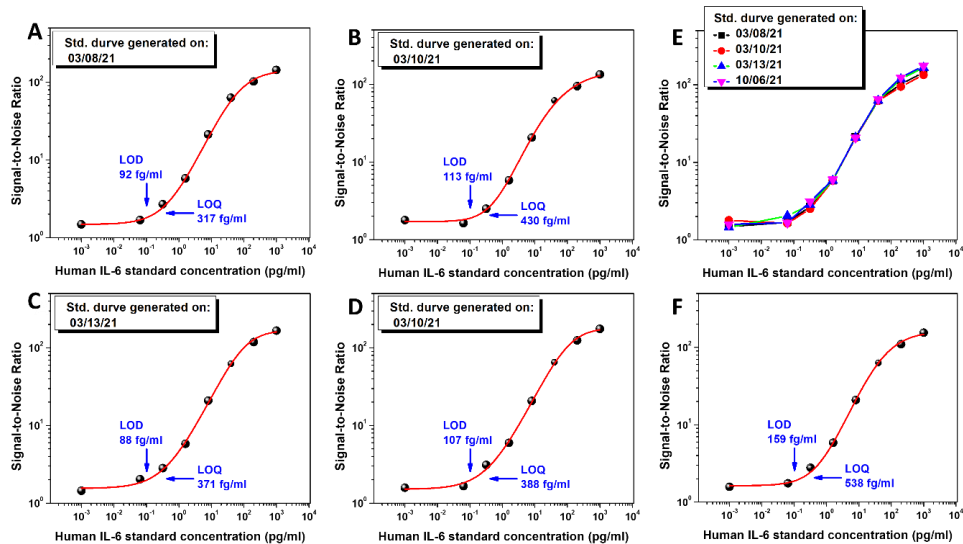


**Figure B- 18:** (A-D) Dose-dependent signal-to-noise ratio of multiple IL-6 p-LFA standard curves generated on different dates. (E) Overlaid dose-dependent signal-to-noise ratio of different standard curves

depicting minimal deviation from one another. **(F)** Dose-dependent signal-to-noise ratio obtained by taking the average values from all four standard curves and its bioanalytical parameters. Error bars in figure F represent standard deviations from 8 different samples.

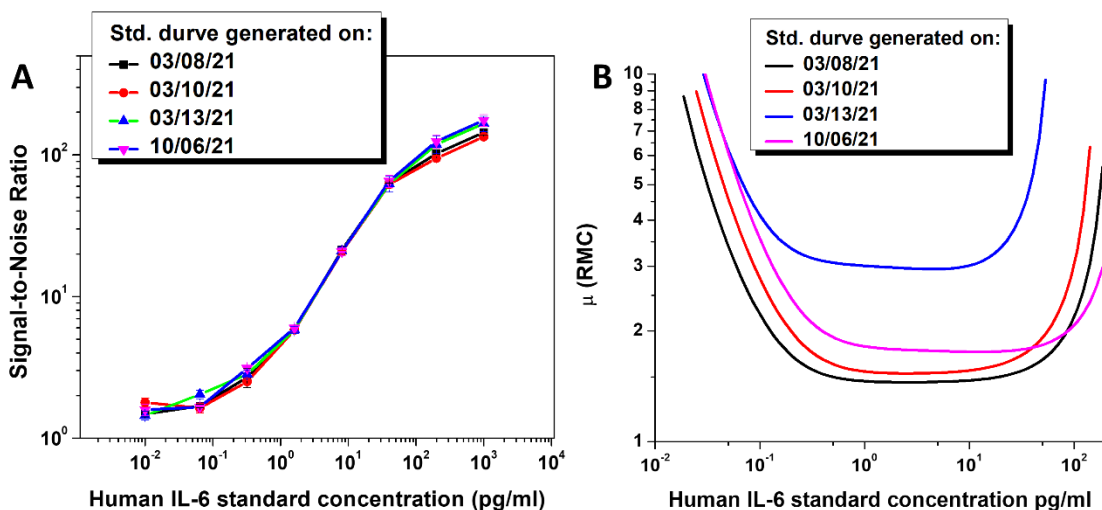


**Figure B- 19:** **(A)** Overlaid dose-dependent signal-to-noise ratio of different standard curves depicting minimal deviation from one another. **(B)** Resolution of molecular concentration (RMC) curves for four different standard curves.

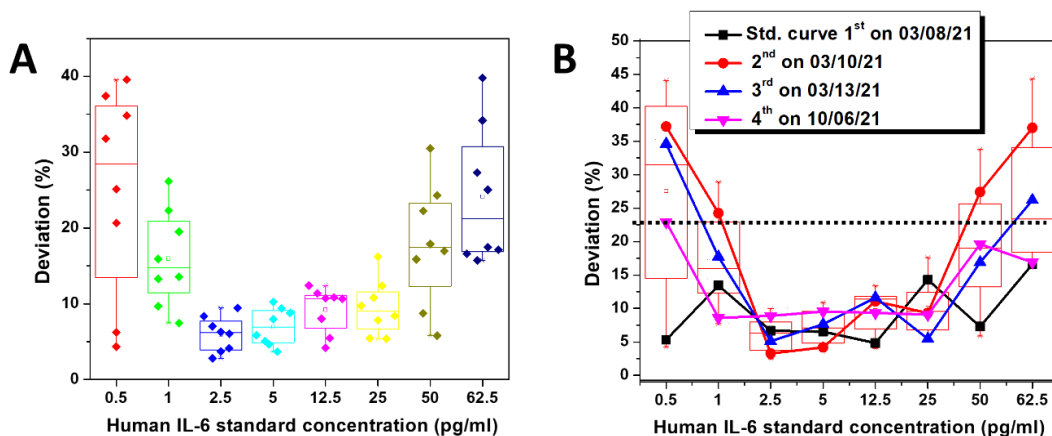


**Figure B- 20:** Multiple IL-6 standard curves were generated and samples with varying IL-6 concentrations (0.5 pg ml<sup>-1</sup> to 62.5 pg ml<sup>-1</sup>) were tested in standard-free manner. Their experimental concentrations were determined using each standard curve, and deviation from actual concentration was calculated. **(A)** Samples were tested in duplicates in standard-free manner and for each test, experimental values were determined using 4 standard curves, thus, 8 data points corresponding to each concentration are plotted in the box plot. **(B)** Deviation in the average experimental values of the samples corresponding to each standard curve. Center line is median; center square is mean; box limits are first and third quartile which are 25% and 75% respectively; 1.5 times of interquartile range is defined by cross marks; the upper whisker is the first number

that is less than upper quartile + 1.5 times of inter quartile range; Outliers are the data points located outside the 1.5 times of interquartile range.

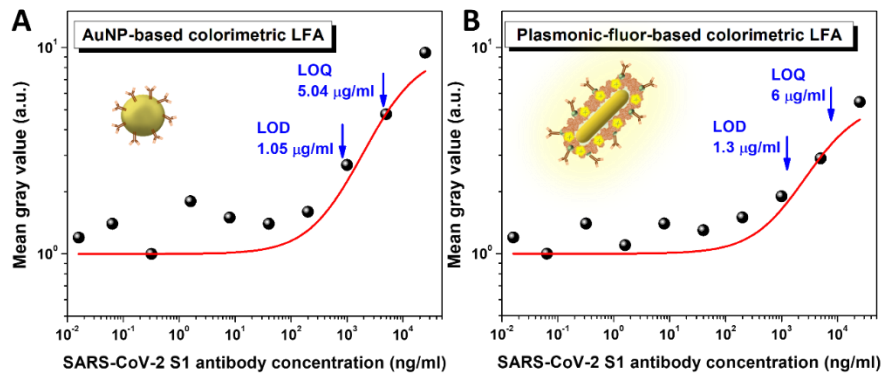


**Figure B- 21:** Dose-dependent mean gray values obtained from nitrocellulose membrane corresponding to different concentrations of SARS-CoV-2 S1 antibody solutions acquired from (A) AuNP-based and (B) plasmonic-fluor-based SARS-CoV-2 antibody LFA.

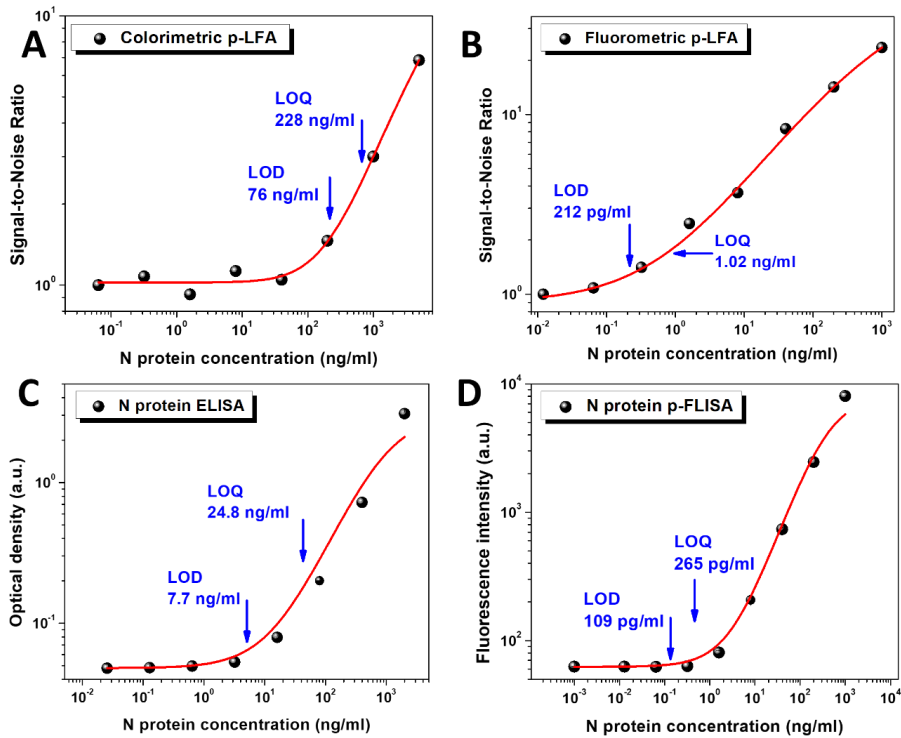


**Figure B- 22:** Dose-dependent signal-to-noise ratio of (A) colorimetric and (B) fluorometric p-LFA for detection of N protein. (C) Dose-dependent optical density corresponding to different concentrations of N protein in ELISA. (D) Dose-dependent fluorescence intensity corresponding to different concentrations of

N protein in plasmonic-fluor linked immunosorbent assay (p-FLISA). (C and D) Both the assays were implemented on microtiter plate and the sample-to-answer time was 4 h.

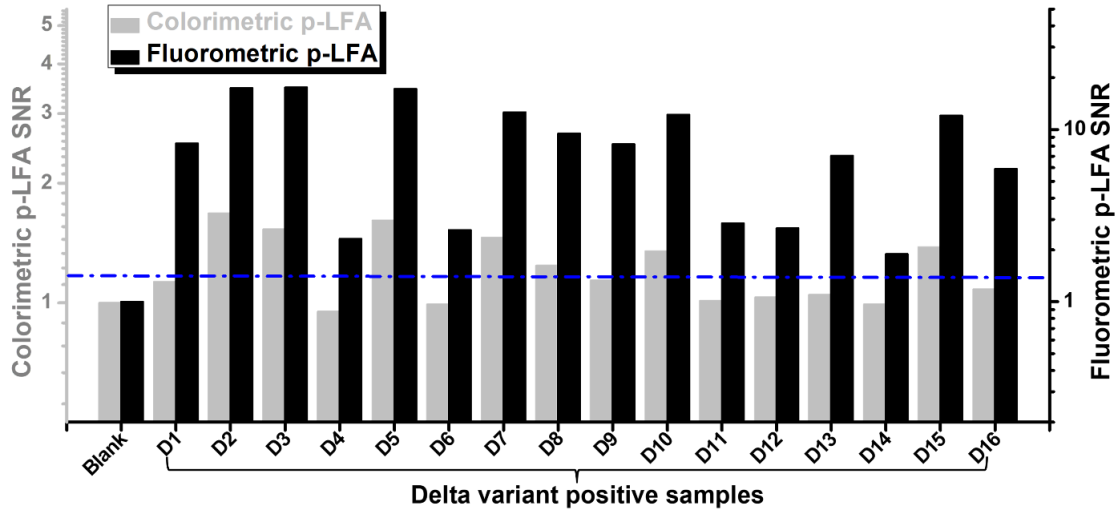


**Figure B- 23:** N-protein signal-to-noise ratio in PCR-positive Delta B.1.617.2 variant NP swab samples determined by colorimetric p-LFA (gray bars) and fluorometric p-LFA (black bars).

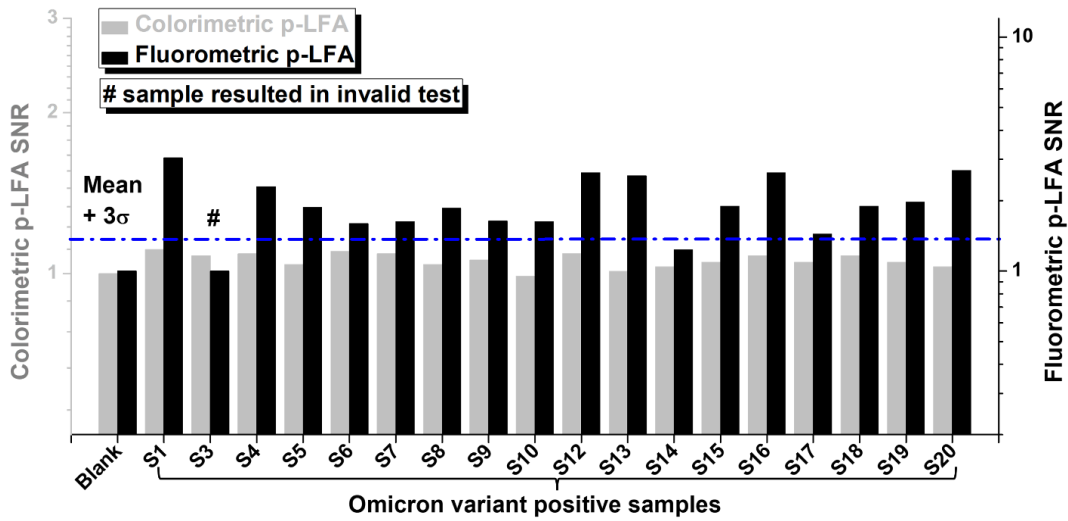


**Figure B- 24:** N-protein signal-to-noise ratio in PCR-positive Omicron BA.1 variant NP swab samples determined by colorimetric p-LFA (gray bars) and fluorometric p-LFA (black bars).

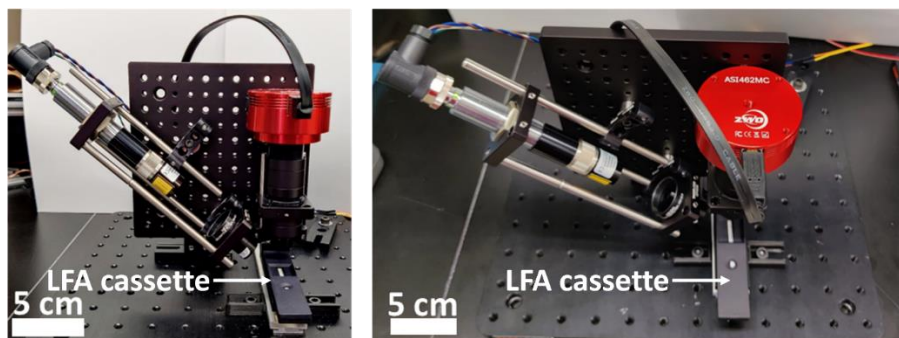


**Figure B- 25:** Photograph of the portable fluorescence scanner for different angle. The size of the scanner is 25 cm x 25 cm x 19 cm (LxBxH).

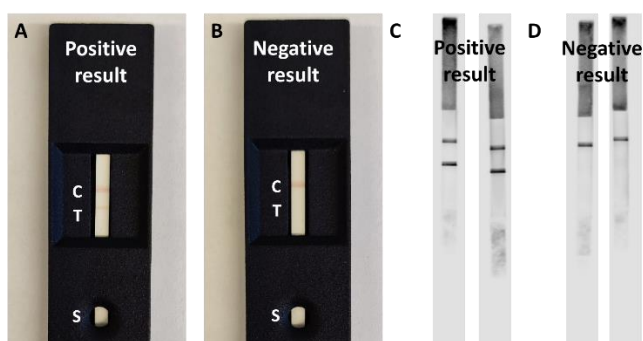


**Figure B- 26:** Photographs of LFA cassette employed in the study. S, C and T corresponds to the sample pad, test line and control line, respectively. Representative photographs of LFA cassette displaying (A) positive and (B) negative result from p-LFA strips with colorimetric control line. Representative fluorescence images of the p-LFA strips displaying (C) positive and (D) negative result from p-LFA strips with fluorometric control line.

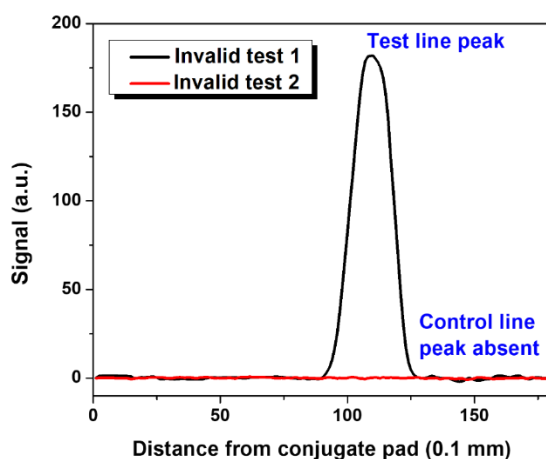


**Figure B- 27:** Representative invalid tests obtained using the portable scanner. If a test has no signal at the control line, it is reported as an invalid test.

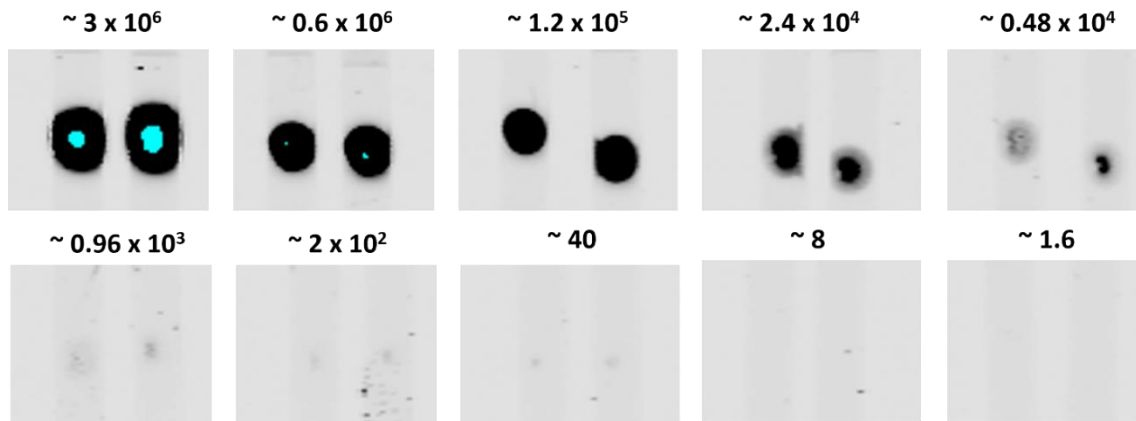


**Figure B- 28:** Fluorescence images of the LFA strips drop-casted with 0.5 µl of different numbers of plasmonic-fluors (mentioned in parenthesis).

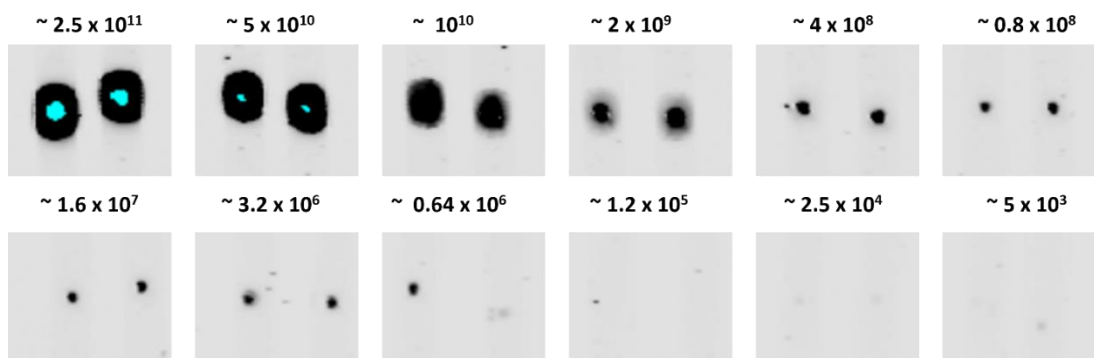


**Figure B- 29:** Fluorescence images of the LFA strips drop-casted with 0.5 µl of different concentrations of molecular-fluorophores (mentioned in parenthesis).

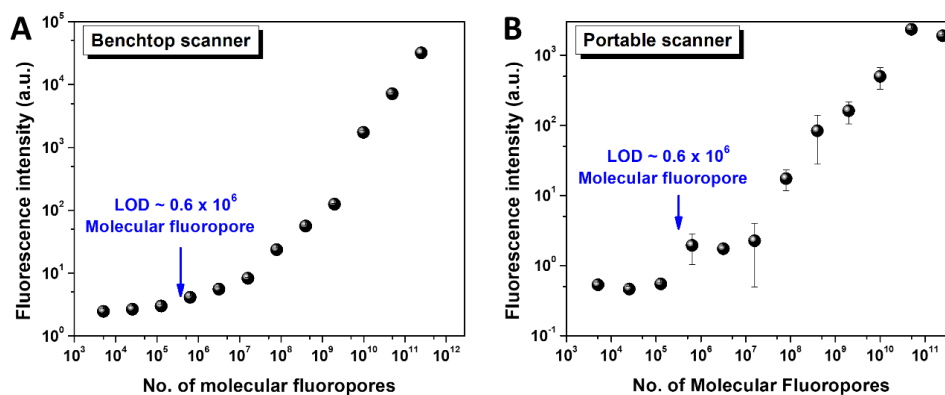


**Figure B- 30:** (A) Fluorescence intensities and (B) area under the curve values obtained from LFA strips, drop-casted with different concentrations of molecular fluorophores, when scanned using benchtop (LICOR) and portable scanner, respectively.



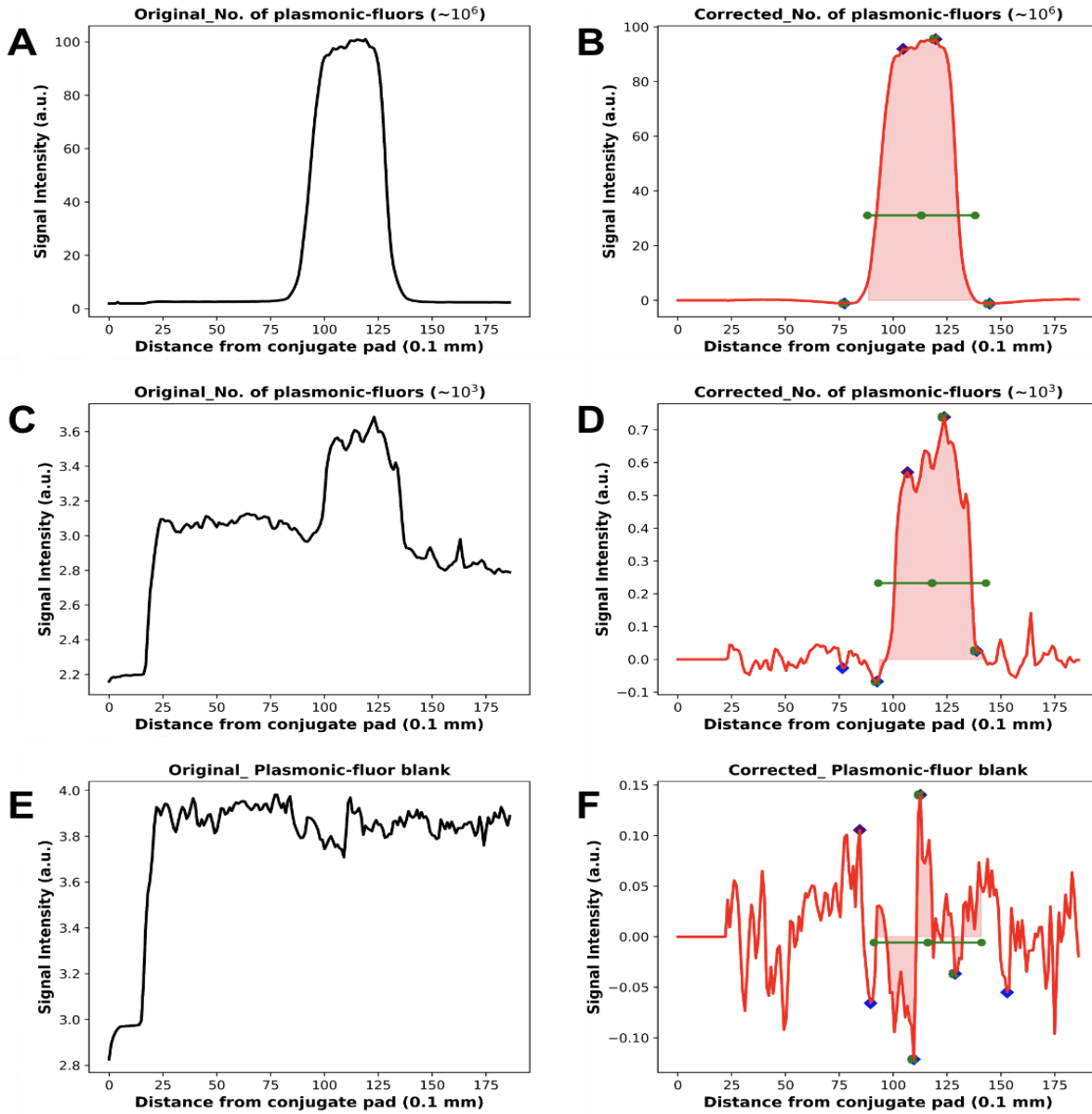


**Figure B- 31:** Representative examples of data processing conducted on data acquired by portable scanner from LFA strips drop-casted with (A, B)  $\sim 10^6$  and (C, D)  $\sim 10^3$  number of plasmonic-fluors, and (E, F) 1XPBS (blank).

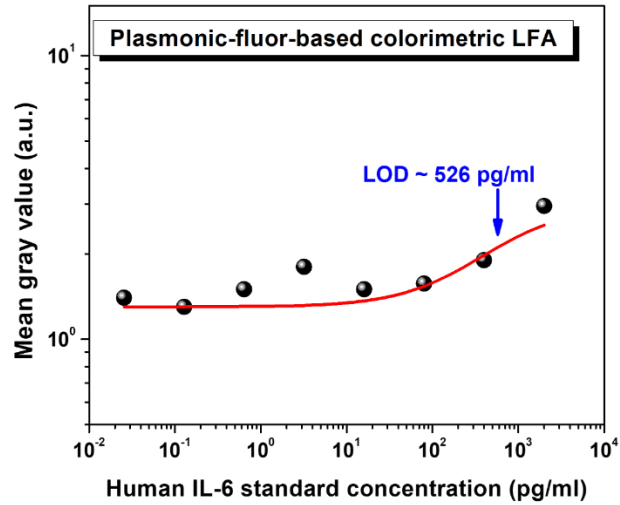


**Figure B- 32:** Dose-dependent mean gray values obtained from test line of the nitrocellulose membrane corresponding to different concentrations of IL-6 solutions acquired from plasmonic-fluor-based IL-6 LFA.

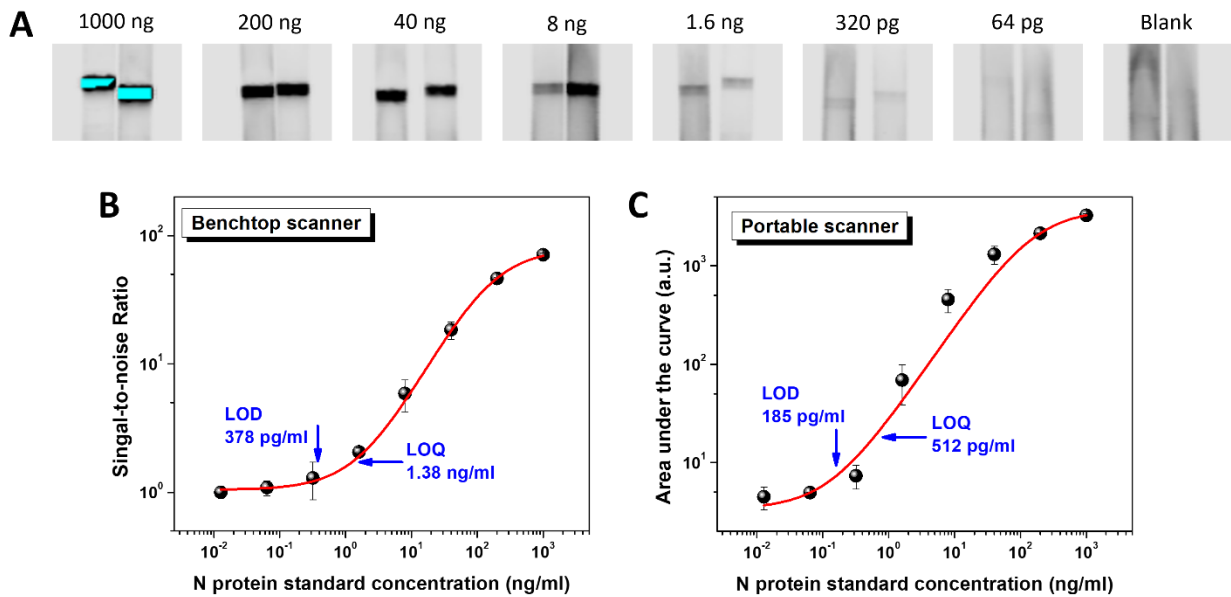


**Figure B- 33:** (A) Dose-dependent fluorescence images of the nitrocellulose membrane corresponding to different concentrations of N protein solutions acquired from plasmonic-fluor-based N protein LFA and measured by (B) benchtop scanner and (C) portable scanner.

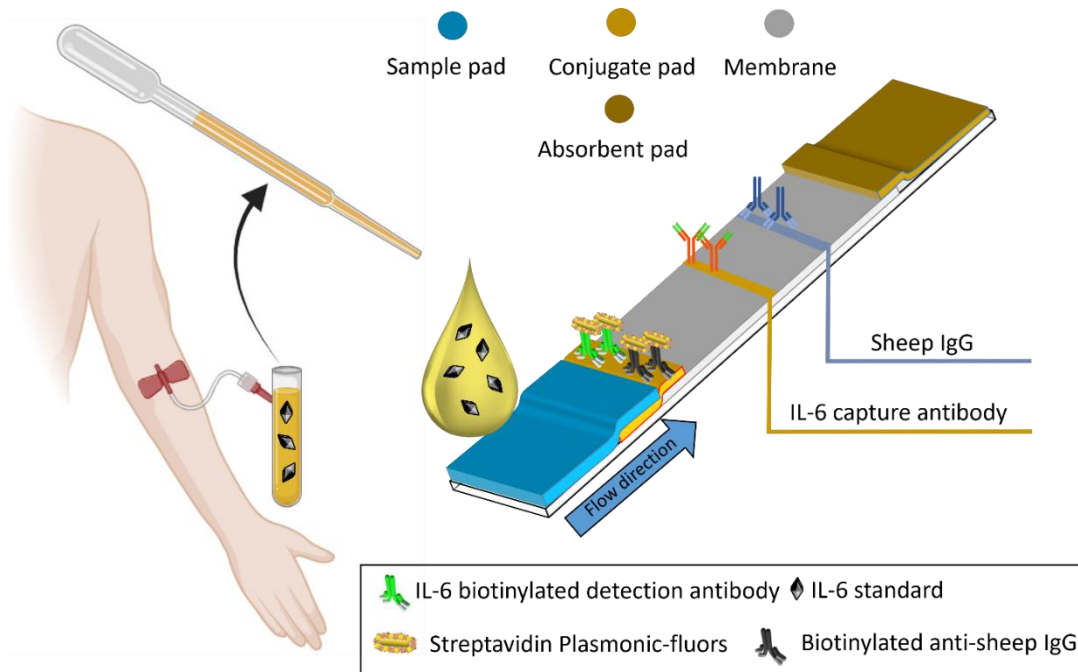


**Figure B- 34:** Schematic illustration of the full strip IL-6 p-LFA employed for the quantitative detection of IL-6 in the serum of COVID-19 positive (PCR confirmed) individuals.

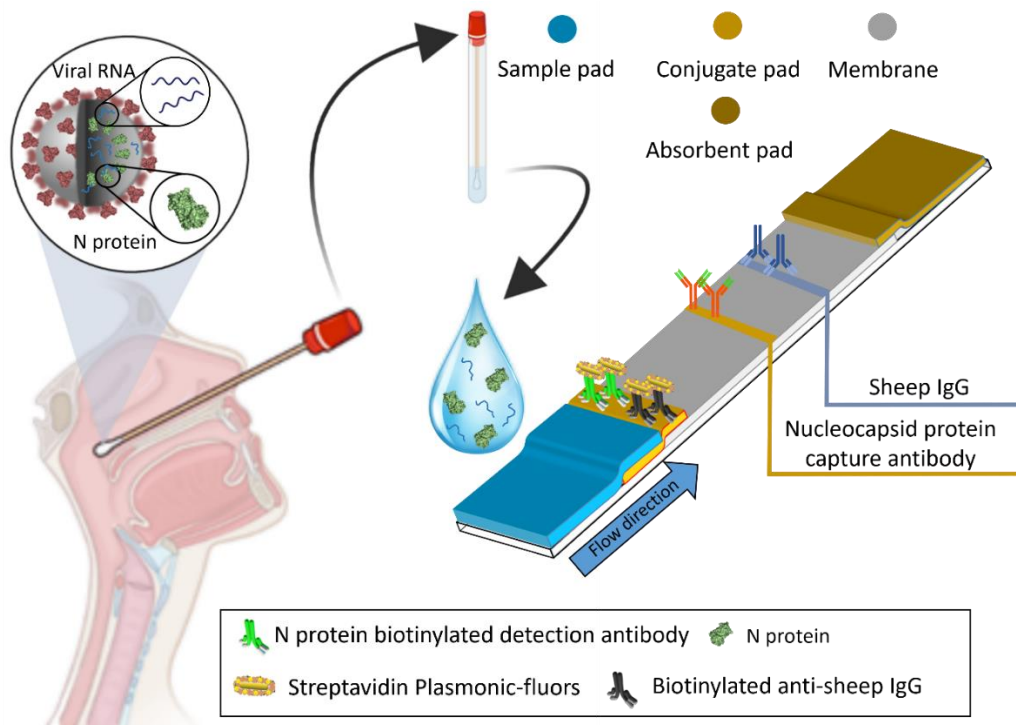


**Figure B- 35:** Schematic illustration of the full strip N protein p-LFA employed for the quantitative measurement of N protein concentration present in the nasal swab samples of COVID-19 positive (PCR confirmed) individuals.

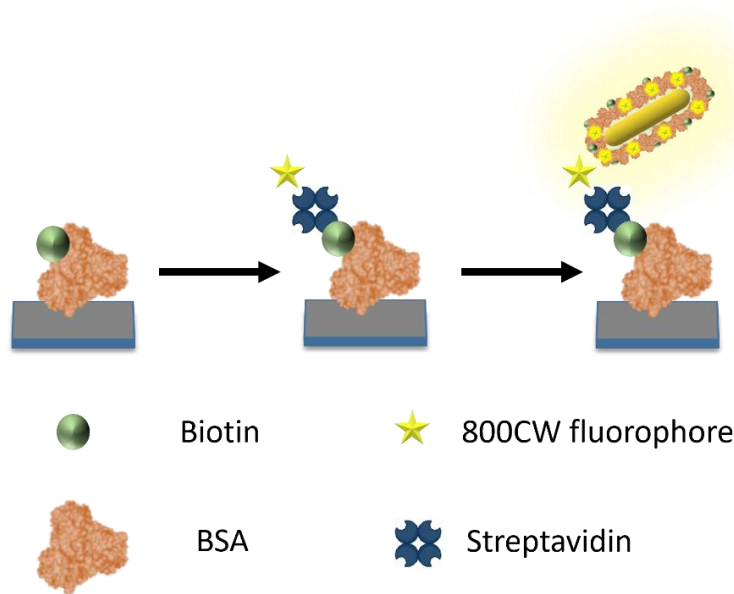


**Figure B- 36:** Schematic illustration of experiment designed to understand the enhancement of fluorescence signal using plasmonic-fluors compared to conventional fluorophores.

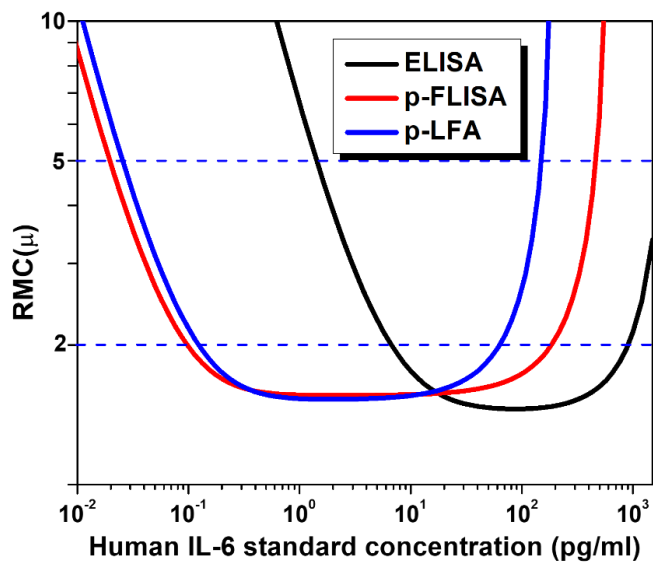


**Figure B- 37:** RMC curves for ELISA, p-FLISA and p-LFA calculated via equations listed in supplementary information. The blue dashed line indicates the RMC cutoffs that can be used to determine the quantitative performance of the assay over a certain range of concentrations. The relevant RMC parameters are listed in **Table B-1**.

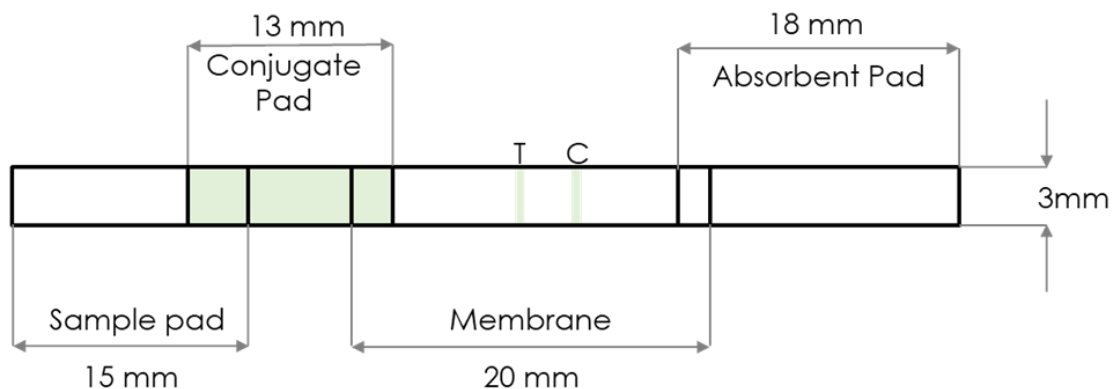


**Figure B- 38:** Schematic illustration of assembly of LFA components. The prepared sample pad, conjugate pad, membrane, and adsorption pad were then assembled with a 2 mm overlap between each pad and cut to strips with a width of 3mm using a strip cutter.

**Table B- 1:** RMC function and bioanalytical parameters of human IL-6 ELISA, p-FLISA and p-LFA to compare the performance of the assays in terms of their ability to resolve

Parameter	ELISA	p-FLISA	p-LFA
$\mu_{\min}$	1.46	1.56	1.45
Concentration at $\mu_{\min}$ (pg ml <sup>-1</sup> )	83.43	1.99	2.47
Range of $\mu < 2$ (pg ml <sup>-1</sup> )	6.71–900.9	0.1–184.1	0.13–86.08
Range of $\mu < 5$ (pg ml <sup>-1</sup> )	1.42–1762	0.02–463.8	0.03–181
Limit-of-detection (pg ml <sup>-1</sup> )	2900	0.016	0.093
Limit-of-quantitation (pg ml <sup>-1</sup> )	9100	0.058	0.298

**Table B- 2:** Details of the 19-PCR positive patient samples.

Sample #	Age	Comorbidities*	Duration of symptoms (days)	Symptoms	Radiographic findings at diagnosis/testing: Chest X-ray	Severity/Critical illness/ Intensive care requirement
----------	-----	----------------	-----------------------------	----------	---	---

					(CXR) or Computed Tomography (CT) imaging	
<b>S1</b>	33	Asthma	4	Chest pain and constipation-nonspecific symptoms.	clear lungs	nil
<b>S2</b>	57	none	7	Shortness of breath, Hypoxic Treated with remdesivir	Bilateral (b/l) interstitial infiltrates s/o viral pneumonia	nil
<b>S3</b>	49	none	14	Flu like symptoms 2 weeks ago.	CT chest : Interstitial thickening and parenchymal infiltrates	nil
<b>S4</b>	59	none	3	Cough malaise, Shortness of breath x 3 days, Hypoxia+	b/l lower lobe infiltrates.	ICU admit for seizure unrelated to COVID
<b>S5</b>	62	COPD	2	Shortness of breath.	clear lungs	nil
<b>S6</b>	77	HTN, CKD	1	Shortness of breath.	b/l lower lobe infiltrates	Non – invasive ventilation, ICU admit
<b>S7</b>	27	Psychosis	asymptomatic	None. COVID PCR + 2 weeks prior	clear lungs	nil
<b>S8</b>	55	HIV (poorly controlled)	14	Cough, Shortness of breath 2 weeks. Hypoxia+	left lower pneumonia	nil
<b>S9</b>	53	ESRD, DM	2	Shortness of breath, Fever, Loss of taste.	b/l diffuse interstitial opacity	nil

<b>S10</b>	37	none	asymptomatic	Presurgical screening. Tibial fracture	clear lungs	nil
<b>S11</b>	71	DM	3	Loss of taste, Malaise, Shortness of breath	Patchy consolidation b/l	nil
<b>S12</b>	41	DM	3	Chest pain- diagnosed as costochondritis.	clear lungs	nil
<b>S13</b>	58	DM	3	Flu like illness, fever, myalgia	clear lungs	nil
<b>S14</b>	69	DM, CAD	3-5	Few days flu like symptoms,	b/l diffuse interstitial opacities	ICU admit Ventilated for hypoxic respiratory failure. Died
<b>S15</b>	44	none	14	Cough, Shortness of breath for 2 weeks	clear lungs	nil
<b>S16</b>	70	none	2	Fever, Cough, Shortness of breath	b/l mild interstitial opacities	nil
<b>S17</b>	61	HTN	6	Cough, Shortness of breath	b/l interstitial and airspace opacities	nil
<b>S18</b>	42	Obesity CHF	2	Shortness of breath, cough, diarrhea, and myalgias	Multifocal PNA	ICU admit. Increase from home vent settings
<b>S19</b>	47	COPD	7	Shortness of breath.	clear lungs	nil

\*DM= diabetes mellitus, COPD= chronic obstructive pulmonary disease, ESRD = End stage renal disease, HIV= human immunodeficiency virus infected, CHF= congestive heart failure, CAD coronary heart disease

**Table B- 3:** Results of the 19 PCR-positive patient samples (wild type SARS-CoV-2) tested by fluorometric and colorimetric p-LFA, and commercial antigen test (BD veritor™). Table also lists the N protein concentration of these samples obtained from fluorometric p-LFA demonstrating its quantitative analysis ability.

Sample #	CT value (average of 2 tests)	p-LFA fluorometric result (concentration in ng/ml)	P-LFA colorimetric result (concentration in ng/ml)	FDA-approved BD veritor™ (commercial antigen kit) result
S1	40.7	Positive (20.58)	Negative	Negative
S2	19.2	Positive (5.75)	Negative	Positive
S3	27.9	Positive (58.93)	Positive (below LOQ)	Negative
S4	30.5	Negative	Negative	Negative
S5	42.8	Positive (54.72)	Positive (below LOQ)	Negative
S6	22.6	Positive (6.93)	Negative	Positive
S7	39.5	Positive (4.93)	Negative	Negative
S8	21.8	Positive (856)	Positive (570.6)	Positive
S9	18.2	Positive (222)	Positive (292.3)	Positive
S10	36.3	Positive (1.49)	Negative	Negative
S11	18.8	Positive (2.45)	Negative	Positive
S12	39.5	Positive (213.9)	Positive (268.6)	Negative
S13	20.7	Positive (73.12)	Positive (below LOQ)	Positive
S14	23.8	Positive (160.3)	Positive (below LOQ)	Negative
S15	32.7	Positive (8.09)	Negative	Negative
S16	29.3	Positive (112.6)	Positive (below LOQ)	Negative



<b>S17</b>	27.8	Positive (2.31)	Negative	Positive
<b>S18</b>	23.5	Positive (27.47)	Negative	Positive
<b>S19</b>	42.3	Positive (7.1)	Negative	Negative

**Table B- 4:** Results of the 16 PCR-positive Delta B.1.617.2 variant samples (confirmed by gene sequencing) tested using fluorometric and colorimetric p-LFA. Table also lists the N protein concentration of these samples obtained from fluorometric p-LFA demonstrating its quantitative analysis ability.

<b>Sample #</b>	<b>CT value 1</b>	<b>CT value 2</b>	<b>p-LFA fluorometric result (concentration in ng/ml)</b>	<b>p-LFA colorimetric result (concentration in ng/ml)</b>
<b>D1</b>	20.26	20.09	Positive (44.63)	Negative
<b>D2</b>	22.5	24.3	Positive (358.6)	Positive (299.3)
<b>D3</b>	24.8	26.8	Positive (367.5)	Positive (233.9)
<b>D4</b>	25.02	25.15	Positive (1.81)	Negative
<b>D5</b>	22.6	24.3	Positive (348.1)	Positive (268.2)
<b>D6</b>	23.1	24.8	Positive (2.51)	Negative
<b>D7</b>	20.7	22.5	Positive (135.7)	Positive (below LOQ)
<b>D8</b>	18.4	20.1	Positive (63.17)	Positive (below LOQ)
<b>D9</b>	13.3	14.2	Positive (43.56)	Negative
<b>D10</b>	17.98	18.17	Positive (124.5)	Positive (below LOQ)
<b>D11</b>	15.25	15.17	Positive (3.18)	Negative
<b>D12</b>	18.86	18.85	Positive (2.66)	Negative
<b>D13</b>	22.56	22.23	Positive (29.39)	Negative
<b>D14</b>	15.24	15.08	Positive (below LOQ)	Negative
<b>D15</b>	17.59	16.95	Positive (120)	Positive (below LOQ)

<b>D16</b>	15.9	15.44	Positive (19.05)	Negative
------------	------	-------	------------------	----------

**Table B- 5:** Results of the 17 PCR-positive omicron BA.1 samples (confirmed by gene sequencing) tested using fluorometric and colorimetric p-LFA. Table also lists the N protein concentration of these samples obtained from fluorometric p-LFA demonstrating its quantitative analysis ability.

<b>Sample #</b>	<b>CT value 1</b>	<b>CT value 2</b>	<b>p-LFA fluorometric result (concentration in ng/ml)</b>	<b>p-LFA Colorimetric Result</b>
<b>O1</b>	19.22	19.19	Positive (3.74)	Negative
<b>O3</b>	18.32	17.45	Invalid test (control line was not visible)	Negative
<b>O4</b>	19.59	19.28	Positive (1.76)	Negative
<b>O5</b>	18.51	18.25	Positive (below LOQ)	Negative
<b>O6</b>	17.71	17.54	Positive (below LOQ)	Negative
<b>O7</b>	18.81	18.42	Positive (below LOQ)	Negative
<b>O8</b>	20.04	19.98	Positive (below LOQ)	Negative
<b>O9</b>	18.56	18.17	Positive (below LOQ)	Negative
<b>O10</b>	19.08	18.28	Positive (below LOQ)	Negative
<b>O12</b>	18.93	18.53	Positive (2.35)	Negative
<b>O13</b>	19.11	18.51	Positive (2.2)	Negative
<b>O14</b>	18.69	18.42	Positive (below LOQ)	Negative
<b>O15</b>	20.22	19.66	Positive (0.99)	Negative
<b>O16</b>	20.41	19.84	Positive (2.54)	Negative
<b>O17</b>	18.77	18.2	Positive (below LOQ)	Negative
<b>O18</b>	17.94	17.53	Positive (0.99)	Negative
<b>O19</b>	19.97	19.95	Positive (1.13)	Negative
<b>O20</b>	18.2	17.71	Positive (2.71)	Negative

**Table B- 6:** Details of 17 PCR-positive omicron BA.1 samples (confirmed by gene sequencing).

Sample #	Age	Comorbidities*	Duration of symptoms (days)	Symptoms	Radiographic findings at diagnosis/testing: Chest X-ray (CXR) or Computed Tomography (CT) imaging	Severity/Critical illness/ Intensive care requirement
<b>S1</b>	82		2	Cough, Runny nose	NA	No
<b>S3</b>	34		2	Fever, Runny nose	NA	No
<b>S4</b>	35		1	Sore throat, Diarrhea	NA	No
<b>S5</b>	30		2	Fever; Cough; Muscle Aches	NA	No
<b>S6</b>	52		1	Cough, Sore throat	NA	No
<b>S7</b>	38		2	Fever,Cough,Sore throat	NA	No
<b>S8</b>	57		1	Fever, Cough	NA	No
<b>S9</b>	50		1	Cough	NA	No
<b>S10</b>	26		2	Chills, Nasal Congestion	NA	No
<b>S12</b>	28		2	Cough Headache, Nasal congestion	NA	No
<b>S13</b>	63		1	Headache, Nasal congestion	NA	No

<b>S14</b>	51		1	Fever, Runny nose	NA	No
<b>S15</b>	39		1	Cough	CXR : Normal	No
<b>S16</b>	27		1	Cough, Sore throat	NA	No
<b>S17</b>	46		1	Cough, Sore throat	NA	No
<b>S18</b>	25		2	Cough, Fever, Muscle aches	NA	No
<b>S19</b>	81	ESRD Lung cancer	2(9)	Cough,Dyspnea	CXR: Multifocal Pneumonia	Moderate disease (tested 9 days ago negative)
<b>S20</b>	30		2	Headache, Nasal congestion	NA	No

**Table B- 7:** N protein concentration determined by p-LFA strips and measured by portable and benchtop scanner.

<b>Sample #</b>	<b>N protein conc. determined by p-LFA and measured by portable scanner</b>	<b>N protein conc. determined by p-LFA and measured by benchtop scanner</b>
<b>S3</b>	36.09	55.62
<b>S5</b>	41.65	51.81
<b>S8</b>	216	259
<b>S9</b>	184.3	201.1
<b>S12</b>	154.6	197.2
<b>S13</b>	67.18	62.12
<b>S14</b>	101.2	154.9
<b>D2</b>	268.6	325.5

<b>D3</b>	253.7	329.5
<b>D5</b>	267.7	315.1
<b>D7</b>	138	113.7
<b>D8</b>	105.8	53.26
<b>D10</b>	97.9	112.6
<b>D15</b>	129	110.9

**Table B- 8:** IL-6 concentration determined by p-LFA strips and measured by portable and benchtop scanner; and determined by p-FLISA and measured by benchtop scanner.

<b>Sample #</b>	<b>IL-6 conc. (pg/ml) determined by p-LFA and measured by portable scanner</b>	<b>IL-6 conc. (pg/ml) determined by p-LFA and measured by benchtop scanner</b>	<b>IL-6 conc. (pg/ml) determined by p-FLISA and measured by benchtop scanner</b>
<b>1</b>	213.5	245.5	359.5
<b>2</b>	65.54	88.3	46.97
<b>3</b>	125.2	99.79	108.8
<b>4</b>	18.57	28.96	8.75
<b>5</b>	12.72	16.74	1.61
<b>7</b>	39.31	29.11	33.87
<b>8</b>	66.75	52.13	161
<b>9</b>	66.96	80.88	24.94
<b>10</b>	55.65	75.74	69.25
<b>11</b>	58.93	42.50	82.95
<b>12</b>	58.95	52.89	60.21

<b>13</b>	87.02	48.71	51.89
<b>14</b>	11.66	7.31	60.07
<b>15</b>	30.07	45.16	34.47
<b>17</b>	56.75	46.51	63.01
<b>18</b>	19.92	29.5	28.35
<b>19</b>	326.6	383.4	17.31
<b>21</b>	489.3	337.5	549.4
<b>22</b>	953.2	1046	1003
<b>23</b>	302.4	379.2	119.9
<b>24</b>	36.24	27.91	61.91
<b>25</b>	602.1	749.5	746.3
<b>26</b>	168	198.9	125.2
<b>27</b>	101.4	67.92	97.06
<b>28</b>	61.73	45.75	12.01
<b>29</b>	56.98	41.42	99.58
<b>30</b>	70.45	101.7	16.73
<b>32</b>	348.3	293.1	516.5